ABSTRACT

Title of dissertation: A DEEP X-RAY SURVEY OF THE LOCKMAN HOLE NORTHWEST

Yuxuan Yang, Doctor of Philosophy, 2005

Dissertation directed by: Professor Richard F. Mushotzky
NASA Goddard Space Flight Center

I present the X-ray analysis of the *Chandra* Large Area Synoptic X-ray Survey (CLASXS) of the Lockman Hole Northwest field. The contiguous solid angle of the survey is ~ 0.4 deg^2 and the flux limits are 5×10^{-16} erg cm^{-2} s^{-1} in the $0.4-2$ keV band and 3×10^{-15} erg cm^{-2} s^{-1} in the $2-8$ keV band. The survey bridges the gap between deep pencil beam surveys, and shallower, larger area surveys, allowing a better probe of the X-ray sources that contribute most of the 2–10 keV cosmic X-ray background. A total of 525 X-ray point sources and 4 extended sources have been found. The number counts, X-ray spectra evolution, X-ray variability of the X-ray sources are presented. We show 3 of the 4 extended sources are likely galaxy clusters or galaxy groups. We report the discovery of a gravitational lensing arc associated with one of these sources.

I present the spatial correlation function analysis of non-stellar X-ray point sources in the CLASXS and Chandra Deep Field North (CDFN). I calculate both redshift-space and projected correlation functions in comoving coordinates. The correlation function for the CLASXS field over scales of 3 Mpc$< s <$ 200 Mpc

can be modeled as a power-law of the form $\xi(s) = (s/s_0)^{-\gamma}$, with $\gamma = 1.6^{+0.4}_{-0.3}$ and $s_0 = 8.05^{+1.4}_{-1.5}$ Mpc. The redshift-space correlation function for CDFN on scales of 1 Mpc$< s <$ 100 Mpc is found to have a similar correlation length, but a shallower slope. The real-space correlation functions are derived from the projected correlation functions. By comparing the real- and redshift-space correlation functions, we are able to estimate the redshift distortion parameter $\beta = 0.4 \pm 0.2$ at an effective redshift $z = 0.94$. We found the clustering does not dependence significantly on X-ray color or luminosity.

A mild evolution in the clustering amplitude is found, indicating a rapid increase of bias with redshift. The typical mass of the dark matter halo derived from the bias estimates show little change with redshift. The average halo mass is found to be log $(M_{halo}/M_{\odot}) \sim 12.4$.

A DEEP X-RAY SURVEY OF THE LOCKMAN HOLE NORTHWEST

by

Yuxuan Yang

Dissertation submitted to the Faculty of the Graduate School of the
University of Maryland, College Park in partial fulfillment
of the requirements for the degree of
Doctor of Philosophy
2004

Advisory Committee:

Professor Richard F. Mushotzky, Advisor
Professor Christopher S. Reynolds, Co-advisor, Chair
Professor M. Coleman Miller
Professor Gregory W. Sullivan
Professor Sylvain Veilliux

To my family

PREFACE

In the early 2000, soon after the launch of the *Chandra* observatory, it has been found that most of the 2–10 keV Cosmic X-ray background (CXB) can be resolved into point sources, presumably AGNs. This result was confirmed later by a set of deep *Chandra* and *XMM-Newton* observations. It has also been shown that about 2/3 of the *Chandra* detected AGNs in the deep fields show no broad emission lines, and many of them looks normal in optical band. This means that the majority of AGNs were previous unknown! There are many unexpected results came out of these surveys.

However, most deep surveys were performed on small fields of size < 0.1 deg^2, and could be affected by cosmic variance. To better understand the X-ray selected AGNs, particularly the sources at the "knee" of the number counts curve, Richard invested his *Chandra* GTO time, and later Dr. Amy Barger obtained additional observing time on *Chandra* to perform a medium depth, wide field survey (we later call CLASXS). The data from this survey and the *Chandra* deep field North were systematically followed up with *Keck* and *Subaru*. The data set forms the largest sample of *Chandra* selected AGNs with a high level of redshift measurements.

I joined this project in the Fall of 2001, in the wave of excitement of the new discoveries from *Chandra* and *XMM*. The question I had in mined was how X-ray selected AGNs traces the large scale structure of the universe. The clustering of AGNs carries important information about the host galaxies. Combined with the

X-ray luminosity function, we can better understand the environment of AGNs. Because of the much higher spatial density of the X-ray selected AGNs compared to the optical selected samples, deep X-ray surveys best probe the quasi-linear regime of the structure formation. After three years of hard work (including two non-sleeping Christmas nights calibrating positions of X-ray sources before the *Keck* observing runs), we are now able to reach some interesting results. We have obtains so far the best X-ray luminosity function, and the best X-ray spatial correlation function of X-ray selected AGNs. Six papers have come out on this survey.

At the early phase of the project we spent a large amount of time on the angular clustering of the X-ray sources. Part of the reason is that we did not have redshift data for most of the sources until early 2004, making it impossible to study the spatial clustering. However, the signal-to-noise ratio (S/N) of the angular correlation function, particularly for the soft band detected sources, is very weak. By adding more small blank fields from the *Chandra* archive, we only managed to slightly increase the S/N. This is because the increase of S/N by adding non-contiguous fields roughly proportional to the square-root of the number of fields. The best way to make improvements is to obtain a larger contiguous field. We have been bidding for more *Chandra* field for three years without success. The interpretation of the angular correlation also need additional assumption on the evolution of AGN clustering. Fortunately, with spectroscopic redshift of a large fraction of the sources, the clustering of X-ray selected AGNs can be much better determined. For this reason, I decide not to include the study of angular correlation function in this dissertation.

This work sits on the intersection of the research of the Active galactic Nuclei, the CXB, and the large scale structure of the universe. I will focus mainly on AGNs rather than cosmology. This is justified because by comparing with our knowledge of the large scale structure, the formation of supermassive blackholes is much less known. Larger X-ray survey will eventually show that AGN is a useful tool for cosmology.

Before I joined this project, I have worked on observations of local AGNs, particularly NGC 4151, with Prof. Andrew Wilson. I have also spent a summer working on X-ray observation on supernova remnants with Dr. Rob Petre. These studies gave me good introduction to X-ray astronomy and AGN.

During the years at Maryland, I have authored or co-authored 9 papers. I am first author of 4 of them.

ACKNOWLEDGMENTS

I would like to thank my adviser, Professor Richard Mushotzky for giving me the invaluable opportunity to work on this extremely exciting project, and giving me the most need guide through the research. He always point me to the most up-to-date literature and helped to resolve almost every question I brought to his door. His knowledge on a broad range of topics is really extraordinary. I also would like to express my gratitude to all the time he spent on correcting my English on every paper and proposal that I wrote, escorting me at Goddard for a long period after 9/11. I feel I am very lucky to have a chance to work with such an extraordinary adviser.

I am deeply indebted to Dr. Chris Reynolds. He has given me many useful suggestions and helps during the study. He has generously provided the computer on which I was able to carry out my research. Without his efforts, this project will be much more delayed.

My special thanks to my collaborators: Profs. Amy Barger, Len Cowie and Dr. Aaron Steffen. Without their hard work on planning and carrying out the optical observations, this thesis is impossible.

I owe my gratitude to Prof. Andrew Wilson and Dr. Rob Petre. They have opened the door of X-ray astronomy for me.

I thank all the Professors who have taught excellent graduate courses at As-

tronomy and Physics Department, particularly Profs. Virginia Trimble, Sylvain Veilleux, Mike A'Hearn, Patrick Harrinton, Cole Miller, Stacy McGaugh and Derek Richardson.

I thank colleagues at both GSFC and Maryland for the discussions and helps on many things. I also like to thank all the administration and system supporting staff at GSFC and and Maryland for their hard work to make our life easier. Many thanks to Dr. John Trasco and Ms. Mary Ann Phillips for all the work they have done to help us sale smoothly through our study, and the help on various extra paper works to assist my security clearance at GSFC.

Lastly, I owe my deepest thanks to my wife, Haihong, for her support and encouragements.

TABLE OF CONTENTS

LIST OF FIGURES

Chapter 1

Introduction

1.1 Active Galactic nuclei: An Overview

Active galactic nuclei or AGNs, refers to a family of active galaxies, all of which show the existence of energetic phenomena in an unresolved central region. The luminosity of AGN ranges from $L \sim 10^{39} - 10^{46}$ erg cm^{-2} s^{-1}, usually brighter than the total light from the host galaxy. The continuous energy output and energy distribution of AGNs cannot be explained directly by stars.

Most researchers now come to believe that all AGNs are powered by radiation from accretion onto black holes. The most striking evidence supporting the radiating blackhole scenario come from the X-ray spectral observations. Many AGNs clearly show a skewed broad florescent Fe Kα, which can be beautifully explained by an origin only a few Schwarzchild radii away from the central blackhole. The shape of the line is an effect of general relativity (See Reynolds & Nowak 2003 for a review). The commonly accepted picture of AGNs is that a supermassive blackhole (SMBH) with mass in the range $10^6 - 10^9\,\mathrm{M}_\odot$ is accreting and releasing $\sim 10\%$ of the rest mass energy from the accreting gas. The luminosity of an AGN is bounded by the Eddington luminosity, at which the pressure from Thompson scattering balances the gravitational force on the gas particles. In this dissertation I will use the term AGN to refer to radiating SMBHs.

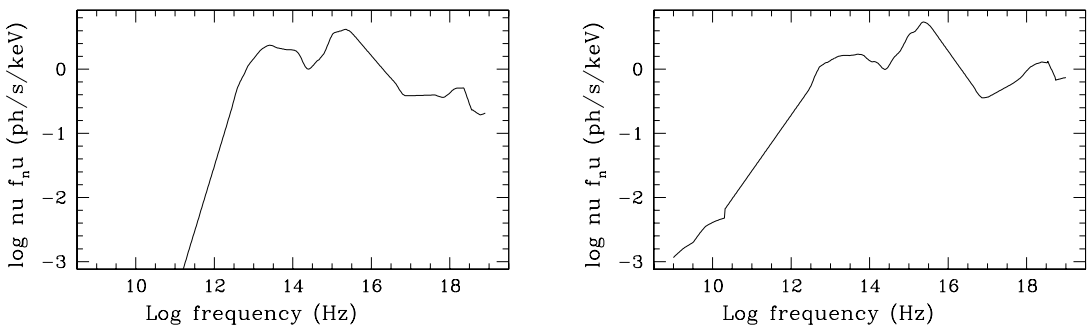

Figure 1: The medium spectral energy distribution large samples of radio quite (left panel) and radio loud (right panel) quasars. Figure from Elvis et al. (1994).

AGNs radiates in all electromagnetic waves. The broad band spectral energy distribution (SED) of the optically selected AGNs can be described by a power-law with roughly equal energy per decade from $10^{13}-10^{20}$ Hz (Elvis et al. 1994 Figure 1), with a "big blue bump" in UV and another weaker bump in IR band. Superimposed on this spectra are strong optical and UV lines from hydrogen, highly ionized C, N, and O, and a complex of low-ionized Fe lines.

1.2 Zoo of AGNs and the "Unified models"

Classification sometimes is helpful in finding orders in the seemingly chaotic data, but sometimes just generate more confusion. The classification of AGNs seems more of the latter. To make things worse, the AGN nomenclature sometimes has nothing to do with classification. When calling an AGN a Seyfert 1 or BL Lac,

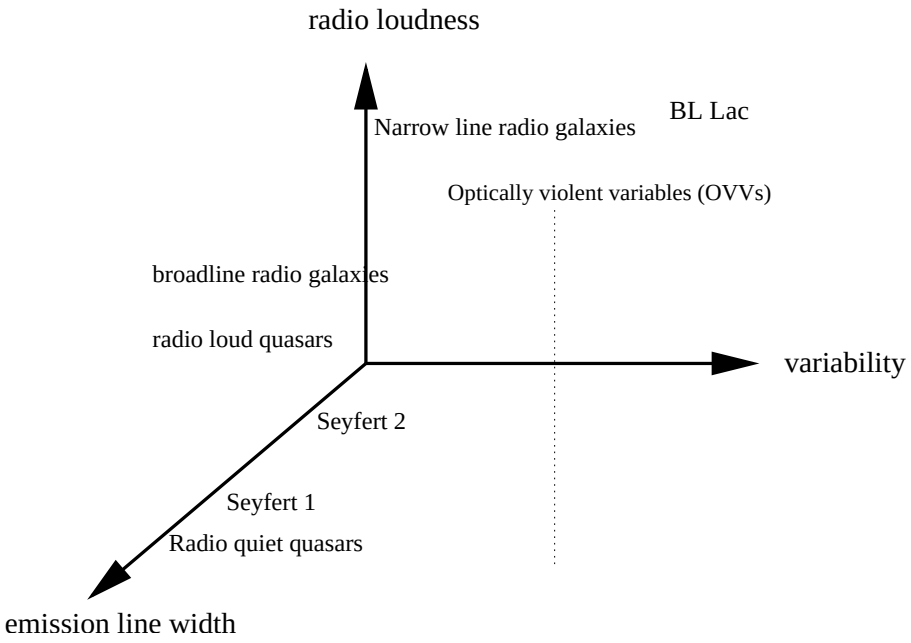

Figure 2: The observational features for different AGN types. Figure adapted from Krolik (1999)

it does not really tell what the object is, but a "radio loud AGN" certainly says something of its nature.

Despite the diversity in their names, AGNs can usually be characterized by three observation features: the emission line width, the radio loudness, and the variability. Krolik (1999) shows some of the common types and their observation in the diagram in Figure 2.

The disparate AGN varieties may simply be caused by the viewing angle of intrinsically identical objects. The models that try to unify the AGN appearances with viewing angle effects are called the *unified models*. The anisotropy of AGNs can be caused either by the intrinsically anisotropic emission from the accretion disk or jets, or by anisotropic obscuration. In the latter case, the obscuration may occur

very close to the SMBH by flared accretion disk, or in the interstellar medium. The unified model is successful in unifying the Seyfert galaxies. The obscuring clouds lies at a distance 10^{19} cm $\lesssim$ r $\lesssim$ 10^{20} cm from the nucleus, which can block the broadline region (BLR – the region where the broad emission lines originate). If the broad line is completely blocked from the line-of-sight, and only narrow lines are observed, then the source is a Seyfert 2. If there is no obscuring cloud in the line-of-sight, the source will have strong broadlines, and the source is classified as Seyfert 1.

Some times the terms "type 1" and "type 2" are used when detailed classification is not possible. Type 1s are sources with no evidence of obscuration while the type 2s are those showing clear obscuration. In optical, type 1s usually refer to sources with clear broad emission lines and type 2s are identified with narrow emission lines. In the X-ray band, on the other hand, type 1 and type 2 are distiguished using column density. It has been noted that the X-ray and optical types do not always agree (Matt 2002)

While more and more evidence supporting the existence of SMBH in AGNs and massive galaxies in general, little is known about how these massive gas swallowing monsters come to be and how they evolve. Since the AGN phase is believed to play an critical role in the formation and growth of SMBHs, the study of an unbiased sample of AGNs is the key to understand AGNs as a population. The best way to obtain such a sample is through large X-ray surveys and follow them up with optical observations, as we will discuss below.

1.3 AGN searching methods

1.3.1 Optical Selected AGNs

Based on their drastically different optical spectra and/or colors from normal galaxies or any superposition of stellar spectra with temperature of $10^3 - 10^5$ K, AGNs can be selected using the colors and color ratios (Sandage 1971). Over the last 30 years, many surveys uses the Schmidt's (1969) for selecting quasars. The source is a candidate quasar if it shows:

- non-stellar color in the nucleus;
- luminous semi-stellar nucleus;
- time variability;
- strong emission lines;
- a lack of proper motion;
- a Lyman break features or color at high redshift.

These criteria certainly have covered most characteristics of known AGNs, they are optimized for detecting quasars, and will not detect Seyfert 2 galaxies which do not have strong broad emission lines.

The most recent large optical survey is the Sloan Digital Sky Survey (SDSS) program, which uses 5 colors in selecting quasars (Fan et al. 1999). While programs such as the SDSS are very efficient in selecting quasars, they may not be able to produce a complete sample in the sense of sampling the SMBHs without bias. The

technique designed in the surveys based on the above criteria basically focus on excluding stars rather than selecting all the quasars, given that the stars are much more copious than quasars (at m = 18, there are 500 stars for each quasar, and the selection must be better than 0.2% to avoid severe contamination!). Even with careful color selection criteria, selections based only on color can lead to inclusion of large number of star forming galaxies. One extreme example is the Byurakan survey, which selected objects by searching for blue continua, 90% of the objects found are starbursts rather than Seyferts.

The host galaxy can overwhelm the light from AGNs in two situations. For an intrinsically low luminosity AGN, the star light, particularly the blue light from starbursts, can dilute the color of AGNs. Such effect is quantified by Richards et al. (2001). Below an optical luminosity of 6×10^{44} erg s^{-1}, the dilution effect cannot be ignored. It has been realized recently that a significant fraction of AGNs are obscured. The effect of extinction can greatly reduce the optical light. Such AGNs are very hard to be selected by optical technique.

Selection based on emission lines using low resolution spectra have little contamination. The completeness of such surveys is very hard to evaluate, given that the signal-to-noise depend on the equivalent width of the lines. Objects at different redshifts have to use different set of lines. The completeness of emission line detections is one of the fundamental problems with most high redshift surveys, since optical spectra is still the best method to obtain high quality redshift.

On long enough time scales virtually all AGNs variable (Veron & Hawkins 1995; Giveon et al. 1999). Searching AGNs using optical variability requires a large

amount of photometric monitoring. So far the method have not produce significantly large sample. However, the method will be very useful when the technology for large optical monitoring is available.

1.3.2 Radio and IR selected AGNs

Radio and IR emissions can penetrate gas and dust rather easily, making the radio and IR band less subject to obscuration than the optical band. Radio observations were the first to identify AGNs and jets. Radio observations, particularly those from VLBI or VLBA, can produce very accurate positions for optical follow-up.

However, it has been realized for 40 years that radio selected AGNs tends to have small overlapping with optically selected AGNs. Only 10% of the optically selected AGNs are "radio loud" (White et al. 2000), and less than 30% of the radio selected AGNs are "optical loud" – showing no sign of strong emission lines, and very weak non-thermal continuum (Ivezić et al. 2002; Magliocchetti et al. 2002; Sadler et al. 2002).

While IR radiation is an isotropic bolometric luminosity indicator, the biggest problem with IR selected AGN is contamination. The IR color is only subtly different from normal galaxies (Kuraszkiewicz et al. 2003) and the issue of how to separate out dusty AGNs from starburst galaxies is a issue long been debated (Veilleux 2002).

1.3.3 X-ray selected AGNs

X-ray radiation seems to be a universal characteristic of AGNs. Very few "X-ray quiet" AGN is known. There are several advantages to search AGNs in X-rays:

- High contrast between AGN and star light. This allows detection of very low luminosity AGNs. The X-ray radiation from stellar populations are mostly from high mass X-ray binaries and the so called ultra-luminous X-ray sources (ULXs). Only below a luminosity of $L_x \sim 10^{42}$ erg s^{-1} contributions from ULXs become important. Since most of the ULXs are not found in the nucleus, *Chandra* observatory, with its sub-arcsecond resolution, can separate out most of the off-nucleus sources (Hornschemeier et al. 2003) .

- Penetrating power of X-rays. Column densities which reduces the optical flux in V band by two orders of magnitude ($N_H \sim 10^{22}$ cm^{-2}) only reduce flux by ~ 3 in the 0.5–10 keV band. In the 2–10 keV surveys, about half of the bright objects are highly reddened in optical and often invisible in the UV. In a fixed energy band, redshift increases the energy of the band pass in the rest frame of the source by a factor of 1+z, which effectively reduces the effect of absorption from that source. At $z \sim 10$ the absorption need to be Compton thick to "kill" the X-ray flux (Figure 3).

- Larger amplitude of X-ray variability on shorter time scales compared with optical variability.

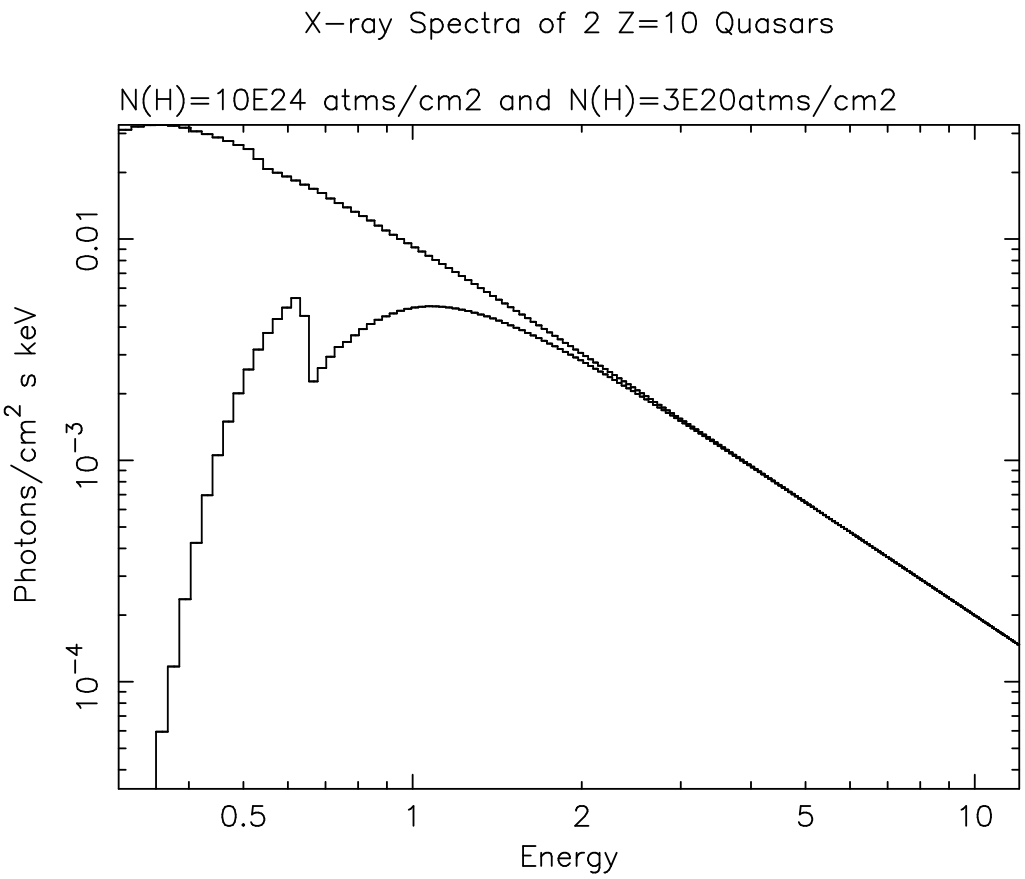

Figure 3: X-ray spectra of two AGNs at $z \sim 10$, one with no absorption and the other with a line-of-sight column density of 10^{24} cm^{-2} with pure photo-electric absorption. Figure from Mushotzky (2004).

The two fundamental selection effects in optical surveys, dilution and obscuration are therefore far less important in the X-ray band. The only uncertainty in the completeness of X-ray surveys is the fraction of sources which are Compton thick (with line-of-sight column density $N_H > 1.5 \times 10^{24}$ cm^{-2}). It has been argued that about 40% of the AGNs found locally are Compton thick. However, this statement is based on *known* AGNs rather than on a complete local sample, the true fraction of Compton thick sources is in fact unknown. Gamma-ray missions like *SWIFT* will

be able to survey large enough area to determine this fraction. The fundamental problem for X-ray surveys is that it is very difficult to obtain redshift using X-ray spectra, because most of the X-ray sources detected have too few counts. Therefore, X-ray observations have to be followed-up with optical telescope for the redshifts of the X-ray sources.

To sum up, the hard X-ray selected AGNs is a superset of AGNs selected in optical, IR and radio band. The major uncertainty in the completeness is the fraction of Compton thick sources.

1.4 X-ray Surveys prior to *Chandra*

1.4.1 Point sources

The first large X-ray survey were performed from *Uhuru* (Gursky & Schwartz 1977) and *Ariel-V* (Pounds 1979) small satellites in the 2–6 keV band in the 1970s. Detailed follow-up work of the previously unidentified, high-latitude X-ray sources in the early surveys (Ward et al. 1980) discovered that most of them were previously unknown AGNs showing non-thermal continua, narrow weak lines, and strong reddening compared to the optically selected AGNs.

Einstein and *ROSAT* surveys have provided very large samples of soft X-ray selected AGNs (Puchnarewicz et al. 1996; Fischer et al. 1998; Zickgraf et al. 2003). At flux $> 10^{-13}$ erg cm^{-2} s^{-1} there is only ~ 1 *ROSAT* source per square degree. The error circle of *ROSAT* is sufficiently small that unique identifications can be made on the X-ray position alone for sources brighter than $m \sim 20$ mag in the B

and V band. Below $> 10^{-13}$ erg cm^{-2} s^{-1}, the error boxes are too large for unique identification. In this case, optical broad line AGNs are searched within the error boxes. Soft X-ray selected AGNs shows a moderate correlation of optical and X-ray properties, with a narrow range of X-ray-to-optical ratio, and most of the objects are broadline AGNs in optical.

Before *Chandra*, the hard X-ray AGN samples were most obtained by *ASCA* (Akiyama et al. 2003) and *BeppoSax* (Fiore et al. 2000) through serendipitous surveys. The poor angular resolution (FWHM $\sim 1' - 3'$) limits the fluxes of the optical counterparts to $R < 21$ mag for *BeppoSax* HELLAS survey and $R < 19$ mag for *ASCA* Large Area Sky Survey to avoid confusion. The nature of the hard X-ray selected AGNs is rather different from the *ROSAT* sample, with $\sim 1/3$ do not show broadlines in optical. The X-ray-to-optical ratio is also more scattered than that of the soft X-ray selected samples.

1.4.2 Cosmic X-ray background

The cosmic X-ray background (CXB) was first discovered in 1962 (Giacconi et al. 1962) from rocket flights, with an intensity of $\sim$ 1.7 photons (2–10 keV) cm^2 s^{-1} sr^{-1}. The isotropic nature of CXB above 2 keV indicates its extragalactic origin. The background radiation appears very uniform. *ASCA* observations shows that on angular scales of 0.5 degree^2, the rms variance is $< 6\%$ (Kushino et al. 2002). The spectra of the CXB below 10 keV can reasonably be described as a single power-law with photon index of $\Gamma = 1.4$, but deviates strongly at higher en-

ergies. On the other hand, a thermal plasma with single temperature of 40–60 keV seem to produce better fit over the energy range probed by *HEAO-1 A2* experiment (Marshall et al. 1980). Soon after the discovery of the CXB, however, it was realized that the hard XRB cannot be dominated by truely diffuse emission from hot gas, because such hot gas would leave on the Cosmic Microwave Background a trace of inverse Compton scattering. Such a signature was not observed. Later imaging observations from *Einstein* have found that a significant fraction of the CXB can be resolved into point sources. After removing these point sources from the CXB spectrum, the single temperature thermal model no longer produce good fit.

The known bright X-ray sources in the universe which are abundant enough to account for the observed CXB are AGNs. *ROSAT* deep surveys of the 0.5–2 keV extragalactic CXB had resolved $\sim 80\%$ of the emission into point sources to a flux limit of 10^{-16} erg cm^{-2} s^{-1} (Hasinger et al. 1998). However, there is a difficulty in extrapolating this result to hard band CXB. Most of the *ROSAT* observed X-ray are broad line AGNs in optical observations, with X-ray power-law index around 1.9, very different from the spectral shape of the hard CXB. A different population of AGN, either with very flat spectral index or obscured by gas and dust with column density $N_H > 10^{22}$ cm^2 is needed to account for the hard CXB spectra. It has been suggested that most of these AGNs are probably type 2 quasars, a luminous version of Seyfert 2 galaxies.

The "mystery" of CXB has played a very important role in our understanding of the evolution history SMBHs. The CXB provide an integration constrain on the spectrum, luminosity function, and redshift distribution of AGNs.

1.5 *Chandra* deep surveys

The *Chandra* X-ray observatory (see Chapter 2) has greatly improved our view of AGNs. The great advantage of *Chandra* is its exquisite spatial resolution. Combined with the excellent position accuracy, *Chandra* is able to survey as deep as 10 Ms without the problem of source confusion. Unique source identification can be achieved at a very faint optical magnitudes ($I \sim 28$). Unlike observations in other wavelength (except in radio), the certainty of the optical counterpart does not rely on spectroscopic confirmation.

Chandra also have very low background (only $10^{-7}\mathrm{s}^{-1}\mathrm{pixel}^{-1}$ in the 0.5–8 keV for ACIS-I CCD detector), making it capable of detecting sources with only a few counts. It is therefore possible to detect large number of sources. The sensitivity of the deepest *Chandra* surveys (Chandra Deep Field North or CDFN with 2 Ms and Chandra Deep Field South or CDFS with 1 Ms) reaches 7000 deg^{-2} (Bauer et al. 2004), which is 10–20 times higher than the deepest optical spectroscopic surveys.

The findings of the *Chandra* deep surveys is rather surprising (see Brandt & Hasinger 2005 for a review). Less than 30% of the optical counterparts have strong broadlines, while many of the rest 70% are pure absorption line objects (Barger et al. 2003), or have very low optical fluxes. Sources with $I > 25$ are hard to identify spectroscopically. Many of these appear to be obscured AGNs at $z \sim 1 - 4$ when multi-wavelength properties are considered (Barger et al. 2003; Alexander et al. 2001). Some sources have no optical detection, even at the faintest optical limits, and are termed as extreme X-ray/optical radio sources; most of these sources

are detected in near IR images (Koekemoer et al. 2004).

The X-ray spectra of the sources detected by *Chandra* is flatter than the *ROSAT* sources. The composition of the point sources fit the spectra of 2–10 keV CXB very well (Mushotzky et al. 2000). Deep *Chandra* surveys and later the *XMM-Newton* surveys have shown that $> 90\%$ of the hard X-ray CXB is resolved, and the uncertainties are the normalization of CXB itself and the cosmic variance, particularly at $\sim 10^{-14}$ erg cm^{-2} s^{-1}, where the AGN contribution to the CXB peaks (Cowie et al. 2002 see Figure 4). The latter issue can be resolved by wide field surveys as described in Chapter 3.

The results from *Chandra* have shown that the X-ray observations are far more efficient than any other technique in finding AGNs. AGNs dominate the X-ray sources in the sky above a hard X-ray flux of 10^{-16} erg cm^{-2} s^{-1}. Most of the X-ray selected AGNs are unlikely to be selected with optical surveys. A large fraction of the *Chandra* detected AGNs are likely to be obscured AGNs. Instead of being type 2 quasars, as expected previously, most of the sources discovered have luminosity of Seyfert galaxies and most are found at $z < 1$. These results greatly improve our view of the evolution of SMBHs.

1.6 Evolution of SMBHs: a new perspective

1.6.1 Evolution of the X-ray Luminosity function

It has been noticed soon after the discovery of quasars that the spatial density of quasars increase sharply with redshift and peak at $z \sim 2-3$. Schmidt (1968, 1970)

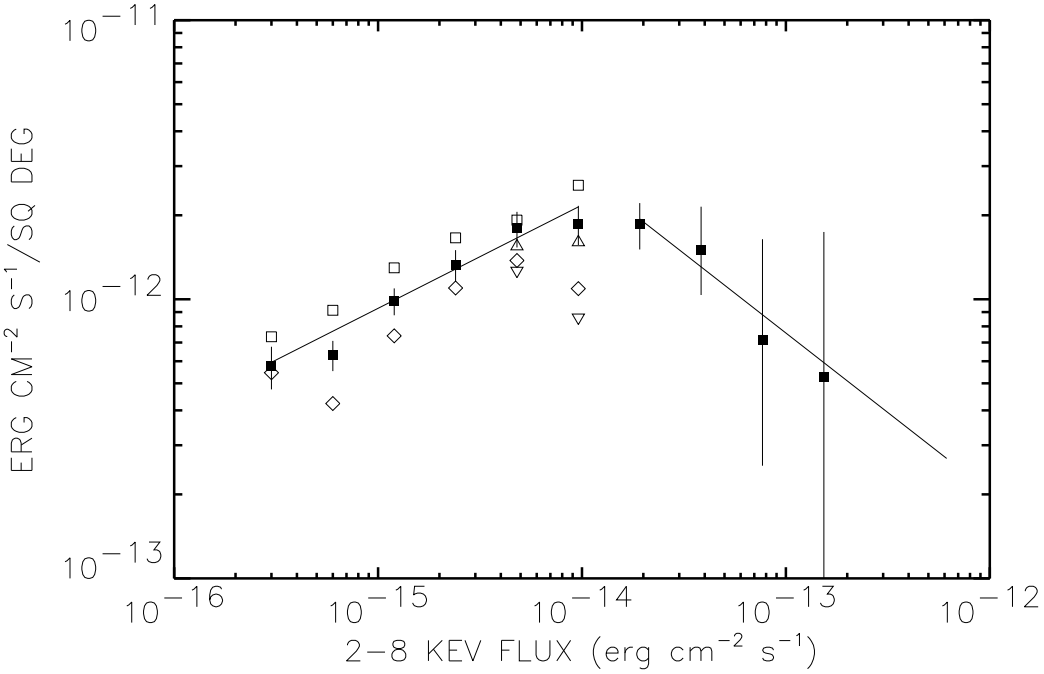

Figure 4: The contribution to the XRB versus flux. The solid boxes are the measured values in the combined sample. The lines show the values from the power-law fits. The open boxes show the CDFN, the open diamonds the CDFS, the open upward pointing triangles the SSA13 field, and the open downward pointing triangles the SSA22 field. The individual fields are shown only below 10^{-14} erg cm^{-2} s^{-1} where the error bars are small. Figure from Cowie et al. (2002).

found roughly a factor of 100 increase of the quasar spatial density from redshift 0 to 2. The same trend was found in radio galaxies. Why there is such a strong evolution is very puzzling. In some low redshift AGNs, spectra of young stars can be seen, indicating star formation may be important in fueling the AGN activity. However, the cosmic star formation seem to peaks at redshift of 1 rather than 2–3. The gap between AGN and star formation history has long been a mystery.

With extensive optical follow-up from *Keck* telescope, Barger et al. (2005) show that the *Chandra* detected AGNs have a peak redshift of 1 instead of 2. The evolution of luminosity density inferred resembles remarkably with the best measured star formation history (Figure 5). This agrees in general with the expectation that AGNs and star formation evolves in a self-regulated manner: star formation fuels the AGNs while AGN feedback heat and clear the gas and ultimately halt the star formation.

The evolution of X-ray luminosity function over $z = 0 - 1.2$ can be best described by a pure luminosity evolution. Most of the luminosity density in this redshift range is produced by AGNs which does not show broadlines. The very steep decrease of luminosity density is interpreted as the decrease of AGN activity, or downsizing.

1.6.2 Clustering of AGNs: what can we learn?

Another fundamental question needs to be addressed is the environment of AGNs or, put another way, where SMBH are formed. However, the host galaxies

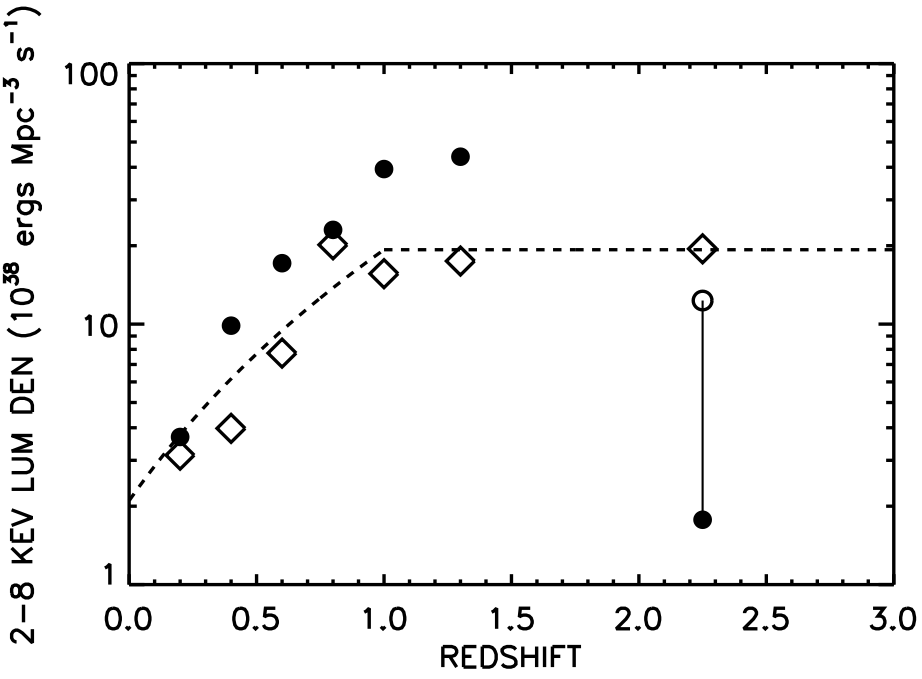

Figure 5: Incompleteness corrected evolution with redshift of the rest-frame $2-8$ keV comoving energy density production rate, $\dot{\lambda}_X$, of $L_X \geq 10^{42}$ ergs s^{-1} optically-narrow AGNs (*solid circles*). Open diamonds show the evolution of the broad-line AGNs. Vertical bar in the $z = 1.5 - 3$ redshift interval shows the range from the spectroscopically measured value for the optically-narrow AGNs (*solid circle*) to the maximally incompleteness corrected value (*open circle*; see text for details). Dashed curve shows the pure luminosity evolution maximum likelihood fit for broad-line AGNs over the range $z = 0 - 1$ and a flat line at $z > 1$. Figure from Barger et al. (2005).

of AGNs at high redshift are relatively difficult to observed because the surface brightness of galaxies decrease with $(1+z)^{-4}$.

Spatial clustering analysis provides an alternative approach to the question. In the standard Cold Dark Matter (CDM) structure formation paradigm, the mass in the universe can be approximated as spherical or ellipsoidal halos. The formation of large scale structure can be imagined as a process of constant merging and collapsing of these halos. The more massive halos tends to be more clustered. From the clustering property, we can infer the typical mass of the halos.

Large scale AGN surveys have been traditionally carried out in the optical band with dedicated telescopes. The most recent of these are the Sloan Digital Sky Survey (SDSS, Schneider et al. 2004) and the Two Degree Field Survey (2dF, Croom et al. 2005, C05 hereafter). These surveys have found that the bright quasars have a clustering property very similar to the clustering property of local normal galaxies. However, since the spatial density for quasars is very low, the typical scales probed by these surveys are a few hundred Mpc, where the clustering signal is very low. X-ray selected AGNs, particular the *Chandra* selected sources have a much higher spatial density. This make them ideal probe for large scale structure traced by AGNs.

The most extensive X-ray AGN surveys so far performed used the *ROSAT* telescope (Mullis et al. 2004). Since most of the sources in the *ROSAT* sample are broadline AGNs, it is not surprising that the clustering of *ROSAT* samples agrees with that found in optical surveys.

The clustering results on hard X-ray AGNs are so far contradictory. Earlier

studies of a small number of individual *Chandra* fields seem to indicate that the hard band number counts in these small fields has fluctuations larger than expected from Poisson noise (Cowie et al. 2002; Manners et al. 2003) but the result is contradicted with larger samples of *Chandra* fields (Kim et al. 2004). Basilakos et al. (2004) found a 4σ clustering signal in hard X-ray sources at $f_{2-8keV} > 10^{-14}$ erg cm^{-2} s^{-1} using angular correlation functions on a XMM detected AGN sample from a 2 deg^2 survey. A similar result was also found earlier in our 0.4 deg^2 *Chandra* field (see below) using the count-in-cells technique (Yang et al. 2003). Using the Limber equation Basilakos et al. (2004) argue that the hard X-ray sources are likely to be more strongly clustered than the optically selected AGNs. Gilli et al. (2003) reported the detection of large angular-redshift clustering in the Chandra Deep field South, which seems to be dominated by hard X-ray sources. Using the projected correlation function for the optically identified X-ray sources from the CDFN and CDFS, Gilli et al. (2005) found that the average correlation amplitude in the CDFS is higher than that in the CDFN, and the latter is consistent with the correlation amplitude found in optically detected quasars.

All the X-ray surveys so far either uses angular correlation function, or only produce the space correlation function of the whole sample, which commonly cover a broad redshift interval. The proper interpretation requires the assumption of the evolution of clustering. unfortunately, the commonly used assumptions are proved to be too simple.

1.7 Outline of the dissertation

In this dissertation I present our moderate deep *Chandra* survey CLASXS of the Lockman Hole Northwest. The survey is intended to bridge the gap between ultra-deep *Chandra* surveys such as CDFN and CDFS, and the much shallower large area surveys from *ASCA* and *ROSAT*. This allows us to better determine the number counts at the "knee" and hence the contribution of point sources to the CXB. The wide contiguous field allows us to computer the spatial correlation function without being strongly affected by cosmic variance. This allows us, for the first time, to directly study the evolution of clustering of X-ray selected AGNs.

In Chapter 2, I discuss the *Chandra* instrumentation and the data reductions.

In Chapter 3, I present the CLASXS survey, the data, reduction details, and the X-ray catalog (which can be found in full in Appendix A). I will discuss the number counts of soft and hard X-ray sources and compare them with previous results. The X-ray spectral properties and time variability are also presented.

In Chapter 4, I summarize the optical follow-up observations of the field. I will show that the *Chandra* angular resolution is crucial for correct identifications.

In Chapter 5, I present the analysis of extended sources and gravitational lensing in our survey.

In Chapter 6, The analysis of spatial correlation function of X-ray selected AGNs based on CLASXS and CDFN will be shown.

I summarize our results in Chapter 7. In Appendix B, I will present an analysis of the correlation between blackhole mass and X-ray luminosity of AGNs; and in

Appendix C, some basics cosmology equations and their meaning are discussed.

Through out this dissertation, I will adopt a cosmology with $H_0 = 71$ and a flat universe with $\Omega_M = 0.27$ and $\Omega_\Lambda = 0.73$.

Chapter 2

Chandra Observatory: Instrumentation and data reduction

In this chapter I will described some basics of the *Chandra* instrumentation and data reduction issues. The intention of this chapter is to provide the basic "principles" rather than details. This is because: (1) more details can always be found in publications as well as the *Chandra* X-ray Center (CXC) web pages. (2) The calibration and performance are constantly updated. The method and software for data reduction has also been improved constantly. The software used in this analysis may very likely to be obsolete in a year's time.

To avoid the chapter becoming too long, I will only discuss the instruments and reduction issues that are related to this work. Most of the material in this chapter are derived from the *Proposer's Observatory Guide* (POG), Weisskopf et al. (2003), and the software manuals and science threads at the CXC web site (*http://asc.harvard.edu/*).

2.1 The *Chandra* X-ray Observatory

The *Chandra* X-ray Observatory is an efficient high-resolution X-ray telescope with a suite of advanced imaging and spectroscopic instruments. The telescope was initiated as a result of an unsolicited proposal submitted to NASA in 1976 by Giacconi and Tananbaum. The subsequent study led to the definition of the then named Advanced X-ray Astrophysics Facility (AXAF). The mission is one

component of NASA's Great Observatory Program, including the Hubble Space Telescope, the Compton Gamma-ray Observatory, and the recently launched Spitzer Infrared telescope. In 1998 the mission was named in honor of the Nobel Prize winner Dr. Subramanyan Chandrasekhar. The telescope was launched on July 23, 1999 using space shuttle Columbia.

The flight system of *Chandra* is 13.8 m long and 4.2 m diameter, with 19.5 m solar-panel wingspan. The orbit of *Chandra* is highly elliptical with a nominal apogee of 140,000 km and a perigee of 10,000 km. The inclination to the equator is 28.5°. The orbital period is 63.5 hr, and the satellite is above the radiation belt for more than 75% of the orbital period.

The principal science components of *Chandra* includes the High Resolution Mirror Assembly (HRMA), the Aspect System, the focal plane Science Instruments (SIs), and the Objective Transmission Gratings. A schematic plot of *Chandra* with the major instruments labeled is shown in Figure 6.

2.1.1 The X-ray telescope

The heart of the observatory is the X-ray telescope. The HRMA is made of four concentric Wolter-1 telescopes. Each of the telescope contains a hyperboloid and a paraboloid mirror (Figure 7). The double reflected X-ray photons are focused at the detector plane. Similar grazing mirror design have also been used in *Einstein* and *ROSAT*.

The telescope has a focal length of 10 m and the unobscured geometric clear

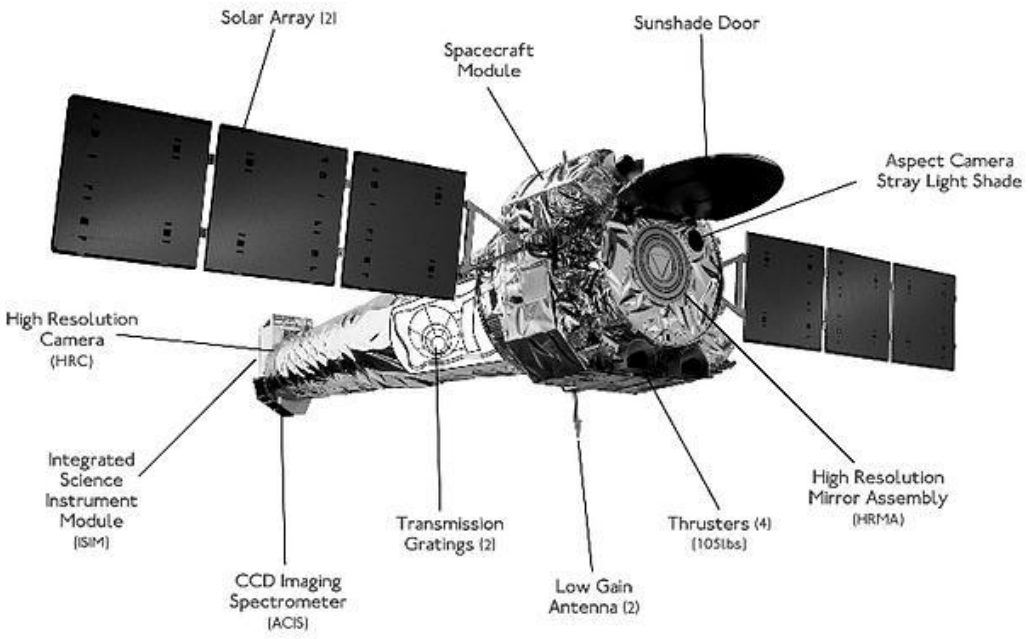

Figure 6: The *Chandra* Observatory with the major subsystems labeled. Figure from Weisskopf et al. (2003).

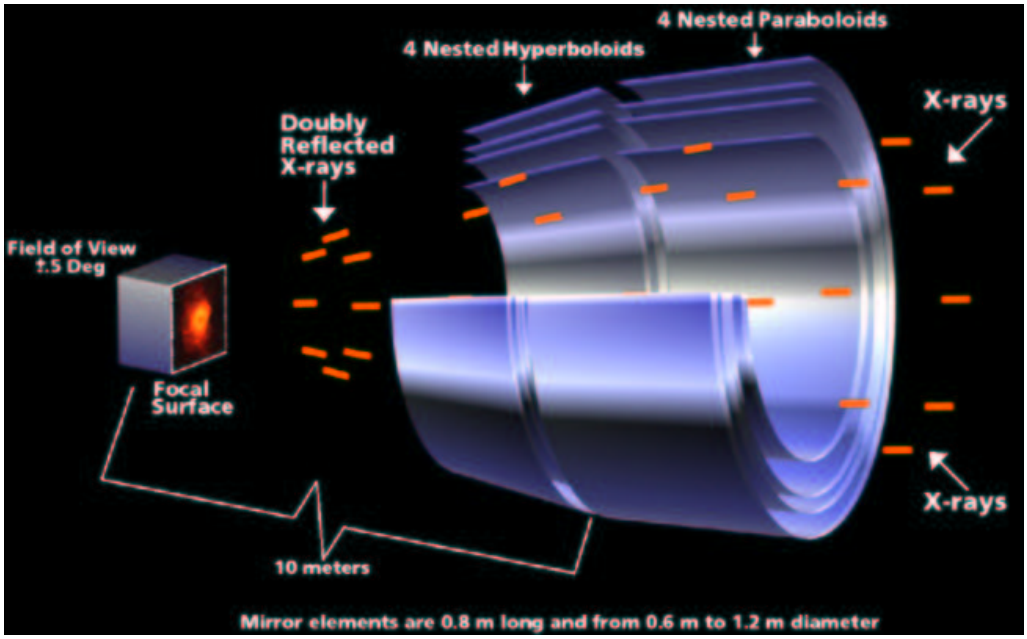

Figure 7: A schematic diagram of the HRMA mirrors

aperture of 1145 cm^2. Since reflectivity depends on energy as well as grazing angle, the HRMA throughput varies with X-ray energy. The on-axis effective area as a function of energy is shown is Figure 8. The effective area decrease with off-axis angle because of vignetting, which can be seen in Figure 9. The energy dependence of this effect is relatively weak for the commonly used 0.5 – 8 keV band. For a flat power-law spectrum X-ray source, the effective area at $8'$ off-axis in the 0.5–2 keV band is only $\sim 5\%$ higher than that in 2–8 keV band.

The telescope on-axis point spread function (PSF) measured during ground calibration had a FWHM of $0.5''$. The on-axis PSF from ray tracing models and that from the in orbit measurements are shown in Figure 10. The size of the PSF is a strong function of off-axis angle and photon energy. This is shown in Figure 11.

2.1.2 The ACIS detector

The Advanced CCD Imaging Spectrometer (ACIS) contains 10 , 1024×1024 pixel CCDs arranged in two groups: ACIS-I is an array with 4×4 CCDs, used for imaging, and ACIS-S is arranged in a line to be used either for spectroscopy with the gratings or for image. A schematic drawing of the ACIS focal plane is shown in Figure 12. The square pixel has a physical size of 24 μm, corresponding to an angular size of ~ 0.492 $''$. Each CCD covers a sky region of $16.9'$ by $16.9'$.

The X-ray CCD is very similar to the CCD used in the optical astronomy, which is an array of Metal-Oxide Semiconductor (MOS) capacitors. The metal gate structure on one surface of CCD defines the pixel. The ACIS front-illuminated (FI)

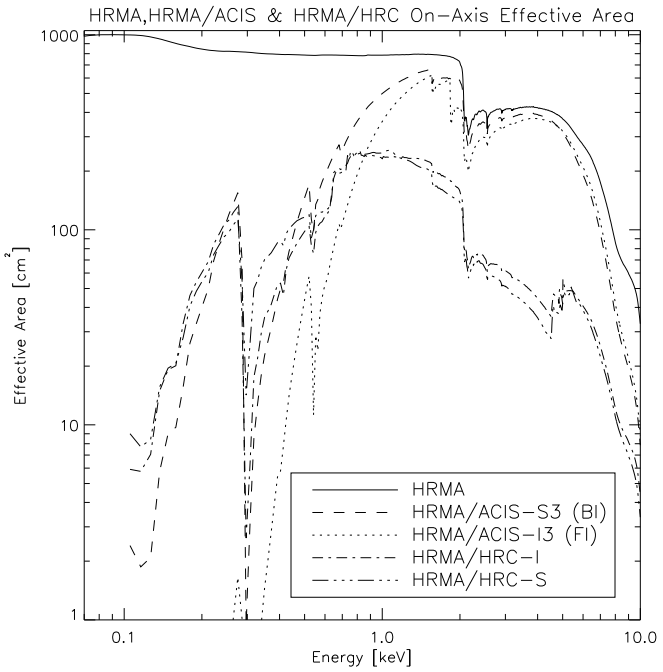

Figure 8: The HRMA, HRMA/ACIS and HRMA/HRC effective areas versus X-ray energy. The structure near 2 keV is due to the iridium M-edge. The HRMA effective area is calculated by the ray-trace simulation based on the HRMA model and scaled by the XRCF calibration data. The HRMA/ACIS effective areas are the products of HRMA effective area and the Quantum Efficiency (QE) of ACIS -I3 (front illuminated) or ACIS -S3 (back illuminated). The HRMA/HRC effective areas are the products of HRMA effective area and the QE of HRC-I or HRC-S at their aimpoints, including the effect of UV/Ion Shields (UVIS). Figure from Chandra Proposer's Observatory Guide (Online at http://asc.harvard.edu/proposer/POG/html/).

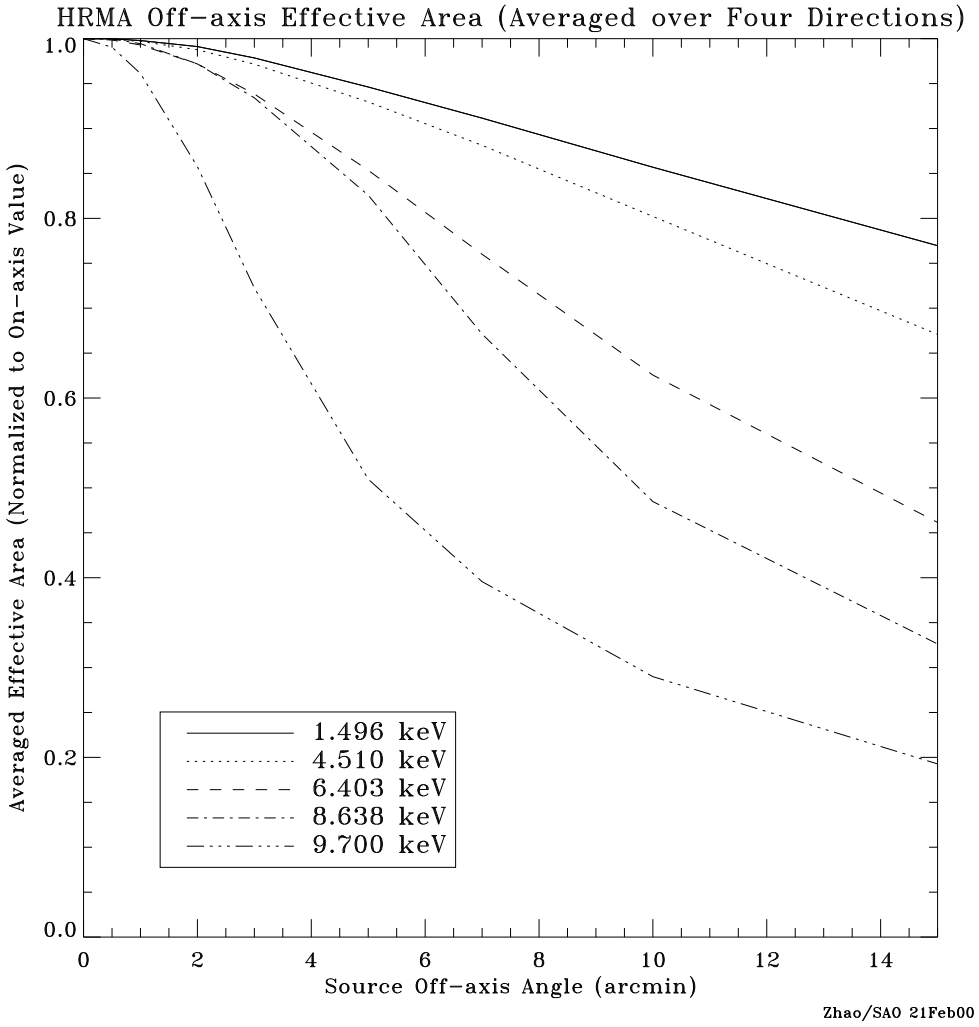

Figure 9: The HRMA effective area versus off-axis angle, averaged over azimuth, for selected energies, normalized to the on-axis area for that energy.

CCDs have the gate structure facing the X-ray incident beam. Two of the chips on the ACIS-S array (S1 and S3) have had the insensitive, undepleted bulk silicon material on the back of the CCD removed. They are mounted to have the backside illuminated by the incident X-ray. The back-illuminated (BI) CCD chips are more sensitive to soft X-ray photons.

The capacitors can store charge within potential wells. Photo-electric absorp-

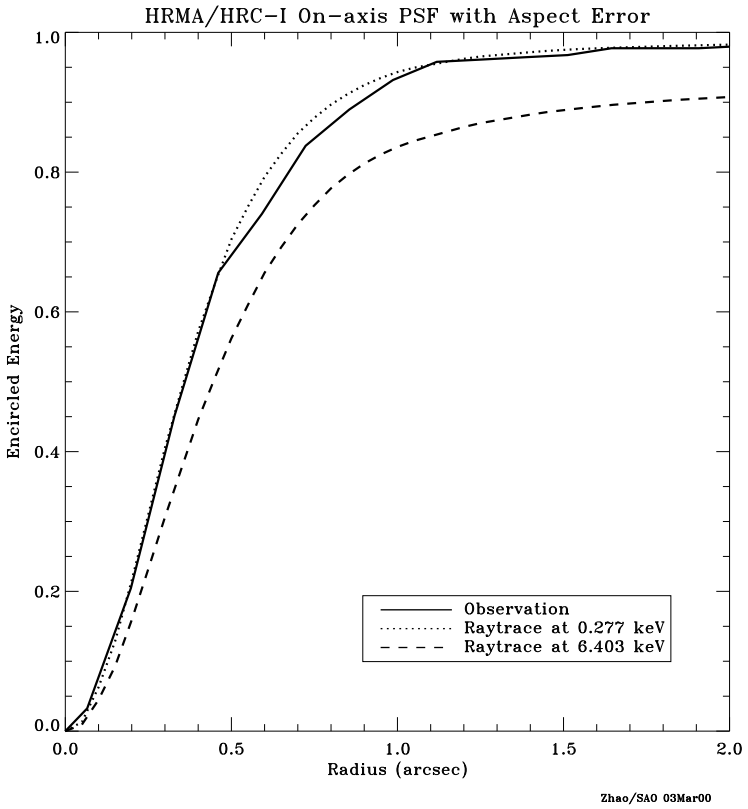

Figure 10: The predicted and observed fractional encircled energy as a function of radius for an on-axis point source with HRC-I at the focus of the telescope. Flight data from an observation of AR LAC is also shown.

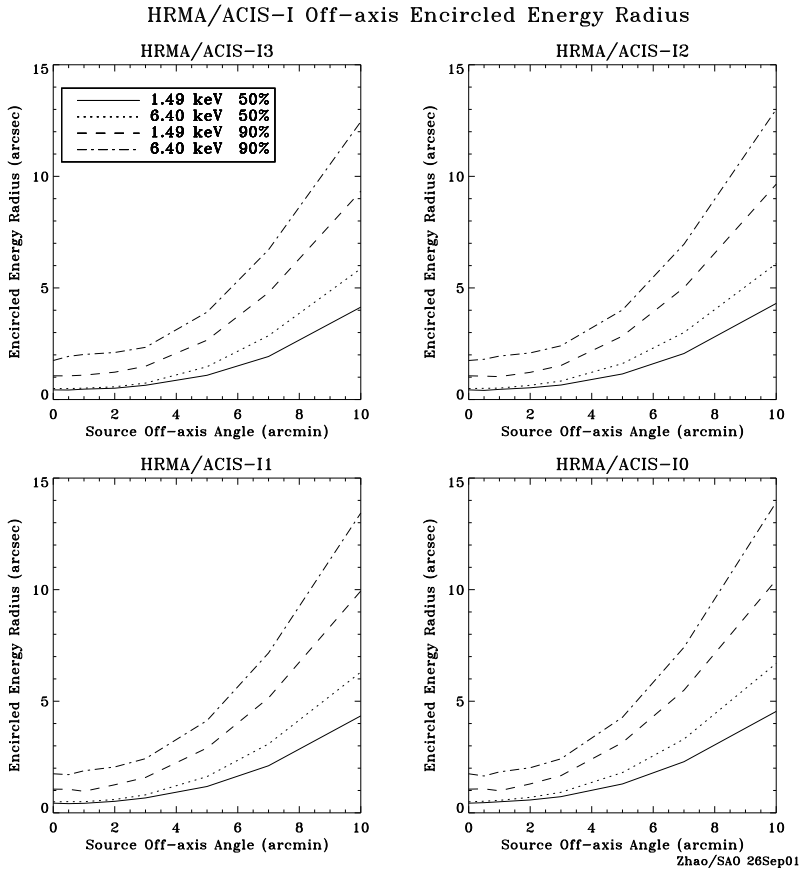

Figure 11: HRMA/ACIS-I encircled energy radii for circles enclosing 50% and 90% of the power at 1.49 and 6.40 keV as a function of off-axis angle. The ACIS-I surface is composed by four tilted flat chips which approximate the curved Chandra focal plane. The HRMA optical axis passes near the aimpoint which is located at the inner corner of chip I3. Thus the off-axis encircled energy radii are not azimuthally symmetric. The four panels show these radii's radial dependence in four azimuthal directions - from the aimpoint to the outer corners of the four ACIS-I chips. These curves include the blurs due to the ACIS-I spatial resolution and the Chandra aspect error.

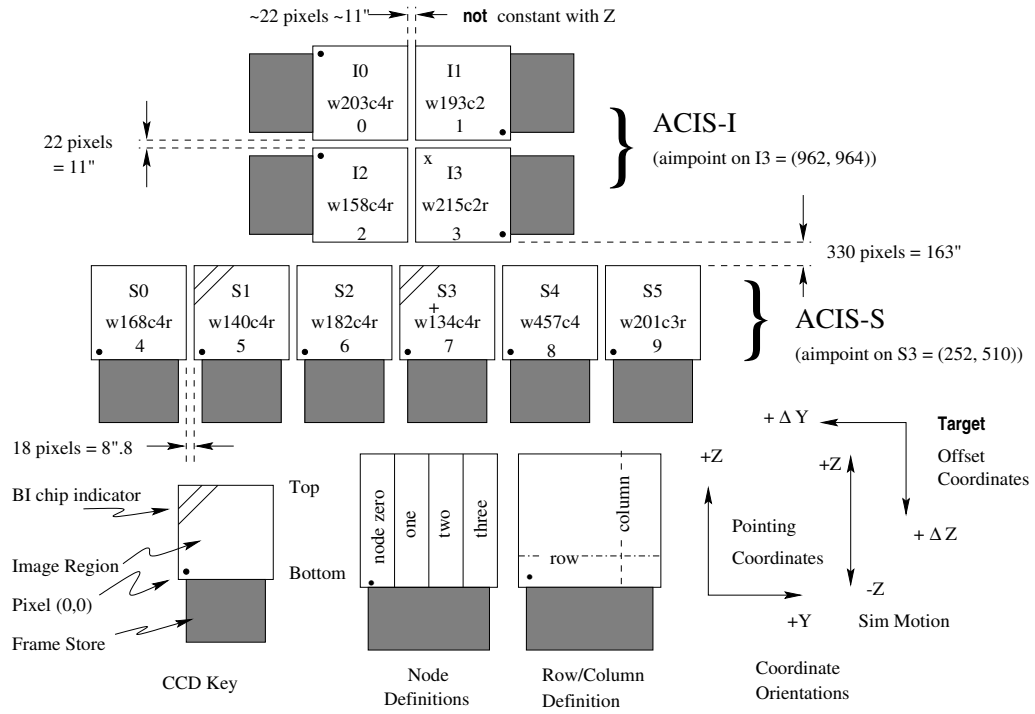

Figure 12: A schematic drawing of the ACIS focal plane; insight to the terminology is given in the lower left.

tion of an X-ray photon results in a liberation of a proportional number of electrons. The charge is confined by electric fields to a small volume near the interaction site. The volume is usually larger than one pixel. In the ACIS, each pixel contain three "phases" or "sub pixels" which are single capacitors. By alternating the voltage in sequence on the three electrodes spanning one pixel, the charge can be transfered from one pixel to the next. The CCD have an "active" section which is exposed to the incident X-ray, and a shielded frame storage region. The standard frame exposure time is 3.2 s, although shorter frame time can be achieved with small window mode (only a fraction of the CCD is used; this is useful for bright sources, where

the probability of multiple photon hitting the same pixel within one frame time is significant). A good determination of the charge deposited by an event is critical to the spectral resolution. The fraction of charges lost during the pixel-to-pixel transfer or charge transfer inefficiency (CTI), and the readout noise are the major factors. The readout noise for ACIS is < 2 electrons rms. The total system noise ranges from 2-3 electrons (rms) and is dominated by off-chip analog processing electrons.

The spatial resolution is limited by the physical size of the CCD pixels (0.492 $''$). For the on-axis observation, approximately 90% of the encircled energy lies within 4 pixels of the center pixel at 1.49 keV and within 5 pixels at 6.4 keV. For far off-axis sources, the PSF of the HRMA dominates the spatial resolution. Since ACIS is basically a photon counting device, in observation the spacecraft is dithered so that the gaps between the CCDs can have some exposure and the pixel-to-pixel variation can be smoothed out. The dither is removed using the aspect data during the ground processing. The absolute accuracy of position is $0.4''$and the image reconstruction accuracy is $0.3''$.

The FI CCDs are designed to have better energy resolution than the BI chips. After launch the energy resolution for the FI chips was found to be a function of row number, best explained by damages to the CCDs by low energy protons encountered unexpectedly when passing the radiation belt and reflected off the X-ray telescope. The BI chips are not affected because the buried channels and gates are in the direction opposite to the HRMA, which is difficult for low energy protons to penetrate. The position-dependent energy resolution of the FI chips depends significantly on the ACIS operating temperature. Since activation, the ACIS operating temperature

has been lowered in steps and is now set at the lowest temperature thought safely and consistently achievable ($\sim -120°$C). The damage induced CTI has so far been modeled and correction procedures are implemented to recover the loss of energy resolution.

2.2 ACIS data processing and reduction

The *Chandra* X-ray Center (CXC) performs standard or commonly refereed as "pipeline" data processing. Since the calibration is constantly updated, re-processing are often needed. I will discuss briefly the procedures in the ACIS data processing and reduction. While I will focus on ACIS-I, most of the steps are the same for ACIS-S. Details can be found in the *Science thread* online at *http://asc.harvard.edu/ciao/threads/index.html*

All the data processing can be performed with the Chandra Interactive Analysis of Observations (CIAO) software, which can be downloaded from the CXC web site. The data set obtained from CXC contains two levels of data products, including the event lists, images and source lists. Level 1 event list is the raw data while level 2 event list has been filtered and is meant for scientific analysis. The observation ancillary files, which contains information about the telescope aspect, CCD bad pixels, good time intervals, bias maps, masks and so on, are also included.

If the data need to be reprocessed to use the best calibration available, one starts with the level 1 event list. The event list register all the events with their coordinates, CCD number, node number, event time and energy. This step can be

done with the *acis_process_events* procedure which performs a set of tasks, including applying the ACIS gain map (now includes the time dependent gain change), the CTI correction and so on. The central part of the task is to calculate the grades of the events. The task typically uses a 3×3 (5×5 when observation uses the VFAINT mode) island of pixels centered on the event to determine the shape formed by the pixels which has been activated. A cosmic ray background incident tends to produce multiple events with shapes different from common X-ray photons. The shape is then coded to a grade system (in all calibrations only a subset of the grades – ASCA grades 0, 2, 3, 4 and 6 are used) for filtering. Figure 13 shows a charged particle striking the BI and FI chips. The rejection efficiency for FI CCDs are higher then BI CCDs.

The event list can then be filtered for high backgrounds time intervals (by inspecting the background light curve), the bad grades, and apply the good time intervals. The resulting file is a level 2 event list. The event list can then be rebinned by the columns to make images, spectra or light curves for further analysis.

2.3 ACIS Source detection

CIAO provide three detection tools:

- *celldetect*: A classic sliding box algorithm.
- *wavdetect*: Multi-scale filtering using wavelet transformation.
- *vtpdetect*: Uses the Voronoi tessellation and percolation to find over dense regions of events. The method works directly on the event list.

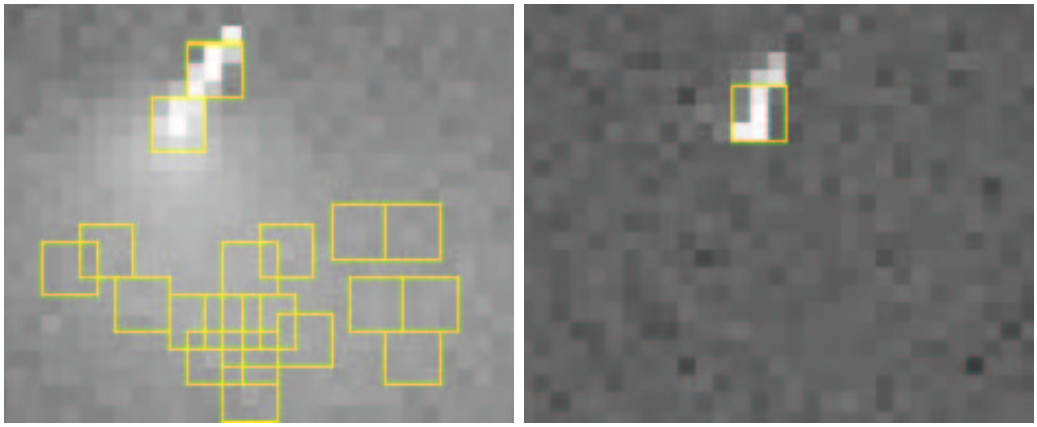

Figure 13: Enlarged view of an area of a FI chip I3 (left) and a BI chip (right) after being struck by a charged particle. There is far more "blooming" in the FI image since the chip is thicker. The overlaid 3x3 detection cells indicate that the particle impact on the FI chip produced a number of events, most of which end up as ASCA Grade 7, and are thus rejected with high efficiency. The equivalent event in the BI chip, is much more difficult to distinguish from an ordinary x-ray interaction, and hence the rejection efficiency is lower.

Celldetect does not perform very well in separating close sources and can produce multiple detections for off-axis point sources because of the broadened PSF. It is therefore commonly used for preview. *Wavdetect* is more commonly used because of its high sensitivity. *Vtpdetect* on the other hand is better suited for detecting extended source.

2.3.1 *Wavdetect*

Wavelet detection uses a family of oscillatory functions (wavelet functions) that are scalable and are non-zero within a limited region. The integration of the

function is zero. The simplest example is the "top hat" function with amplitude A and width w, flanked by two negatively valued troughs with total integrated area $-Aw$. Any function with zero normalization with the form

$$W_{a,\sigma}(x) \equiv \frac{1}{\sigma} W\left(\frac{x-a}{\sigma}\right) \tag{2.1}$$

may be used as a wavelet function. σ is the scaling or dilation parameter and a is the translation parameter.

The localized nature of wavelet function allows determination of both the location and the dominate frequency (scale) of a source simultaneously. By convolving the wavelet with an image (correlation map), the problem of source detection boils down to the problem of finding the statistical significant correlation peaks in the correlation map. Details of the algorithm is described in Freeman et al. (2002).

The algorithm use a simple unimodal wavelet function $W(\sigma_x, \sigma_y, x, y)$ to detect sources in an image D. This function is convolved with D to produce a "correlation image" C:

$$C(\sigma_x, \sigma_y, x, y) \;=\; \int\int dx'\, dy'\, W(\sigma_x, \sigma_y, x-x', y-y')\, D(x', y') \equiv \;<W*D>\,. \tag{2.2}$$

The expectation value of $C(\sigma_x, \sigma_y, x, y)$ is zero, if there are no sources within the limited spatial extent of the wavelet function, and the background count rate is locally constant, because the normalization of $W(\sigma_x, \sigma_y, x, y)$ is zero. For convenience we can write W in two parts so that $C \;=\; <PW*D> + <NW*D>$, where PW and NW denote the positive and negative amplitude portions of the wavelet function, respectively. If a clump of counts is contained within PW, then the contribution of the positive term will C outweighs that of the negative term, producing

a maximum. If the scale sizes are smaller, then the wavelet function will extend over a smaller region within the clump, the resulting C may or may not be a local maxima, and $C \rightarrow 0$ when the scale of the wavelet is very small. For larger scale sizes, the correlation value tends asymptotically to a maximum, $C_{\max}$, provided that there are no sources very close.

By computing the probability S that a false source is accepted, also called the significance, in each image pixel (i, j) in the $C(\sigma_x, \sigma_y, x, y)$ map, one can tell if a clump is a source or noise.

$$S_{i,j} \;=\; \int_{C_{i,j}}^{\infty} dC p(C|n_{B,i,j}) \tag{2.3}$$

$n_{B,i,j}$ is the inferred number of background counts within the limited spatial extent of the wavelet function, and $p(C|n_{B,i,j})$ is the probability sampling distribution for C given $n_{B,i,j}$, which in practice is computed using simulations. If $n_{B,i,j}$ is estimated from the raw data themselves, this estimate will be biased if source counts are present, so that $S_{i,j} \gtrsim S_{i,j,\mathrm{true}}$. Thus an iterative procedure is used to remove source counts from the image and replace them with the background estimates. The usual number of iterations depends upon many factors, but is usually $\approx$ 3-4. With this final background estimate, one computes a final significance $S_{i,j}^{\mathrm{final}}$ for each value $C_{i,j} =< W*D >_{i,j}$ (the correlation of the wavelet function with the raw image data) so that a final listing of source pixels may be made. After this algorithm is used to determine lists of source pixels for many wavelet scale sizes, cross-identification of pixels across scales is performed to create the final source list.

The CIAO *wavdetect* contains two parts: *wtransform*, which convolve the

wavelet functions of a set of scales with the input image; and *wrecon* uses the *wtransform* output products to construct source lists, measure parameters for each detection, and create various maps. The two part can be ran separately. The most important input parameters are:

- scales: the scales of wavelet function which determines how many scaled transforms will be computed;
- sigthresh: The significance threshold for source detection. A good value to use is the inverse of the total number of pixels in the image, e.g. $\sim 10^{-6}$ (the default) for a 1024×1024 field.

Exposure maps (created by using the aspect histogram and instrument map, represents the effective exposure in the image) can be used with *wavdetect* so that the exposure variations can be taken into account when computing the significance. The PSF files for *Chandra* is used so the best scales can be used to extract source counts. For images taken from other telescopes, unless PSF file is supplied, the smallest scale used for detection is used for source extraction, leading to erroneous results. This, however, does not affect source detection.

While *wavdetect* is very sensitive in detecting weak sources, very good in separating very close sources, they tend to be CPU intensive, particularly on large images with many scales. The cross talk between scales also could eliminate legitimate sources if too many scales are used. It has also been found that the obtained source properties (count rate) may not be correct (see Chapter 3). The source counts are recommended to be extracted with other software.

2.3.2 *Vtpdetect*

On a 2-dimension random point distribution, a Voronoi tessellation can be constructed so that each point is assigned a unique convex polygon. The formation of these cells can be imagined through the following process. Each of point starts with a small circle with the same radius centered on it. The circle expands at a constant rate. Once two adjacent circles touch, the contact point stops expanding, but the rest part of the circle continue to expand until all the space is filled (see Figure 14). The polygon defines an area for each point, and the inverse of the area of the polygon is the density at that point. The probability distribution function of the area for a Poisson process can be used to assign probability to the cells which are overdense.

By applying the algorithm on the spatial distribution of X-ray events, a map of overdense cells can be constructed. In practice the flux, defined as the inverse of the product of the cell area and the exposure time, is used instead of area so the exposure effect can be included. The sources are then found by connecting all the neighboring cells above the flux threshold. The merit of this method is that it make best use of the event list in finding extended sources, and is not affected by binning or the geometry of the detecting cells, as in other detecting methods.

When running the CIAO *vtpdetect*, the user can choose the maximum probability of a false source (*limit*). A threshold is then calculated using the probability provided. This threshold can be rescaled (through *scale* parameter) to allow better detection sensitivity or better ability of de-blending point sources. Addition con-

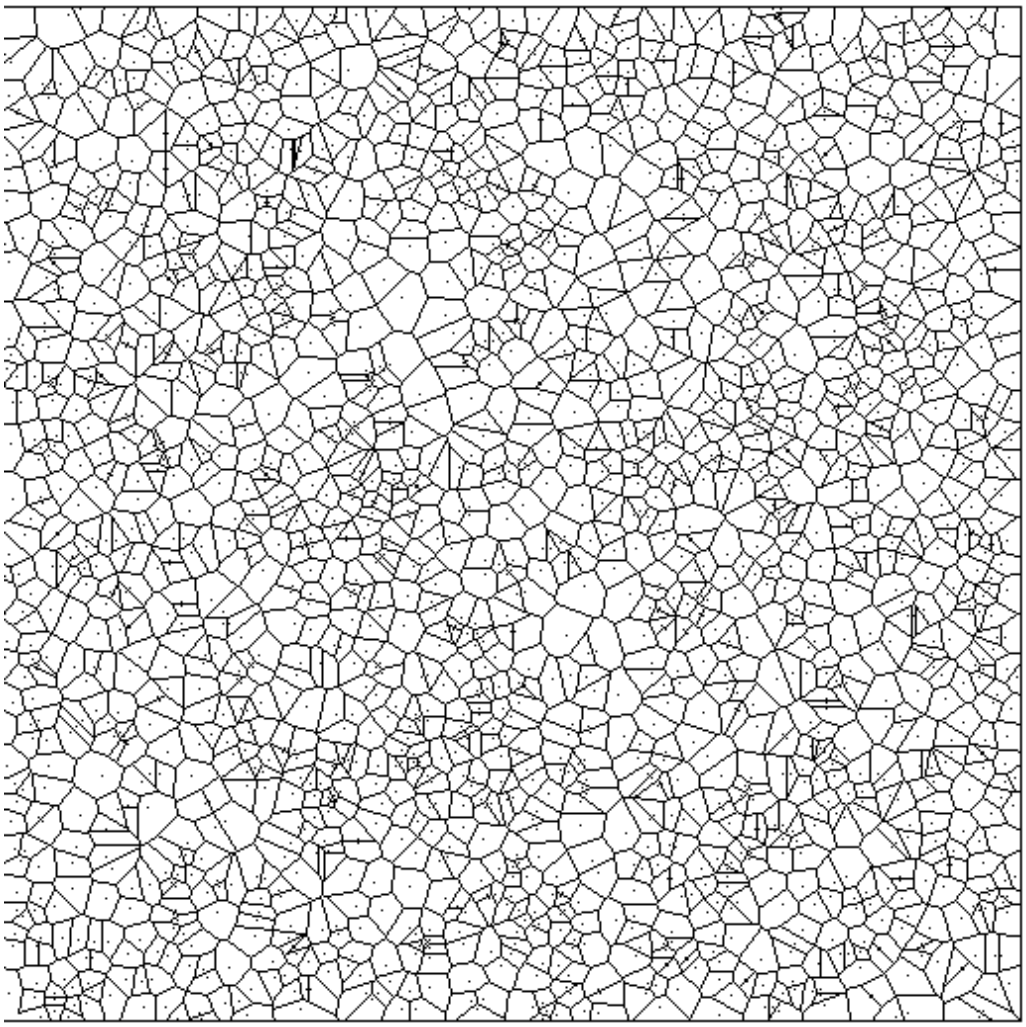

Figure 14: An example of a Voronoi tessellation for 2000 random points. (Figure from the *Chandra Detection Manual*).

strain come from the minimum number of counts per source (*coarse*), which is useful in removing point sources.

The major problem with *vtpdetect* is that it tends to blend point sources. Visual inspection of the source list is needed to remove point sources.

2.4 ACIS Spectral analysis

The spectra of an X-ray source and the background can be extracted using the CIAO tool *dmextract*. The background can be chosen from a region close to the source, or from the background files. The resulting spectrum is in fact a convolution of the original spectrum with the ACIS response and the effective area. To understand the source spectrum, the response and effective area of the instrument need to be obtained. These are made by utilizing the calibration file and the observation data such as the gain map and aspect data. Two files will be generated in the process: the response matrix file (RMF) and the ancillary response file (ARF). The RMF maps the energy to pulse hight (or position) space and ARF contains the effective area and quantum efficiency as a function of energy averaged over time. The process of creating the RMF and ARF can be done in one step using meta task *psextract* or do it step-by-step by running each of the tasks separately.

The quantum efficiency at low energy (below 2 keV) was found to decrease with time, best explained by molecular deposition contaminating the optical blocking filter or the CCDs. This degradation is most severe at energies below 1 keV. At 1 keV, the degradation is approximately 10%. Correction for this effect has been included since the calibration release CALDB 2.26. Data processed using CALDB prior to version 2.26 are corrected within the *Chandra* data fitting package *sherpa* with a separate *SLANG* script *acisabs.sl* or the UNIX shell wrapper *apply_acisabs* on the ARF. This change can also be accounted for using a spectral fitting model ACISABS by Chartas & Getman (URL:*http://www.astro.psu.edu/users/chartas/xcontdir/xcont.html*).

To obtain the original source spectrum from the observed spectrum is always a challenge because the inverse problem is not easily solvable and the solution can be very unstable. Fortunately, in most cases the general form of the source spectrum can be reasonably assumed based on the type of the source. By folding the assumed model and the response of the instrument, and compare the result with the observed spectrum, the problem boils down to finding the model parameters that best describe the data. Finding a global minimum of χ^2 (or other fitting statistics) in the parameter space is the goal of model fitting. The method, however, can neither distinguish between models which produce equally good fit, nor can it distinguish between equally deep local minimums. Good scientific judgement is always needed. XSPEC is the most commonly used spectral fitting tool. The software is a command driven interactive fitting package which provide a large library of spectral models and provide plenty expandability. The program can also be used to compute model flux and luminosity.

Chapter 3

CLASXS: The Survey and the Point Source Catalog

3.1 Introduction

The ultradeep *Chandra* surveys cover very small solid angles. In the case of the *Chandra* Deep Fields (CDFs), the combined sky coverage is ~ 0.2 deg^2. About 40% variance between fields is seen in the integrated fluxes in the $2-8$ keV band (Cowie et al. 2002), likely as a result of the underlying large scale structure. To determine the fractional contribution of point sources to the cosmic X-ray background (CXB) with enough accuracy, and to understand how the CXB sources trace the large scale structure, a sufficiently large solid angle is needed. While very large area surveys exist above 10^{-13} erg cm^{-2} s^{-1} (2–8 keV) from *ASCA* (Akiyama et al. 2003), the data around 10^{-14} erg cm^{-2} s^{-1}, where the point source contribution to the CXB peaks, is limited.

Several intermediate, wide-field, serendipitous *Chandra/XMM-Newton* surveys (Baldi et al. 2002; Kim et al. 2004; Harrison et al. 2003) were designed to increase the solid angle to several degrees at a $2-8$ keV flux limit of 10^{-14} erg cm^{-2} s^{-1}. One of the advantages of such surveys is that they sample randomly across the sky, so the probability of all of them hitting overdense or underdense regions is small. This is useful in determining the normalization of LogN-LogS. On the other hand, serendipitous surveys suffer from the non-uniform observing conditions for each pointing, and

in most cases, the pointings contain bright sources. The biases introduced by these non-uniformities are hard to quantify. The serendipitous surveys also have little power in addressing the question of large scale structure traced by X-ray selected AGN, due to the small solid angle of each pointing, sparse and random positions on the sky, and the non-uniformity of the observations. With serendipitous surveys, it is also difficult to perform extensive optical spectroscopic follow-up observations, which are critical in obtaining the redshifts and spectral classifications of the X-ray sources. This is due in part to the advent of large format detectors for imaging and spectroscopy (like those on the Subaru and Keck telescopes), which are more efficient at targeting large-area, contiguous X-ray surveys, rather than many isolated ACIS-I pointings.

A contiguous, large solid angle survey can compensate for these disadvantages and bridge the gap between the ultradeep "pencil beam" surveys and the large area serendipitous surveys in determining both the normalization of the LogN-LogS and the large scale structure.

In 2001, we began the *Chandra* Large Area Synoptic X-ray Survey (CLASXS) of the multiwavelength data-rich *ISO* Lockman Hole-Northwest (LHNW) region. The survey currently covers a solid angle of ~ 0.4 deg^2 and is sensitive to a factor of $2-3$ below the "knee" of the $2-8$ keV LogN-LogS. Such a choice of solid angle and depth maximizes the detection efficiency with *Chandra*. The large solid angle is important for obtaining statistically significant source counts at the "knee" of the LogN-LogS and to test for variance of the number counts on larger solid angles. The choice of solid angle is based on the *ASCA* results that the rms variance of the

$2-10$ keV CXB on a scale of 0.5 deg^2 is $\sim 6\%$ (Kushino et al. 2002). The expected variance at the angular scale of our field should be less than the uncertainty of the CXB flux. The uniform nature of the survey allows an unbiased measurement of AGN clustering.

Our survey region is covered by the deepest 90 and 170μm ISOPHOT observations (Kawara et al. 2004), as well as abundant multiwavelength observations, including the planned *Spitzer Space Telescope* (SST) Wide-Area Infrared Extragalactic Survey (SWIRE, Lonsdale et al. 2004). We performed extensive optical follow-up observations using Subaru, CFHT, WIYN, and Keck to obtain multicolor images and spectra of the X-ray sources (Steffen et al. 2004, hereafter Steffen04; see Chapter 4). These observations provide critical information on the redshifts, spectroscopic classifications and luminosities of the X-ray sources, as well as on the morphologies of the host galaxies.

3.2 Observations and Data reduction

3.2.1 X-ray Observations

We surveyed the LHNW field centered at $\alpha = 10^h34^m$, $\delta = 57°40'$ (J2000). The region has the lowest Galactic absorption ($N_H \equiv 5.72 \times 10^{19}\,\mathrm{cm}^{-2}$; Dickey & Lockman 1990). All 9 ACIS-I observations were obtained with the standard configuration. The pointings are separated from each other by $10'$ (Figure 15). The fields are labeled LHNW1-9 for reference hereafter. The overlapping of the fields allows a uniform sky coverage, because the sensitivity of the telescope drops

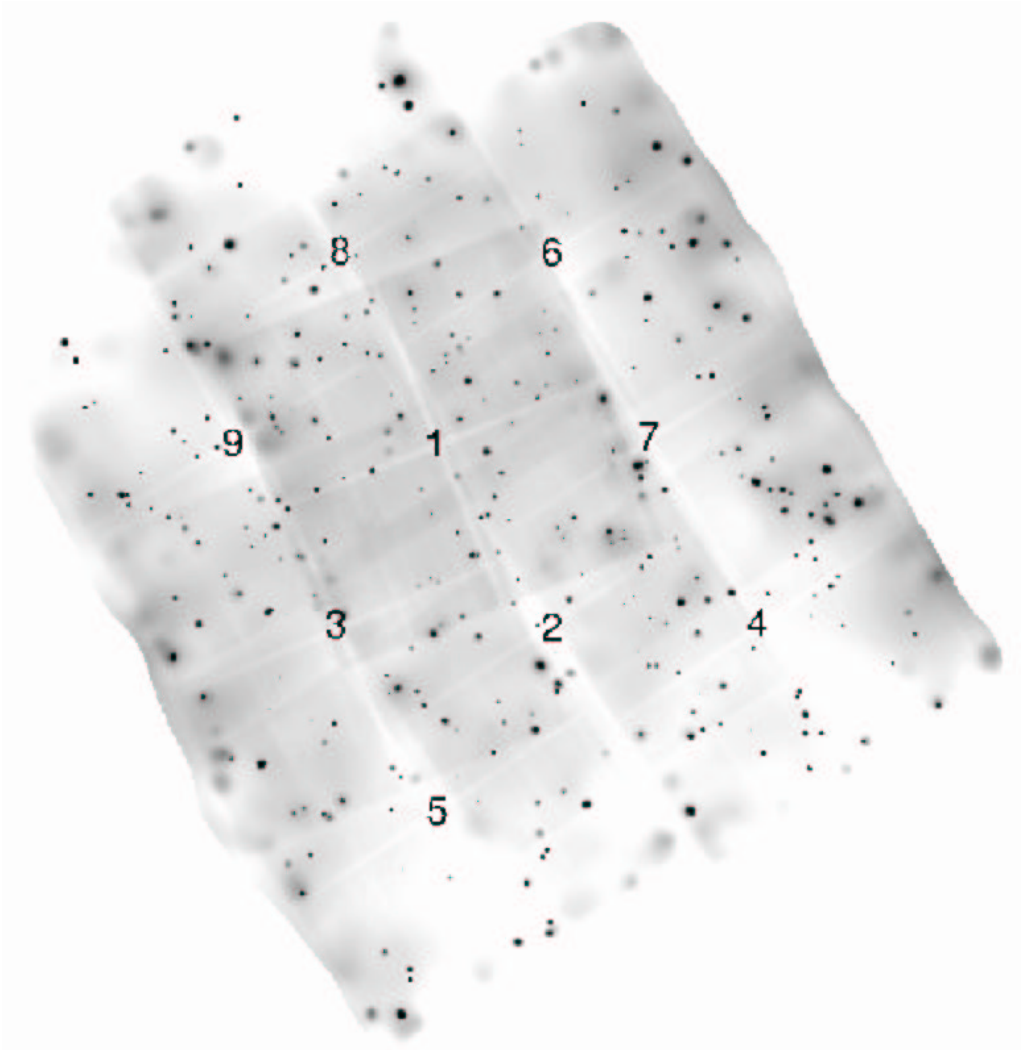

Figure 15: Layout of the 9 ACIS-I pointings. Gray scale map shows the adaptively smoothed full band image. The exposure maps are added (light gray) to outline the ACIS-I fields. Fields are separated by $10'$ from each other. The field numbers (LHNW1-9) are shown at the center of each ACIS-I field.

Table 3.1. Observation Summary

Target Name	α_{2000}	δ_{2000}	Obs ID	Sequence #	Observation date	Exposure[a]
LHNW1	10 34 00.24	+57 46 10.6	1698	900057	05/17/01 18:29:38	72.97 ks
LHNW2	10 33 19.82	+57 37 13.8	1699	900058	04/30/01 10:59:38	40.74 ks
LHNW3	10 34 36.12	+57 37 10.9	1697	900056	05/16/01 12:46:50	43.72 ks
LHNW4	10 32 04.20	+57 37 15.6	3345	900184	04/29/02 03:23:45	38.47 ks
LHNW5	10 34 00.31	+57 28 15.6	3346	900185	04/30/02 02:03:59	38.21 ks
LHNW6	10 33 20.28	+57 55 15.2	3343	900182	05/03/02 09:11:41	34.04 ks
LHNW7	10 32 44.23	+57 46 15.2	3344	900183	05/01/02 20:03:06	38.54 ks
LHNW8	10 34 36.26	+57 55 15.6	3347	900186	05/02/02 14:16:27	38.46 ks
LHNW9	10 35 14.28	+57 46 15.2	3348	900187	05/04/02 11:01:47	39.52 ks

[a]Total good time with dead time correction.

significantly at large off-axis angles. Fields LHNW1-3 were observed during April 30th to May 17th 2001, and the rest of the fields were observed during April 29th to May 4th 2002. All fields except LHNW1 have exposure times of ~ 40 ks. LHNW1 is located at the center of the field and has an exposure time of 73 ks. The observations are summarized in Table 3.1.

The data is reduced with CIAO v2.3 and the calibration files in CALDB v2.20. The data reduction has later been updated with CIAO v3.01 and CALDB 2.23 to allow the use of CTI corrected calibration files. We followed the CIAO analysis threads[1] in reducing the data, including the correction of known aspect problems, CTI problems, and removing high background intervals. Background flares were found in LHNW3 and LHNW6 and have been removed. The resulting event lists were rebinned into $0.4-2$ keV (soft), $2-8$ keV (hard), and $0.4-8$ keV (full) broadband images. Spectral weighted exposure maps were made for each band for

[1]available online at http://asc.harvard.edu/ciao/

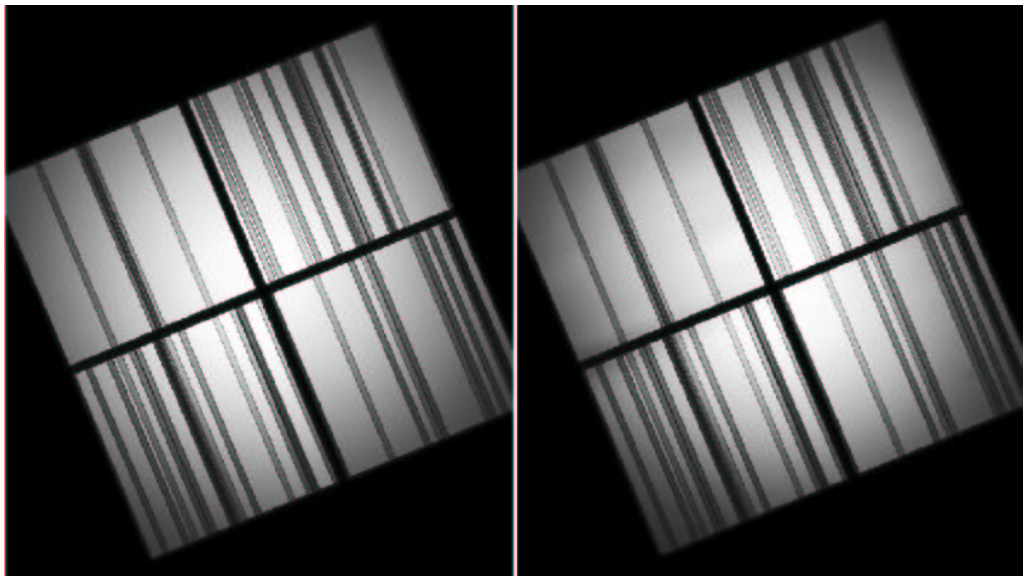

Figure 16: The exposure map of LHNW3 in soft (left) and hard band (right)

each observation, using the observation specified bad pixel files. To obtain the proper estimates of source flux, we make spectral weighed exposure maps using the CIAO script *merge_all*. Examples of the soft and hard band exposure maps are shown in Figure 16.

3.2.2 Source detection

The detection sensitivity of *Chandra* drops rapidly beyond $6'$ off-axis. For this reason, we overlapped our ACIS-I fields so that the sensitivity of the survey would be uniform across the field. Since the added signal-to-noise from merging the observations is relatively small, we chose to detect sources in each observation individually and merge the catalogs, rather than to detect sources directly on the merged image. This method certainly loses some sensitivity for very dim sources. However, since our major interest is to obtain a uniform sample for statistical and follow-up

purposes, such a choice is justified. The method also simplifies the source flux extraction because the PSF information could easily be used. Multiple detections of sources in independent observations are very useful for checking and improving the X-ray positions of the sources. Multiple detections also provide an opportunity for measuring the variability of these sources.

We ran *wavdetect* on the full resolution images with wavelet scales of $1, \sqrt{2}$, 2, $2\sqrt{2}$, 4, $4\sqrt{2}$,8. Although using larger scale sizes could help to detect very far off-axis sources, it is not very useful for our survey, because of the overlapping of fields. It also increases the computation time to use a large number of scales. We chose to use a significance threshold of 10^{-7}, which translates to a probability of false detection of 0.4 per ACIS-I field based on Monte Carlo simulation results (Freeman et al. 2002).

3.2.3 Source positions

Observations performed before May 02, 2002 suffer from an systematic aspect offset as large as $2''$ from an error in the pipeline software. This systematic error was carefully calibrated by the CXC and corrections are provided. For the affected fields, LHNW1, 2, 3, 4, 5, and 7, we corrected this error following the standard procedures (see *Chandra* analysis thread [2]).

We further matched the small off-axis X-ray positions reported in each field from *wavdetect* to the optical images (see § 4.2). Corrections were then found to maximize the matches. Such corrections are very small. The astrometric improvement

[2]online at http://asc.harvard.edu/ciao/threads/arcsec_correction/

also only marginally improved the matching between the X-ray catalogs, thanks to the excellent astrometric accuracy of the instrument. The corrected X-ray catalogs from each observation were then merged (§ 3.3). A further absolute astrometric correction was applied to the merged X-ray catalog to match to the radio sources in the field.

3.2.4 Source fluxes

Wavdetect is excellent at detecting sources, but it is not always the best method for flux extraction. Three issues could contribute to an incorrect estimation of source counts in *wavdetect*. First, the flux measurements in *wavdetect* use a monochromatic PSF size, which, by default, corresponds to an enclosed energy of 0.393 at the energy of choice, or the 1σ integrated volume of a normalized two-dimensional Gaussian. Though this parameter is adjustable, larger enclosed energy values could cause confusion of close sources. Since the construction of source cells is carried out by convolving the source image with wavelet functions, the "smearing" effects of the convolution can in general make the source cell large enough to include most of the source photons, but the fraction of the flux recovered varies from source to source. Second, due to the statistical fluctuations in the source photon distribution, some sources show multiple peaks in the convolved image. Unless perfect PSF information is available, randomness should exist in determining which peak belongs to a single source. This problem is particularly severe when the source is very off-axis and the PSF shape cannot be approximated by a Gaussian. The third issue is the

background determination, a problem other methods also share. The background in *wavdetect* is obtained in the immediate neighborhood of the source. This is useful because of the known large background fluctuations. However, if the background is drawn too close to the source, the PSF wing would likely be taken as background. This could result in an over-subtraction of the background and lead to underestimated source counts. In *wavdetect*, the problem is treated by re-iteration of source removal (see § 2.3.1). However, our experiments show that the commonly used number of re-iteration does not clean the source very well. Increasing the number of iteration can improve the results, but will greatly increase the computing time. This effect is seen in a correlation of source counts with background density in the *wavdetect* results. All of these issues would lead to an underestimation of source counts. This has been noticed in the analysis of the deep *Chandra* fields (Giacconi et al. 2002, Hornschemeier, private communication).

Because of the spectral differences of the sources and the sensitivity differences between energy bands, sources detected in one band are not always detected in another at high significance. There is no simple way within *wavdetect* to provide upper limits for these sources. To obtain the source fluxes or upper limits in the non-detection band, an alternative flux extraction method is needed.

For these reasons, we wrote an aperture photometry tool for source flux extraction. The method uses a simple circular aperture which matches the size of the PSF. To do this, we first compared the broadband PSFs derived from our observations with the PSF size file provided with CIAO, as described below.

Broadband PSFs

Both the PSF library used by the CIAO tool *mkpsf* and the circularly averaged PSFs used by the detection codes (psfsize20010416.fits) are generated at monochromatic energies using simulations of the telescope. Spectral weighted average energy is usually used for selecting the PSF file for broadband images. Since the spectra of the X-ray sources are mostly unknown, an average spectrum has to be assumed. Whether such selected PSFs agree with the observed broadband PSFs needs to be tested. We constructed "average PSFs" for different off-axis angles using sources which have no neighbors within $40''$ in our 9 observations (Figure 17). It should be noted that these PSFs are inaccurate at large scales because the PSF wings, which span more than $1'$, could not be well determined in these observations. The source images from the same off-axis annuli are stacked, and the curves-of-growth are constructed. The background regions are fitted with quadratic forms using nonlinear least-square fits. To compare with the library PSFs used by *wavdetect*, we linearly interpolated the library PSFs to the off-axis angles and the spectral weighted averaged energies. To account for the fact that part of the PSF wings had been fitted as background in our data, we did the same "background fitting" on the interpolated PSFs. This allows a comparison of the observed curve with the interpolated PSF. The broadband PSFs are generally narrower than the interpolated PSFs, except for one case in the hard band where the off-axis angle is large.

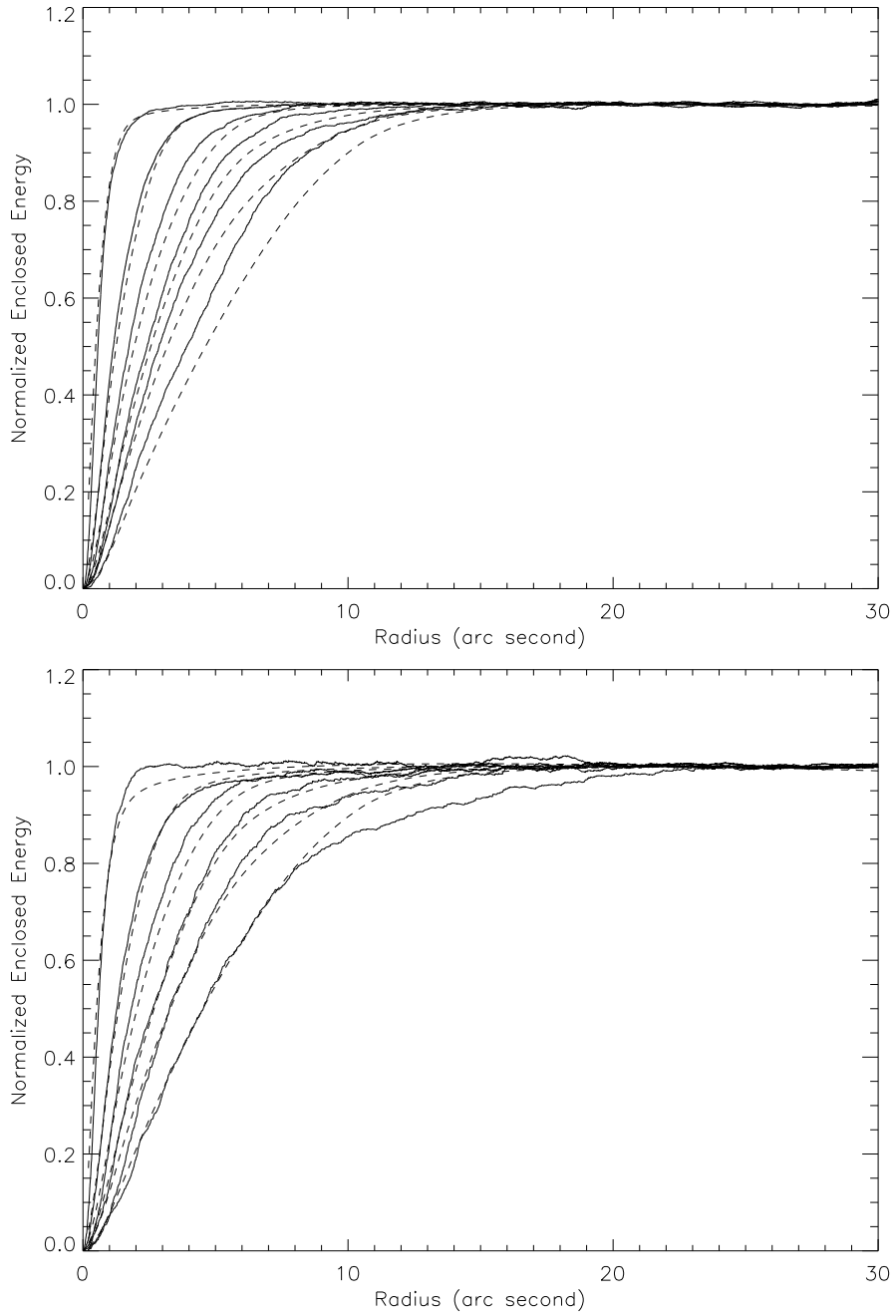

Figure 17: Broadband PSFs obtained from our observations *(solid lines)* compared with the monochromatic PSFs from the PSF library *(dashed lines)*. Both the observed broadband PSFs and the monochromatic PSFs are normalized to the wing. From the narrowest to the broadest, each broadband PSF is constructed within each of the off-axis angle intervals $0'$–$4'$, $4'$–$6'$, $6'$–$7'$, $7'$–$8'$, $8'$–$9'$, $9'$–$12'$. The library PSFs are taken at the midpoints of these off-axis intervals. (a) Soft band PSF vs. 0.91 keV library PSF; (b) hard band PSF vs. 4.2 keV library PSF.

Aperture photometry

We perform flux extractions in the following way. We use circular extraction cells, choosing the radius of cells from the PSF library at a nominal enclosed energy of $\sim 95\%$ (the true enclosed energy should be >95% based on the discussion above) if the cell size is $> 2.5''$. For source close to the aim point, a fixed $2.5''$ radius was used. The background is estimated in an annulus region with an area 4 times as big as the source cell area, with inner radius $5''$ larger than the source cell radius. To avoid nearby sources being included in the background region, the background region is divided into 8 equal-sized segments (Figure 18). The mean background counts are estimated, excluding the segment which contains the highest number of events. Then the 3σ Poisson upper limit is derived using the approximations provided in Gehrels (1986). The background is then recalculated with only the background segments that contain counts less than the upper limit. The net counts are obtained by subtracting the background from the source counts within the source cell. We compare the obtained net counts with the net counts obtained with *wavdetect* (Figure 19). While they mostly agree, the source photons derived from our method are, on average, higher than those from *wavdetect*, especially for low-count sources. The average increases are 4%, 7%, and 8% for the soft, full, and hard bands, respectively. We hand-checked the sources with large discrepancies from the two methods, and we found our estimates to be more reliable.

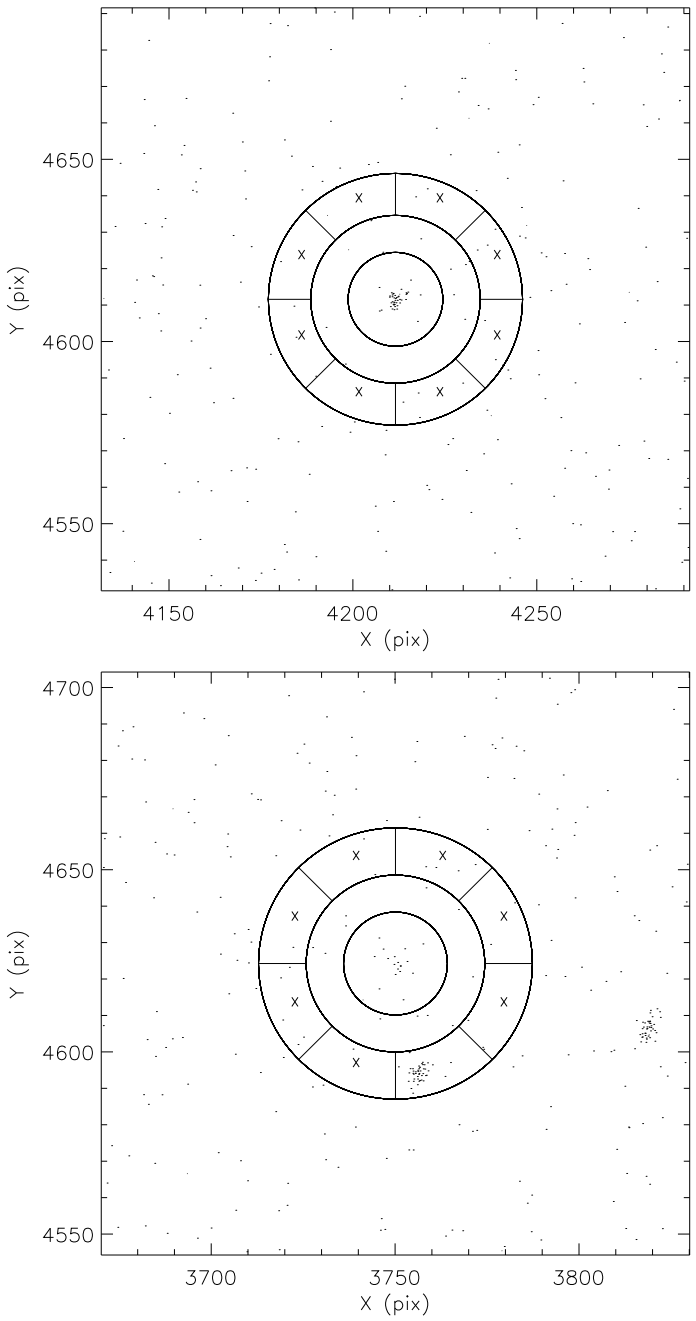

Figure 18: Examples of the source and background regions used in the flux extraction. The smaller circle is the source region. The background regions are shown as segments of an annulus. Segments with counts below 3σ of the mean are used in the final background estimation and are marked with 'X' symbols. (a) An isolated source; (b) a source with a close neighbor.

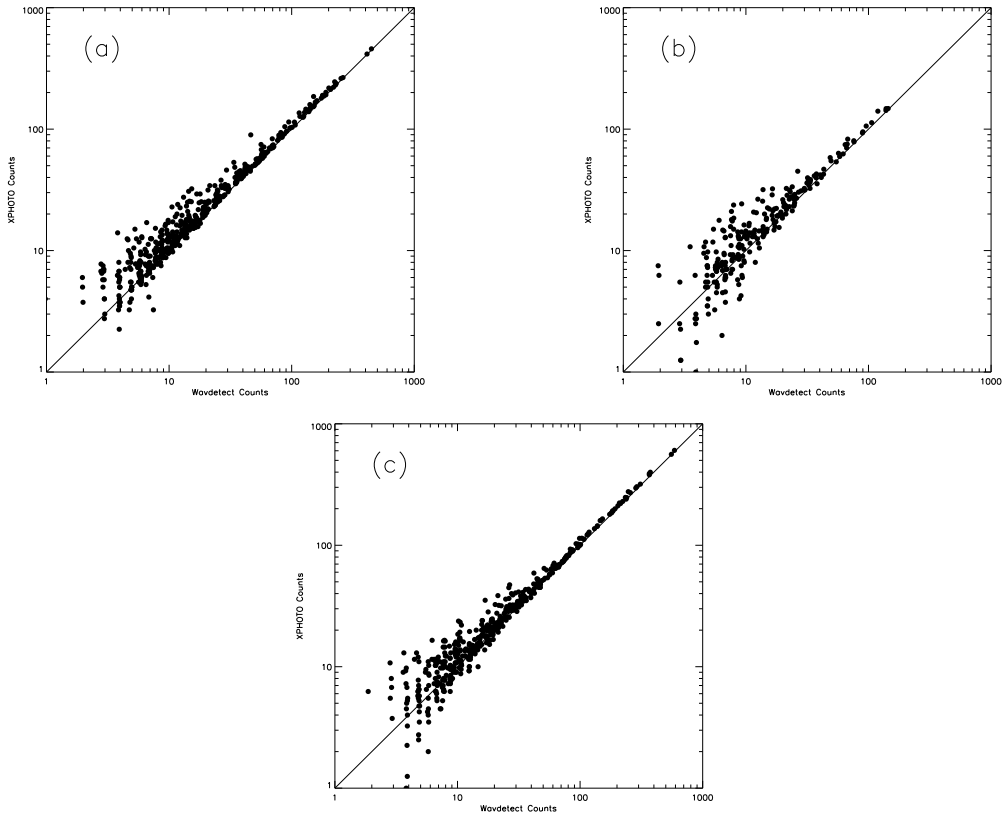

Figure 19: Comparison of net counts from *wavdetect* and our aperture photometry (marked as XPHOTO) for the (a) soft, (b) hard, and (c) full bands.

Exposure time and flux conversion

The prerequisite for using exposure maps is that the effective area is only weakly dependent on energy. This is not the case for our broadband images, where the effective area changes rapidly with energy. Using exposure maps blindly, even the spectrally weighted ones, will inevitably introduce large errors in the resulting fluxes. However, the vignetting (the positional changes of sensitivity) is less sensitive to energy. In other words, if we normalize the exposure maps obtained at different energies to the aim points, then the differences between such "normalized exposure maps" are very small.

Based on this fact, we use the exposure maps only to correct for vignetting and compute the flux conversion at the aim point using spectral modeling. We first make full resolution spectrally weighted exposure maps (using monochromatic maps do not change the results significantly). For each source, the exposure map is convolved with the PSF generated using *mkpsf* and normalized to the exposure time at the aim point. This is the effective exposure time if the source is at the aim point.

The conversion factor is then obtained at the aim point by assuming the source has a Galactic absorbed, single power-law spectrum. The power-law index is calculated using the hardness ratio of each source, defined as $HR \equiv C_{hard}/C_{soft}$, where C_{hard} and C_{soft} are the count rates in the hard and soft bands. XSPEC was used in computing the conversion from HR to Γ and for calculating the conversions. The degradation of quantum efficiency during the flight of the observatory has been

accounted for using the script *apply_acisabs* on the ARFs.

3.3 The X-ray Catalog

We first merged the three band catalogs. We used a 3σ error ellipse from the *wavdetect* output as the identification cell. Flux extraction was then performed on all entries in the merged catalogs in all bands using the best position of the sources. We compared the three band catalogs with the optical catalog to find the astrometric corrections for each observation, as described in § 3.2.3. The nine catalogs were then merged. The fluxes of the sources with more than one detection in the 9 fields were taken from the observation in which the effective area of the source was the largest, except for those sources with more than 2 detections having normalized areas $> 80\%$, where we took the averaged flux. We visually checked the final catalog to ensure the correctness of the merging process. The final catalog contains 525 sources. We present the final catalog in two tables in Appendix A.

The distribution of the source off-axis angles in the merged catalog is shown in Figure 20. It can be seen that most of the sources fall within the$< 6'$ range. Figure 21 shows the distribution of sources with multiple detections. About 1/3 of the sources have more than one observation.

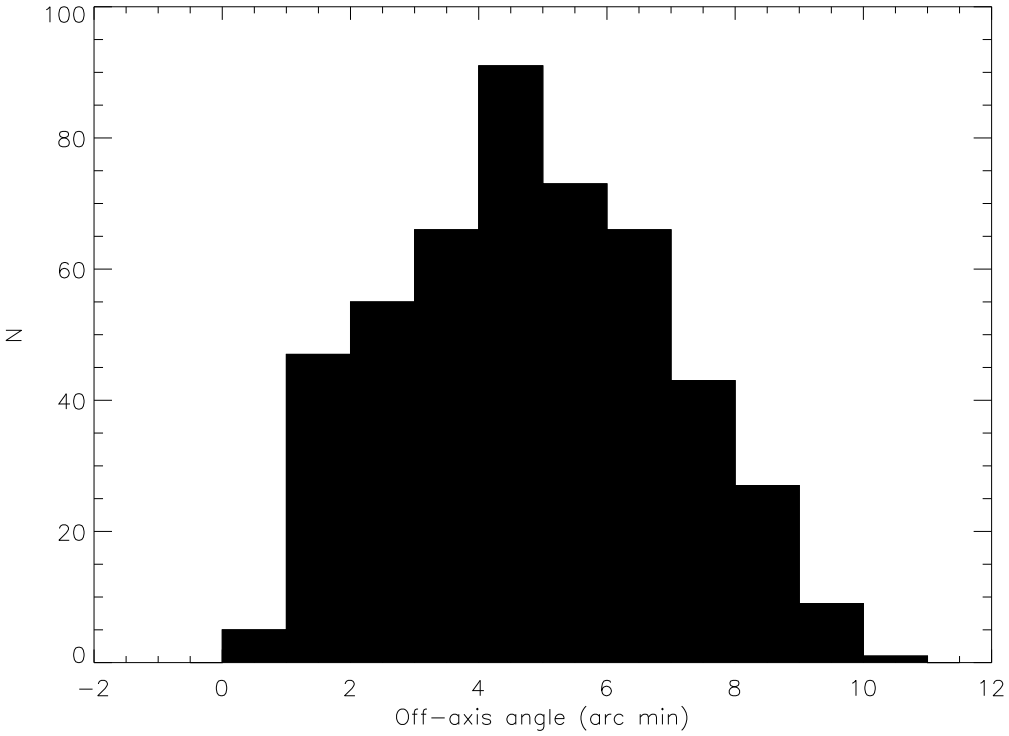

Figure 20: Distribution of off-axis angles of the best positions.

3.4 Number counts

3.4.1 Incompleteness and Eddington Bias

Incompleteness can be caused by energy or positional dependence of the sensitivity of X-ray telescopes. Because the spectrum of a source carries important information on the physical nature of the source itself, sources of different spectra are usually categorized as different types. The energy dependent sensitivity acts like a filter in selecting "hard" and "soft" types of X-ray sources. The soft band detected sources always contain more soft spectrum objects than the hard band detected sources and *vice versa*. Unless the fraction of each type remains constant for all fluxes (which we now know is not true), the energy dependent incompleteness

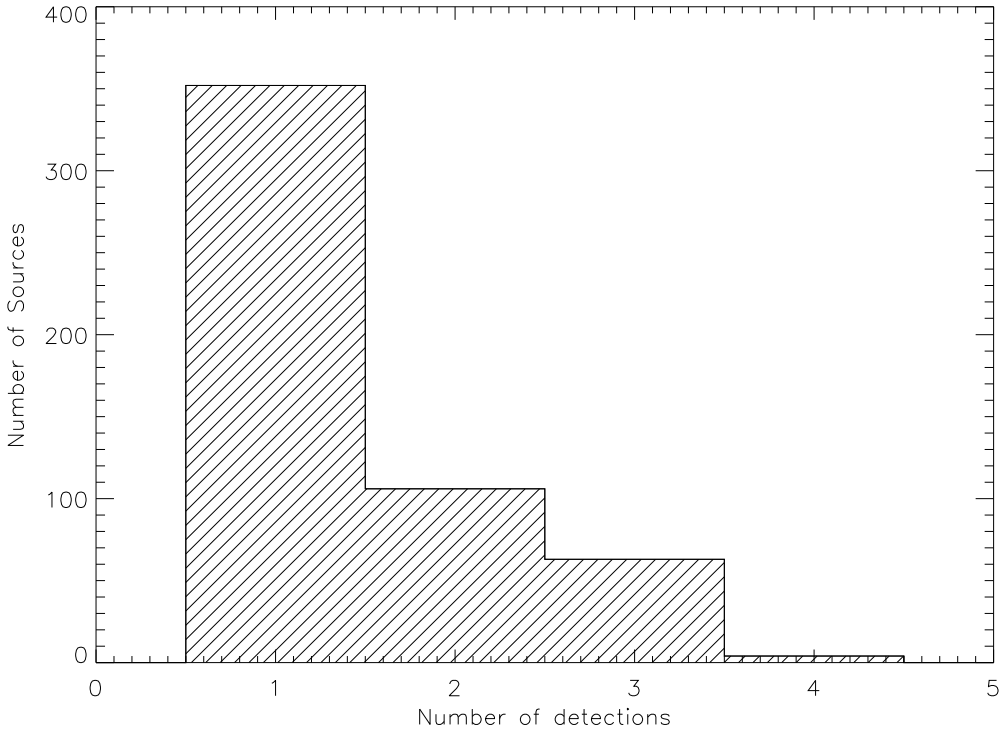

Figure 21: Distribution of multiple detections.

cannot be easily corrected. This issue is very important in interpreting the fraction of different types of objects in flux limited surveys. It is desirable to obtain number counts for each type of source, but it is hard to do that for the CXB sources, where spectra are hard to determine. For our medium deep survey, it is sensible to follow the tradition and only discuss the number counts in energy bands.

The positional dependent incompleteness is caused by vignetting and aberration of the X-ray optics. The vignetting causes the effective area to drop with off-axis angle, and the aberration makes the off-axis PSF larger so that it includes a larger number of background events in the source cell. The net effect is that the sensitivity of source detection drops with increasing off-axis angle. The sky area is therefore flux dependent.

These effects can be investigated via Monte Carlo simulations. We first generated background images using observations of fields #1 and #4, which represent the 70 ks and 40 ks exposures. Point sources are removed from the images, and the holes left in the images are filled by sampling the local background.

Random sources are generated uniformly on the background images. The fluxes of the sources are generated by randomly sampling a complete subset of the combined *Chandra* Deep Fields catalog (Alexander et al. 2003). The subset contains only sources with hard band fluxes $> 5 \times 10^{-16}\,\mathrm{erg\,cm^{-2}\,s^{-1}}$ and effective exposure times > 200 ks. The input fluxes are converted to on-axis counts assuming power-law spectra with $\Gamma = 1.4$. The exposure map for each image is consulted to find the vignetting effect at the source location, and the normalized exposure is multiplied by the true counts to obtain the "observed" net counts. Only sources with more than 3 counts are used in the simulation to avoid adding too many undetectable dim sources to the background. We use the CIAO tool *mkpsf* to generate realistic source shapes at the source positions and energies. The PSF is then sampled to have the same number of photons as in the source. We chose to use *mkpsf* instead of using the *Chandra* simulator MARX because we find the PSF library used by *mkpsf* better resembles sources at large off-axis angles. The number density of the sources is chosen to be 2 times higher than the observed density to increase the number of simulated sources without affecting detections. We ran 100 simulations on the 2 fields and the three energy bands and detected the sources using *wavdetect* with identical parameter settings to those we used in preparing the observed catalog. Because of the large computation time, the number of simulations that can be done

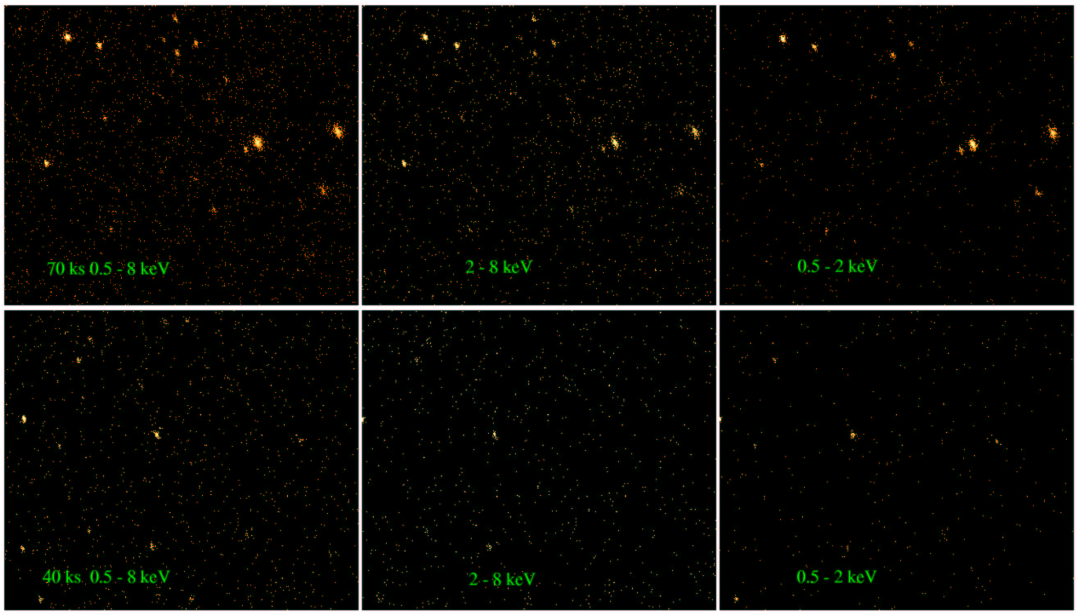

Figure 22: The simulated images with 40 and 70 ks exposures in three bands.

is limited. An example of the simulated images is shown in Figure 22.

We then compared the output catalogs with the input source catalogs. Because of the small size of the simulation, the completeness within $4''$ is not well determined, and a 5% uncertainty exists in the determined fractions. Fortunately, the PSF effect is small at such small off-axis angles. For a given flux threshold, the fraction of source detections drops monotonically with off-axis angle. This relation is fitted between $4'$ and $10'$ with a linear least-squares fit. The 95% complete off-axis angle limit is then taken from the interpolation of the fit. The resulting 95% completeness flux thresholds map is shown in Figure 23. We note that at large off-axis angles, the sensitivity drops rapidly. This is partly due to the choice of wavelet scales. When the largest scale used becomes smaller than the PSF size of the source, *wavdetect* is no longer sensitive. This effect, however, is not important for our observations, because

most of the sources of interest are within 6′ off-axis, thanks to the overlapping of fields. Sources at very large off-axis angles are excluded from the study of the LogN-LogS. The combined solid angle versus flux thresholds is shown in Figure 24.

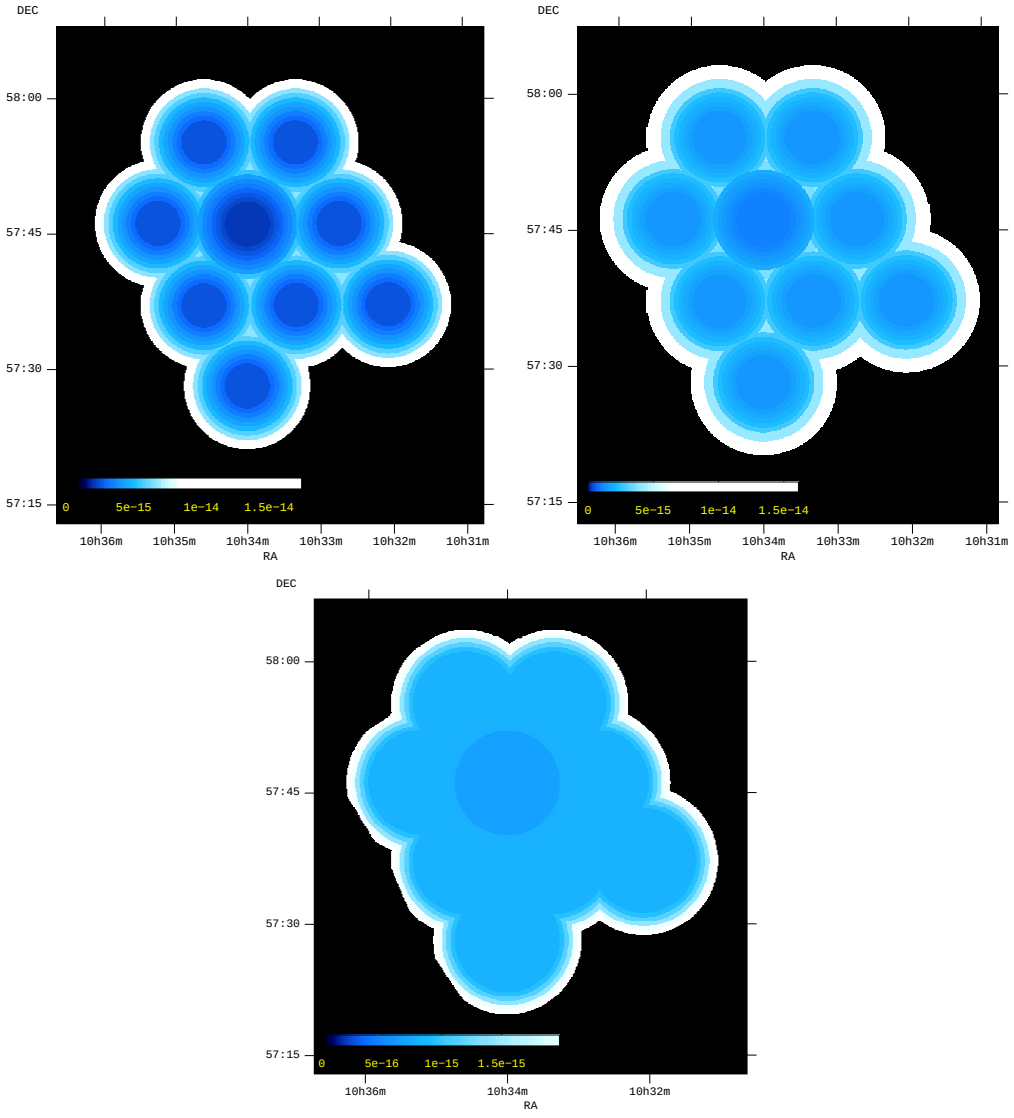

Figure 23: The 95% completeness threshold for CLASXS fields in 2–8 keV (upper-left), 0.5–8 keV (upper-right) and 0.5–2 keV (bottom) bands.

The Poisson fluctuations in the source fluxes could result in an overestimation of number counts close to the detection limits. This is known as the Eddington Bias.

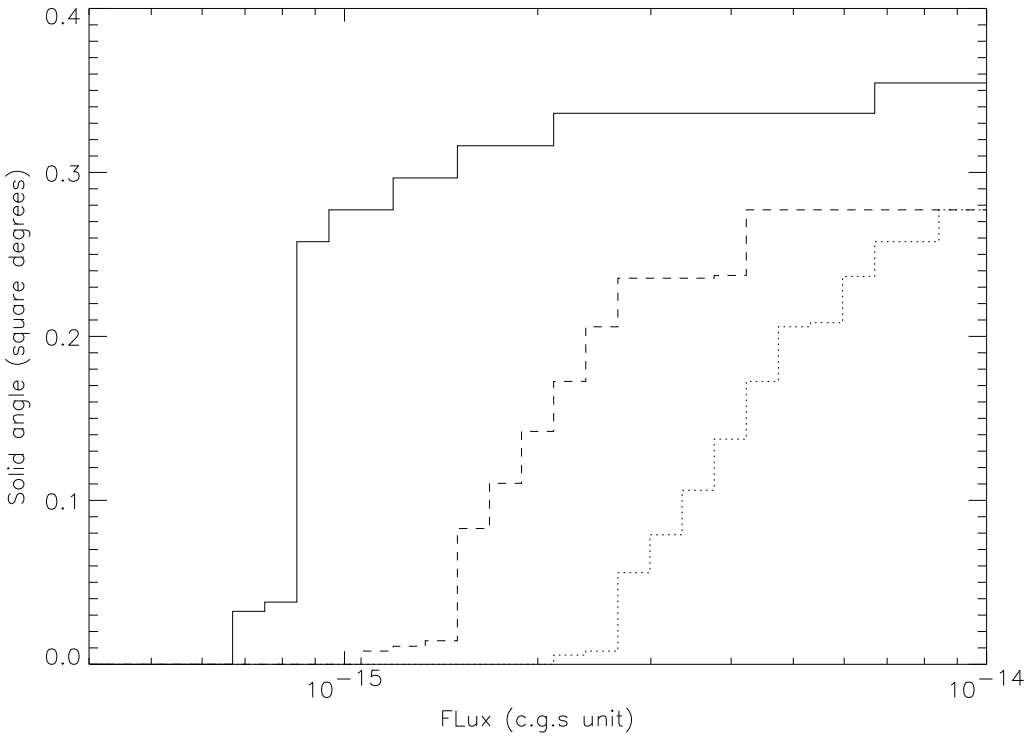

Figure 24: Survey effective solid angle vs. flux. Soft band (solid line); full band (dashed line); hard band (dotted line)

The effect depends both on the slope of the LogN-LogS and the level of fluctuation. For the CLASXS field, the detection threshold is below the "knee" of the LogN-LogS, and the Eddington bias is relatively small. We corrected this bias using the method described in Vikhlinin et al. (1995). In Figure 25, we compare the average input flux with the average output flux at different off-axis angles from the simulations. For the soft band, the correction is only important below 2×10^{-15} erg cm^{-2} s^{-1}. For the hard band, the correction is important below 8×10^{-15} erg cm^{-2} s^{-1}. We fit flux–flux curves in Figure 25 for the different off-axis angles with fourth order polynomials and correct the source fluxes in the observed catalog using these fits.

3.4.2 Number counts

Sources are selected by consulting the threshold map at the source positions and including only those with Eddington bias corrected fluxes higher than the threshold map values. Sources very far off-axis are excluded from the analysis. With these selections, we used a total of 310 and 235 sources in the soft and hard bands, respectively, to construct the LogN-LogS. The cumulative LogN-LogS relations are computed using the formula

$$N(>S) = \sum_{S_i > S} \frac{1}{\Omega(S_i)} \tag{3.1}$$

where Ω is the complete solid angle. We show the results in Figure 26 in the soft and hard bands with 1σ Poisson errors. The differential LogN-LogS for the two bands are shown in Figure 27, which are calculated using the formula

$$\frac{dN}{dS} = \sum \frac{1}{\Omega_i \Delta S}\,, \tag{3.2}$$

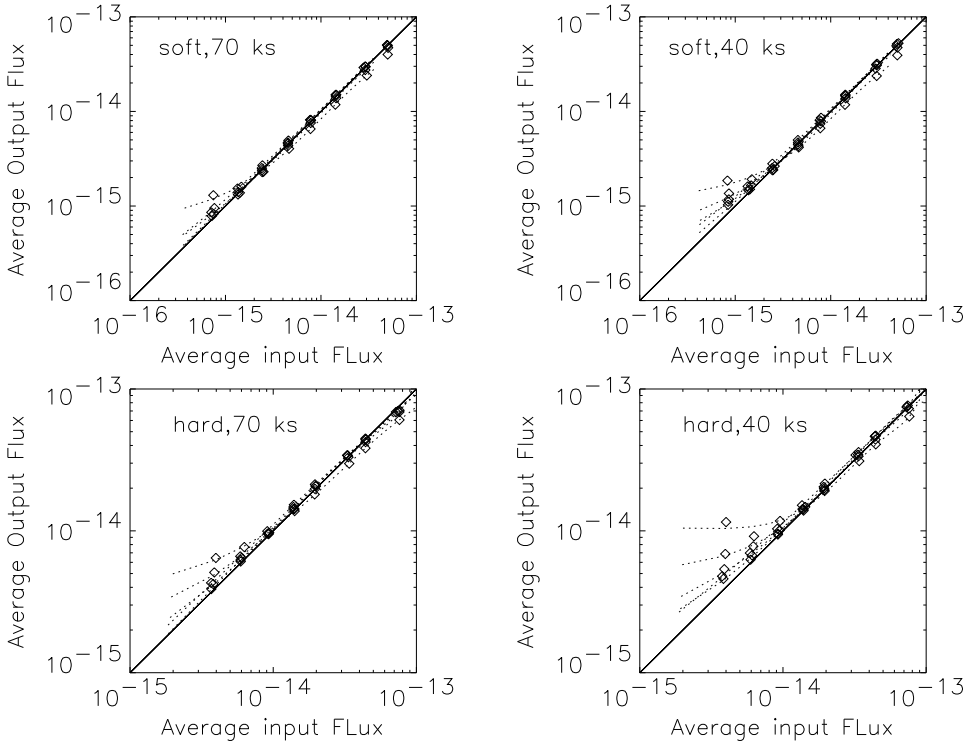

Figure 25: Average output fluxes from *wavdetect* vs. average input fluxes for the simulated sources at a set of off-axis angles *(diamonds)*. The Eddington bias is seen in the overestimates of output flux at low fluxes. The bias also increases at large off-axis angles. The best fit of the biases are shown as dotted lines for off-axis angle intervals $0'$–$2.5'$, $2.5'$–$4'$, $4'$–$6'$, $6'$–$8'$, and $> 8'$.

in units of $\deg^{-2}$ per 10^{-15} erg cm^{-2} s^{-1}. We fit the resulting differential number counts with single or broken power laws in the form of

$$\frac{dN}{dS} = n_0 \left(\frac{S}{10^{-14}} \right)^{-\alpha} \tag{3.3}$$

using error weighted least-square fits. Since our survey best samples the "knee" of the LogN-LogS, the slope of the power-laws are not well constrained due to the lack of data points both far above and below the "knee". On the other hand, n_0 is better determined, to within 1%.

For the soft band, we fit the number counts between 10^{-15} and 10^{-14} erg cm^{-2} s^{-1} with a power law. We find the best-fit parameters to be $\alpha = 1.7 \pm 0.2$ and $n_0 = 12.49 \pm 0.02$. The slope is in good agreement with previous observations, such as the *Chandra* Deep Field-North (1.6 ± 0.1, Brandt et al. 2001), SSA13 (1.7 ± 0.2, Mushotzky et al. 2000), and the compiled wide fields from *Chandra*, *XMM-Newton, ROSAT*, and *ASCA* ($1.60^{+0.02}_{-0.03}$, Moretti et al. 2003; hereafter, Moretti03). The normalization also shows excellent agreement with the compiled results from the large area survey of Moretti03, which has an effective solid angle at 10^{-14} erg cm^{-2} s^{-1} larger than that of CLASXS. Above 10^{-14} erg cm^{-2} s^{-1}, the slope steepens, but the fluctuations in the number counts make it difficult to find a reasonable fit. However, the LogN-LogS is apparently consistent with a slope of $\alpha = 2.5$, shown as the dotted line at these fluxes.

Similarly, we model the hard band number counts with a broken power law and obtain the following best-fit parameters. For $S > 10^{-14}$ erg cm^{-2} s^{-1}, $\alpha = 2.4 \pm 0.6$ and $n_0 = 45.6 \pm 0.5$; for $3 \times 10^{-15} < S < 2 \times 10^{-14}$ erg cm^{-2} s^{-1}, $\alpha = 1.65 \pm 0.4$ and

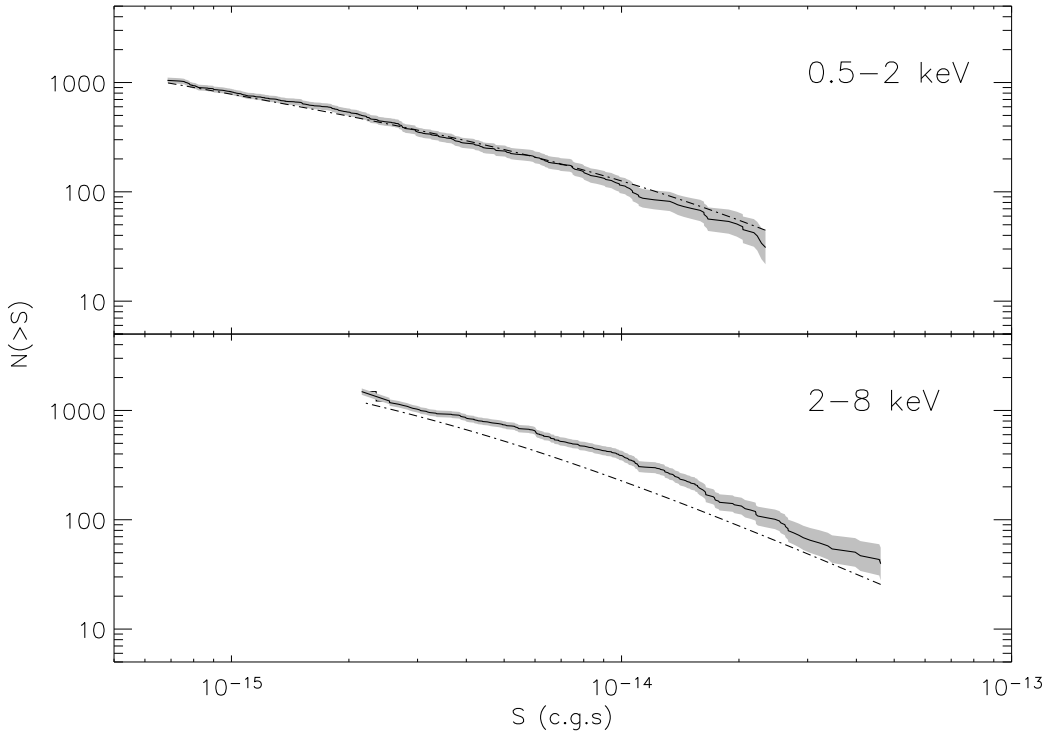

Figure 26: Cumulative LogN-LogS for the soft and hard bands. The 1σ error is shaded. Dash-dotted line represents the best fit from Moretti03. Hard band LogN-LogS from Moretti et al. is rescaled to that of $2-8$ keV, assuming $\Gamma = 1.4$.

$n_0 = 38.1 \pm 0.2$. For comparison, we also plot the best-fit cumulative LogN-LogS from Moretti03 and differential LogN-LogS from the SEXSI fields (Harrison et al. 2003) and from Cowie et al. (2002). At fluxes below $8 \times 10^{-15}\,\mathrm{erg\,cm^{-2}\,s^{-1}}$, the differential LogN-LogS for all the fields agrees within the errors. The difference in the total counts at a flux limit between the CLASXS field and the Moretti03 fields is also small. An apparent difference is seen around 10^{-14} $\mathrm{erg\,cm^{-2}\,s^{-1}}$: the total counts at $10^{-14}\,\mathrm{erg\,cm^{-2}\,s^{-1}}$ are $\sim 70\%$ higher than those from Moretti03. This is significant at greater than the 3σ level.

3.4.3 Point Source Contribution to the CXB

The integrated flux between 3×10^{-15} and $8 \times 10^{-14}\,\mathrm{erg\,cm^{-2}\,s^{-1}}$ from the LogN-LogS is $(1.2 \pm 0.1) \times 10^{-11}$ ergs $\mathrm{cm^{-2}\ s^{-1}\ deg^{-2}}$. This is $\sim 20\%$ higher than that from Moretti03 and SEXSI in the same flux range. Since there is little difference in the number counts between the CLASXS fields and the other large solid angle surveys at fluxes lower than $8 \times 10^{-15}\,\mathrm{erg\,cm^{-2}\,s^{-1}}$, we should expect little difference below the survey limit on the same angular scales. If integrated to lower fluxes, and including the integration from *ASCA* above $8 \times 10^{-14}\,\mathrm{erg\,cm^{-2}\,s^{-1}}$, the fractional difference between the CLASXS field and the other large solid angle surveys can be reduced to $\sim 10\%$ without considering the possible biases. This difference is higher than expected from the variance in the CXB from *ASCA* observations but is consistent with recent observations with *RXTE/PCA*, where a 7% variance is seen among several ~ 1 $\mathrm{deg^2}$ fields (Revnivtsev et al. 2004).

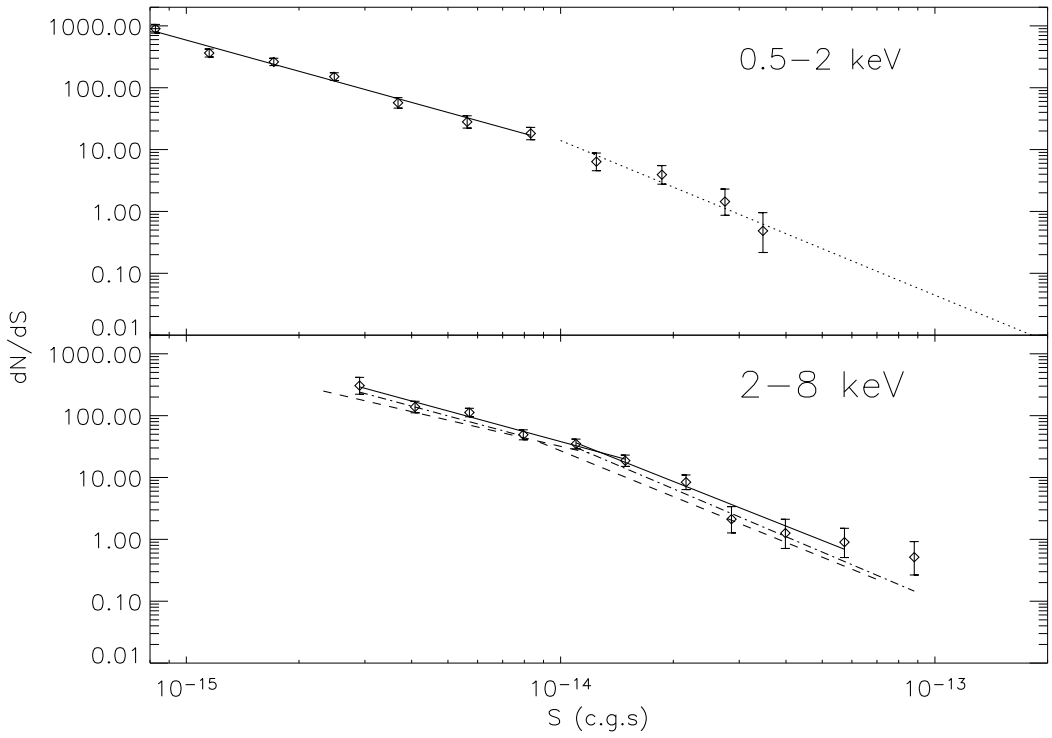

Figure 27: Differential LogN-LogS for the soft and hard bands. The unit of dN/dS is number per $10^{-15}\,\mathrm{erg\,cm^{-2}\,s^{-1}}$. Best-fit power laws are shown as solid lines. Dotted line represents a power law with a fixed index of -2.5. The data do not constrain the slope at high fluxes well. Dashed line shows the best fit of the hard band LogN-LogS from the SEXSI survey (Harrison et al. 2003) and the dash-dotted line is the best fit from Cowie et al. (2002).

The uncertainty of the hard CXB itself is $\sim 10-15\%$. The differences in the integrated point source fluxes from various large fields are within this uncertainty. In terms of the true contribution from point sources to the CXB, a field with a solid angle of ~ 0.3 deg^2 seems to be large enough to be representative.

The large difference in the cumulative number counts at the "knee" between our fields and the other large fields seems to indicate that the sources that emerge at this flux are more clustered on the sky than the soft band selected sources. However, caution must be taken because the fluxes between the surveys are not calibrated. A small systematic error in flux estimates could result in significant change in the number counts above the "knee" of the LogN-LogS.

3.5 Spectral properties the CXB sources

We employ the hardness ratio to quantify statistically the spectra of the CXB sources in our field. Figure 28 shows the distribution of hardness ratio versus full band flux. We have also marked the hypothetical photon indices (Γ), assuming the hardness ratio change is purely due to the slope change of a single power-law spectrum. At fluxes $> 3 \times 10^{-14}$ erg cm^{-2} s^{-1}, most sources cluster around $\Gamma \sim 1.7$. At lower fluxes, the hardness ratio distribution scatter increases and the relative number of hard sources increases. Below 3×10^{-15} erg cm^{-2} s^{-1}, the data show a paucity of hard sources. This is a selection effect caused by the sensitivity in the hard band being lower than in the soft band for most spectra. We stacked the sources in flux bins and calculated the hardness ratios of the stacked spectra. Figure 29 shows

the stacked hardness ratios from both the CLASXS $> 10^{-14}$ erg cm^{-2} s^{-1} sample and the combined CDFs $> 10^{-15}$ erg cm^{-2} s^{-1} sample. The flux thresholds are chosen to avoid selection effects caused by the sensitivity differences between the soft and hard bands. It is apparent that the results from our data and those from the CDFs agree well.

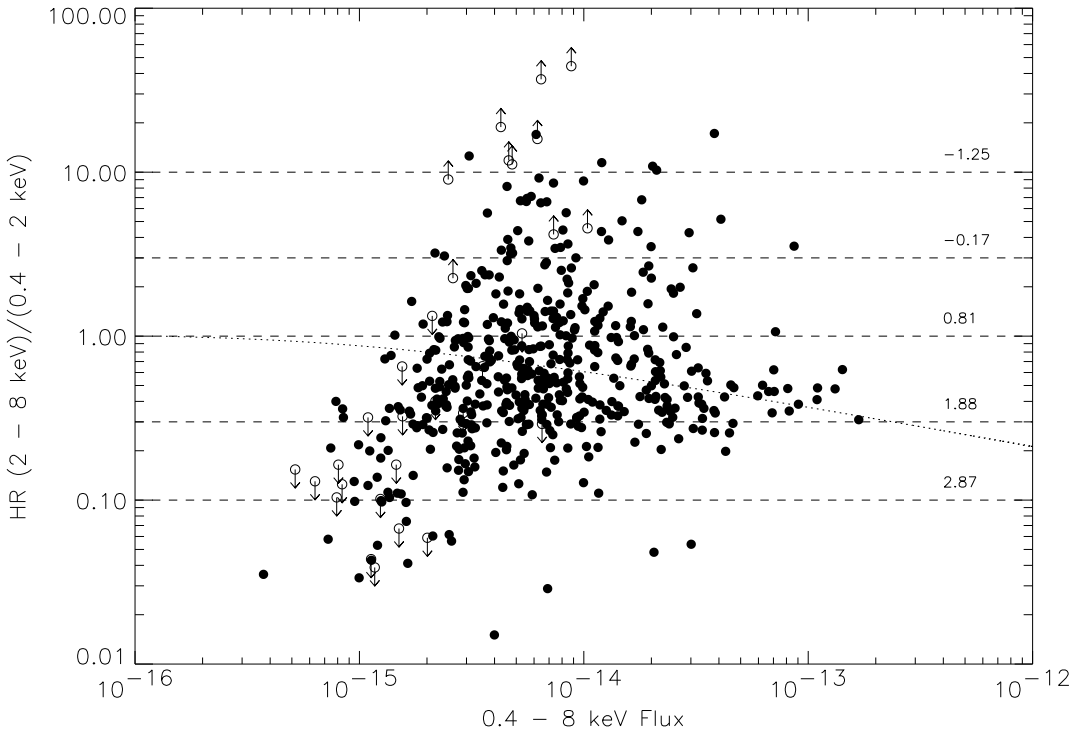

Figure 28: Hardness ratio vs. full band flux for the CLASXS sources. Open circles with arrows represent the upper or lower limits. Dashed lines with numbers label the hypothetical spectral indices, assuming the source spectra are single power laws with only Galactic absorption. Dotted line represents the typical error size of the hardness ratio for a source with hardness ratio of 1.

The spectral flattening at low fluxes has been observed by several authors (e.g., Mushotzky et al. 2000; Tozzi et al. 2001; Piconcelli et al. 2003; Alexander

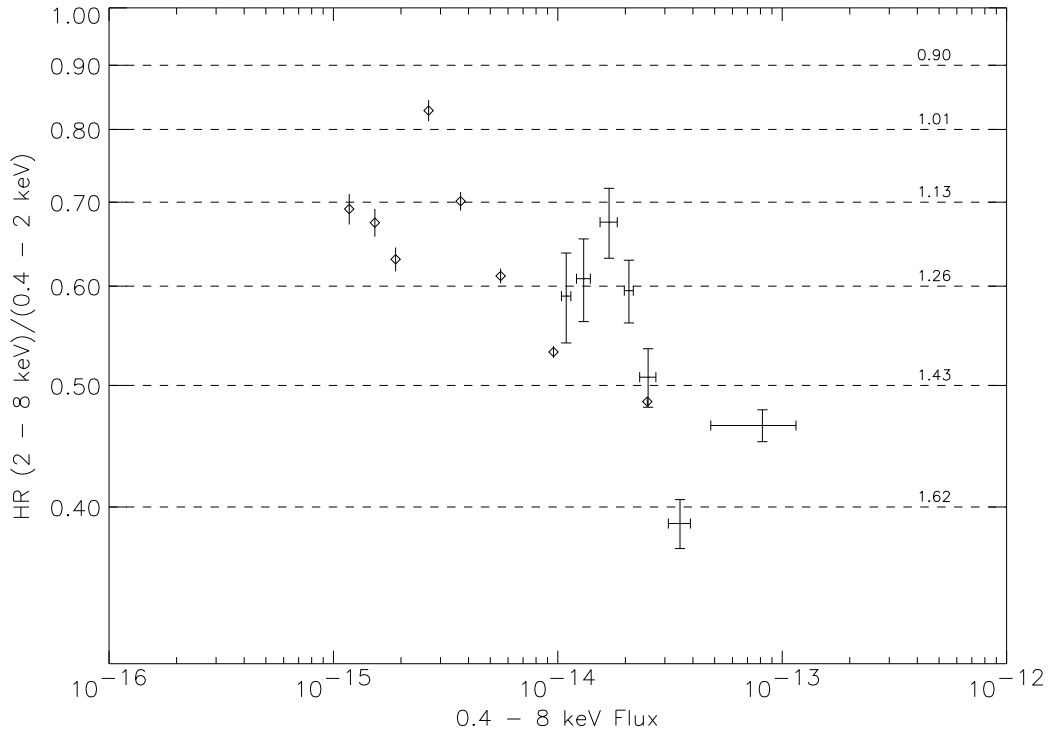

Figure 29: Hardness ratio of the stacked sources in different flux bins. Crosses are the CLASXS sources and diamonds are the combined CDFs sources (Alexander et al. 2003). Sources with fluxes below 8×10^{-15} erg cm^{-2} s^{-1} in the CLASXS catalog and 1×10^{-15} erg cm^{-2} s^{-1} in the CDFs catalogs are not included to avoid incompleteness. Dashed lines are as in Figure 28.

et al. 2003) with observations of different depths. Spectral analysis with *XMM-Newton* observations indicate that such a flattening is mainly caused by absorption. These obscured AGN must dominate the population around the "knee" of the LogN-LogS to account for the flat spectrum of the CXB. Since most of the *XMM-Newton* spectral observations have reached a few times 10^{-14} erg cm^{-2} s^{-1} (Piconcelli et al. 2002), and the mean spectrum at this threshold is still too soft compared with that of the CXB, a sharp increase of obscuration or a change of spectral shape at a flux $\sim 10^{-14}$ erg cm^{-2} s^{-1} is inevitable. Such a sharp change is seen in the change of hardness ratio in our wide-field sample.

3.6 A First Look at X-ray Variability at High redshifts

X-ray variability is an important factor in distinguishing AGN from starburst galaxies. Almost all AGN vary in X-rays, except those sources which are Compton thick. Alexander et al. (2001) showed that only a small fraction of the optically faint X-ray sources vary. Possible explanations could be that a large fraction of the optically faint sources are Compton thick, or that the amplitude of variation of the optically faint sources is much lower than that of the broad and/or narrow-line AGN at the same flux thresholds.

We examine the variability of sources that have been detected in more than one of our observations. Since the observations were taken in two groups, separated by about one year, and each group of observations were taken within a few days (see Table 3.1), we are able to test variability on timescales of days and/or one year,

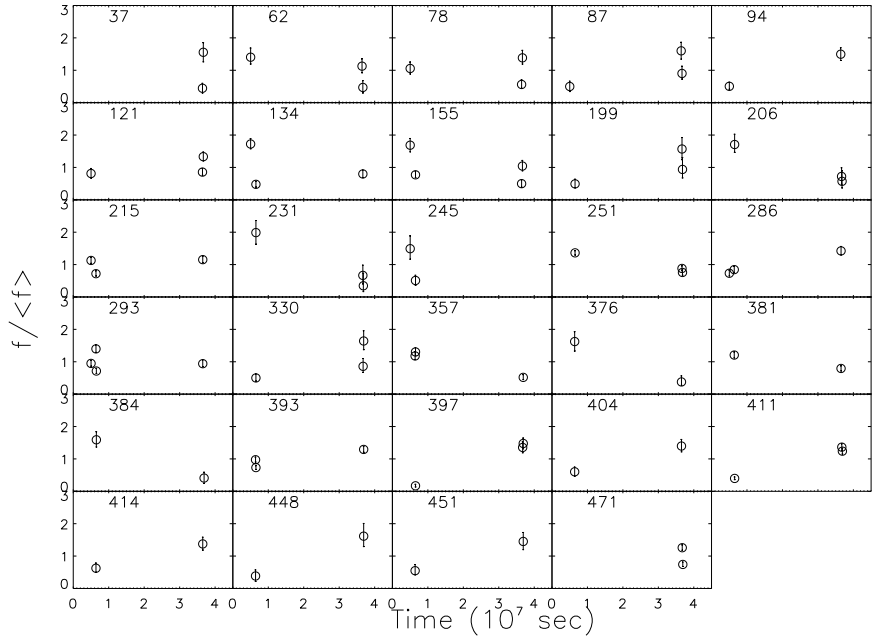

Figure 30: Light curves of the sources detected to be variable. The fluxes are normalized to the mean of all the observations. Numbers in the plots are the source numbers in the catalog. (a) Soft band; (b) hard band; (c) full band.

depending on the location of the source.

For timing analysis with low counts per bin, the usual χ^2 statistic is inadequate. We use the C-statistic (Cash 1979) in testing the significance of variability. Cash (1979) showed that the C-statistic (a reduced form of likelihood ratio) written as

$$\Delta C = -2 \sum_{i=1}^{N} [n_i ln(e_i) - e_i - n_i ln(n_i) + n_i] \tag{3.4}$$

is asymptotic to a χ^2 distribution with $N-1$ degrees of freedom, where n_i is the observed counts in the *ith* sample, e_i is the expected counts in that sample, and N is the total number of samples used. We restricted the sample for the variability test to sources with expected counts greater than 10 in all observations. The null hypothesis rejection probability was chosen to be 0.01.

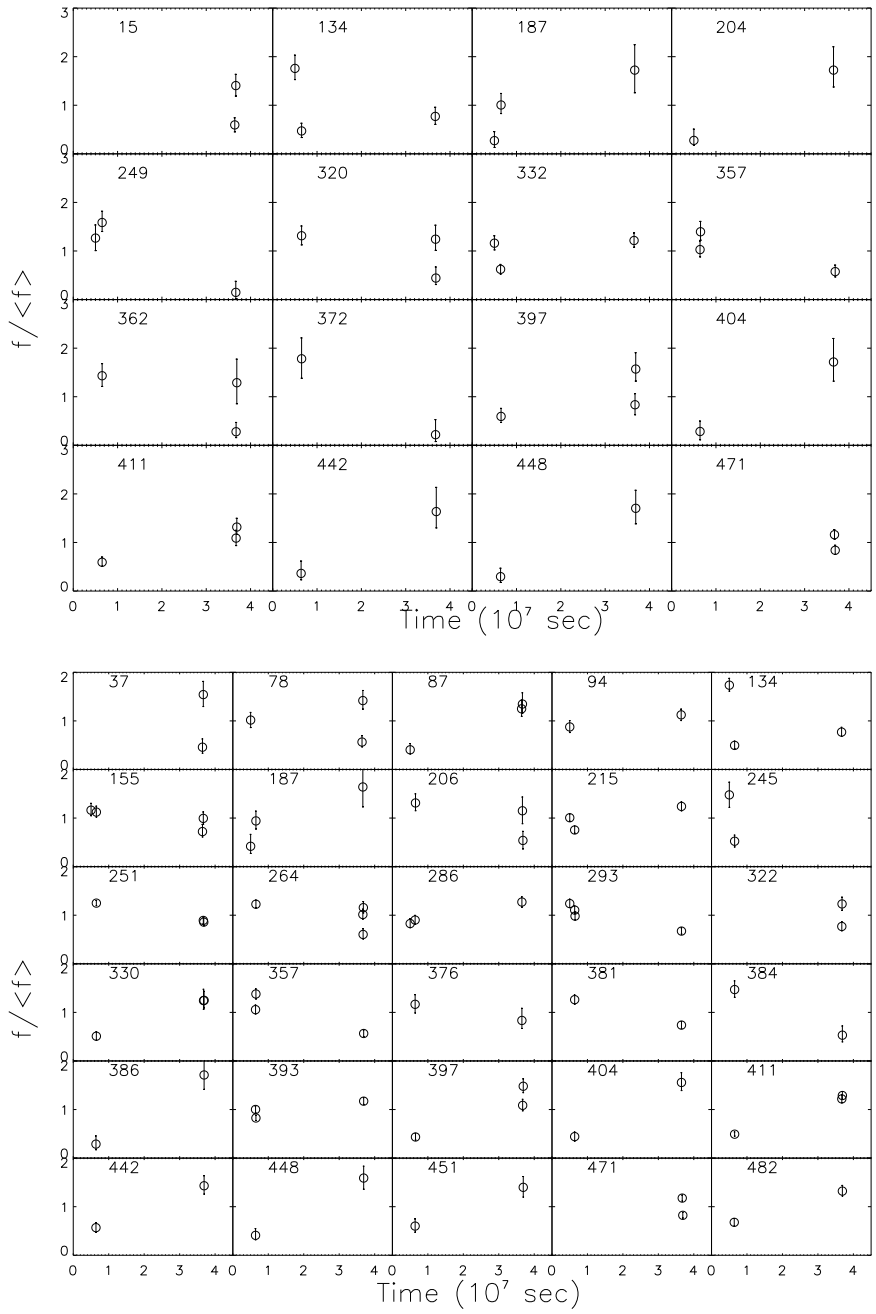

Figure 30 (continued)

A total of 168 sources were tested for variability, of which 42 sources are significantly variable and 28 sources show variability on timescales of days. There are 29, 16, and 30 variable sources detected in the soft, hard, and full bands, respectively. Figure 30 shows the light-curves of the sources that were tested to be variable in any of the three energy bands. In the top panel of Figure 31, we show the fraction of variable sources detected versus flux. Between $4 - 8 \times 10^{-14}$ erg cm^{-2} s^{-1}, 70% of the sources tested show variability. This fraction drops dramatically as the flux decreases and, at 10^{-14} erg cm^{-2} s^{-1}, reaches below 20%. This is at least in part due to the selection effect that larger variability is needed at lower fluxes to make the test significant. At fluxes above 8×10^{-14} erg cm^{-2} s^{-1}, only one of the four sources tested (25%) was found to be variable.

Following Nandra et al. (1997), we define the magnitude of variability as the "excess variance", the error subtracted rms variance

$$\sigma_{rms}^2 = \frac{1}{N\mu^2} \sum_{i=1}^{N} [(f_i - \mu)^2 - \sigma_i^2] \tag{3.5}$$

where f_i is the flux in each observation, μ is the mean of the fluxes, and σ_i is the Poisson error of the flux. By assuming the same power density spectrum of X-ray variability for all AGN, σ_{rms}^2 can be used as a good indicator of whether the variability exceeds the Poisson noise. It has been found that there exists a good anti-correlation between σ_{rms}^2 and AGN luminosity (Nandra et al. 1997) in local AGN samples.

In Figure 32, we show the excess variance of sources that had been detected to be variable versus X-ray flux in the three energy bands. At high fluxes, the average

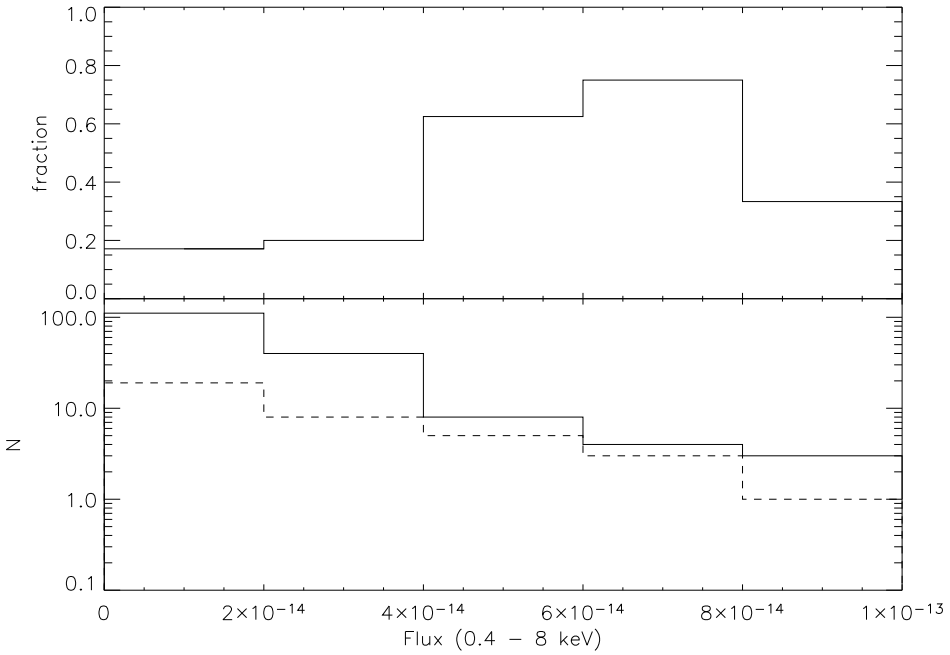

Figure 31: *(Upper panel)* Fraction of sources that are variable in different flux bins. *(Lower panel)* Number of variable sources *(dashed histogram)* and total number of sources tested for variability *(solid histogram)* in the same flux bins as in the upper panel.

σ^2_{rms} is significantly lower than at lower fluxes. As mentioned above, variability is harder to detect for low flux sources, unless the source is more variable than that of the brighter sources, so this bias could explain why there are very few low flux, low variability sources in the plot. In addition, the sources we detect to be variable are generally soft. This is consistent with the observation from the CDFs that optically faint sources (most of which are hard spectrum AGN) are less variable (Alexander et al. 2001).

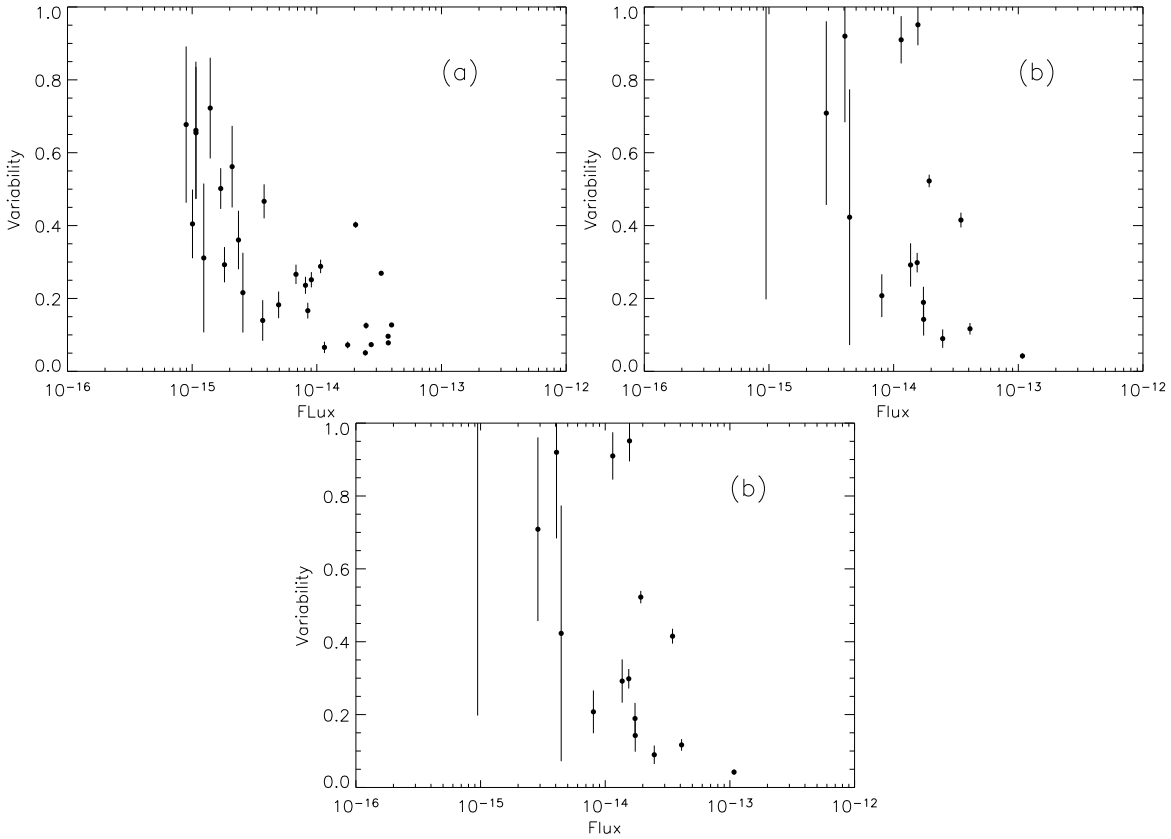

Figure 32: Excess variability for the variable sources in each energy band vs. the flux of that band. (a) Soft band; (b) hard band; (c) full band.

Spectral variability

Very little is known about the spectral variability of the sources that contribute the most to the CXB due to a lack of data. Spectral variability is seen in about half of the well-studied brighter sources, with a general trend of softening of the $2-10$ keV spectra with increasing source intensity. But a counterexample is NGC7469, where the spectrum flattens when the source flux increases (Barr 1986). The variability could be accounted for either with a change in the relative normalization of the different spectral components or by variation in the absorption.

In Figure 33, we show hardness ratios versus full band fluxes for the variable sources. While most of the sources show either no clear spectral variability, or a trend of spectral softening with increasing flux, there are a number of sources that clearly become harder with increasing flux. There are also a few sources that exhibit a mixed trend. On average, these sources tend to have softer spectra with increasing flux.

3.7 Summary

In this chapter, we presented the CLASXS X-ray catalog. Our survey covers a $\sim$ 0.4 deg^2 contiguous area in an uniform manner and reaches fluxes of 5×10^{-16} erg cm^{-2} s^{-1} in the $0.4-2$ keV band and 3×10^{-15} erg cm^{-2} s^{-1} in the $2-8$ keV band. We found a total of 525 point sources and 4 extended sources. We summarize our results as follows.

The number counts in the $0.4-2$ keV band agree very well with other large

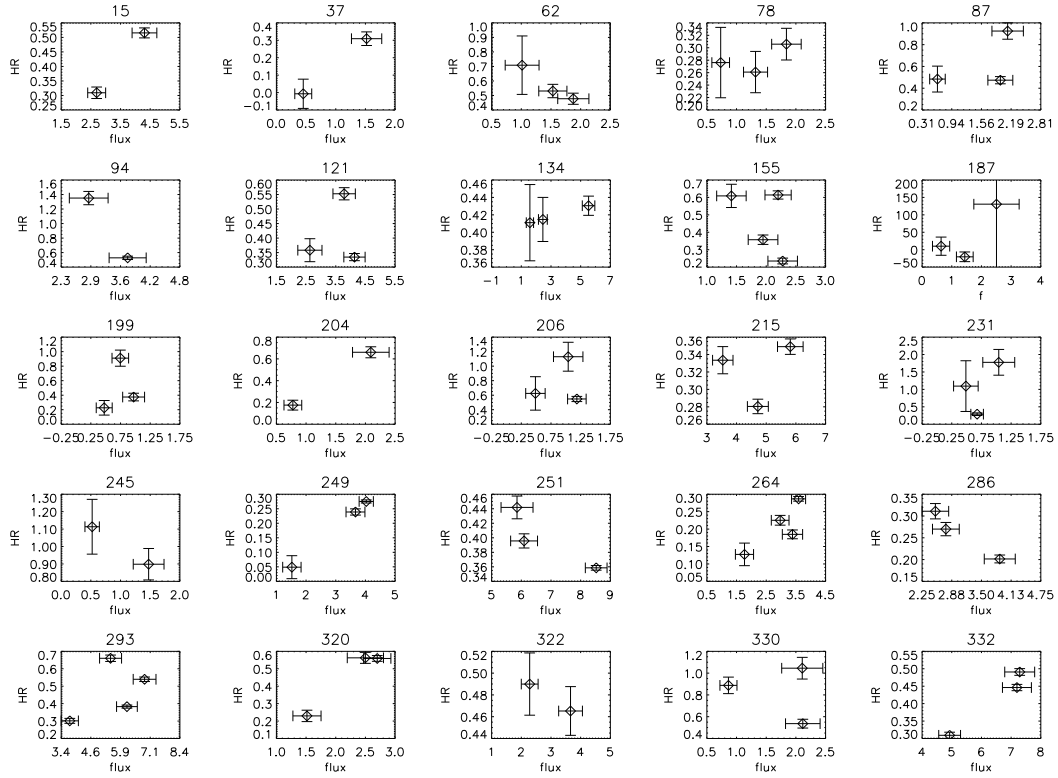

Figure 33: Spectral variability vs. full band fluxes for all the variable sources. The fluxes are in units of $10^{-14}\,\mathrm{erg\,cm^{-2}\,s^{-1}}$. Numbers on top of each plot are the source numbers in the catalog.

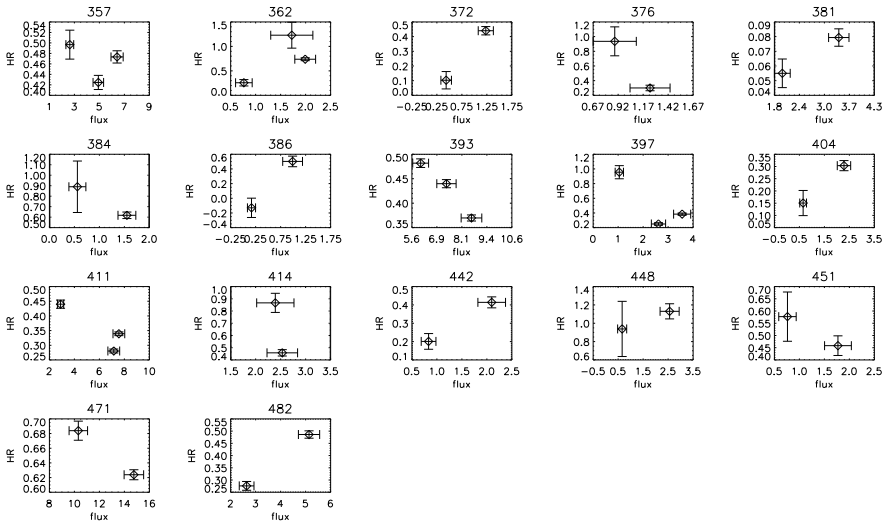

Figure 33 (continued)

area surveys. On the other hand, the number counts in the $2-8$ keV band deviate significantly from other large area surveys at the "knee" of the LogN-LogS, possibly as a result of the underlying large scale structure. The total $2-8$ keV band flux agrees with the observed CXB flux within the observed variance of the CXB, indicating that the true normalization of the CXB can be determined using fields with solid angles $\sim 0.3-0.4$ deg^2.

The hardness ratios of the sources in the CLASXS field show a significant change at $f_{2-8\ \mathrm{keV}} \sim 10^{-14}$ erg cm^{-2} s^{-1}, which bridges the range sampled by previous studies and confirms the results found in deep *Chandra/XMM-Newton* surveys. About 60% of the sources with full band fluxes $> 4\times10^{-14}$ show significant variability, while the fraction drops dramatically with decreasing flux, at least partly due to selection effects. Most sources show no change of hardness ratio or anti-correlation

with flux. But some sources show a positive correlation or mixed trends.

Chapter 4

Optical Identifications and Spectroscopic Follow-up

As mentioned earlier, optical follow-up is critical in obtaining redshift and spectral type of X-ray selected AGNs. These information will be used to obtain the X-ray luminosity function and spatial correlation function. The details of the observation and reduction are discussed in Steffen et al. (2004) and Barger et al. (2005). I will summarize the observations and basic methods used in the data reduction. This will provide the useful information to understand the systematics introduced from optical observations when we try to combine the X-ray results with these observations. I will also discuss the importance of the high spatial resolution of *Chandra* in obtaining the correct counterparts, particularly to the optical normal AGNs.

4.1 Imaging observation

Deep optical images were taken from the Subaru 8.2m telescope using the Suprime-Cam camera; and from the Canada-France-Hawaii Telescope (CFHT) with CFH12K camera. The observations, the 2σ limiting magnitudes can be found in Tabel 4.1.

The optical sources are detected using the SExtractor (Bertin & Arnouts 1996) and the source fluxes were extracted using the IDL program APER from the IDL

Table 4.1. Summary of Optical Images

Band	Telescope	Average seeing (arcsecond)	Integration (hr)	2 σ limit (AB mag)	Total area (deg^2)	Deep area (deg^2)
B	Subaru 8.2 m	0.96	1.7	27.8	0.27	0.20
B	CFHT 3.6 m	0.97	5.8	27.6	0.49	0.49
V	Subaru 8.2 m	1.15	6.4	27.5	0.36	0.20
R	Subaru 8.2 m	0.96	5.2	27.9	0.27	0.20
R	Subaru 8.2 m	0.61	2.0	27.7	0.81	0.81
R	CFHT 3.6 m	0.89	11.9	27.9	0.49	0.49
I	Subaru 8.2 m	1.30	0.9	26.4	0.36	0.20
z'	Subaru 8.2 m	1.01	1.3	26.2	0.36	0.20
Z	CFHT 3.6m	0.95	23.8[a]	26.3	0.49	0.49

[a]Taken in two separate 11.9 hr integrations

Astronomy User's Library[1]. A fixed 3″ diameter aperture is used to extract source magnitudes. Aperture corrections are made by examining the curve-of-growth for isolated, moderately bright ($R = 20 - 26$) sources. The sources brighter than $R = 20$ Mag are saturated.

4.2 Optical Counterparts of X-ray point sources

Optical counterparts of the X-ray sources are matched using fixed search radius. In cases when multiple counterparts are found in the search radius, the source closest to the X-ray position is chosen to be the tentative counterpart. We used these positions to make the global adjustments to the X-ray positions as discuss in § 3.2.3. We search for the counterparts again with the new X-ray positions.

In Figure 34, we show the (X-ray − optical) astrometric offsets for the CLASXS sources. Histograms for the right ascension and declination offsets are shown above and to the right, respectively. The average astrometric discrepancies in both axis are 0.0 ± 0.5 arcseconds. We ran simulations to examine the probability of an X-ray source being assigned an incorrect optical counterpart. The probability of a chance projection is a strong function of the limiting optical magnitude in the catalog, since there are many more sources at the faint end. The concentric circles represent the probability of a source with a random right ascension and declination being assigned an optical counterpart from the full optical catalog ($R < 27.9$). The inner circle is 10%, and the other circles increase outward with 10% increments. The majority

[1]online at http://idlastro.gsfc.nasa.gov/homepage.html

of CLASXS sources have (X-ray − optical) separations of less than 0.5″ (1 σ) for which there is only a 2% probability of an incorrect X-ray/optical match. With our search radius of 2″, we calculate that 30% of the CLASXS sources that in fact have no optical counterpart will be assigned an incorrect optical counterpart. Almost all of these will be with optically faint sources. If we limit the optical sources to those spectroscopically accessible ($R < 24$), we find only an 8% chance of an incorrect X-ray/optical overlap using a 2″ matching radius.

4.3 Spectroscopic observations and redshifts

Optical spectra were obtained using the multi-fiber spectrograph HYDRA on the WIYN 3.5 m telescope for bright ($I < 19$) sources, and with the Deep Extragalactic Imaging Multi-Object Spectrograph (DEIMOS) on the 10 m Keck II telescope for fainter sources. For the HYDRA observations, we used a low-resolution grating, 316@7.2, centered at 7600 Å, yielding a wavelength coverage of 4900 − 10300 Å with a resolution of 2.64 Åpixel^{-1}. The red bench camera was used with the 2″ "red" HYDRA fibers to maximize the sensitivity at longer wavelengths. To obtain a wavelength solution for each fiber, CuAr comparison lamps were observed in each HYDRA configuration. Our HYDRA masks were designed to maximize the number of optically bright sources in each configuration, while minimizing the amount of overlap between configurations. Fibers that were unable to be placed on a source were assigned to a random sky location. We observed 2.7 hrs on two HYDRA configurations in 2001 February, 7.4 hrs on two configurations in 2002 February ,

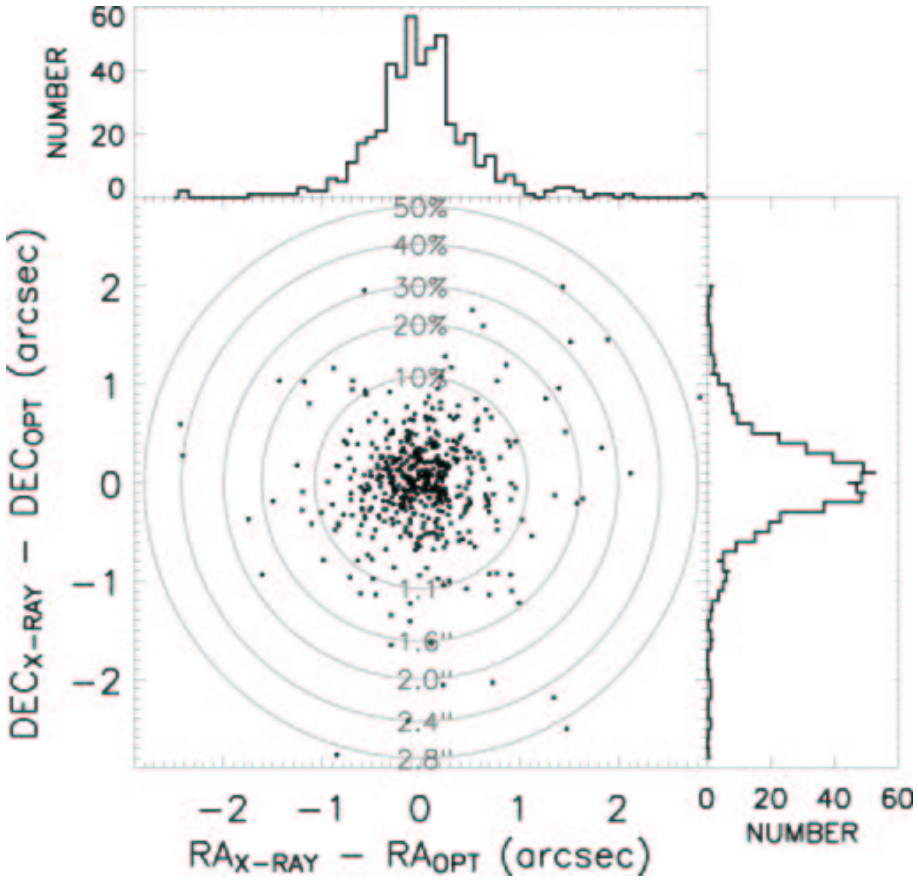

Figure 34: (X-ray − optical) astrometric offsets for the 484 CLASXS sources with detected optical counterparts. Histograms for the R.A. (decl.) separations are shown on top (*right*). The mean values for the R.A. and decl. offsets are both 0.0 ± 0.5 arcseconds. Concentric gray circles represent the probability of a source with a random R.A. and decl. being assigned an optical counterpart. The probabilities and search radii (in arcseconds) are given, respectively, at the top and bottom of each circle.

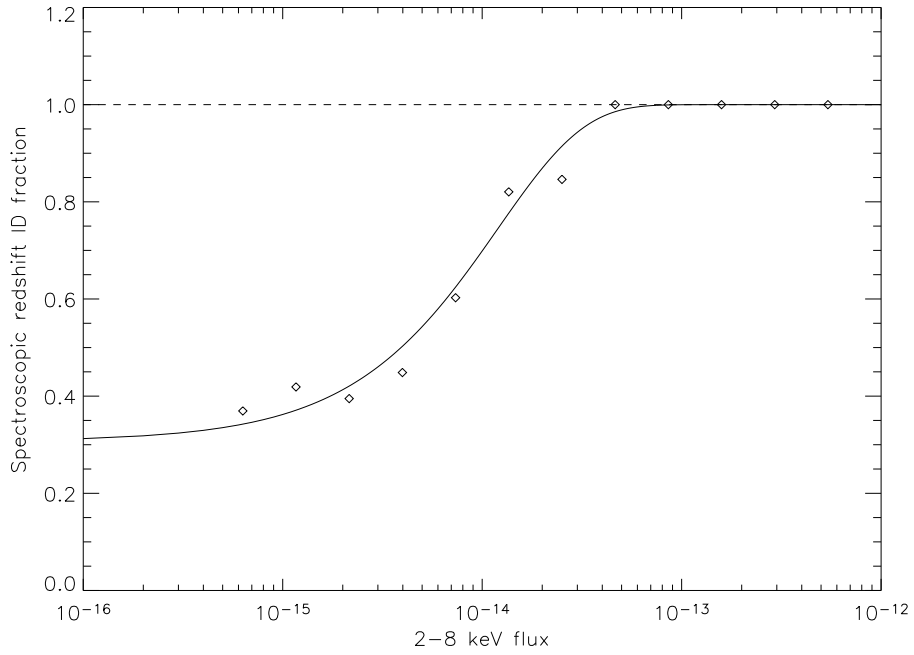

Figure 35: The optical identification fraction as a function of 2–8 keV flux. Solid line shows the best-fit.

and 6.0 hrs on two configurations in 2002 March. To remove fiber-to-fiber variations, on-source observations were alternated with $\pm 7.5''$ "sky" exposures taken with the same exposure times. This effectively reduced our on-source integration times to 1.3, 3.6, and 3.0 hrs in 2001 February, 2002 February, and 2002 March, respectively.

Reductions were performed using the standard IRAF package DOHYDRA. To optimize sky subtraction, we performed a two-step process. In the first step, the DOHYDRA routine was used to create an average sky spectrum using the fibers assigned to random sky locations. This average sky spectrum was then removed from all of the remaining fibers. In the offset images, this step effectively removed all of the sky signal, leaving behind only residuals caused by differences among the fibers. To remove these variations, we then subtracted the residuals present in

the sky-subtracted offsets from the sky-subtracted, on-source spectra. We found this method to be very effective at removing the residuals created by fiber-to-fiber variations with HYDRA.

For the DEIMOS observations, we used the 600 lines mm^{-1} grating, which yielded a resolution of 3.5 Å and a wavelength coverage of 5300 Å. The exact central wavelength depends upon the slit position, but the average was 7200 Å. Each $\sim$ 1 hr exposure was broken into 3 subsets. In each subset the object was stepped 1.5″ in each direction. The DEIMOS spectroscopic reductions follow the same procedures used by Cowie et al. (1996) for LRIS reductions. The sky contribution was removed by subtracting the median of the dithered images. Cosmic rays were removed by registering the images and using a cosmic ray rejection filter on the combined images. Geometric distortions were also removed and a profile-weighted extraction was applied to obtain the spectrum. Wavelength calibration was done using a polynomial fit to known sky lines rather than using calibration lamps. The spectra were individually inspected and a redshift was measured only for sources where a robust identification was possible. The high-resolution DEIMOS spectra can resolve the doublet structure of the [O II] $\sim$ 3727 Å line, allowing spectra to be identified by this doublet alone.

The optical spectra of the X-ray sources in our sample span different rest-frame wavelengths. They also suffer varying degrees of host–AGN mixing. It is therefore very difficult to perform source identifications in a uniform manner. The identification selection function is rather complex and to properly quantify. It is found, however, that the optical and X-ray fluxes only show good correlation at

$f_{2-8\ keV} > 10^{-14}\,\mathrm{erg\,cm^{-2}\,s^{-1}}$. AGN light is more prominent at higher fluxes and therefore easier to detect. At $f_{2-8\ keV} < 10^{-14}\,\mathrm{erg\,cm^{-2}\,s^{-1}}$, the optical light from more and more AGNs starts to be either obscured or simply overwhelmed by the light from host galaxy. The identification of X-ray sources are biased to those optically brighter ones. The net effect is that the spectroscopic identification is a strong function of X-ray flux. We so far identified a total of 272 source. The fraction of sources with spectroscopic redshift as a function of hard X-ray flux is shown in Figure 35.

4.4 Spectroscopic Classifications

Because the non-uniform manner of the optical spectra, only rough classification could be made based on various spectral features. We call sources without any strong emission lines (EW([OII])$<$ 3 Å or EW(Hα+NII)$<$ 10 Å) *absorbers*; sources with strong Balmer lines and no broad or high-ionization lines *star formers*; sources with [NeV] or CIV lines or strong [OIII] (EW([OIII] 5007 Å) $>$ 3 EW(Hβ)) *high-excitation (HEX) sources*; and, finally, sources with optical lines having FWHM line widths $>$ 2000 km s^{-1} *broad-line AGNs*. Sometimes combine the absorber and the star former classes into a *normal galaxy* class.

Table 4.2 gives the breakdown of optically identified CLASXS sample by spectral type. Hereafter, we call all of the sources that do not show broad-line (FWHM$>$ 2000 km s^{-1}) signatures "optically-narrow" or non-broadline AGNs. However, we note that there may be a few sources where our wavelength cover-

Table 4.2. Number of X-ray Sources Per Spectral Type For Identified CLASXS Sources

Class	Number	fraction
Stars	20	4%
Star Formers	73	14%
Broad-line AGNs	106	20%
Seyferts	44	8%
Absorbers	28	5%

age is such that we are missing lines which would result in us defining the spectrum as broad-line.

It is obvious that the optically identified sources contains larger fractions of optically active galaxies than the whole sample. Only $\sim 1/3$ of the optically normal AGNs are identified. The effect of this incompleteness on the X-ray luminosity function is addressed in Barger et al. (2005). The true nature of the optical normal AGNs at high redshift is still a puzzle.

4.5 Compare with *XMM-Newton*

We have shown that the spatial resolution of *Chandra* is needed to properly identify optical counterparts at high magnitudes. The commonly asked question is

that, given the larger collecting area, *XMM-Newton* seem to be the more adequate instrument than *Chandra* in surveying CXB sources. In fact, the $\sim 3''$ XMM positions are not adequate to determine the correct $R > 24$ optical counterparts to the X-ray sources. The surface density of galaxies and stars to $R = 24$ is approximately 16.6 arcmin^{-2}, so with a search radius of $3''$, we may expect a random field contamination of about 15%. By $R = 24 - 26$ the field surface density is 50.1 arcmin^{-2}, and thus we may expect that half of the optical identifications using an *XMM* error circle will be incorrect. Without the correct optical identifications, one cannot determine the redshifts.

Chapter 5

Extended Sources

5.1 Detection

We searched the $0.4 - 2$ keV images of each observation for extended sources using the *vtpdetect* tool provided in CIAO. The method uses Voronoi tessellation and percolation to identify dense regions above Poisson noise. This method performs best on smooth overdense regions but could confuse crowded point sources. We chose to use a threshold scale factor of 0.8 and a maximum probability of false detection of 10^{-6} and to restrict the number of events per source to > 30. We used default values for the rest of the parameters. This choice of parameters maximizes the detection of low surface brightness sources at high significance. We visually examined the source list to screen out apparent blended point sources. The candidates were then selected by comparing the 99% PSF radius with the equivalent radius of the source region, and only sources with a PSF ratio (defined as $\sqrt{A/\pi}/r_{99}$, where A is the area of the source region reported by *vtpdetect*, and r_{99} is the 99% PSF radius at the off-axis angle) higher than 10 were considered extended (Table 5.1).

Four sources were found to be significantly extended, and all but Source 3 have an off-axis angle of $< 5'$ in the X-ray observations. Source 3 is at an off-axis angle of $8.4'$. With the X-ray image alone, one could not rule out the source being a blend of point sources. However, a bright gravitational lensing arc found in the optical

Table 5.1. Extended Sources

Source #	α_{2000}	δ_{2000}	$\Delta\alpha$ ($''$)	$\Delta\delta$ ($''$)	θ ($'$)[a]	PSF ratio[b]	Net Counts[c]	Field[d]
1	10 35 25.4	+57 50 48	2.628	1.044	4.786	37.89	100.1 ± 11	9
2	10 35 13.4	+57 50 17	3.312	1.476	4.029	39.33	87.7 ± 11	9
3	10 35 37.9	+57 57 15	3.060	1.476	8.422	19.09	77.0 ± 10	8
4	10 34 30.8	+57 59 12	3.132	2.196	4.016	16.69	30.7 ± 6.6	8

[a]Off-axis angle in the field the source is detected.

[b]Defined as $\sqrt{A/\pi}/r_{99}$, where A is the area of the source region from the *vtpdetect* report and r_{99} is the 99% PSF radius at the off-axis angle.

[c]Net counts reported by *vtpdetect*

[d]LHNW field number where the source has the smallest off-axis angle.

image (see §5.6) at the X-ray peak makes it very likely that the X-ray emission is associated with a cluster. Considering the non-uniformity of the detection due to vignetting and PSF effects, the number counts for extended sources above $3.7 \times 10^{-15}\,\mathrm{erg\,cm^{-2}\,s^{-1}}$ are roughly $> 10\ \mathrm{deg^{-2}}$. This agrees with the LogN-LogS of clusters at these fluxes found in the CDFs (Bauer et al. 2002). It is interesting to note that all 4 extended sources are found on only two of the overlapping ACIS-I fields in the north of the LHNW region.

5.2 Comparing with Optical images

Optical observations are describe in Chapter 4. X-ray contours overlaid on R band optical images are shown in Figure 36. We examined the number counts of galaxies within circular cells with fixed radii of $0.5'$. At a threshold of $R < 24$, a total of 19, 28, 18, and 9 galaxies were found within the cells centered at the X-ray peaks of each extended source. Because a star is found at $0.6'$ south-east of the X-ray peak of Source 2, the galaxy counts could be underestimated. Compared with the expected 6.7 galaxies per cell obtained from the whole field, the overdensities of galaxies in Sources 1 and 2 are $> 3\sigma$, while the overdensity of galaxies in Source 3 is $\sim 3\sigma$. Source 4 does not show significant clustering of galaxies in the R band image. Sources 1 and 2 are very close to each other, with a separation of $\sim 2'$. The closeness and the elongated morphology of the two sources suggest that they are undergoing interactions. Source 3 is extended along the east-west direction with multiple peaks. All 4 sources show bright elliptical galaxies at the X-ray peaks.

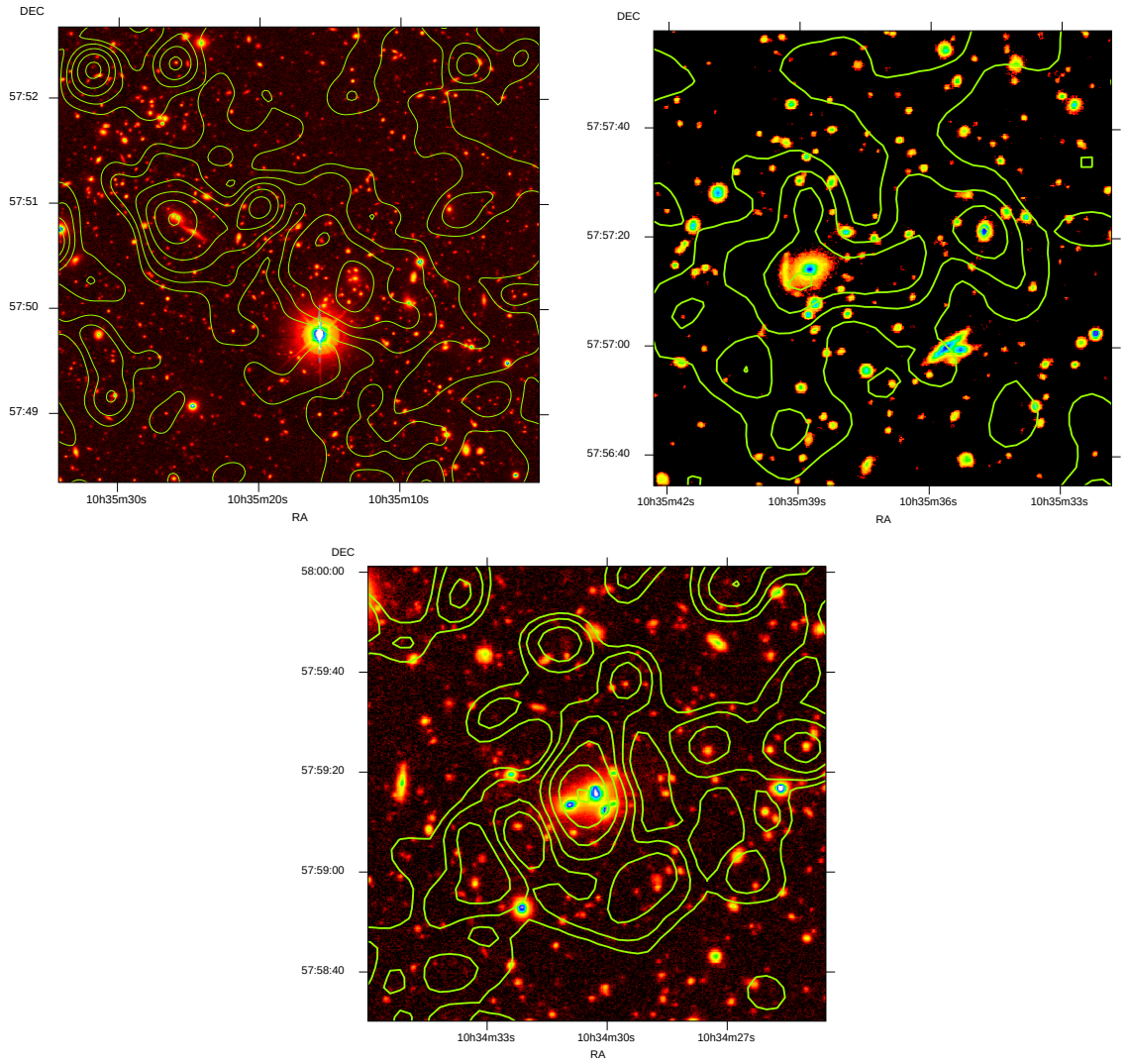

Figure 36: Adaptively smoothed X-ray images of the extended sources superposed on R band images.(a) Sources 1 and 2; (b) Source 3; (c) Source 4.

5.3 X-ray spectra

We extract very coarse spectra (grouped to > 15 counts per bin to allow the use of the χ^2 statistic) and attempt to constrain the properties of the clusters. We fit the data with a simple MEKAL model in XSPEC (v11.2), with a fixed abundance of 0.3 of the solar value and a fixed Galactic absorption. We restrict the spectral fitting to within $0.5 - 5$ keV, because the signal-to-noise ratio is poor outside of this range. The source extraction and background regions of Sources 1 and 2 are

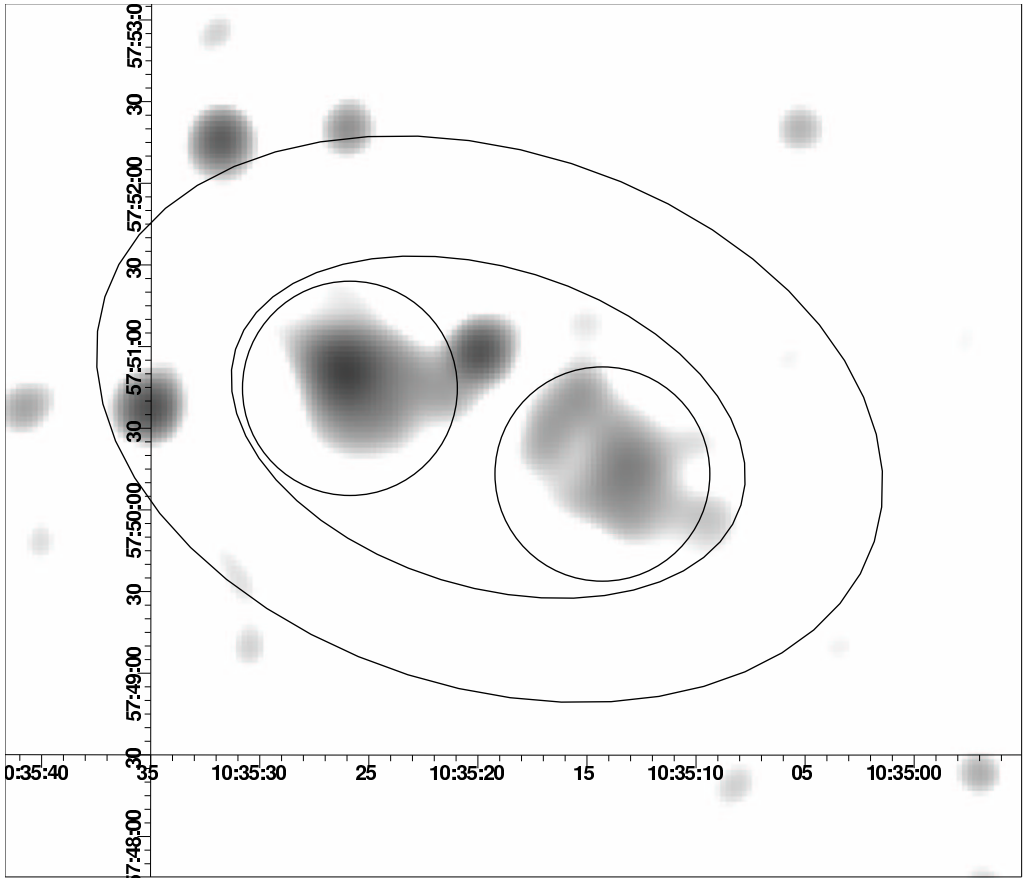

Figure 37: Regions for spectral extraction of Sources 1 and 2 on the Gaussian smoothed gray scale map of the clusters. The Gaussian kernal size is $6''$. Source regions are shown as circles. Elliptical annulus region is for the background extraction.

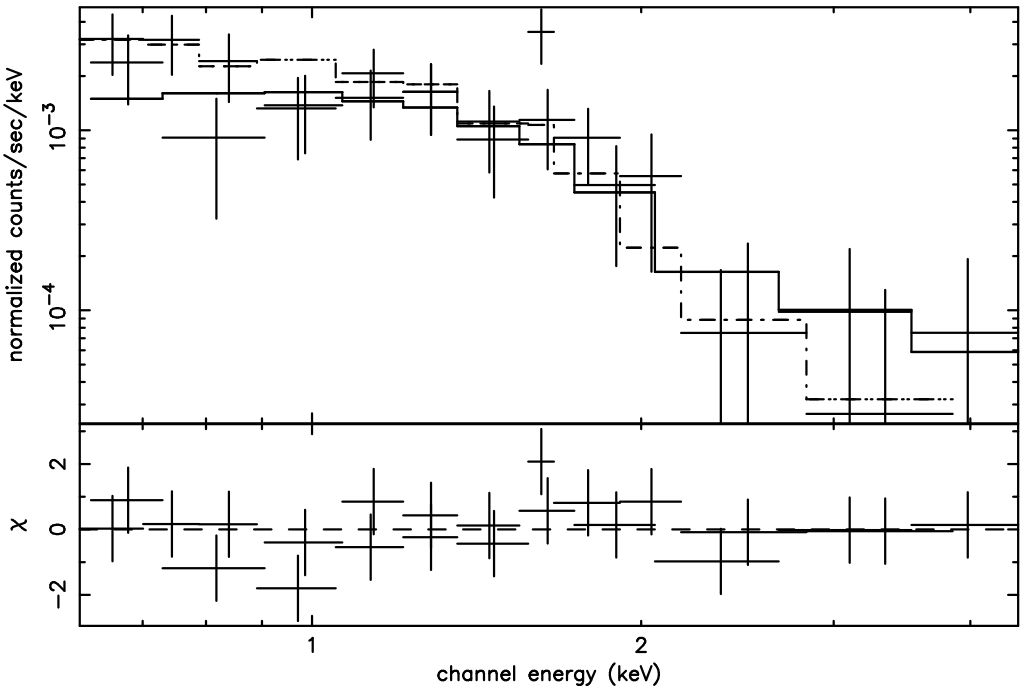

Figure 38: X-ray spectra and best-fit MEKAL models of Source 1 *(dash-dotted line)* and Source 2 *(solid line)*.

shown in Figure 37. The regions avoid the point sources between the two clusters. The spectra are shown in Figure 38. For Source 1, we found the best fit to be kT= $1.4^{+1.0}_{-0.2}$ keV and $a = 0.5^{+0.2}_{-0.2}$, with a reduced $\chi^2 = 8.8$ for 9 degrees of freedom. This agrees with the redshift estimates using the optical data (Table 5.2). Fitting the same model to the spectrum of Source 2 with the redshift fixed to $z = 0.5$ yields kT= $3.1^{+13.5}_{-1.6}$ keV, with a reduced $\chi^2 = 4.6$ for 9 degrees of freedom. The constraint on the temperature is poor, but the probability that the temperature of Source 2 is significantly different than that of Source 1 is low. This can be seen in Figure 39, where the joint probability contour of the temperature from the two sources is shown. The confidence level for the two sources having different temperatures is only 2σ. Combining the two data sets and fixing $z = 0.5$, we find kT= $1.7^{+2.2}_{-0.5}$ keV.

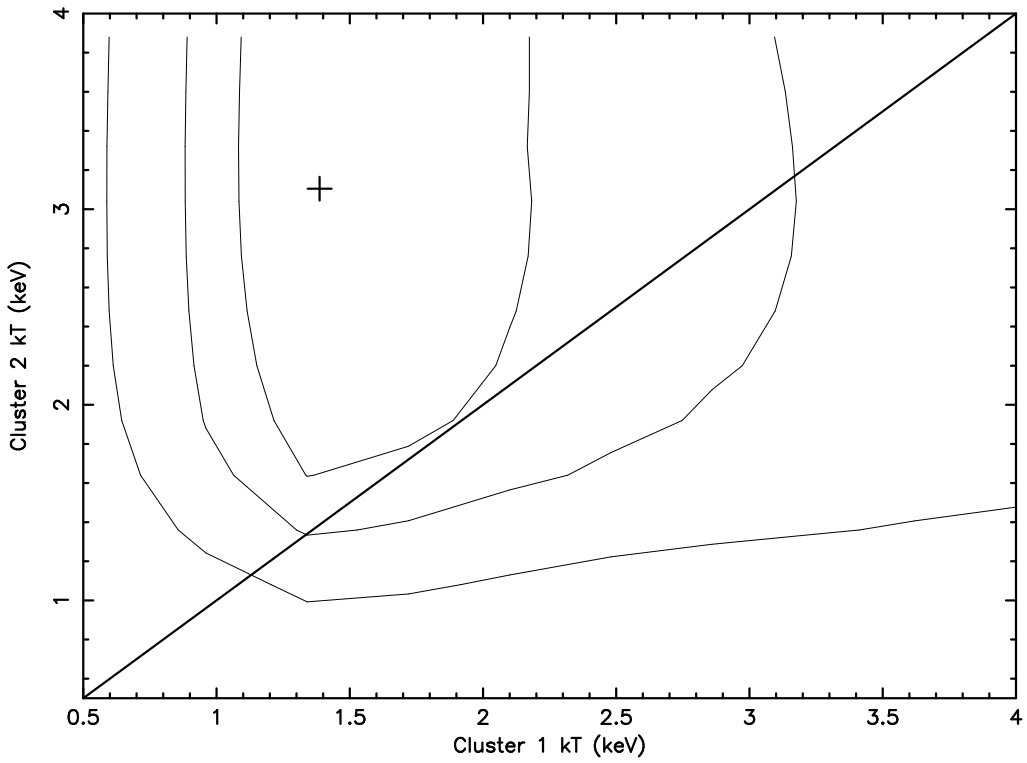

Figure 39: Combined probability contour of the temperature of Sources 1 and 2. Contour lines are 1, 2, and 3σ confidence levels. Cross is the best-fit temperature. Solid line represents the equality of the temperature of the two clusters.

Table 5.2. Redshift estimates for the extended Sources

Source #	z_{RS}	z_{BCG}	z_{X-ray}
1	0.50	$0.59^{+0.08}_{-0.08}$	0.5 ± 0.2
2	0.50	$0.55^{+0.09}_{-0.09}$	0.5 ± 0.2
3	.....	$0.73^{+0.09}_{-0.08}$	.....
4	0.45	$0.45^{+0.06}_{-0.05}$	.....

The spectrum of Source 3 shown in Figure 40 was extracted from a circular region with radius 36″. The background was extracted from an annulus with inner radius 36″ and outer radius 60″. The data cannot constrain the model very well, but a simple fit with an absorbed power-law shows that the spectrum is very soft with photon index $\Gamma = 2.6$ and reduced $\chi^2 = 7.2$ for 7 degrees of freedom. Fitting with a MEKAL model and assuming a redshift of $z = 0.73$ (see §5.5), we obtain a temperature of $2.3^{+1.0}_{-0.9}$ with reduced $\chi^2 = 0.77$. The temperature is insensitive to the redshift between $z = 0.4 - 1.4$. The fact that the MEKAL model fits the data better makes it less likely that Source 3 is a blend of several point sources.

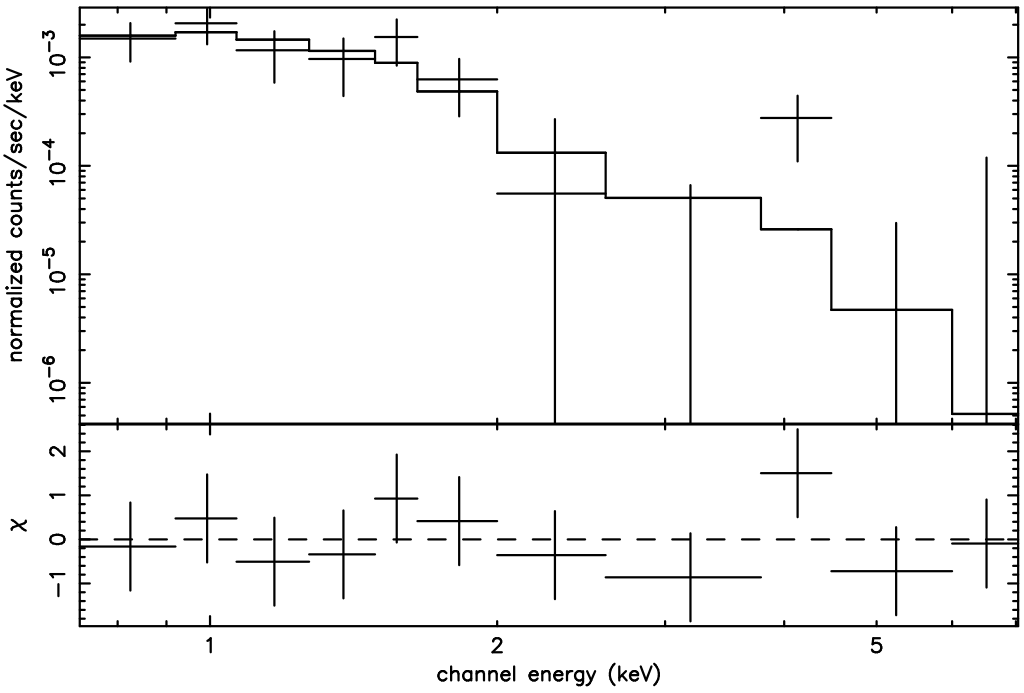

Figure 40: X-ray spectrum of Source 3 and the best-fit MEKAL model.

With only 30.7 net counts, it is impossible to model the spectrum for Source 4. However, the source has very few counts above 2 keV, indicating that the temperature should be low if the source is at $z > 0.4$, as implied from the optical data.

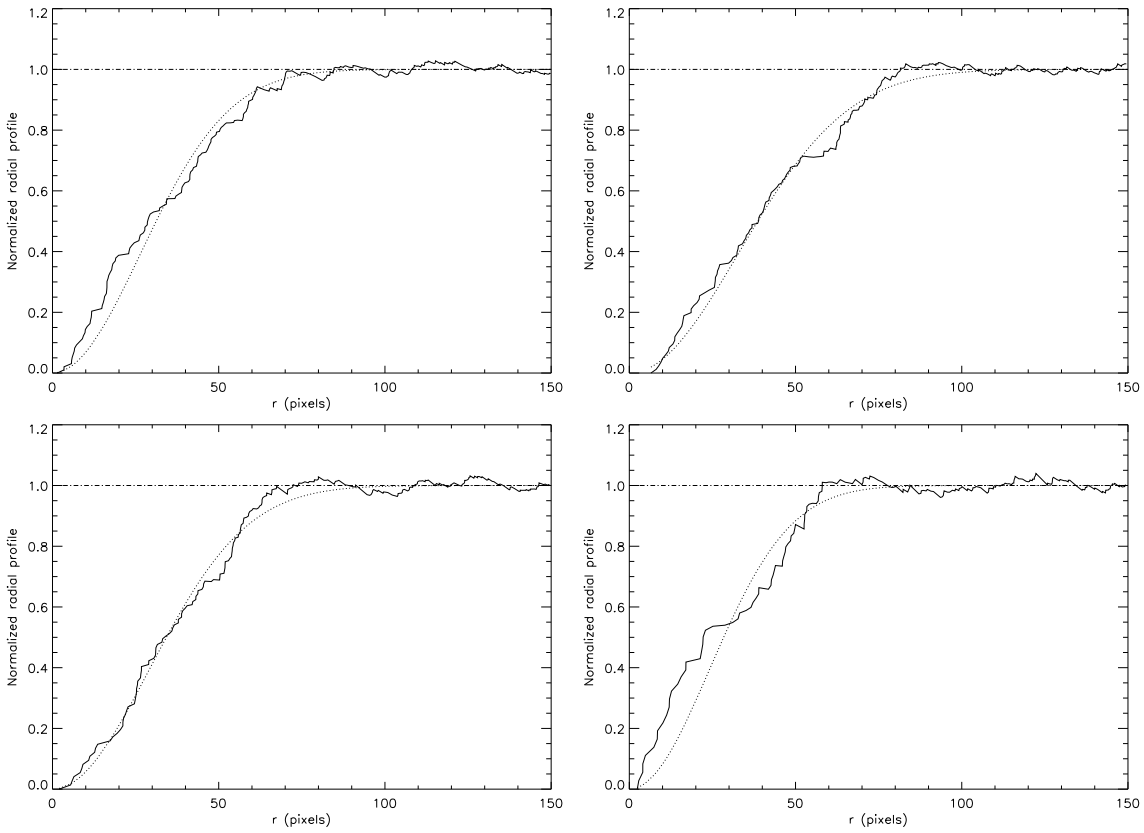

Figure 41: Curve-of-growths for the extended sources (Sources 1 – 4 shown in pannels (a) –(d)) normalized to the best-fit background. Dotted line shows the best fit of an integrated 2 dimensional Gaussian.

The virial masses of the extended sources can be roughly estimated using the best-fit $M - L$ relation (Finoguenov et al. 2001), $M_{500} = 2.45 \times 10^{13}$ $T^{1.87}$, where M_{500} is the mass within a radius where the overdensity is 500. The results are shown in Table 5.3. All of the sources belong to low mass clusters or groups, and this result is not very sensitive to the redshift because of the very soft spectra.

5.4 Angular sizes

The angular sizes of the sources were quantified by the widths of the radial profiles. We fitted the radial profiles of the sources with integrated 2-D Gaussian curves, which describe the low S/N ratio data reasonably well. We constructed the cumulative counts as a function of off-source radius (curve-of-growth). Exposure maps were applied to correct for vignetting. Nearby point sources were removed and replaced with background noise. The background regions were selected visually and fitted with a quadratic form plus a constant. The curves-of-growth were then normalized to the best-fit backgrounds. The normalized curve-of-growth for each source is shown in Figure 41. This left only one parameter to be determined—the widths of the curves. The best-fit core radii are listed in Table 5.3.

5.5 Redshifts

We infer the redshifts of the extended sources using the red sequence method, as well as the brightest cluster galaxy (BCG) method. Based on observations of clusters, there is usually a population of early-type galaxies which follow a color-magnitude relation (red sequence). This relation changes with redshift in a predictable way, such that a robust two-color photometric redshift can be obtained (Gladders & Yee 2000). Color-magnitude plots of the sources within $0.5'$ of the X-ray centers are shown for each extended source in Figure 42. Red sequences can be clearly seen in Sources 1, 2, and 4. By comparing with the models from Yee & Gladders (2001), we can estimate the redshifts for these three extended sources

Table 5.3. Properties of the extended sources

Source #	z_{fix}	kT[a]	M_{500}[b]	core radius ($''$)	$f_{0.5-8keV}$[c]	L_{bol}[d]
1	.50	$1.4^{+0.8}_{-0.4}$	$0.45^{+.0.61}_{-.21}$	12.9	1.6	2.2
2	.50	$3.1^{+6.5}_{-1.4}$	$2.0^{+15.}_{-1.4}$	17.0	1.2	1.5
3	.73	$2.3^{+1.0}_{-0.9}$	$1.2^{+1.2}_{-.64}$	14.7	1.5	5.1
4	.45	1.0 (fixed)	.24	11.8	.42	.45

[a]Listed are single parameter 1σ errors.

[b]unit: 10^{14} $M_\odot$

[c]Unit: $10^{-14}\,\mathrm{erg\,cm^{-2}\,s^{-1}}$.

[d]Unit: $10^{43}\,\mathrm{erg\,s^{-1}}$.

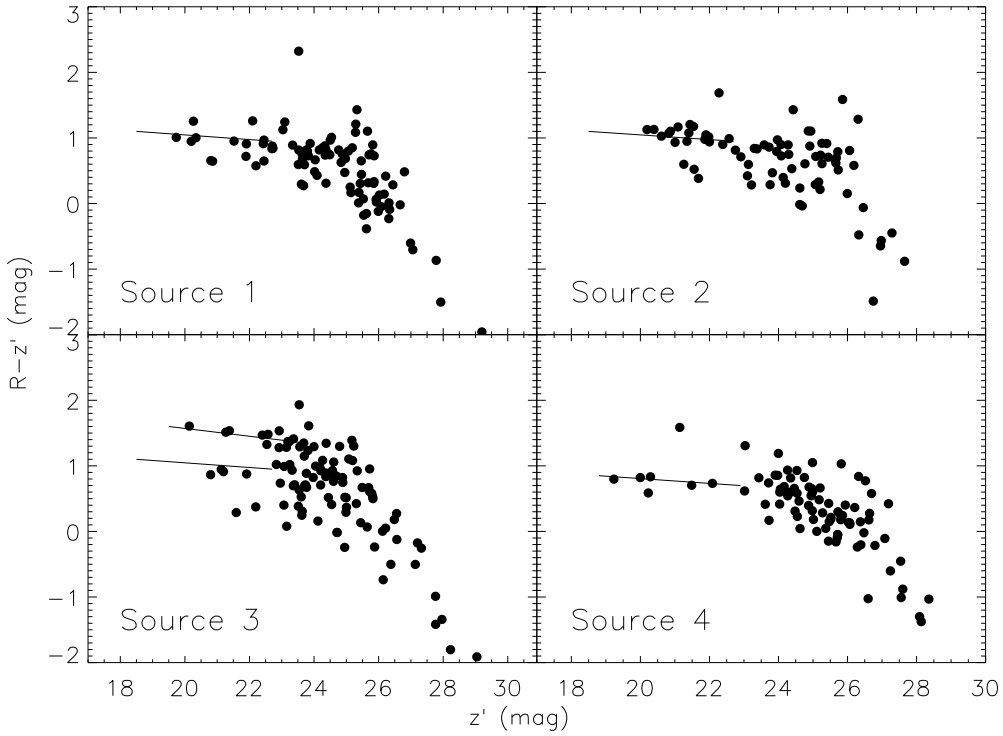

Figure 42: Color-magnitude plot for the galaxies within 0.5′ of the X-ray center. Solid lines show the model red sequence from Yee & Gladders (2001) at the redshifts that best match the observations in Source 1 ($z = 0.5$), 2 ($z = 0.5$), and 4 ($z = 0.45$). In the plot for Source 4, the red sequences for $z = 0.5$ (lower solid line) and $z = 1.0$ (upper solid line) are shown.

(Table 5.2). Source 3 does not show a clear red sequence.

BCGs are often used as distance indicators, because they have almost constant luminosity (Humasom, Mayall, & Sandage 1956). One of the difficulties in applying this method is that with optical images alone, it is hard to distinguish between the background and the cluster members, unless a density peak can be clearly determined. In our case, this is less worrisome because bright spheroidal/lenticular galaxies are found at the X-ray peaks of all of the extended sources. This clearly

associates these galaxies with the clusters. Furthermore, these galaxies are also the brightest early-type galaxies in the regions where X-ray emission is significant.

Following Postman & Lauer (1995), we use the $L_m - \alpha$ relation to find the redshift. We fit the radial profile around 2″–6″of each of the BCGs to obtain the magnitudes within radius r_m and the slope of the profile

$$\alpha \equiv dlogL_m/dlogr|_{r_m}, \tag{5.1}$$

where L_m is the luminosity within r_m. The empirical relation between the absoluted R magnitude and α is

$$R = -20.896 - 4.397\alpha + 2.738\alpha^2. \tag{5.2}$$

We eye examine the profile so that nearby galaxies are not included in the aperture. The redshift of the BCG can be found by solving

$$m_R - R = 5\log d(z) - 5 + K_R(z), \tag{5.3}$$

where m_R is the R magnitude of the BCG, $d(z)$ is the luminosity distance. In the R band K-correction is performed by

$$K_R = 2.5\log(1 + 0.96z). \tag{5.4}$$

The resulting redshifts are listed in Table 5.2.

While it appears that the BCG method produces higher redshifts than the red sequence method, the differences are not significant, given the large uncertainties in both methods. The redshifts of Sources 1 and 2 also agree with the spectral fitting results from the X-ray data.

The X-ray luminosities of the extended sources are listed in Table 5.3, assuming the red sequence-determined redshifts except for Source 3, where BCG redshift is adopted. Within errors, the temperatures and luminosities of the sources agree with the scaling law found in high-redshift X-ray clusters (Ettori et al. 2003), but the constraint is weak.

5.6 Discovery of a gravitational lensing arc

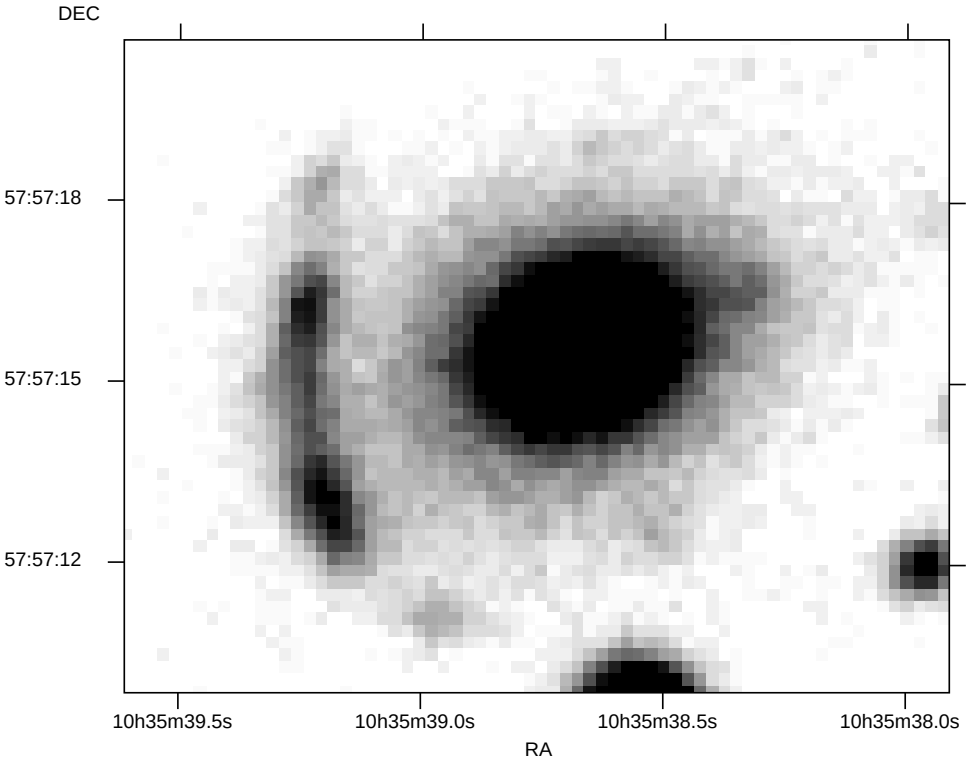

Figure 43: R band image of the gravitational lensing arc found associated with Source 3.

We have found a gravitational lensing arc close to Source 3 (Figure 43). The arc has an angular radius of $\sim 6''$. A bright spheroidal galaxy is clearly associ-

ated with the arc. A possible counter arc is seen connecting to the west of the bright galaxy but is not fully resolved. With B, V, R, I, and z' observations, we can estimate photometric redshifts for the cD galaxy and the arc using the publicly available photometric redshift code Hyperz (Bolzonella et al. 2000). We find photometric redshifts for the cD galaxy and the arc of $z = 0.45$ and $z = 1.7$, respectively. The redshift of the galaxy is slightly different than the redshift of the cluster obtained using the BCG method. From our experience, one often needs at least 7 colors to obtain a secure photometric redshift. The redshift estimates therefore need verification.

If the source is at $z_{src} \sim 0.45$ and the arc is at $z_{arc} \sim 1.7$, then we can estimate the mass within the Einstein radius (reasonably approximated by the radius of the arc) as

$$M(\theta < \theta_E) = 1.1 \times 10^{14} (\frac{\theta}{30''})^2 (\frac{D_{LS} D_L}{D_S}) M_\odot \,, \tag{5.5}$$

where D_L, D_S, and D_{LS} are, respectively, the angular diameter distances (in units of Gpc) of the lens, source, and the distance between the lens and source. With $z_{src} \sim 0.45$ and $z_{arc} \sim 1.7$, we obtain $M(\theta < \theta_E) \sim 3.3 \times 10^{12}$ $M_\odot$. We compare this mass with what would be expected if the source were a group of galaxies at $z = 0.45$, assuming the mass profiles are self-similar. By fixing the redshift, the X-ray spectra yield a temperature of 2.2 keV. The virial radius is roughly $r_{500} = 0.63 \times \sqrt{kT} = 955$ kpc (Finoguenov et al. 2001), where r_{500} is defined as the radius within which the overdensity is 500. The size of the arc at $z \sim 0.45$ is $r_{arc} \sim 37$ kpc $= 0.036 r_{500}$. Comparing with the mass profiles of NGC2563, NGC4325, and

NGC2300 (Mushotzky et al. 2003), the mass inside the Einstein radius agrees very well with that of a group of galaxies. The virial mass of the group can then be estimated to be $\sim 1.2 \times 10^{14}$ $M_{\odot}$ (Finoguenov et al. 2001).

If the cluster is at $z \sim 0.7$, as implied from the BCG method, and if the best-fit temperature $kT = 0.23$ keV is assumed, then we can search for the best redshift of the lensed galaxy, so that the mass within the Einstein radius agrees with the mass profile of groups. We find that if the lensed galaxy is at $z = 1.8$, then the mass within the Einstein radius is $M(\theta < \theta_E) \sim 3 \times 10^{12} M_{\odot}$, which fits the mass profile of groups.

If the redshift estimate is correct, then the arc system is very similar to the one discovered in the *ROSAT* deep survey of the Lockman Hole (Hasinger et al. 1998b). High-redshift gravitational lensing arcs are rare objects so far observed. However, since our large area survey is very similar in sky area and depth to the *ROSAT* Deep Survey, and since both have produced a detection of a strong arc, the probability of detection seems high. Larger area surveys of X-ray selected clusters of galaxies with deep optical follow-up would help to determine the probability of detection. Such observations should put useful constraints on Ω_m and on the density of galaxies at high redshifts (Cooray 1999).

It is interesting to note that all four of our clusters may have redshifts $z \sim 0.4 - 0.5$ and are located within a region of only $\sim 20'$ at the north-east corner of our field. This corresponds to a comoving radius of ~ 5 Mpc. The implications of such large scale structure on the CXB need to be investigated further.

Chapter 6

Spatial Correlation Function of X-ray Selected AGNs

6.1 Introduction

The early studies on AGN clustering are mostly carried out in optical band on quasars. Since quasars are rare objects, the samples are generally sparse, which makes the clustering difficult to detect. Osmer (1981) first detected a 2σ upper limit of clustering on scales of 100–3000 Mpc. The first significant excess of pairs of quasars was found using the Veron-Cetty & Veron (1984) catalog (Shaver 1984). In the following years, a set of $3-4\sigma$ detections of clustering were found using samples with typical size of a few hundred of quasars (Shanks et al. 1987; Andreani & Cristiani 1992; Shanks & Boyle 1994; Croom & Shanks 1996). The major progress in this field came since the 2dF and SDSS surveys. Even though the spatial density of quasars in these surveys is low, these surveys have enough quasars to probe reasonably well the scale where the rms fluctuation of source density reaches unity (Croom et al. 2001, 2005). This allows the proper quantification of the shape of the correlation function and/or the power spectrum. These observations confirmed earlier claims that the correlation function reaches unity at $r_0 = 6h^{-1}$ Mpc at $\bar{z} \sim 1-2$, similar to that found in the local luminous galaxies. At lower redshift, the best sample of optically selected QSO with $z < 0.3$ yields $r_0 = 8.6 \pm 2\ h^{-1}$ Mpc (Grazian et al. 2004). This is higher than typical clustering length of normal galaxies

($r_0 \sim 5\ h^{-1}$). On the other hand, using the SDSS data, Wake et al. (2004) show that the low luminosity, low redshift AGNs are clustered identically with the non-active galaxies.

The early X-ray surveys concentrate largely on clustering of point X-ray sources on the sky or fluctuations in the CXB. The all sky distribution of CXB is best mapped with HEAO-1 experiment. Treyer et al. (1998) analyzed the power spectrum of the CXB using the *HEAO-1* A2 data. They found the low order multiples are consistent with that the CXB is mostly discrete sources clustering with a biased factor (see below) $b = 1 - 2$. On scales of degree or smaller, only weak fluctuation of CXB was found ($< 2\%$ on $5^\circ \times 5^\circ$, Shafer & Fabian 1983; $< 4\%$ on $1^\circ \times 2^\circ$, Shafer & Fabian 1983). Recent more detailed study of small scale fluctuation from *ASCA* show the rms fluctuation on $0.5\mathrm{deg}^2$ is $\sim 4\%$ (Kushino et al. 2002), while the observations from *RXTE/PCA* yields a 7% variance on scale of $\sim 1\mathrm{deg}^2$ (Revnivtsev et al. 2004). Angular correlation function of discrete sources have been performed using imaging telescopes (Vikhlinin & Forman 1995; Akylas et al. 2000; Giacconi et al. 2002; Basilakos et al. 2004). The interpretation these results requires proper assumption of the evolution of clustering and selection function.

Direct measurements of the spatial correlation function was attempted by Carrera et al. (1998) using a deep pencil beam *ROSAT* survey, but without detecting significant clustering. Significant results have only become available recently (Mullis et al. 2004; Gilli et al. 2005). The clustering of the soft X-ray selected AGNs from a 80 deg^2 North Elliptic Pole sample yields a correlation function very similar to the that of optical quasar. Since most of the AGNs in that sample are broadline

AGNs in optical, the result is not surprising. Gilli et al. (2005) showed that the 0.5–10 keV band selected AGNs in the CDF-N and CDF-S are very similar to the result found in Mullis et al. (2005). However, Gilli et al. (2005) also found the existence of a small number of redshift spikes can significantly change the correlation result from these ultra-deep surveys. The other caveat of the Gilli et al (2005) analysis is that without the knowledge of the evolution of clustering, the interpretation of the spatial correlation function over a broad redshift range is difficult.

In this chapter, I will investigate the clustering and clustering evolution of the X-ray selected AGNs using the CLASXS and CDFN data. This results in a sample of $\sim$ 600 sources with spectroscopic redshifts, the largest *Chandra* sample so far used for the study of spatial correlation function of AGNs. Both data sets are followed-up in optical using the same instrumentation, resulting in very similar systematics. This allows us to combine/compare the results from the two surveys easily. The depth of CDFN and the angular size of CLASXS compensate each other in providing an unbiased picture of the spatial clustering and evolution. In principle, the clustering can be used to study cosmological parameters. In our case, however, the data set is too small to make useful constrains on cosmology. On the other hand, if the standard cosmology is taken as *a priori*, the clustering of AGNs provides very important clue between the SMBHs and their host galaxies.

6.2 Observations and data

As mentioned in Chapter 5, we have made spectroscopic observations for $\sim$ 90% of the 525 CLASXS X-ray sources. A total of 272 source have spectroscopic redshifts. The redshift distribution of these sources are shown in Figure 44. The fraction of sources with spectroscopic redshift as a function of hard X-ray flux is shown in Figure 35.

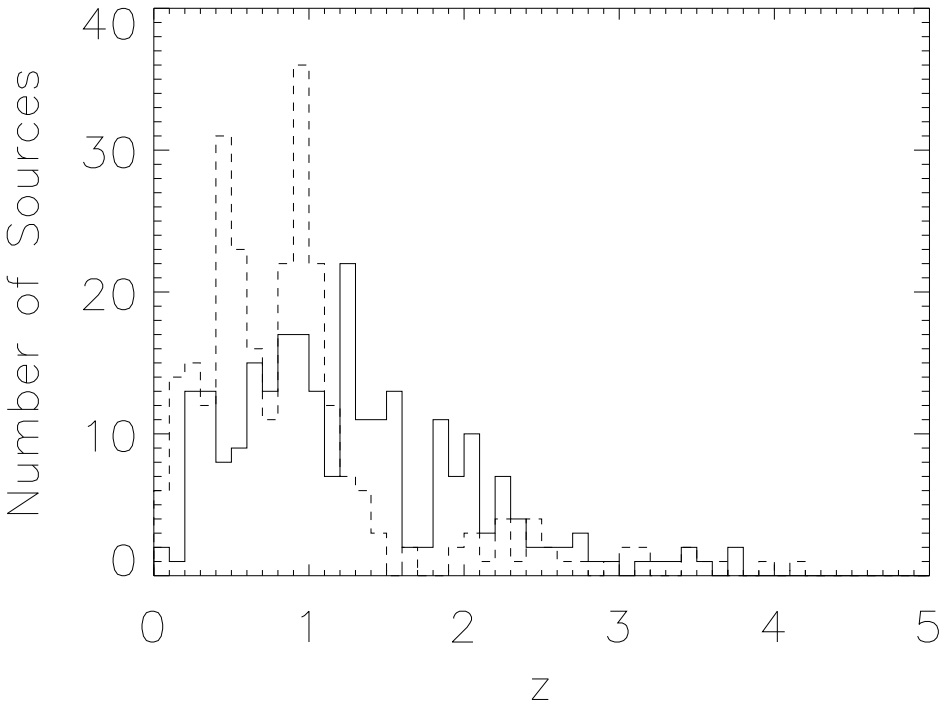

Figure 44: The redshift distribution of optically identified X-ray sources.The solid line: CLASXS field; dashed line: CDFN.

The 2 Ms CDFN is so far the deepest *Chandra* field, reaching a flux limit of $f_{2-8keV} \approx 1.4 \times 10^{-16}$ erg cm^{-2} s^{-1} (Alexander et al. 2003). This is $\sim$ 20 times deeper than the CLASXS field. The areal density of sources in CDFN is also $\sim$ 5

times higher. The optical observation were performed using the same telescopes as that has been used with CLASXS (Barger et al. 2003), which make it easy to compare the redshift results from both observation. We use the published catalog, which contains 306 sources with spectroscopic redshift. The redshift distribution of the CDFN sources is also shown in Figure 44. The fainter X-ray sources in the CDFN are more likely to be found at low redshift, $z < 1$, compared to the CLASXS sources.

6.3 Methods

To quantify spatial clustering in a point process, the most commonly used technique is the two point correlation function. In short, a two point correlation function measures the excess probability of finding a pair of objects as a function of pair separation (Peebles 1980).

$$dP = n_0^2[1 + \xi(r)]dV_1dV_2 \tag{6.1}$$

where n_0 is the mean density and r is the *comoving* distance between two sources.

Observations of low redshift galaxies and clusters of galaxies show that the correlation function of these objects over a wide range of scales can be described by a power-law

$$\xi(r) = (\frac{r}{r_0})^{-\gamma}, \tag{6.2}$$

with $\gamma \sim 1.6 - 1.9$ (Peebles 1980). It should be noted that the correlation function is in fact a function of redshift, which we will discuss in § 6.4. Because of the small sample sizes of most of the AGN surveys, correlation functions over very wide

redshift ranges are commonly used. This only makes sense if the clustering is almost constant in comoving coordinates. Fortunately, this is very close to the truth, as we shall see in § 6.5.

6.3.1 Redshift- and real-space Correlation functions

The nominal distance between sources calculated using the sky coordinates of the sources and their redshifts is sometimes called distance in *redshift-space*, we shall use $\mathbf{s}$ instead of $\mathbf{r}$ to indicate the distance calculated this way. It is apparent that the line-of-sight peculiar velocity of the sources could also contribute to the measured redshift (redshift distortion). This effect is most important at separations smaller than the correlation length. The projected correlation function, which computes the integrated correlation function along the line-of-sight and is not not affected by redshift distortion, is often used to obtain the real space correlation function (Peebles 1980). The projection, however, could make the correlation signal more difficult to measure. In small fields like the Chandra Deep Field North, the projected correlation function is also restricted by the field size, and could be affected by cosmic variance. We will calculate both the redshift-space and projected correlation functions in this paper. This allows us to estimate the correlation functions correctly at both small and large scales.

Following (Davis & Peebles 1983), we define $\mathbf{v_1}$ and $\mathbf{v_2}$ to be the positions of two sources in the redshift-space, $\mathbf{s} \equiv \mathbf{v_1} - \mathbf{v_2}$ to be the redshift-space separation, and $\mathbf{l} \equiv (\mathbf{v_1} + \mathbf{v_2})/2$ to be the mean distance to the pair. We can then compute

the correlation function $\xi(r_p, \pi)$ on a two dimensional grid, where π and r_p are separations along and across the line-of-sight:

$$\pi = \frac{\mathbf{s} \cdot \mathbf{l}}{|\mathbf{l}|}, \tag{6.3}$$

$$r_p = \sqrt{\mathbf{s} \cdot \mathbf{s} - \pi^2}. \tag{6.4}$$

The projected correlation function is defined as the line-of-sight integration of $\xi(r_p, \pi)$:

$$w_p(r_p) = 2 \int_0^{\pi_{max}} d\pi \; \xi(r_p, \pi) = 2 \int_0^{\pi_{max}} dy \; \xi(\sqrt{r_p^2 + y^2}), \tag{6.5}$$

where y is the line-of-sight separation. It has been shown (Davis & Peebles 1983) that, when $\pi_{max} \to \infty$, $w_p(r_p)$ satisfies a simple relation with the real-space correlation function. If a power-law form in Equation 6.2 is assumed, then

$$w_p(r_p) = r_p \left(\frac{r_0}{r_p} \right)^{\gamma} \frac{\Gamma(\frac{1}{2})\Gamma(\frac{\gamma-1}{2})}{\Gamma(\frac{\gamma}{2})}. \tag{6.6}$$

In practice, the integration is not performed to very large separations because the major contribution to the projected signal comes from separations of a few times the correlation length s_0. Integrating to larger π will only add noise to the results. After testing various scales, we found $\pi_{max} = 20 - 40$ Mpc produces consistent results for our samples.

6.3.2 Correlation function Estimator

To obtain an unbiased estimate of the correlation functions, we must correct for selection effects. Usually, these selection effects are determined using random samples generated with computer simulations. By comparing the simulated and

observed pair distribution, the selection functions effectively cancel. We compute the correlation function using the minimum variance estimator

$$\xi = \frac{DD - 2DR + RR}{RR} \tag{6.7}$$

where DD, DR and RR are the numbers of data-data, data-random and random-random pairs respectively, with comoving distances $s_0 - \Delta s/2 < s < s_0 + \Delta s/2$ (L-S estimator, Landy & Szalay 1993). The random catalog is produced through simulations described below to account for the selection effects in observations. The random catalog usually contains a very large number of objects so that the Poisson noise introduced is ignorable. We have checked our results using both L-S and the Davis-Peebles estimators (Davis & Peebles 1983) and found very good agreement between the two methods.

6.3.3 Uncertainties of correlation functions

The uncertainty of the correlation function is estimated assuming the error of the DR and RR pairs are zero, and the uncertainty of DD is,

$$\sigma_\xi = \frac{(1+\xi)}{\sqrt{DD}} \tag{6.8}$$

when DD is large. In the case of small DD, where $\sqrt{DD}$ underestimates the error, we use the approximation formula (Gehrels 1986) to calculate the Poisson upper and lower limits. Since the DDs are in fact correlated, the use of Poisson errors could underestimate the real uncertainty. In the literature *bootstrap* resampling (Efron 1982) is often used to calculate the errors of the correlation function. The method

is particularly useful in cases when the probability distribution function (PDF) of the variable is unknown, or in cases when the variables are derived from Poissonian distributed data using complex transformations, which results in rather complex PDFs. Mo et al. (1992) showed that in the case of large DD, the bootstrap error is $\sim \sqrt{3}$ of the Poisson error. We use Poisson errors in our redshift-space correlation function estimates. On the other hand, we use bootstrap methods when estimating the uncertainties of the projected correlation function. This is because the arbitrary binning and numerical integration used in Equation 6.5 make it difficult to apply Poisson errors directly.

6.3.4 The mock catalog

To account for the observational selection and edge effects, we perform extensive simulations to construct a mock catalog.

The *Chandra* detection sensitivity is not uniform because of vignetting effects, quantum efficiency changes across the field and the broadening of the point spread functions. The consequence is that the sensitivity of source detection drops monotonically with off-axis angles. To quantify this we generate simulated observations of our 40 ks and 70 ks exposure in both soft and hard bands. In Figure 45 we show some of the simulations. Using *wavdetect* (Freeman et al. 2002) on these images we obtain an estimate of the detection probability function at different fluxes and off-axis angles (Figure 46).

With this probability, we can generate randomly distributed sources with the

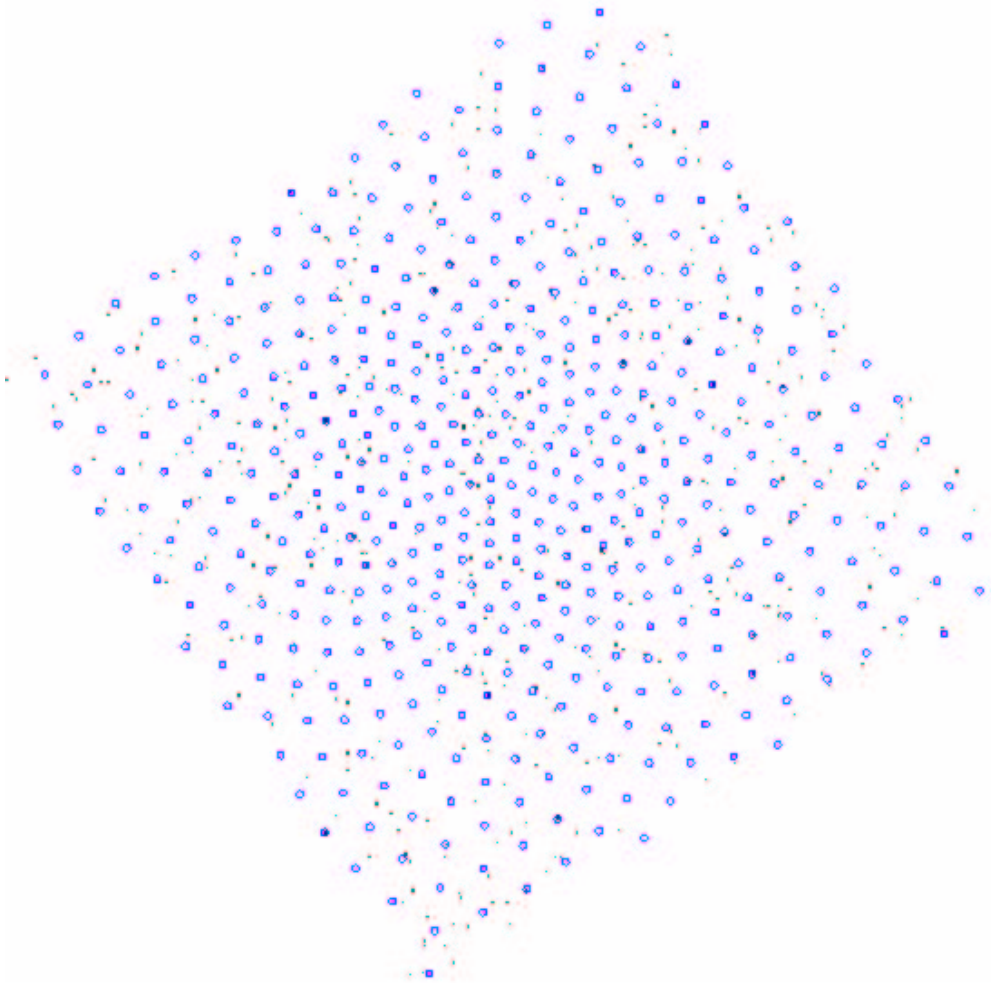

Figure 45: Simulated 40 ks hard band images with sources with various counts. (a) the blue regions shows the input source locations. The red regions in (b)–(e) show the images with input source counts of 3, 4.5, 7, and 16 cts respectively. Detected sources are marked with the 3σ error ellipses in blue.

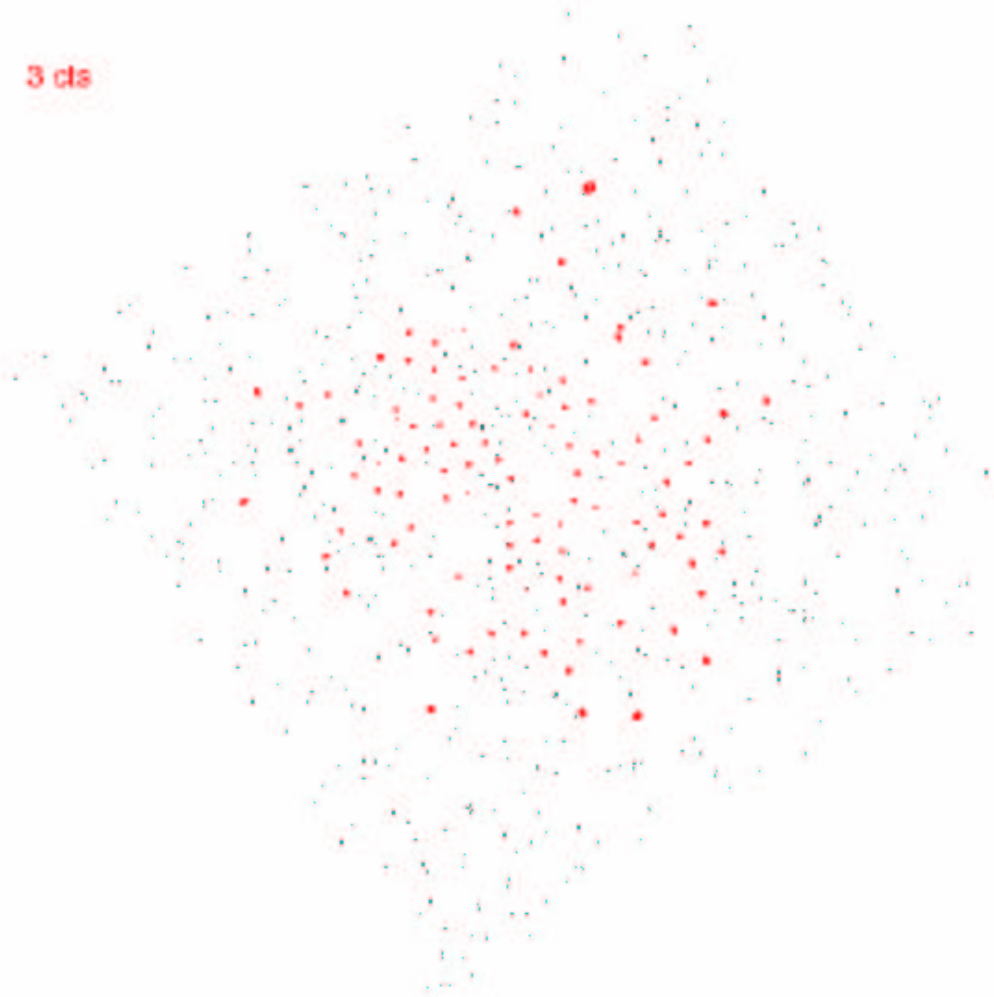

Figure 45 Continue. (b)

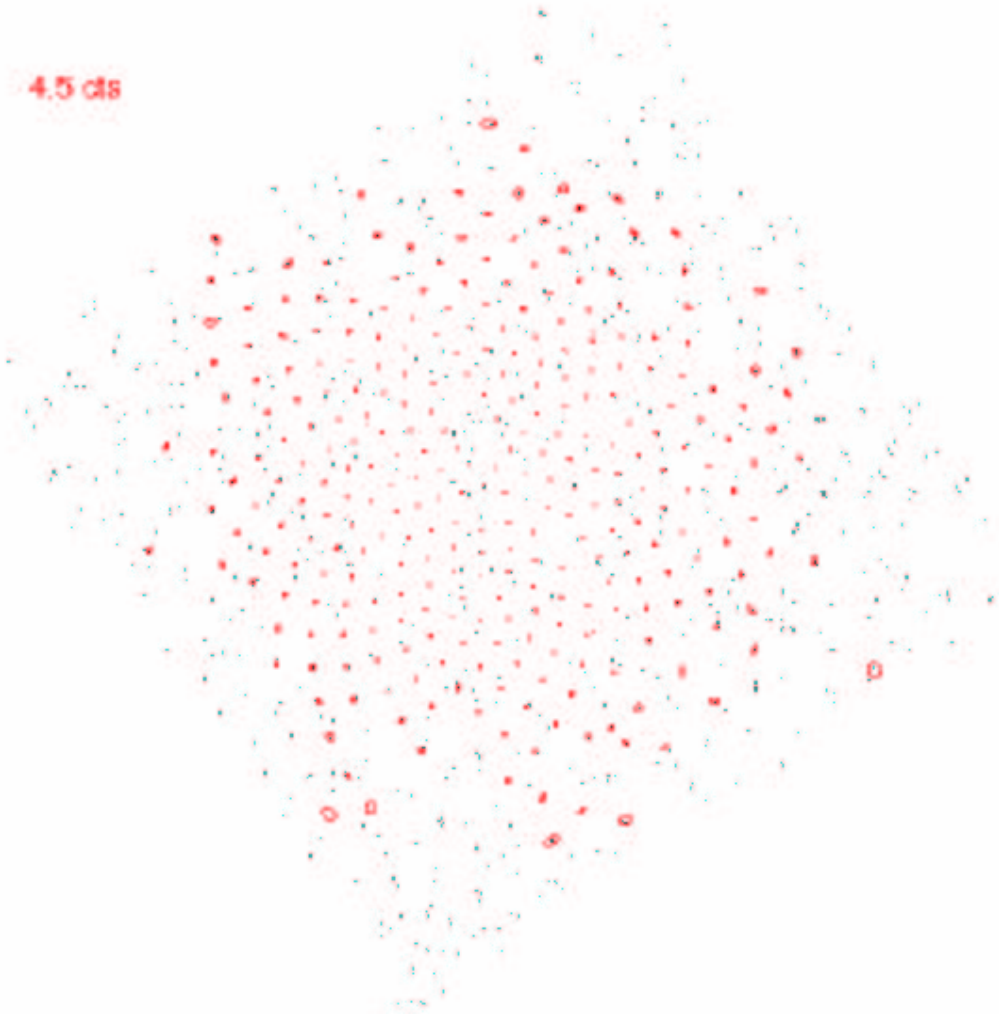

Figure 45 Continue. (c)

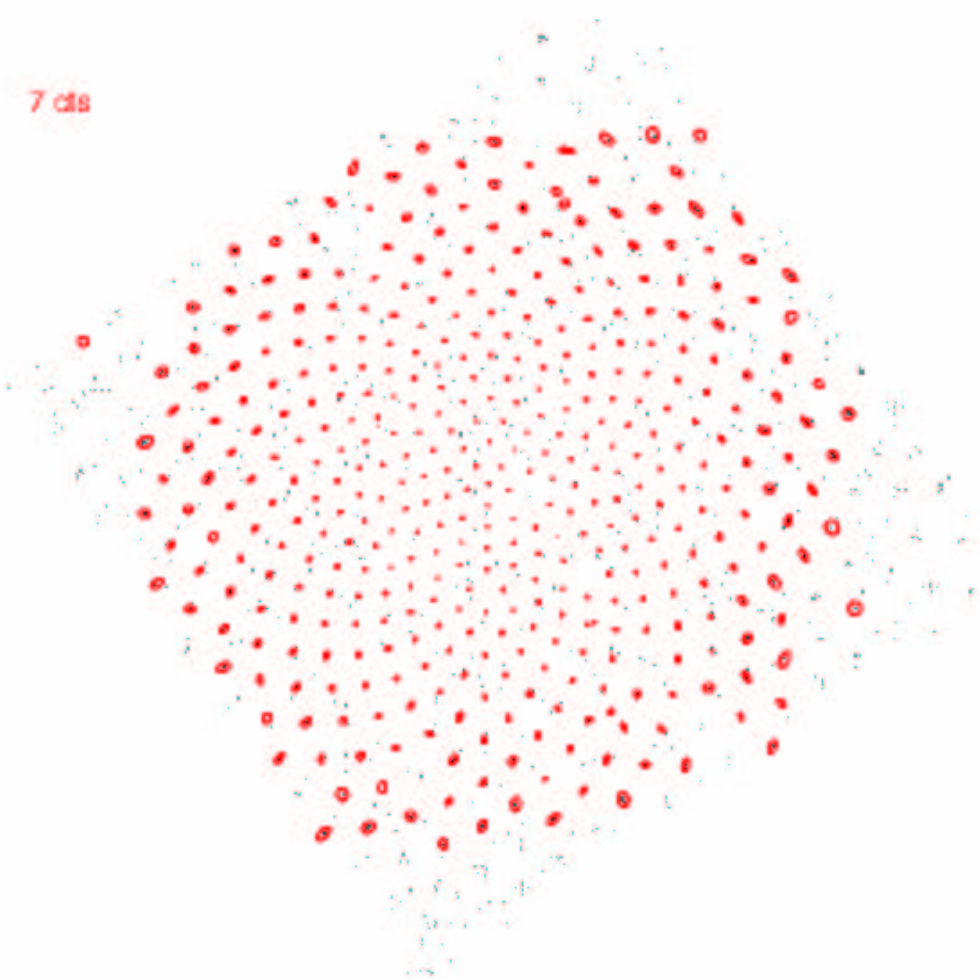

Figure 45 Continue. (d)

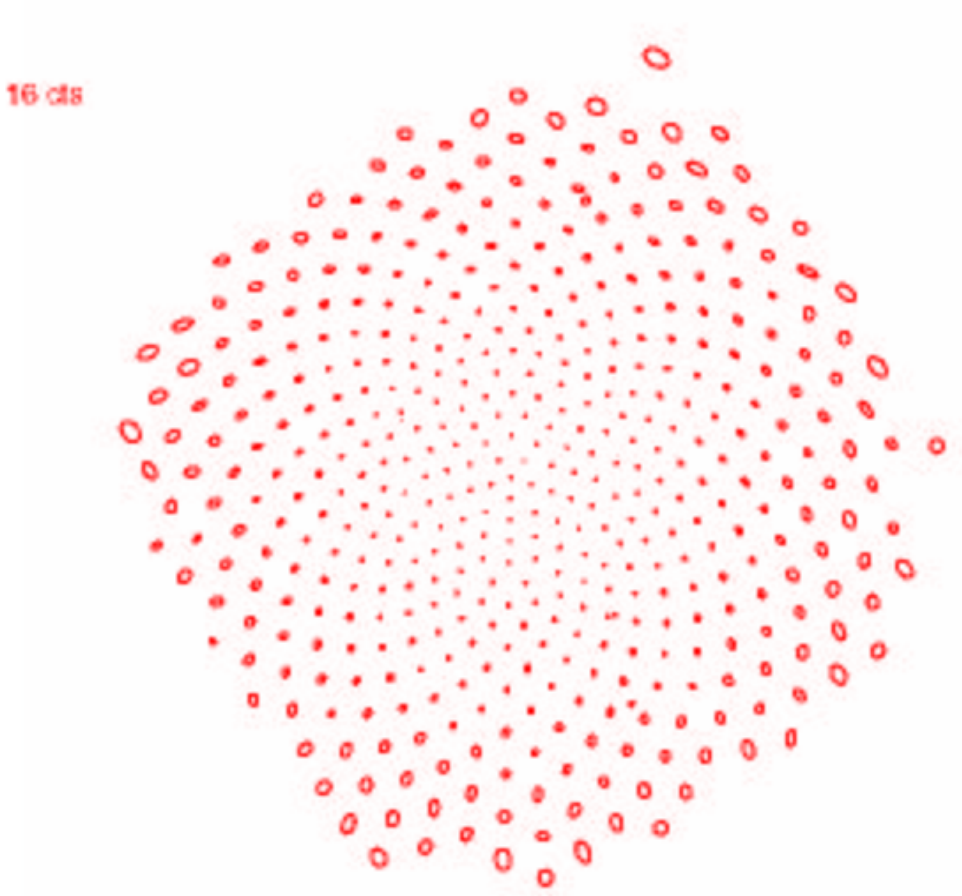

Figure 45 Continue. (e)

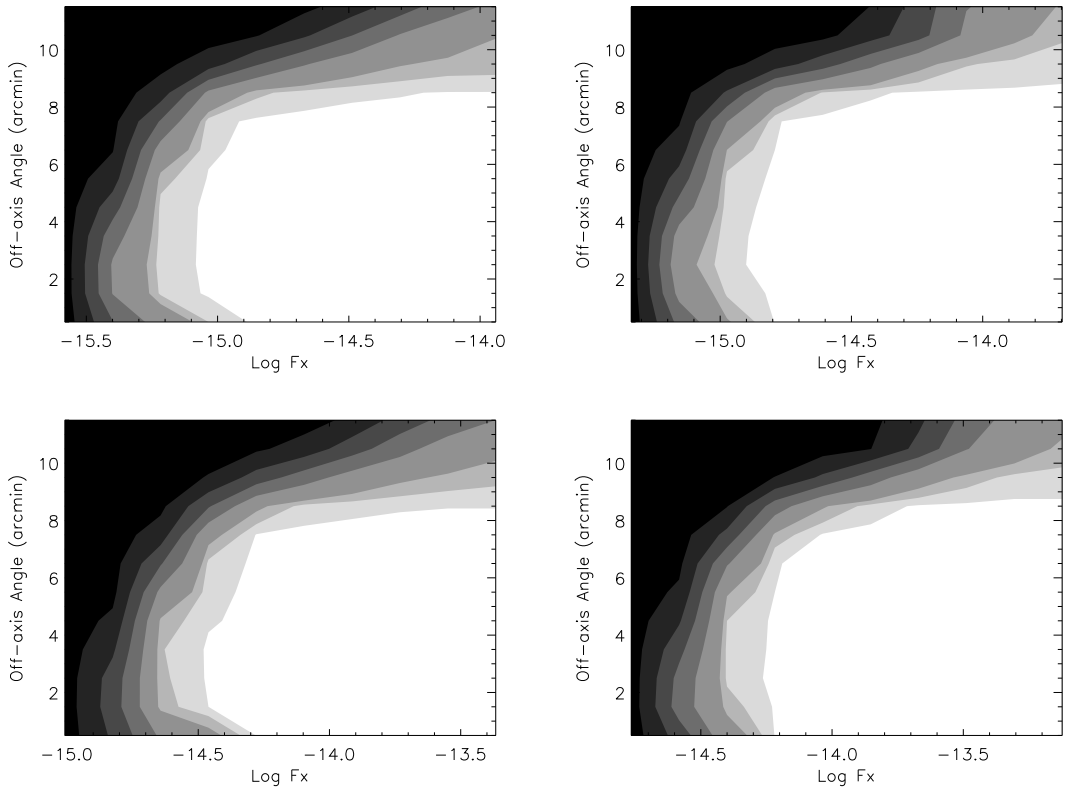

Figure 46: The probability of source detection as a function of off-axis angle and 2–8 keV fluxes. Contour levels are 0.1,0.3,0.5,0.7,0.9, 0.95,0.99. Upper(lower) panels: soft (hard) band; Left (right) panels: 70 ks exposures and 40 ks exposures.

X-ray selection effects to the first order. We use this method instead of running detections on a large number of simulated images because the detection program runs very slowly on these images. We generate source fluxes based on the best fit LogN-LogS from (Yang et al. 2004; see Chapter 3) and then "detections" are run on each of the images. The resulting catalogs from all the nine simulated images are then merged in the same way as for the real data. The resulting random source distribution and the resulting cumulative counts are shown in Figure 47.

We next consider the optical selection effects. Since our spectroscopic observation is close to complete for all sources with R$<$ 24.5, the sky coverage is uniform and only a very small number of very close sources could be missed. The redshift distribution of the sources shows a very weak dependence on the X-ray flux (Figure 48), which is due largely to the weak correlation between X-ray and optical flux in our hard X-ray sample. We can thus "scramble" the observed redshifts and assign them to the simulated sample without introducing a significant bias. The major selection effect in our optical observation is that the optical identifications are biased toward brighter sources.

We select X-ray random sources using the best-fit curve in Figure 35 as a probability function. The optical selection removes a large fraction of X-ray dim sources and therefore reduces the non-uniformity in the angular distribution caused by the X-ray selection effects. The redshift of the random sources were sampled from a Gaussian smoothed ($\sigma_z = 0.2$) redshift distribution from the observations. The purpose of the smoothing is to remove possible redshift clustering in the random sample but still preserve the effect of the selection function. We tested different smooth-

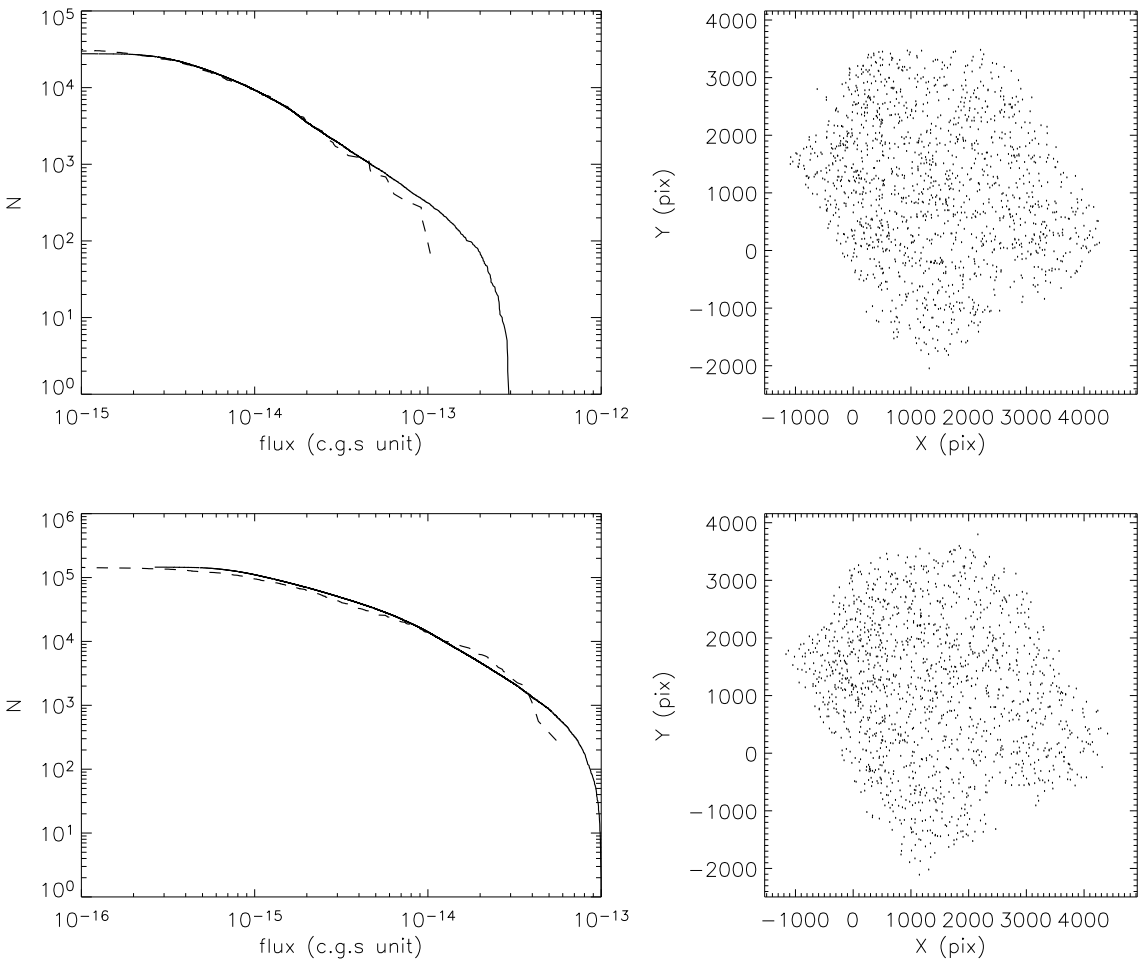

Figure 47: The right panels shows the random sources after detections (only 3000 sources are plotted). The pixel size is 0.492″. The left panels are the cumulated counts of simulated sources (solid line) and that of the observed (dashed line). Top: hard band; bottom: soft band.

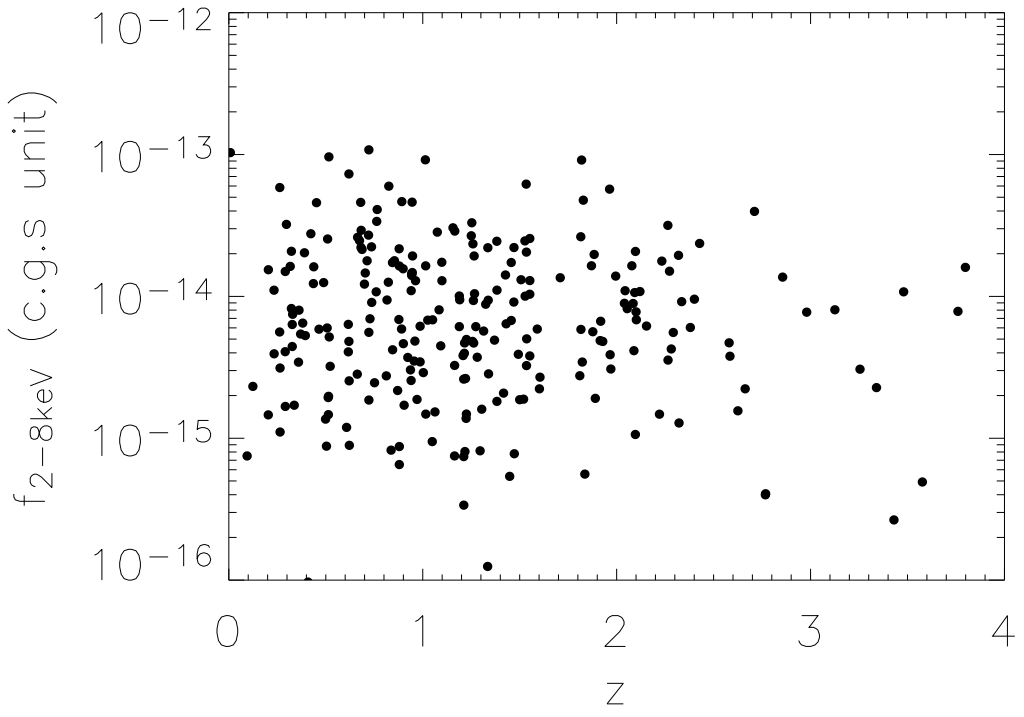

Figure 48: The 2–8 keV flux vs. redshift in CLASXS sample. There is no significant correlation between X-ray flux and redshift.

ing scales $\Delta z = 0.1 - 0.3$ and found the resulting correlation function effectively unchanged.

6.4 Results

6.4.1 Redshift-space correlation function

We calculate the redshift-space correlation function for non-stellar sources with $0.1 < z < 3$ and 2–8 keV fluxes $> 5 \times 10^{-16}$, assuming constant clustering in comoving coordinates. The total number of sources in the sample is 233. The median redshift of the sample is 1.2. We estimate the significance of clustering by comparing the number of detected pairs with separations < 20 Mpc with that expected by simulation. We found the significance of clustering is 6.7σ.

We use the maximum likelihood method in searching for the best-fit parameters (Cash 1979; Popowski et al. 1998; Mullis et al. 2004). The method is preferable to the commonly used χ^2 method because it is less affected by arbitrary binning. The method uses very small bins so that each bin contains only 1 or 0 DD pair. In this limit, the probability associated with each bin is independent. The expected number of DD pairs in each bin is calculated using the DR, RR pairs using the mock catalog. The likelihood is defined as

$$\mathcal{L} = \prod_i \frac{e^{-\mu_i} \mu_i^{x_i}}{x_i!} \tag{6.9}$$

where μ_i is the expected number of pairs in each bin and x_i is the observed number

Table 6.1. Redshift-space Correlation Function

CLASXS Field				CDF-N Field			
s range (Mpc)	s_0	γ	χ^2/dof	s range (Mpc)	s_0	γ	χ^2/dof
10–200	$11.4^{+1.8}_{-3.1}$	$2.4^{+1.1}_{-0.8}$	6.2/8	10–100	$11.5^{+0.8}_{-1.2}$	$2.9^{+1.4}_{-0.8}$	7.9/8
3–30	$8.15^{+1.6}_{-2.0}$	$1.2^{+0.5}_{-0.4}$	3.8 /8	1–20	$11.4^{+1.8}_{-1.4}$	$.96^{+.15}_{-.17}$	6.8/8
3–200	$8.05^{+1.4}_{-1.5}$	$1.6^{+0.4}_{-0.3}$	10.6/8	1–100	$8.55^{+.75}_{-.74}$	1.3 ± 0.1	15.0/8

of pairs. The likelihood ratio defined as

$$S = -2(\ln \mathcal{L} - \ln \mathcal{L}_0) \tag{6.10}$$

and satisfies the usual χ^2 distribution, where $\mathcal{L}_0$ is the maximum likelihood. Since the maximum-likelihood method is not a goodness-of-fit indicator, we quote the χ^2 derived from the binned correlation function (as shown in the figures) and the best-fit parameters from maximum-likelihood estimates.

We fit the correlation functions over three separation ranges. In Figure 49 we show the correlation function and the best-fit with 3 Mpc$< s <$200 Mpc. The best-fit parameters for all three separation ranges are listed in Table 6.1. The measured $\gamma = 1.6$ for 3 Mpc$< s <$200 Mpc is very close to the canonical value. However, the rather large χ^2 implies that the single power-law model may not be a proper description of the data.

For comparison, we also computed the correlation function of the X-ray sources in CDFN in the same redshift interval. We created a mock catalog 50 times larger

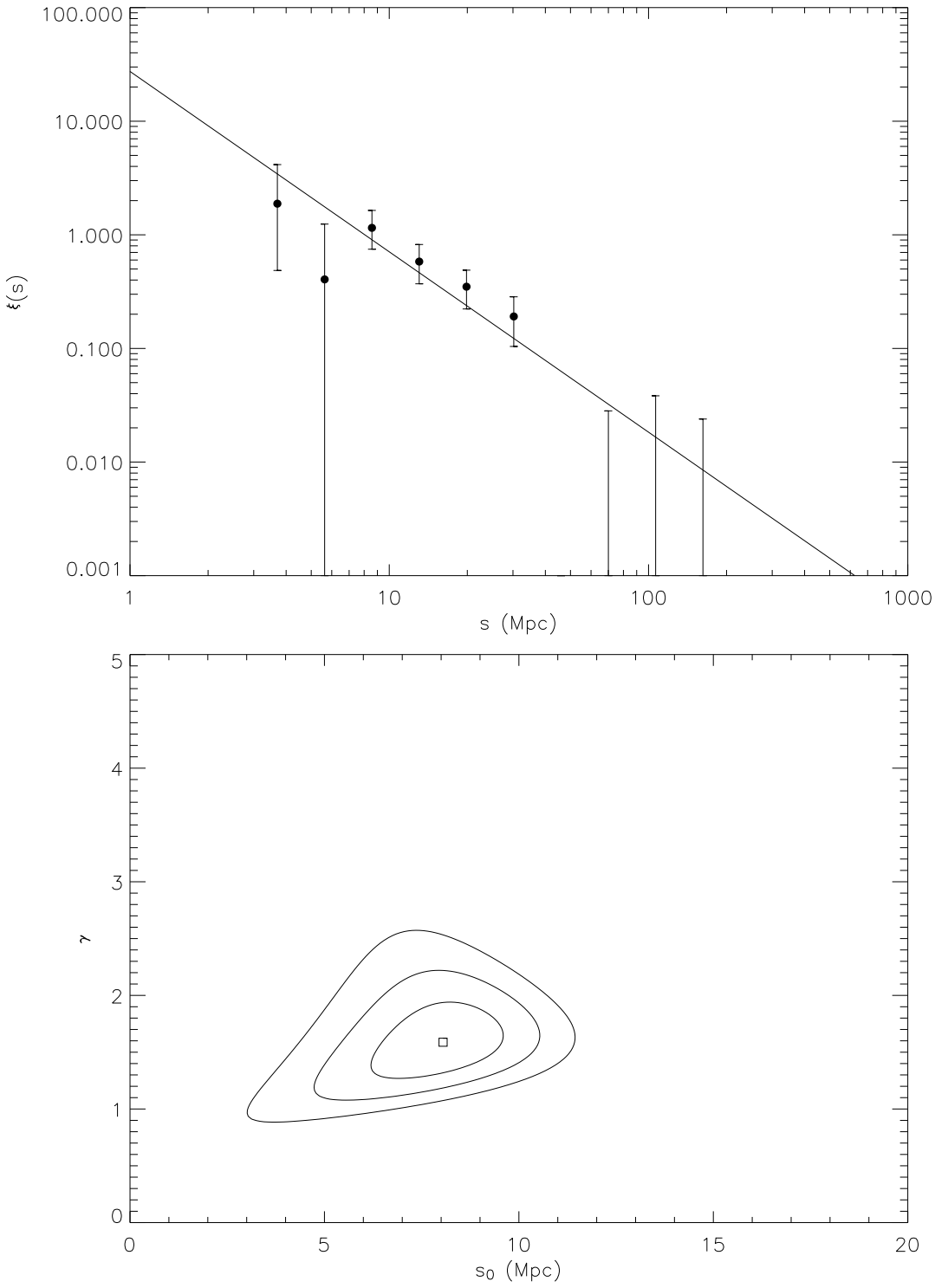

Figure 49: (a). Redshift-space correlation function for CLASXS field with 3 Mpc< s <200 Mpc. (b). Maximum-likelihood contour for the single power-law fit. Contour levels are $\Delta S = 2.3, 6.17, 11.8$, corresponding to 1σ, 2σ and 3σ confident levels for two parameter fit.

than the observation. The positions and redshifts of the random sources are generated by randomizing the observed positions and redshifts. A large Poisson noise was added to avoid artificial clustering in the mock catalog. Such randomization is justified because the clustering signal in a small field like the CDFN mainly comes from clustering along the line-of-sight direction. The randomized sky coordinates are filtered using an image mask to take into account the edge effects. We include all the non-stellar sources in the same redshift interval as we use for CLASXS, which results in 252 sources in the sample. The best-fit parameters for CDFN field over three scale ranges are also shown in Table 6.1. The correlation function over 1 Mpc$< s <$100 Mpc is shown in Figure 50

There is a good agreement of the correlation lengths obtained in the two deep fields. There seems to be a systematic flattening of the slope at small separations ($s \sim 10$ Mpc) in both samples. When the correlation functions are fitted at small and large separations independently, the resulting χ^2s are systematically smaller. As we shall see with the projected correlation function, this flattening is very likely to be real.

6.4.2 Projected correlation function

The projected correlation function is computed using the methods described in § 6.4.2. To test the method, we first compute the projected correlation function for the CDFN and compare the results with that published in Gilli et al. (2005). We selected the same redshift interval for the CLASXS field. A two dimensional

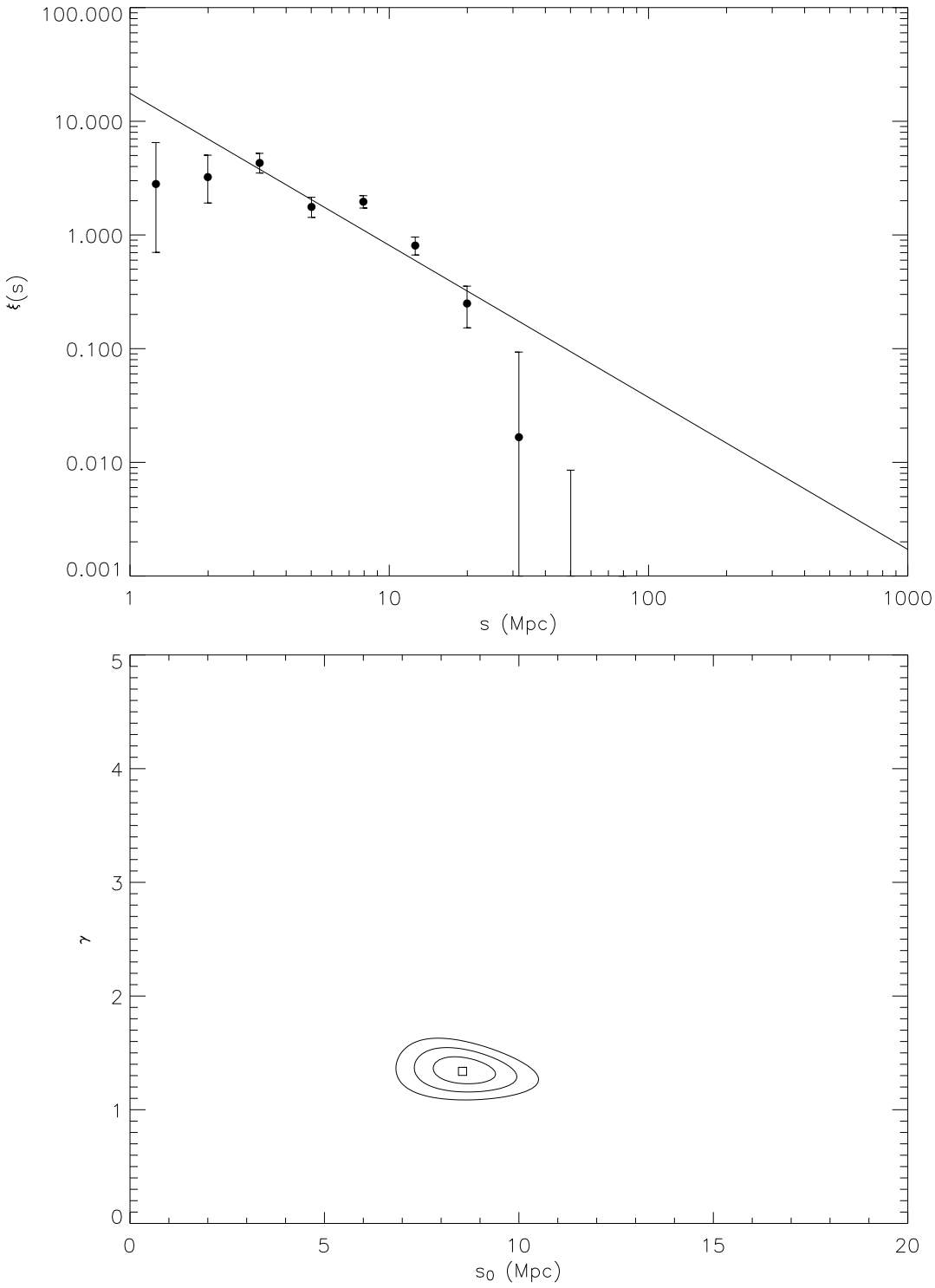

Figure 50: The same as Figure 49 for CDFN except the correlation function is calculated for separation 1 Mpc$< s <$100 Mpc.

correlation function is calculated on a 5×10 grid on the (r_p,π) plane. The 5 intervals along r_p axis covers 0.16–20 Mpc. We integrate the resulting two dimensional correlation function along the line-of-sight to a $\pi_{max} = 20$ Mpc. Our projected correlation function for CDFN is shown Figure 51, and it agrees perfectly with that reported in Gilli et al. (2005) for $z = 0 - 4$.

We next compute the projected correlation function for the CLASXS field. The correlation function is calculated on scales of $r_p = 1 - 30$ Mpc. The 2-D correlation function is integrated to $\pi_{max} = 30$. The result is also shown in Figure 51. It is obvious that the correlation functions of the CDFN and CLASXS fields agree very well at $r_p \sim 10$ Mpc. The slope, however, appears to be flatter in the CDFN field.

We perform a χ^2 fit to the correlation functions using Equation 6.6. The best-fit parameters for CDFN are $r_0 = 5.8^{+1.0}_{-1.5}$ Mpc, $\gamma = 1.38^{+0.12}_{-0.14}$, and the reduced $\chi^2/dof = 2.5/3$. This is in good agreement with the result from Gilli et al. (2005, $r_0 = 5.7$ Mpc, $\gamma = 1.42$). The quoted errors in that paper is smaller than we obtained, but since we adopt a bootstrap error instead of Poisson error in this analysis, the difference is expected. The best-fit parameters for the CLASXS field are $r_0 = 8.1^{+1.2}_{-2.2}$ Mpc, $\gamma = 2.1^{+0.5}_{-0.5}$, and the reduced $\chi^2/dof = 1.6/4$. The correlation length appears to be higher than that of the CDFN, but agrees within the errors. The slope also seems steeper than that of the CDFN and agrees better with the slope of the redshift-space correlation function at $r_p > 10$ Mpc. Since the CLASXS sample does not cover separations < 10 Mpc very well, it is hard to see a slope change in this sample alone. Since the CDFN and CLASXS connect very well at separations where both surveys are sensitive, we try to model the combined data

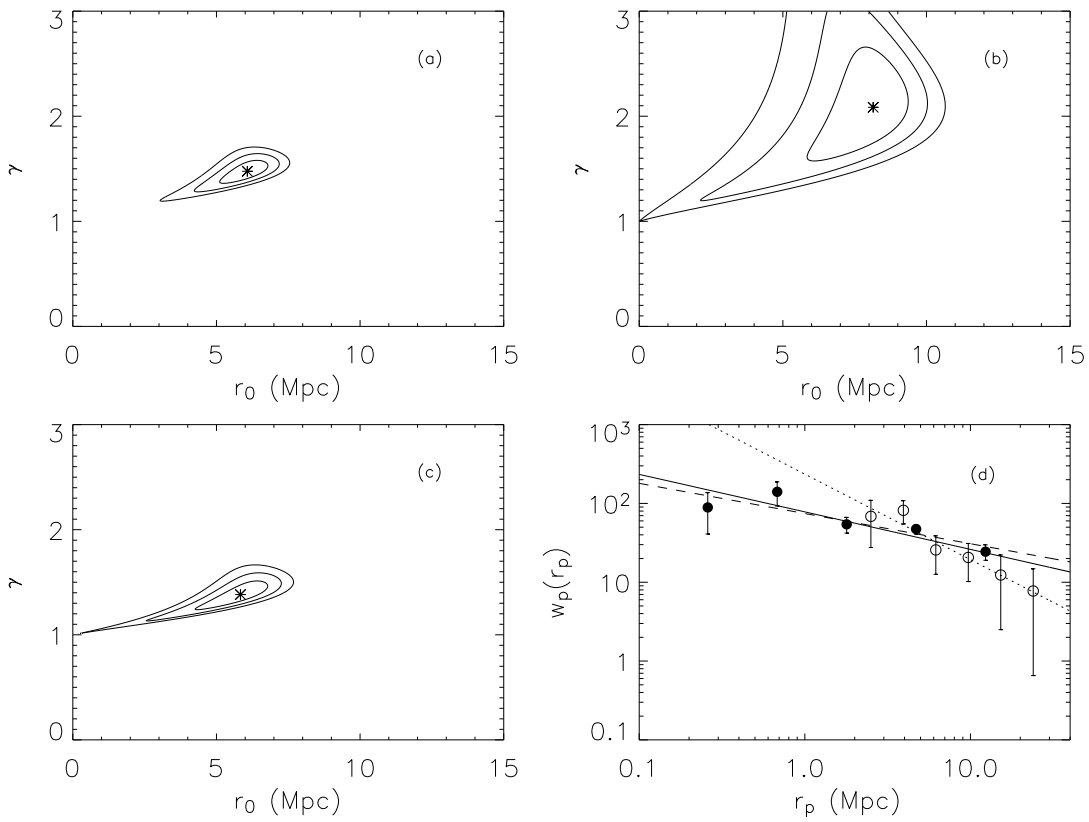

Figure 51: The projected correlation function for CLASXS, CDFN and the best fit. (a)-(c) are the χ^2 contours for CLASXS+CDFN, CLASXS, and CDFN, respectively. Contour levels are for 1σ, 2σ, and 3σ confident level ; (d) The projected correlation function for CLASXS (open circles) and CDFN (black dots) fields. Lines are the best-fit shown in (a)-(c). Solid line: CLASXS+CDFN; Dotted line: CLASXS; Dashed line: CDFN

points with a single power-law. This yields $r_0 = 6.1^{+0.4}_{-1.0}$ Mpc, $\gamma_0 = 1.47^{+0.07}_{-0.10}$, and $\chi^2/dof = 10.7/9$. The reduced χ^2 is much worse than than two samples fitted separately. This again seems to suggest that the slope of the correlation function flattens at small separations.

6.4.3 Redshift distortion

Redshift distortion affects the correlation function (power-spectrum) by increasing the redshift-space correlation amplitude and changing the shape of the 2-D redshift-space correlation function at small scales (such as the well known "finger-of-God" effect, e.g. Hamilton 1992). Since our data is too noisy at small separations, we only discuss the effect of the amplitude boosting of correlation function in redshift-space. Kaiser (1987) showed that to the first order,

$$\xi(s) = \xi(r)(1 + \frac{2}{3}\beta + \frac{1}{5}\beta^2), \tag{6.11}$$

where $\beta \approx \Omega_M(z)^{0.6}/b(z)$ and $b(z)$ is bias. In principle, the redshift-space distortion can be estimated by comparing $\xi(s)$ and $\xi(r)$. To quantify the effect, we use the correlation function estimate at scales where both projected and redshift-space correlation functions are well determined. For the CDFN, we chose the correlation function estimates at 10 Mpc and find $\xi(s = 10\ Mpc)/\xi(r = 10\ Mpc) = 1.75 \pm 0.55$, if the best-fit of $\xi(s)$ on 1-100 Mpc is used. The choice of this scale is justified given that the slope possibly changes below and above 10 Mpc, as seen in the projected correlation function. Since the slope of the redshift- and real-space correlation function is very similar in the CDFN, the ratio is almost constant. For the CLASXS

field, we chose to estimate the ratio at 20 Mpc. We find $\xi(s = 20\ Mpc)/\xi(r = 20\ Mpc) = 1.73 \pm 0.42$ by using the best-fit on 1–100 Mpc for $\xi(s)$. The ratio changes slowly with the scales probed, but is within the errors. We find a general agreement between CLASXS and CDFN. It should be noted that if the best-fits of redshift-space correlation function on small scales are used, the results from the CDFN and CLASXS do not agree. Nonlinear redshift-space distortion and the window function of the two surveys are possible causes. To avoid the random choice of scales, and to make the best use of the data, we combine the two samples to study the redshift distortion effect on $\xi(r_p, \pi)$. Since the projected correlation function of CDFN and and CLASXS agrees in general, we are encouraged to assume that the the two samples, even with the vast difference in flux limits, generally trace the large scale structure in the same way.

In Figure 52. we show the combined $\xi(r_p, \pi)$. The contours show no significant signature of nonlinear redshift distortion, such as the "finger-of-god". We fit $\xi(r_p, \pi)$ with Equation 6.11, assuming the best-fit parameters for the real-space correlation function from the combined sample ($r_0 = 6.1$ Mpc, $\gamma_0 = 1.47$), and ignoring the higher order redshift distortions. We generate the 2-D correlation function at each grid point. By minimizing χ^2 by changing β, we found the best-fit $\beta = 0.4 \pm 0.2$, which corresponds to $\xi(s)/\xi(r) \sim 1.3$, which agrees with the estimates from individual fields above. By fixing $\Omega_M = 0.27$, we can estimate the bias factor of X-ray selected AGNs from β. The median redshift of the combined sample is 0.94, and $\Omega_M(z = 0) = 0.27$ gives $\Omega_M(z = 0.94) = 0.73$. This yields $b \approx 2.04 \pm 1.02$ using the relation $\beta \approx \Omega_M^{0.6}/b$.

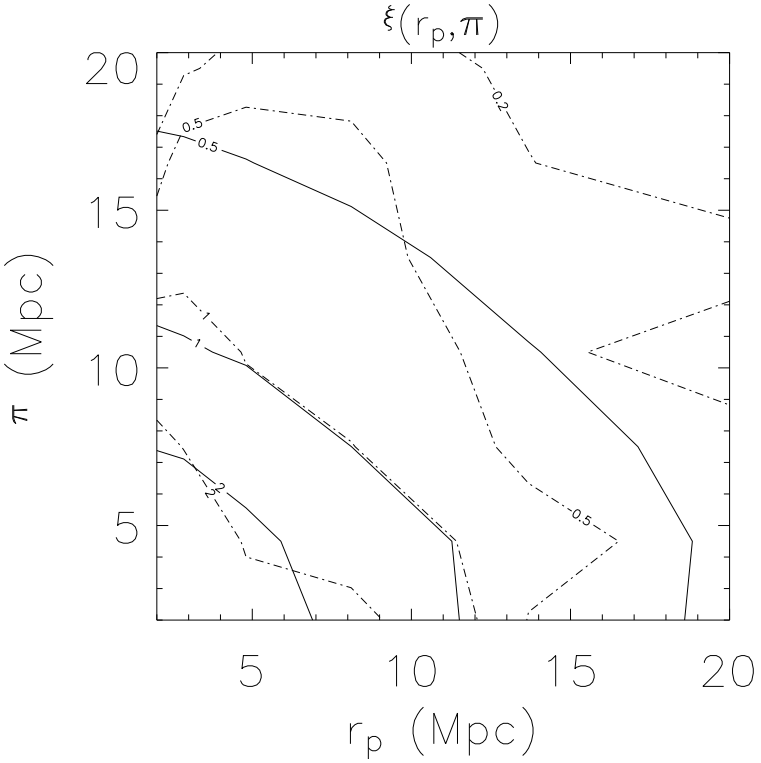

Figure 52: Two dimensional redshift-space correlation function $\xi(r_p, \pi)$ of the combined CLASXS and CDFN data (dashed-dotted contour). Solid line shows the best-fit model. Both the data and model correlation functions are smoothed using a 2×2 boxcar to reduce the noise for visualization only.

6.4.4 X-ray color dependence

We further test if there is any differences in clustering properties between the hard and soft spectra sources in the CLASXS sample. We use the hardness ratio, defined as $HR \equiv C_{2-8keV}/C_{0.5-2keV}$ (where C is the count rate), to quantify the spectral shape of the X-ray sources. Correlation functions of soft ($HR < 0.7$) and hard ($HR \geq 0.7$) sources are calculated the same way as above. The fraction of broad-line AGNs is 56.4% in the soft sample and 15.4% in hard sample. The median redshifts are 1.25 and 0.94 for soft and hard samples, respectively. We compute $\xi(s)$ for both soft and hard sources over scales of 3–200 Mpc.

Using a maximum-likelihood fit, we found $s_0 = 9.6^{+2.4}_{-3.4}$ Mpc, $\gamma = 1.6^{+0.8}_{-0.6}$ for hard sources and $s_0 = 8.6^{+2.2}_{-2.0}$ Mpc, $\gamma = 1.6^{+0.6}_{-0.5}$ for soft sources. We found no significant difference in clustering between the soft and hard sources. This agrees with the results of G04. It is noticeable that the soft sources have a higher median redshift than hard sources. The interpretation of this result must include evolution effects. To avoid this complication, we restricted the redshift range to $z = 0.1 - 1.5$. The best-fit parameters are $s_0 = 9.5^{+3.1}_{-3.7}$ Mpc ($6.2^{+2.7}_{-4.6}$ Mpc) and $\gamma = 1.7^{+0.9}_{-0.6}$ ($2.5^{+1.6}_{-0.9}$) for hard (soft) sources. The difference in clustering parameters between soft and hard sources are well within error. The same analysis on CDFN yields similar results. Thus there is no significant dependence of clustering on the X-ray color.

6.4.5 Luminosity dependence

The cold dark matter (CDM) model of hierarchical structure formation predicts that massive (and hence luminous) galaxies are formed in rare peaks, and therefore should be more strongly clustered. This is seen in normal galaxies (e.g. Giavalisco & Dickinson 2001). Whether this relation can be extended to X-ray luminosity of AGNS is unknown. This is because the X-ray luminosity relates to the dark matter halo mass in a more complex way. The X-ray luminosity is directly linked to the accretion process, and the process is affected by factors such as accretion rate, radiative efficiency, blackhole mass and the details of the dynamical process in the accretion process. We have shown that at least in broadline AGNs, where the blackhole mass can be inferred from the line-width and nuclear luminosity, the Eddington ratio is close to constant over two decades of 2–8 keV luminosity (Barger et al. 2005). If this is the case for all X-ray selected AGNs, we should expect the AGN luminosity to be mainly determined by the blackhole mass, which in turn, should be closely related to the halo mass (Ferrarese 2002), even though the exact form of this relation is highly uncertain. However, the optical quasar surveys such as 2dF found little evidence of correlation between clustering amplitude and ensemble luminosity (C05), probably due to the small dynamical range in luminosity these surveys probe. The X-ray luminosity of sources in the CLASXS and CDFN cover a luminosity range of four orders of magnitudes, making it possible to make such a test.

The 2–8 keV luminosity L_x is calculated from the hard band fluxes, with a

K-correction made assuming a power-law spectra with photon index $\Gamma = 1.8$. This yields

$$L_x = L_O(1+z)^{0.2}. \tag{6.12}$$

In Figure 53 we show L_x vs. redshift for both CLASXS and CDFN. For a better

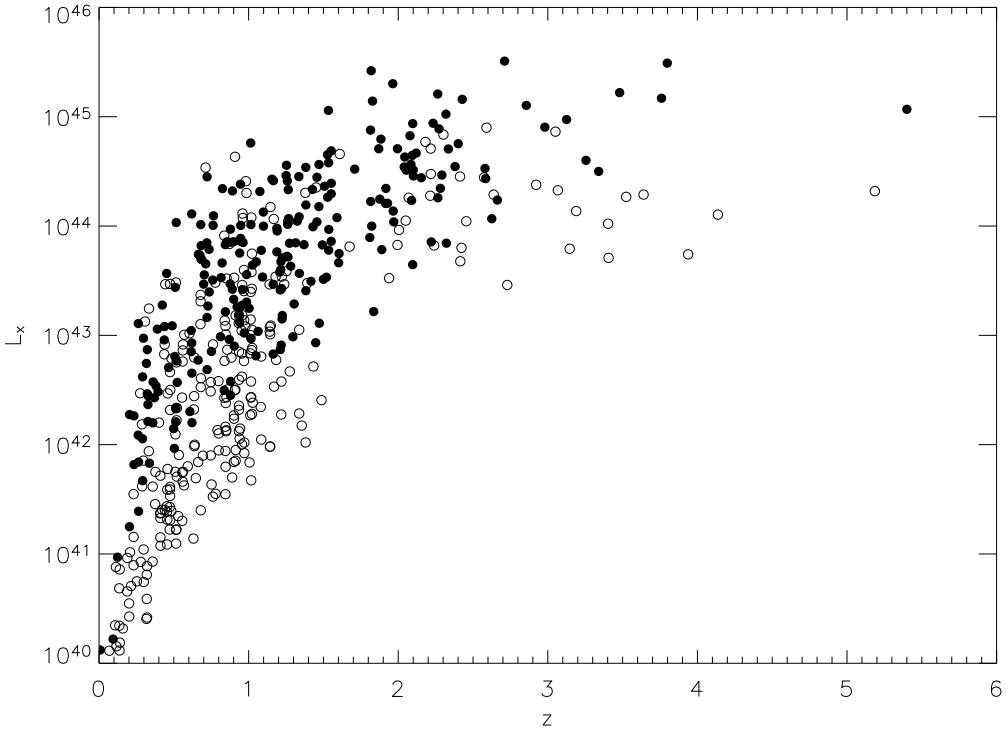

Figure 53: The luminosity of X-ray sources vs. redshifts in CLASXS (dots) and CDFN (open circles)

comparison of the correlation amplitude, we adopt the averaged correlation function within 20 Mpc,

$$\bar{\xi}(20) = \frac{3}{20^3}\int_0^{20} ds\xi(s)s^2. \tag{6.13}$$

The quantity is chosen rather than s_0 because it measures the clustering (directly linked to the rms fluctuations) regardless of the shape of the correlation function.

Table 6.2. Luminosity dependance of Correlation Function

Field	z range	z_{median}	$< L_x >$ ($\mathrm{erg\,s^{-1}}$)	s_0	γ	χ^2/dof	$\bar{\xi}(20)$
CLASXS	0.1–3.0	1.5	3.3×10^{44}	$11.5^{+1.9}_{-2.1}$	$2.0^{+.5}_{-0.4}$	7.2/8	$1.00^{+.25}_{-.24}$
	0.1–3.0	.73	1.5×10^{43}	$7.35^{+1.9}_{-2.0}$	$1.9^{+1.2}_{.54}$	8.8/8	$.41^{+14}_{-.13}$
	0.3–1.5	1.1	1.4×10^{44}	11.0 ± 2.6	$2.3^{+1.6}_{-0.6}$	9.2/8	$1.04^{+.38}_{-.33}$
	0.3–1.5	.81	1.6×10^{43}	$5.30^{+2.9}_{-3.8}$	$1.4^{+0.8}_{-0.5}$	7.8/8	$.28^{+.13}_{-.15}$
CDF-N	0.1–3.0	.98	7.9×10^{43}	13.2 ± 2.9	$.81^{+0.20}_{-0.17}$	8.2/8	$.98 \pm 0.11$
	0.1–3.0	.51	8.3×10^{41}	$5.6^{+1.2}_{-1.1}$	$1.26^{+0.22}_{-0.20}$	11.9/8	$.35 \pm .05$
	0.3–1.5	.96	4.0×10^{43}	$8.0^{+1.5}_{-1.4}$	$1.11^{+.25}_{-.22}$	11.1/8	$.57^{+.08}_{-.07}$
	0.3–1.5	.63	1.0×10^{41}	$6.8^{+1.3}_{-1.2}$	$1.28^{+.27}_{-.21}$	8.4/8	$.43 \pm .08$

On scales of 20 Mpc the clustering is well described by the linear approximation of the structure formation. It is also independent of the assumed H_0 which allows easy comparison with other observations. The error in $\bar{\xi}(20)$ we quote is from the single parameter 1σ confidence interval obtained by fixing the slope of the correlation function to the best-fit.

We split the CLASXS sample into two subsamples at $L_x = 4.5{\times}10^{43}$ $\mathrm{erg\,s^{-1}}$ and the CDFN sample at $L_x = 3.2 \times 10^{42}$ $\mathrm{erg\,s^{-1}}$. Each subsample contain similar number of objects. In Table 6.2 we show the maximum-likelihood fits as well as $\bar{\xi}(20)$s. It should be noted that the correlation amplitude is biased in redshift space. The dominant part of this bias is characterized in Equation 6.11. Comparing with other observations (da Ângela et al. 2005, e.g.), β is likely a weak function of red-

shift in the redshift range probed by our sample, with $\beta \sim 0.4$, this translates to $\xi(s)/\xi(r) \sim 1.3$. We correct the $\bar{\xi}(20)$'s for this bias by dividing them by 1.3. The correlation amplitude for the more luminous sources appears to be higher than that of the less luminous sources, which qualitatively agrees with expectations that X-ray luminosity reflects the dark matter halo mass. The correlation amplitude for the more luminous subsamples are 2.3σ and 5.7σ higher than that of the less bright subsample in the CLASXS and CDFN fields, respectively. However, since the more luminous subsamples also are preferentially found at higher redshifts, the evolution in $\xi(s)$ should be taken into account.

To reduce this complication, we restrict ourselves to sources within the redshift range of 0.3–1.5, where the evolution effect is relatively small (see also § 6.5). In Figure 54 we show L_x vs. $\bar{\xi}(20)$ for both CLASXS and CDFN. By reducing the redshift range, the difference in correlation amplitude between the brighter and dimmer subsample reduce significantly in the CDFN sample, to merely 1.7σ. For the CLASXS field, on the other hand, the correlation amplitude for both subsamples do not show significant change. For comparison, we also plot in Figure 54 the correlation amplitude from the 2dF survey (C05). The X-ray luminosities for the QSOs in the 2dF are obtained by dividing the bolometric luminosities by 35 (Elvis et al. 1994). We perform Spearman's ρ test for correlations between log L_x and $\bar{\xi}$. We found the correlation coefficient $\rho = 0.8$ for X-ray samples, or a corresponding null probability of 20%, indicating a mild correlation between the two quantities. If the 2dF samples are added, however, ρ drops to 0.1, with a null probability of 81%. This means that for the combined optical and X-ray sample there is no correlation

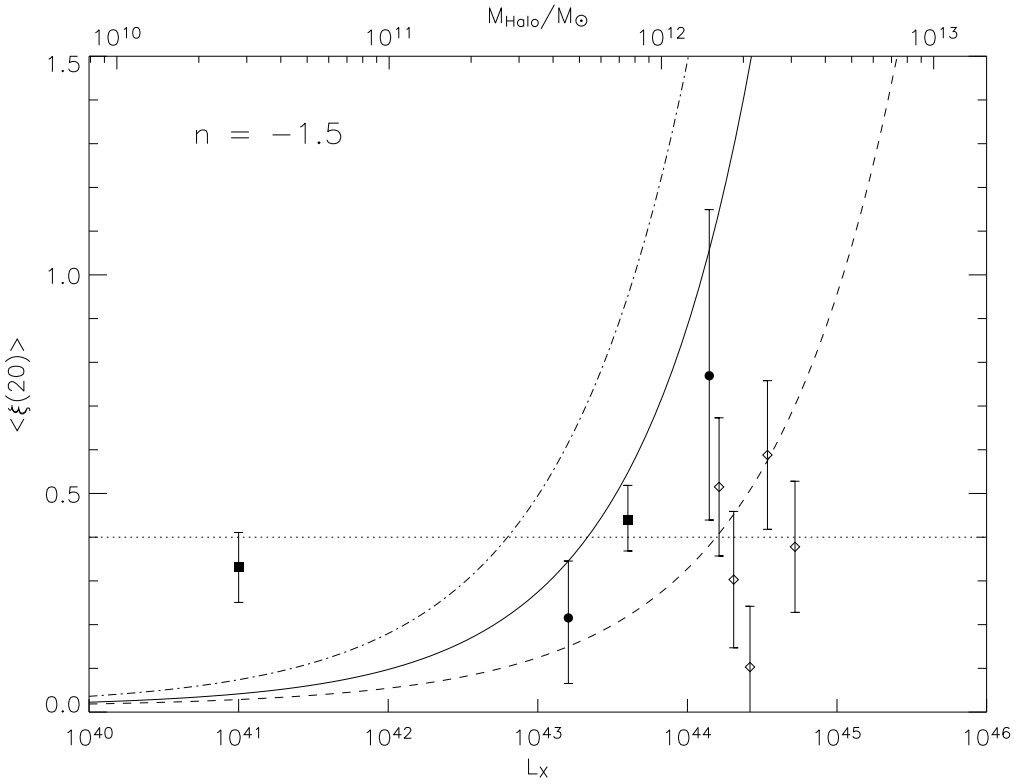

Figure 54: Luminosity dependence of clustering of AGNs. Black dots: CLASXS samples; Filled boxes: CDFN samples; Diamonds: 2dF sample (Croom et al. 2004). Lines are the models for different halo profile from Farrarese (2002). Solid line: NWF profile ($\kappa = 0.1$, $\lambda = 1.65$); Dashed line: weak lensing determined halo profile (Seljak, 2002; $\kappa = 0.67$, $\lambda = 1.82$); Dash-dotted line: isothermal model ($\kappa = 0.027$, $\lambda = 1.82$)

between X-ray luminosity and clustering amplitude.

6.5 Evolution of clustering

Measuring the correlation function over a wide redshift range only makes sense if the correlation function is a weak function of redshift. The best measurements of clustering of 2dF quasars at high redshift show that the correlation function indeed exhibits only mild evolution (C05). In this section, we test the evolution of clustering of X-ray selected AGNs and compare them with other survey results.

6.5.1 Samples

We study the evolution of clustering in both CLASXS and CDFN samples, using the redshift-space correlation function. The sources are grouped in 4 redshift intervals from 0.1 to 3. The sizes of the intervals are chosen so that the number of objects in each interval is similar in the CLASXS sample. This result in a very wide redshift bin above $z = 1.5$. The correlation functions for the CLASXS, CDFN and CLASXS+CDFN fields are shown in Figures 55, 56, and 57, respectively. We group the pair separations in 10 bins in these figures to show the shape of the correlation function. In some bins there could be no DD pairs, and the correlation function is set to -1 without errors. We model the correlation functions using single power-laws and fit the data using the maximum-likelihood method. As we mentioned earlier, the method is not affected by binning. We found on 3–50 Mpc scales that a single power-law provides a good fit to the data except, for the the $z = 1.5 - 3$ interval

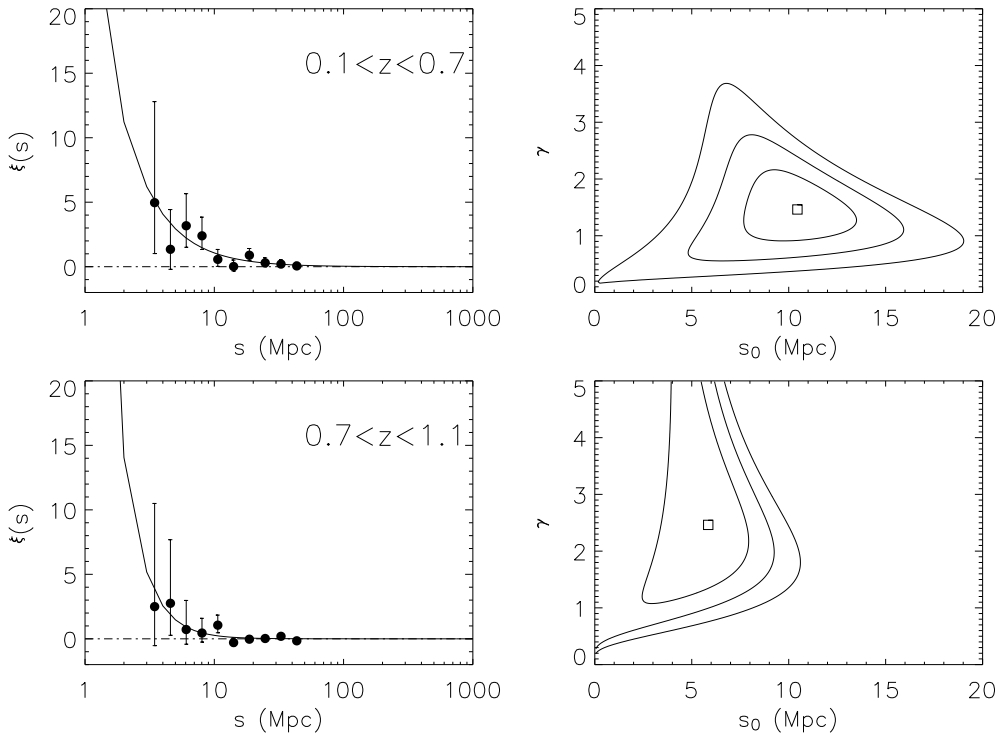

Figure 55: The Redshift-space correlation function for CLASXS field in four redshift bins. Left panels: The correlation functions and the power-law best-fits using maximum-likelihood method. Right panels: the maximum-likelihood contour for the corresponding correlation function on the left. Contour levels correspond to 1σ, 2σ and 3σ confident levels.

in the CDFN, where the sample is too sparse and have very few close separation pairs, we use a separation range of 5–200 Mpc to obtain the fit. The goodness-of-fit is quantified with χ^2. In the case where empty bins exist, we increase the bin sizes until no bins are empty before we compute the χ^2.

The results are summarized in Table 6.3 and the $\bar{\xi}(20)$s as a function of redshift are shown in Figure 58. We have tested fitting the correlation functions over difference scale ranges, and found no significant differences in the resulting $\bar{\xi}(20)$.

Table 6.3. Evolution of redshift-space Correlation Function

Field	z range	$< z >$	N[a]	$< L_x >$[b]	s_0	γ	χ^2/dof	$\bar{\xi}(20)$
CLASXS	0.1–0.7	0.44	57	1.6×10^{43}	$10.6^{+3.2}_{-3.0}$	$1.3^{+0.7}_{-0.5}$	4.1/8	$0.78^{+0.19}_{-0.17}$
	0.7–1.1	0.90	60	6.7×10^{43}	$6.2^{+2.1}_{-2.8}$	$2.3^{+6.0}_{-1.0}$	5.9/8	$0.33^{+0.20}_{-0.16}$
	1.1–1.5	1.27	49	1.1×10^{44}	$6.4^{+5.0}_{-6.6}$	$1.3^{+1.2}_{-0.7}$	1.6/3	$0.39^{+0.20}_{-0.20}$
	1.5–3.0	2.00	67	4.9×10^{44}	$13.6^{+4.2}_{-5.4}$	$1.4^{+0.6}_{-0.5}$	3.1/3	$1.09^{+0.39}_{-0.20}$
CDFN	0.1–0.7	0.46	111	2.8×10^{42}	$6.8^{+0.7}_{-0.6}$	$2.2^{+0.5}_{-0.3}$	12.5/8	$0.35^{+0.04}_{-0.05}$
	0.7–1.1	0.94	91	2.6×10^{43}	$9.4^{+1.3}_{-1.4}$	$1.2^{+0.3}_{-0.2}$	5.6/8	$0.67^{+0.09}_{-0.07}$
	1.1–1.5	1.22	28	3.8×10^{43}	$8.8^{+2.6}_{-2.3}$	$2.1^{+1.0}_{-0.8}$	2.9/8	$0.60^{+0.24}_{-0.22}$
	1.5–3.0	2.24	22	2.4×10^{44}	$14.2^{+8.5}_{-7.9}$	$2.3^{+2.2}_{-1.4}$	1.4/7	$1.6^{+1.2}_{-1.0}$
CLASXS+CDFN	0.1–0.7	0.45	168	7.3×10^{42}	$7.9^{+0.9}_{-0.9}$	$1.9^{+0.3}_{-0.3}$	5.3/8	$0.47^{+0.06}_{-0.05}$
	0.7–1.1	0.92	151	4.3×10^{43}	$10.1^{+1.1}_{-1.0}$	$1.4^{+0.2}_{-0.2}$	5.5/8	$0.72^{+0.08}_{-0.07}$
	1.1–1.5	1.26	77	8.2×10^{43}	$8.4^{+1.8}_{-2.4}$	$2.0^{+0.8}_{-0.6}$	1.8/8	$0.53^{+0.17}_{-0.15}$
	1.5–3.0	2.07	89	4.3×10^{44}	$12.4^{+2.7}_{-3.4}$	$1.7^{+0.5}_{-0.4}$	4.2/7	$1.13^{+0.30}_{-0.24}$

[a]The number of sources

[b]Unit: $\mathrm{erg\,s^{-1}}$

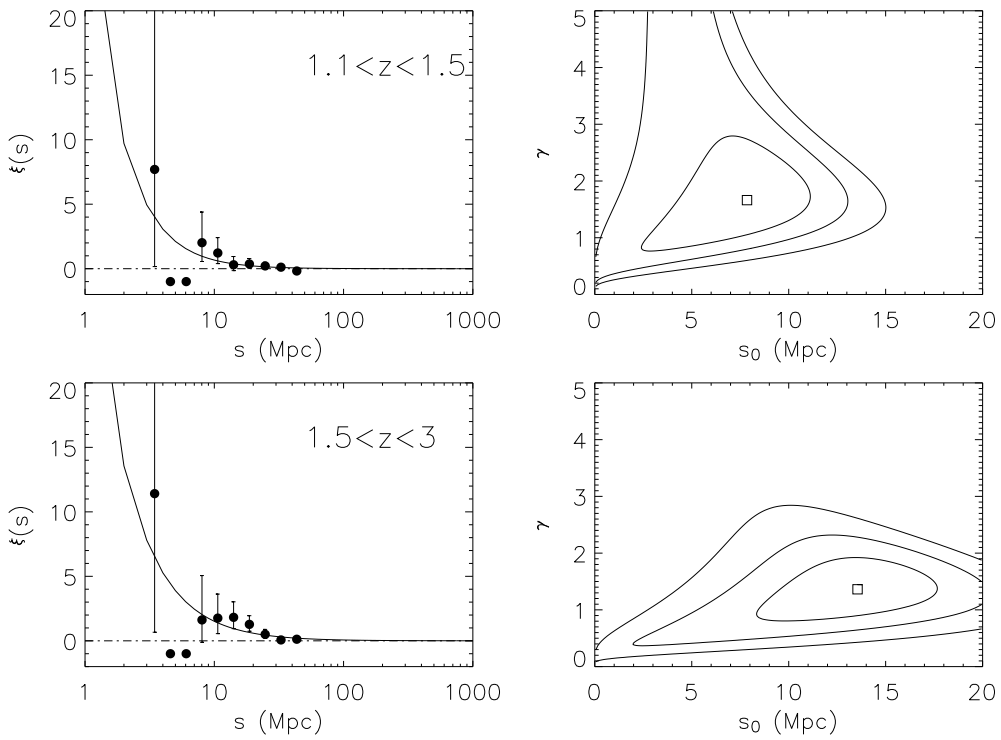

Figure 55 (continued)

There is only mild evolution seen in both the CLASXS and CDFN fields, in agreement with the assumption that clustering is close to constant in comoving coordinates. There are some small discrepancies between the CLASXS and the CDFN clustering strength. These discrepancies give the sense of the field-to-field uncertainty. The decrease of $\bar{\xi}(20)$ from $z \sim 0.44$ to $z \sim 0.9$ in CLASXS field, is not seen in the CDFN. The CDFN sample has very good signal-to-noise ratio at $z \leq 1$ because of the large spatial density. However, the large increase of $\bar{\xi}(20)$ from $z \sim 0.46$ to $z \sim 0.94$, is possibly to caused by cosmic variance, i.e. the two large "spikes" of sources at these redshifts. The issue could be resolved with a larger survey. At the highest redshift, both samples show an increase trend of clustering, but only at the $\leq 2\sigma$ level. The higher clustering can be explained by the order of

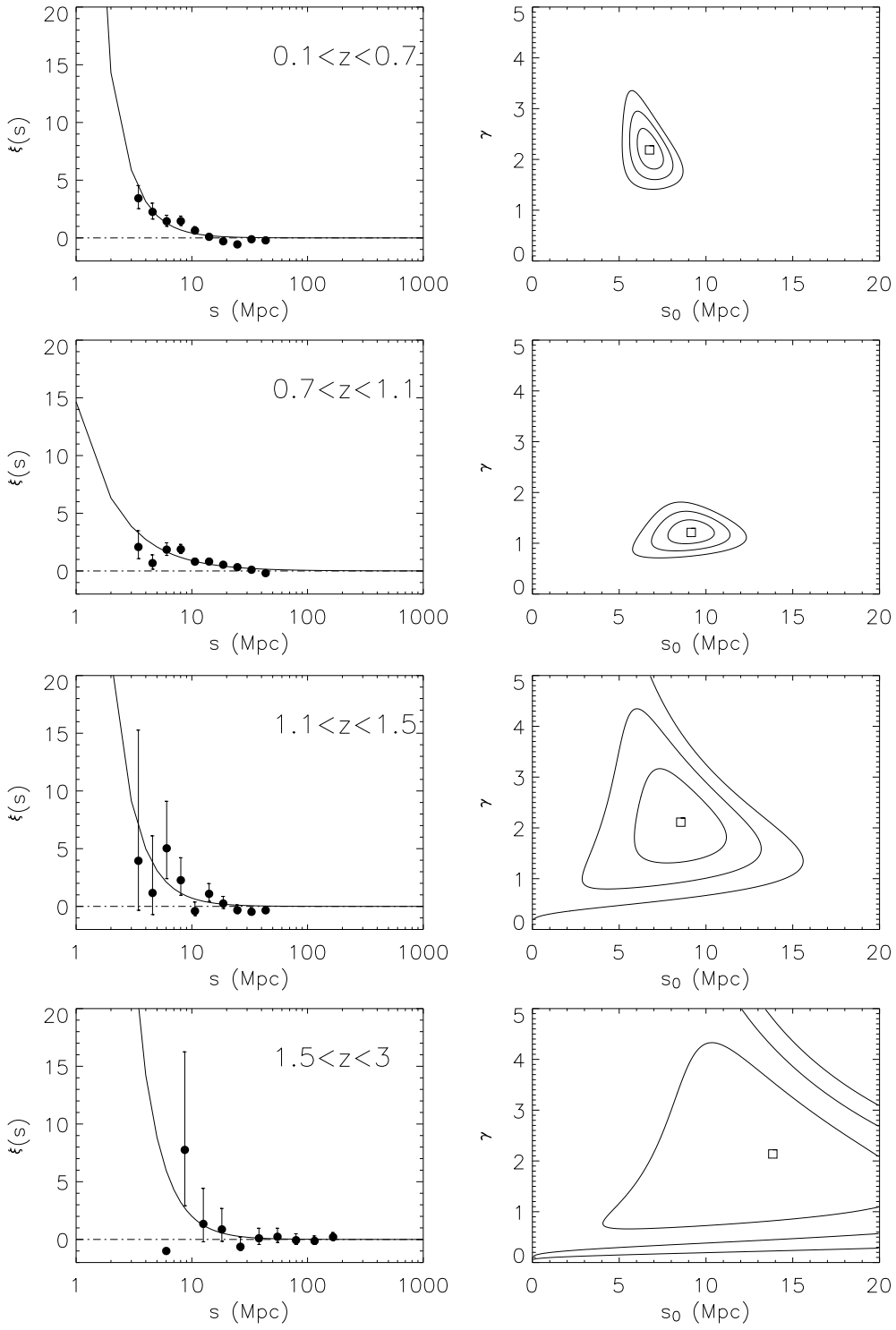

Figure 56: The Redshift-space correlation function for CDFN field in four redshift bins (layout and contour levels are the same as in Figure 55).

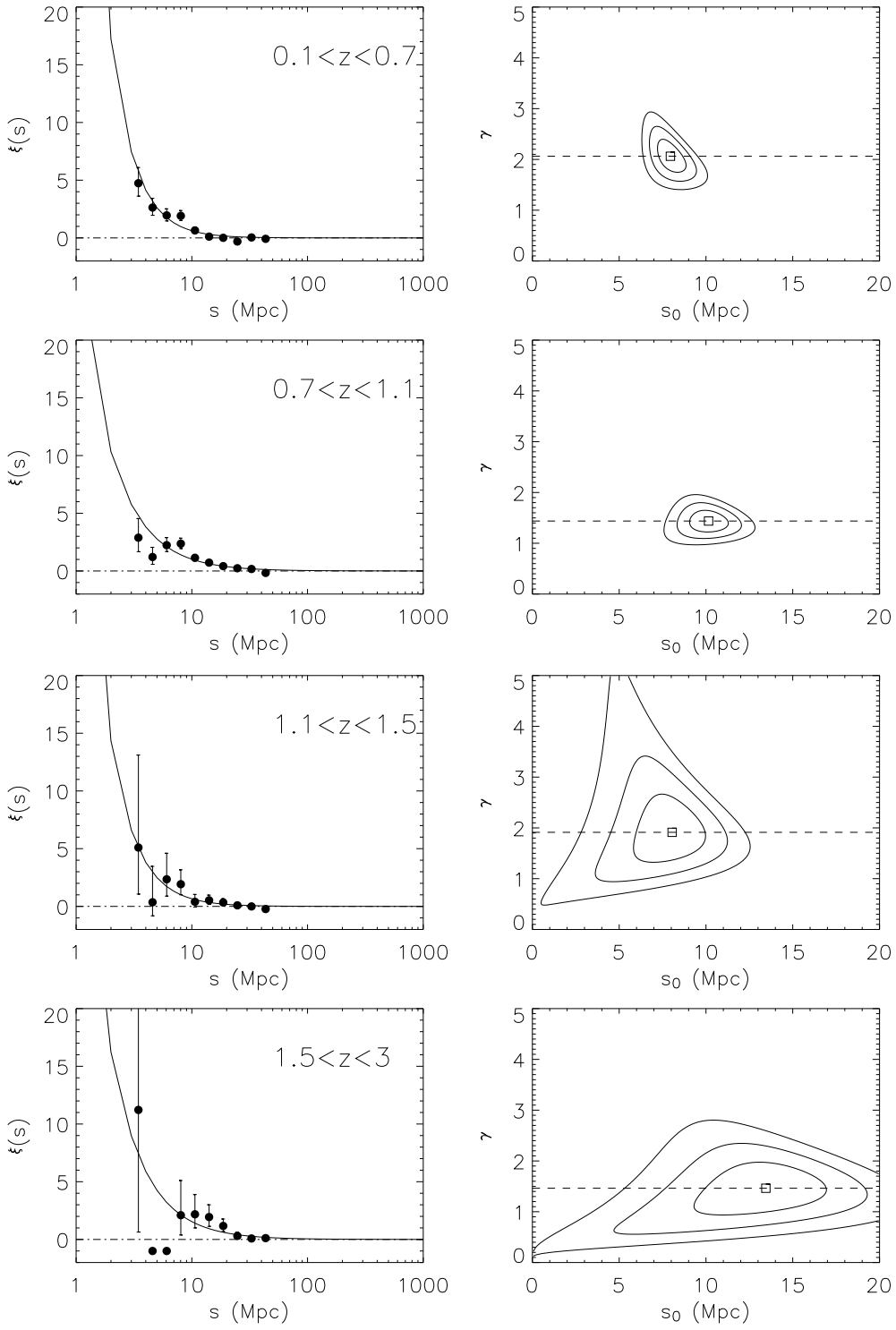

Figure 57: The Redshift-space correlation function for CLASXS+CDFN field in four redshift bins (layout and contour levels are the same as in Figure 55).

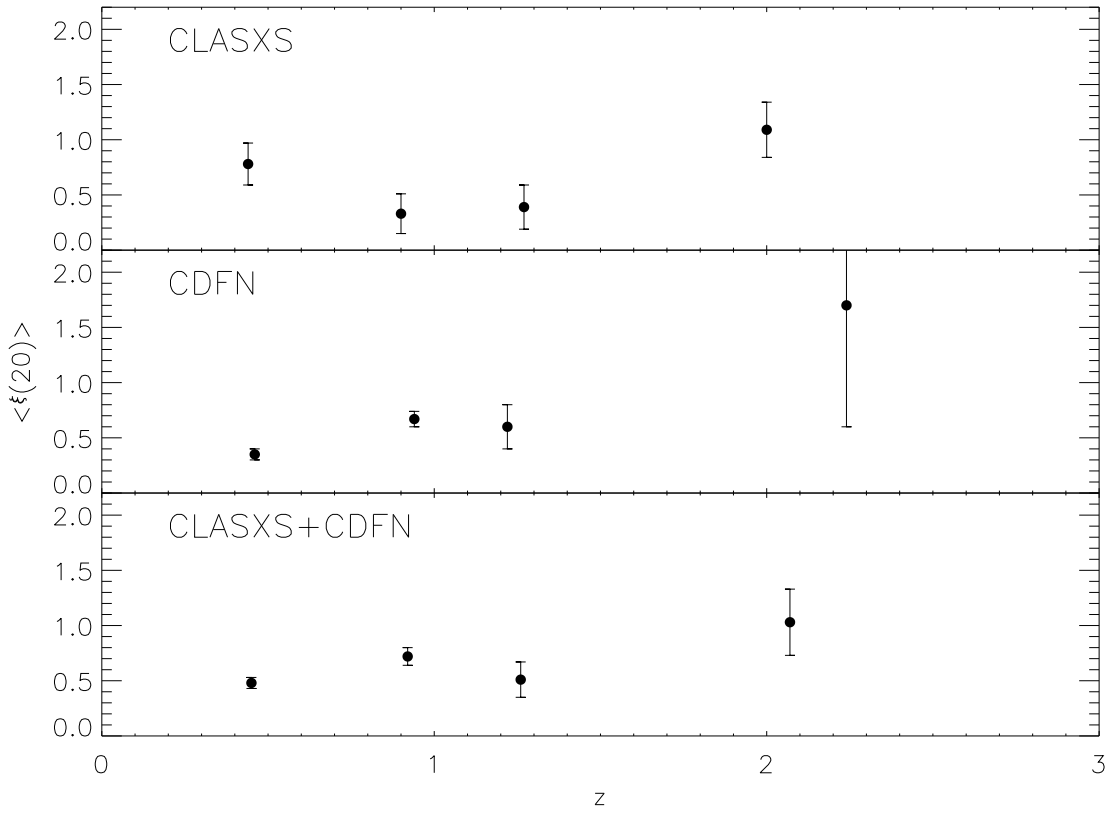

Figure 58: The evolution of clustering as a function of redshift for CLASXS, CDF and the two fields combined.

magnitude increase of luminosity from $z \leq 1$ to $z > 1.5$, caused by the evolution of the luminosity function (Barger et al. 2005) and "Malmquist bias".

6.5.2 Comparing with other observations

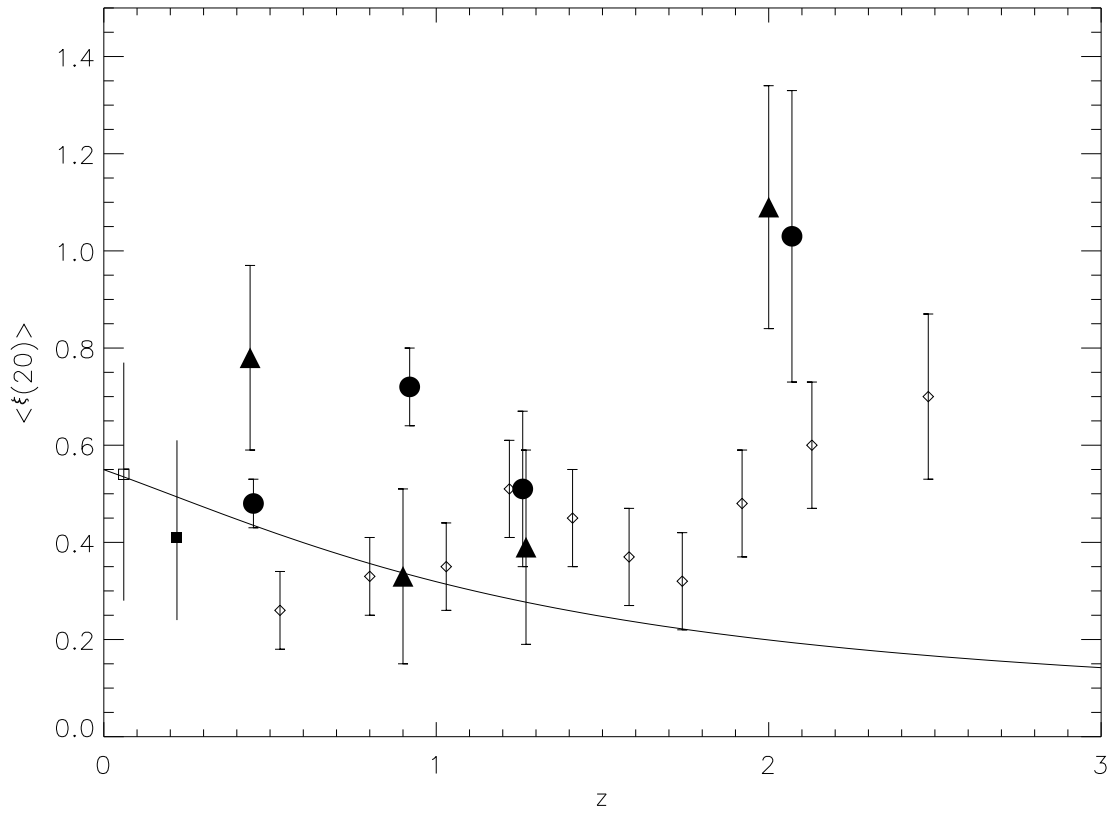

Figure 59: A comparison of clustering evolution in the combined *Chandra* fields (big dots), CLASXS field (big filled triangle), 2dF (diamonds), ROSAT NGP (filled box) and AERQS (empty box). The solid line represent linear evolution of clustering normalized to the AERQS. The dashed lines represent the

In Figure 59 we plot $\bar{\xi}(20)$ as a function of redshift for CLASXS, the combined CLASXS and CDFN, as well as results from the 2dF (C05), the *ROSAT* North Galactic Pole Survey (NGP, Mullis et al. 2004), and the Asiago-ESO/RASS QSO

survey (AERQS, Grazian et al. 2004). We did not correct for redshift distortion for observations which uses redshift-space correlation function. This leads to overestimates of the real-space correlation amplitude. Our correlation function shows a clear

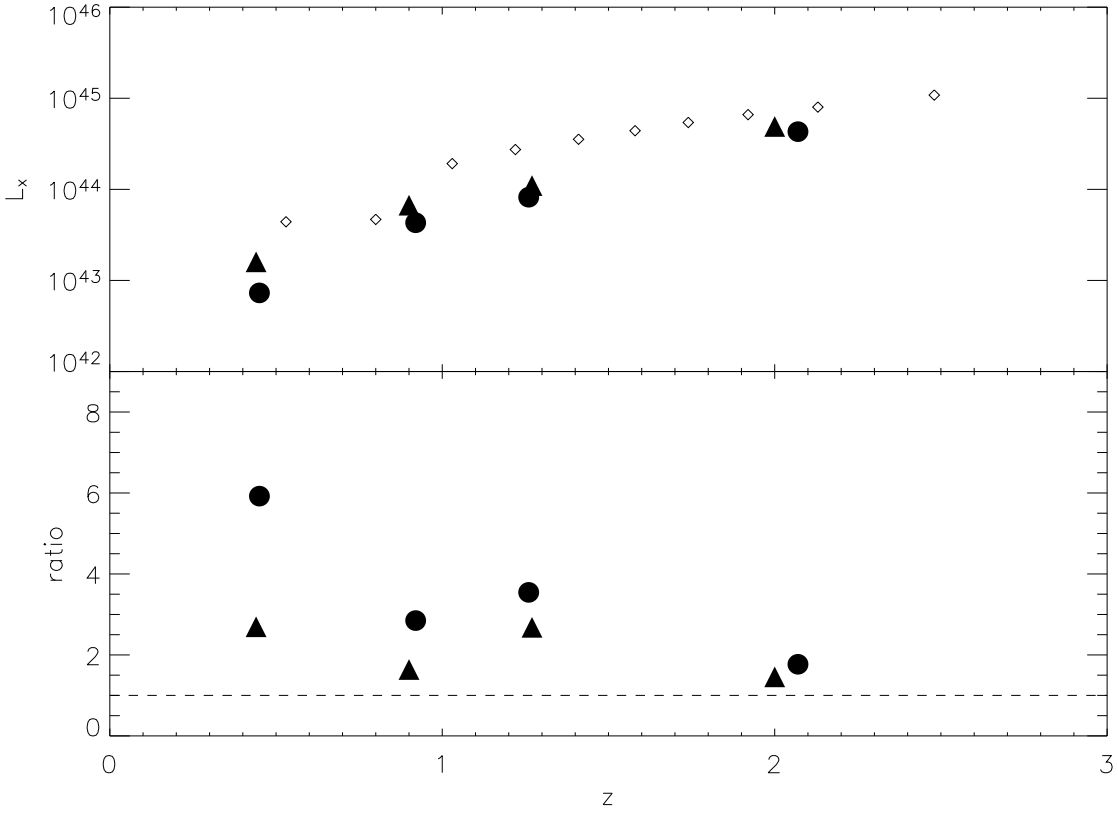

Figure 60: The median luminosities of the 2dF quasar (C04) as a function of redshift (diamonds) compared to the median luminosities of CLASXS sample (triangles) and of CLASXS+CDFN sample (big dots). The lower panel shows the ratio of 2dF median luminosities to the X-ray samples.

agreement with the evolution trend found in C05. However, as seen in § 6.4.5, our measured correlation amplitude on average appears higher than, or at least the same as that of 2dF. This result is surprising because one would expect the 2dF quasars to be more clustered because they are more luminous (see § 6.4.5) than the sources

in the deep X-ray surveys. We compare the X-ray luminosities of the CLASXS and CLASXS+CDFN samples with those of the 2dF in Figure 60. The X-ray luminosities of 2dF quasars are obtained the same way as in § 6.4.5. The luminosity difference between the 2dF sample and X-ray samples is the largest at low redshift and decreases at higher redshift. At $z > 2$, the X-ray sample and the 2dF samples have similar median luminosity. As mentioned in § 6.4.5, the clustering is weakly correlated to luminosity below 10^{43} erg s^{-1}, but the correlation function increases more rapidly above 10^{44} erg s^{-1}. Therefore, we should expect to see the optical sample being more clustered than X-ray samples at medium redshifts. However, the trend is not seen.

6.6 Discussion

6.6.1 Evolution of Bias and the typical dark matter halo mass

In the CDM structure formation paradigm, the continuous density fluctuations can be approximated by discrete dark matter halos. The growth of large scale structure can be seen as merging of the halos. Less massive halos form early and then merge into larger halos. It is obvious that more massive halos tend to be found in denser environment because the chance for merging is higher. This links the clustering property to the halo mass. On the other hand, the formation of stars and galaxies is not only affected by gravitational force, but also affected by gas dynamics and star formation. These processes are generally affected by the mass and the age of the galaxy. The clustering property of luminous matter should thus be different

from that of the halos. The *bias* factor is introduced to account for this difference. In terms of correlation function, the bias can be defined as

$$b^2 \equiv \xi_{light}/\xi_{mass}. \tag{6.14}$$

The bias evolution of optical quasar is extensively discussed in C05. They found that the bias increases rapidly with redshift($b \sim (1+z)^2$). We will follow these arguments to estimate the bias evolution of the X-ray samples.

On scales of 20 Mpc, the clustering of dark matter and AGNs are both in the linear regime, i.e., $\bar{\xi}(20) < 1$. This allows us to measure the bias as a function of redshift by comparing the observed correlation function with the linear growth rate of dark halos in the ΛCDM model. The averaged correlation function of mass can be obtained using

$$\bar{\xi}(20) = \frac{3}{(3-\gamma)J_2(\gamma)}(\frac{8}{20})^{\gamma}\sigma_8^2 D(z)^2 \tag{6.15}$$

where $J_2(\gamma) = 72/[(3-\gamma)(4-\gamma)(6-\gamma)2^{\gamma}]$, $\sigma_8 = 0.84$ is the rms fluctuation of mass at $z = 0$ obtained by *WMAP* observation (Spergel et al. 2003), and we choose the best-fit $\gamma \sim 1.5$. $D(z)$ is the linear growth factor, for which we use the approximation formula from Carroll et al. (1992). The redshift-space distortion is taken into account to the first order through Equation 6.11 and the bias factor is solved for numerically. The result is shown in Table 6.4. The estimate of $b(z = 1) \sim 2.2$ in the combined sample agrees with the result from the redshift-space distortion analysis in § 6.4.3. In Figure 61(a) we show the bias estimates for the CDFN and CLASXS+CDFN samples. The best-fit model from C05 qualitatively agrees with the X-ray results, but the bias of the combined X-ray sample is slightly higher, as expected from their

Table 6.4. Bias evolution and dark matter halo mass

CLASXS			CLASXS+CDFN		
$< z >$	b	$Log_{10}(M/M_{\odot})$	$< z >$	b	$Log_{10}(M/M_{\odot})$
0.44	1.83 ± 0.29	12.9 ± 0.2	0.45	1.41 ± 0.09	12.50 ± 0.09
0.90	1.41 ± 0.50	12.1 ± 0.4	0.92	2.20 ± 0.16	12.72 ± 0.08
1.27	1.83 ± 0.61	12.2 ± 0.4	1.26	2.12 ± 0.43	12.43 ± 0.22
2.00	4.18 ± 0.62	12.7 ± 0.1	2.07	4.15 ± 0.79	12.69 ± 0.18

higher correlation functions.

The simplest model for bias evolution is that the AGNs are formed at high redshift, and evolve according to the continuity equation (Nusser & Davis 1994; Fry 1996). The model is some times called the *conserving model* or the *test particle model*. By normalizing the bias to $z = 0$, the model can be written as

$$b(z) = 1 + (b_0 - 1)/D(z). \tag{6.16}$$

This model is shown in Figure 61(a) as dash-dotted line. The model produces a bias evolution which is slightly too shallow at high redshifts. The correlation function evolution based on this model is also shown in Figure 59, where it underpredicts the observed ξ. This model predicts a decrease of correlation function at high redshift, which is not true based on our results and that of the 2dF. This implies that the bulk of the AGNs observed in the local universe are unlikely to have formed at $z \gg 2$. On the other hand, this is consistent with the idea that the high redshift quasars

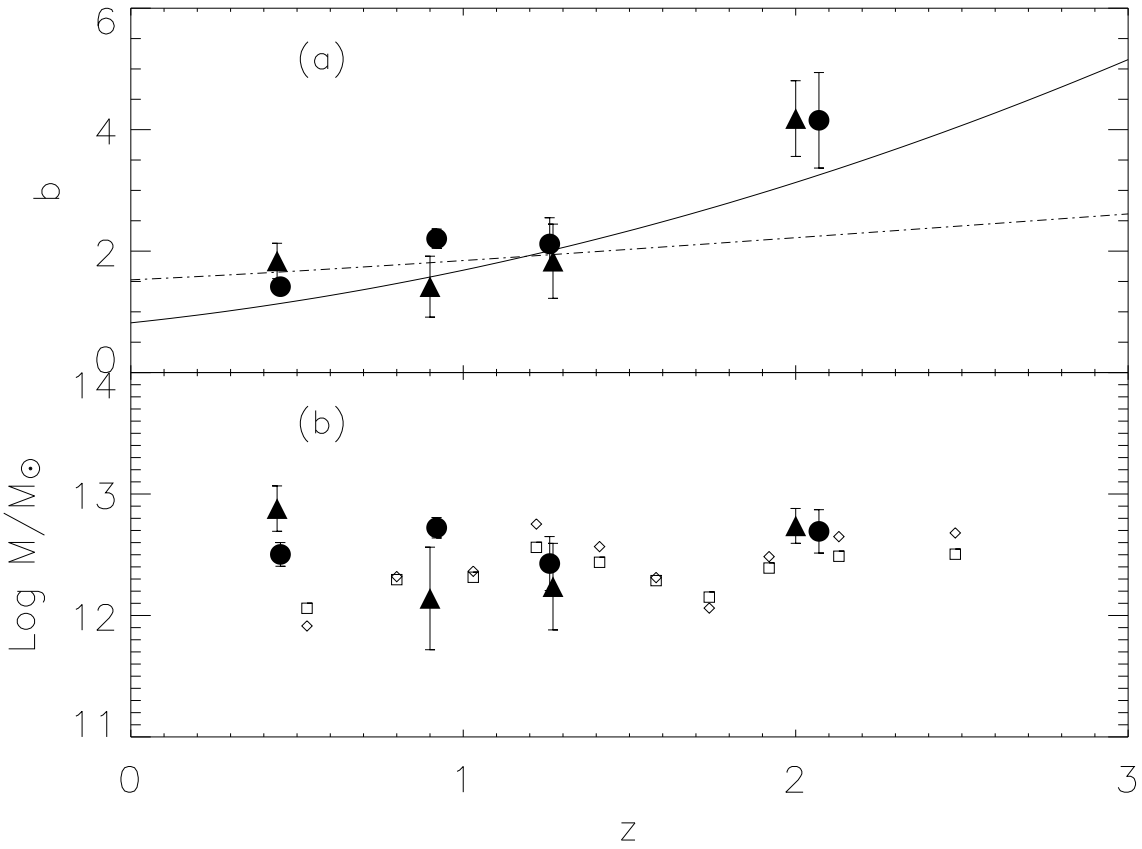

Figure 61: (a) bias evolution.The symbols have the same meaning as in Figure 59. The solid line is the best-fit from C04. Dash-dotted line shows the linear bias evolution model. (b). The mass of host halo of the X-ray sources corresponding to the bias in panel (a).

should have died away long ago.

One of the direct predictions of the CDM structure formation scenario is that the bias is determined by the dark halo mass. Mo & White (1996) found a simple relation between the minimum mass of the dark matter halo and the bias b. By adopting the more general formalism by Sheth, Mo, & Tormen (2001) we can compute the "typical" dark halo mass of the sample. It should be noted that the method assumes that halos are formed through violent collapse or mergers of smaller halos and hence is best applied at large separations, where the halo-halo term dominates the correlation function. This requirement is apparently satisfied by AGNs. Following Sheth, Mo, & Tormen (2001),

$$b(M,z) = 1 + \frac{1}{\sqrt{a}\delta_c(z)}[a\nu^2\sqrt{a} + 0.5\sqrt{a}(a\nu^2)^{(1-c)} - \frac{(a\nu^2)^c}{(a\nu^2)^c + 0.5(1-c)(1-c/2)}], \tag{6.17}$$

where $\nu \equiv \delta_c(z)/\sigma(M,z)$, a = 0.707, c = 0.6. δ_c is the critical overdensity. $\sigma(M,z)$ is the rms density fluctuation in the linear density field and evolves as

$$\sigma(M,z) = \sigma_0(M)D(z), \tag{6.18}$$

where $\sigma_0(M)$ can be obtained from the power spectrum of density perturbation $P(k)$ convolved with a top-hat window function $W(k)$,

$$\sigma_0(M) = \frac{1}{2\pi^2}\int dk k^2 P(k)|W(k)|^2 \tag{6.19}$$

At the scale of interest ($\sim$ 10 Mpc), the power spectrum can be approximated with a power-law, $P(k) \propto k^n$, with $-2 \lesssim n \lesssim -1$ for CDM type spectrum. Integrating

Equation 6.19 gives

$$\sigma_0(M) = \sigma_8 \left(\frac{M}{M_8}\right)^{-(n+3)/6}, \tag{6.20}$$

where M_8 is the mean mass within 8 h^{-1} Mpc.

We can then solve Equation 6.17 for halo mass. The resulting mass is shown in Table 6.4 and Figure 61(b). Consistent with what's been found in C05 for the 2dF, the halo mass does not show any evolution trend with redshift. We found $< \log(M_{halo}/M_\odot) >\sim 12.49 \pm 0.36$, which is consistent with 2dF estimates (C05, Grazian et al. 2004).

The shallow evolution of the clustering amplitude apparently deviates from the clustering evolution of halos, indicating baryonic processes must be of significant importance in the formation and evolution of SMBHs. Using a detailed semi-analytical model (Kauffmann & Haehnelt 2000), where quasars are triggered and fueled by major mergers, Kauffmann & Haehnelt (2002) predicted an evolution of quasar clustering which qualitatively agrees with our result. In other words, our result is consistent with the hierachical merging scenario which includes the physical processes of star bursts.

6.6.2 Linking X-ray luminosity and clustering of AGNs

We have shown that over a very wide range of luminosity, the clustering amplitude of AGNs changes very little. This allows us to put useful constrains on the correlations among X-ray luminosity, blackhole mass M_{BH}, and the dark matter halo M_{halo}.

Using the equivalent width of broad emission lines as mass estimators, Barger et al. (2005) found that the Eddington ratio of broadline AGNs is close to constant. Since the hard X-ray luminosity is an isotropic indicator of the bolometric luminosity, this implies that the blackhole mass is linearly correlated with X-ray luminosity. Barger et al. (2005) found that

$$L_{44} = (\frac{M_{BH}}{10^8\,\mathrm{M}_\odot}), \tag{6.21}$$

where L_{44} is the L_x in units of 10^{44} $\mathrm{erg\,s^{-1}}$. An identical relation is also found at low redshift using a sample of broadline AGNs with mass estimates based on reverberation mapping (Appendix B). The relation, however, is only tested for broadline AGNs. We nevertheless use this relation for non-broadline AGNs by arguing, based on the unified models of AGNs, that this relation should hold because the extinction effect in X-ray band is generally small. Deviations from this relation are expected at low luminosities since many low luminosity AGNs tend to have a low Eddington ratio (Ho 2005).

Blackhole mass have been shown to correlate with velocity dispersion of the spheroidal component of the host galaxies (Gebhardt et al. 2000; Ferrarese & Merritt 2000). This lead to a linear correlation between M_{BH} and the mass of the spherical component. This relation, however, could be different at high redshift (Akiyama 2005). How these relationships translate to the $M_{BH} - M_{halo}$ relation is also unclear and could likely be nonlinear. Ferrarese (2002) showed that M_{BH} – M_{halo} can be modeled with a scaling law

$$\frac{M_{BH}}{10^8\,\mathrm{M}_\odot} = \kappa(\frac{M_{halo}}{10^{12}\,\mathrm{M}_\odot})^\lambda, \tag{6.22}$$

with κ and λ determined by the halo mass profile.

Combining the above and using Equation 6.17, we can calculate the correlation amplitude as a function of X-ray luminosity. In Figure 54 we show the model expectations compared with the observations from CLASXS, CDFN and 2dF. In calculating the bias we have assumed the nonlinear power-law index $n = 3-\gamma$, with the best fit $\gamma = 1.5$. The three lines represent three different halo profiles discussed in Ferrarese (2002). We found that the $L_x - \bar{\xi}(20)$ relation is in fact dominated by the very nonlinear relation between halo mass and correlation amplitude. The difference between different halo profiles is caused mainly by the normalization κ, or roughly the fractional mass of the SMBH, rather than the power-law index λ. One of the important model predictions is that the correlation between X-ray luminosity and clustering is weak below $\sim 10^{43}$ erg s^{-1} and increases rapidly above that. The lack of rapid change of the correlation amplitude indicates the halo mass of AGN cannot be significantly higher than the corresponding threshold. Under the assumed cosmology and bias model, the $L_x - \bar{\xi}(20)$ relation based on the weak lensing derived halo mass profile (Seljak 2002) and the NFW profile (Navarro, Frenk, & White 1997) are consistent with the data, while the isothermal profile predicts a too steep correlation amplitude curve at high luminosity. However, we cannot rule out the latter profile as a reasonable descriptions of the AGN host halo because of the uncertainty in the shape of the correlation function. In Figure 54 we also mark the model dark halo mass corresponding to the Seljak (2002) mass profile. The average correlation amplitude of the combined optical and X-ray sample (dotted-line) corresponds to a halo mass of $\sim 2 \times 10^{12}$ M$_\odot$. While the luminosity in our sample ranges over

five orders of magnitudes, the range of halo mass may be much smaller. The 2dF sample has a high luminosity but has a similar average correlation amplitude as that of the X-ray samples. A possible explanation is that the optical selection technique tends to select sources with a higher Eddington ratio. The correlation amplitude of the CDFN sample at $\sim 10^{41}$ erg s^{-1}, on the other hand, is higher than the model predictions. This is expected because many AGNs with such luminosities are LINERs which are probably accreting with a low radiative efficiency.

It is now clear that the weak luminosity dependence of AGN clustering is consistent with the simplest model based on the observed $L_x - M_{BH}$ and $M_{BH} - M_{halo}$ relations. A large dynamical range in X-ray luminosity, as well as better measurements of correlation function, are needed to better quantify this relation. The luminosity range of the 2dF survey is too small and the optical selection method is also likely biased to high Eddington ratio sources. By increasing our current CLASXS field by a factor of a few will be helpful in better determine the luminosity dependence of AGN clustering, and to put tighter constrains on AGN hosts.

6.6.3 Blackhole mass and the X-ray luminosity evolution

We look again at the M_{BH}–M_{halo} relation in the light of the mass estimates of the dark matter halos from *Chandra* samples. If the Ferrarese (2002) relation is independent of redshift, the nearly constant dark halo mass implies little evolution for the blackhole mass. On the other hand, strong luminosity evolution is seen since $z = 1.2$ in hard X-ray selected AGNs (Barger et al. 2005). This implies a systematic

decrease of the ensemble Eddington ratio with cosmic time. Barger et al. (2005) showed that the characteristic luminosity of hard X-ray selected AGNs

$$L^{\star} = L_0(\frac{1+z}{2})^a, \tag{6.23}$$

where $\log(L_0/\,\mathrm{erg\,s^{-1}}) = 44.11$ and $a = 3.2$ for $z < 1.2$. If the typical blackhole mass does not change with redshift, the observed luminosity evolution can lead to the ensemble Eddington ratio increasing by a factor of ~ 10 from $z = 0$ to $z = 1$. It is hard to understand such a change of the typical Eddington ratio with redshift. One possibility is that a large number of highly obscured and possibly Compton thick AGNs at $z \sim 1$ are missed in the *Chandra* surveys (e.g. Worsley et al. 2005), leading to the observed strong luminosity evolution.

Alternatively, instead of M_{BH}–M_{halo} being independent of redshift, the M_{BH}–v_c could be unchanged with cosmic time, as suggested by Shields et al. (2003). This is theoretically attractive because the feedback regulated growth of blackholes implies a constant M_{BH}–v_c relation (Wyithe & Loeb 2003, WL model hereafter):

$$M_{BH} = 1.9 \times 10^8\,\mathrm{M_\odot} \left(\frac{\eta F_q}{0.07}\right) \left(\frac{v_c}{350\ \mathrm{km\ s^{-1}}}\right)^5, \tag{6.24}$$

where η and F_q are the Eddington ratio and the feedback fraction of the acretion energy returned to the galaxy respectively. This implies that $M_{BH} - M_{halo}$ is in fact a function of redshift:

$$M_{BH}(M_{halo}, z) = \epsilon \left(\frac{M_{halo}}{10^{12}\,\mathrm{M_\odot}}\right)^{2/3} g(z)^{5/6}(1+z)^{5/2}, \tag{6.25}$$

where $g(z)$ is close to unity, and is definded as

$$g = \frac{\Omega_m}{\Omega_m^z}\frac{\Delta_c}{10\pi^2},$$

$$\Delta_c = 18\pi^2 + 82d - 39d^2, d = \Omega_m^z - 1.$$

Croom et al. (2005) showed that this model could lead to a close to constant Eddington ratio in the 2dF sample if the optical luminosity is used to compare with the derived M_{BH}. Since the correlation function is only a weak function of luminosity, as we have demonstrated in § 6.4.5, it is better to estimate the evolution of the Eddington ratio using the characteristic mass of the blackholes from the WL model, and the characteristic luminosity from Equation 6.23. In Figure 62, we show the derived ensemble Eddington ratio, assuming the dark halo mass to be constant and log $(< M_{halo}/M_\odot >) \sim 12.4$. (we adopt the normalization of the WL model so that it matches the prediction of M_{BH} – M_{halo} with a NWF type of halo profile. However, the choice of this normalization is not crucial). In the figure, we see a factor of ~ 2.5 change in the ensemble Eddington ratio from $z = 0$ to $z = 1.2$. This change, however, is smaller than the typical scatter in both the luminosity and halo mass.

6.6.4 Comparison with normal galaxies

We now compare our clustering results with those for normal galaxies. Using the Sloan Digital Sky Survey First Data Release, Wake et al. (2004) found that the clustering of narrow-line AGNs in the redshift range $0.055 < z < 0.2$, selected using emission-line flux ratios, have the same correlation amplitude as normal galaxies. Our samples are not a very good probe at these redshifts, and the best clustering analysis at a comparable redshift for normal galaxies is from DEEP2 (Coil et al.

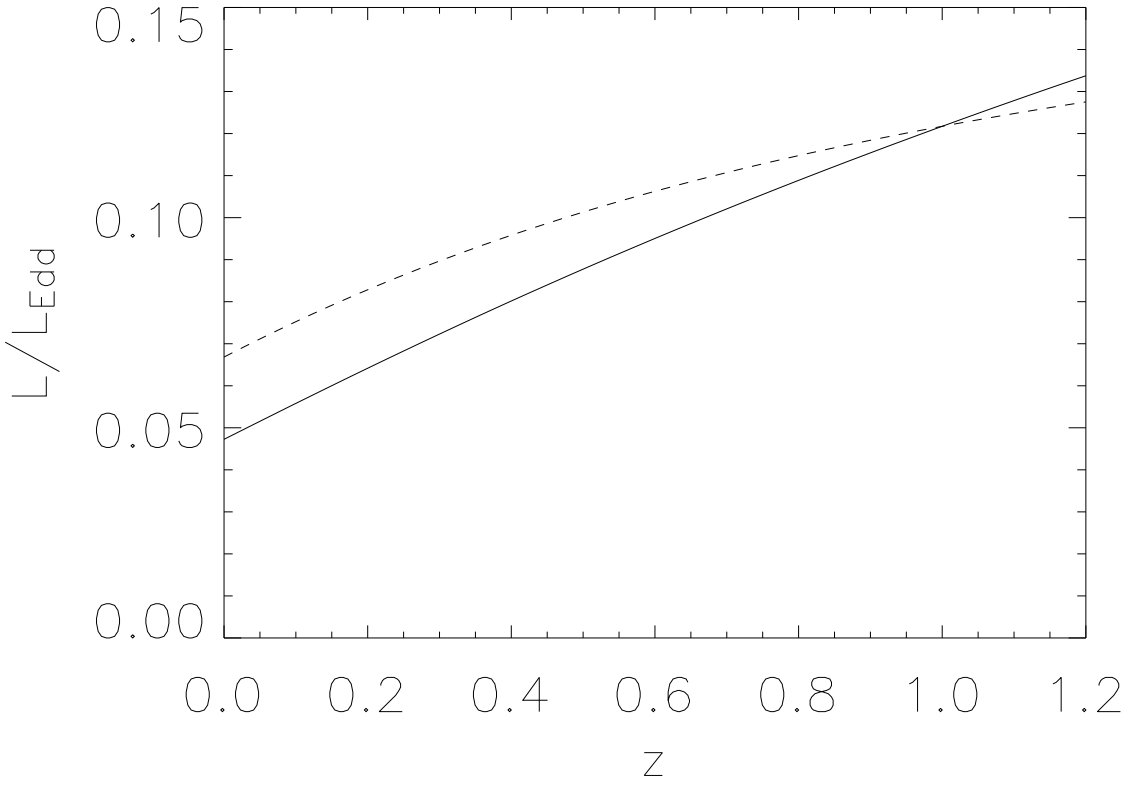

Figure 62: Evolution of Eddington ratio. Solid line: Using the luminosity function from Barger et al. (2005). Dashed line: using luminosity function from Ueda et al. (2001) at $z < 1.2$.

2004). At effective redhsift $z_{eff} \sim 1$, they found $r_0 = 3.19 \pm 0.51$ h^{-1} Mpc, and $\gamma = 1.68 \pm 0.07$, which translates to $\bar{\xi}(20) \sim 0.1$. The correlation amplitude from CLASXS at $z = 0.9$ is $\bar{\xi}(20) \sim 0.33^{+0.20}_{-0.16}$. Considering the redshift-space distortion ($\xi(s)/\xi(r) \sim 1.4$ at $z \sim 1$), the clustering of AGNs in CLASXS field is marginally consistent with the clustering of normal galaxies in DEEP2, but probably larger. On the other hand, the clustering amplitude in the CDFN at a similar redshift is significantly higher, but we cannot rule out the possibility that the stronger clustering is a result of cosmic variance. At higher redshifts, the best estimate for galaxy clustering is from the so called "Lyman break galaxies", named after the technique by which they are found. Adelberger et al. (1998) found, at a typical $z \sim 3$, these galaxies tend to have similar correlation function as galaxies in the local universe, indicating they are highly biased tracers of the large scale structure. In the ΛCDM cosmology, these authors found $b = 4.0 \pm 0.7$. This is very similar to the bias found in the highest bin of our *Chandra* fields (mainly from the CLASXS field), which has a median redshift of ~ 2.0. If we extrapolate the bias of the X-ray sources to $z = 3$, the bias of X-ray sources should be $\sim 5 - 7$, higher than that of Lymann break galaxies.

6.7 Conclusion

In this Chapter we study the clustering and evolution of clustering of *Chandra* selected AGNs with optically identified AGNs from the 0.4 deg^2 *Chandra* contiguous survey of the Lockman Hole Northwest region, CLASXS. The size of field is large

enough to produce a fair sample of X-ray selected AGNs. We supplement our study by employing the published data of the CDFN, which uses exactly the same optical follow-up instrumentation and allows an estimate of correlation functions and systematic errors in both samples in a consistent way. The very similar LogN-LogS of CLASXS and CDFN also suggests that cosmic variance should not be important when the CDFN is included in the analysis. The very deep CDFN gives a better probe of the correlation function at small separations. A total of 233 non-stellar sources from CLASXS and 252 sources from CDFN are used in this study. Correlation function are computed in the redshift-space for both samples. For the whole sample, we have also performed an analysis using the projected correlation. Though noisier and restricted by the angular size of the field, the method is not affected by the redshift-space distortion, which allows us to quantify the effect.

We summarize our results as follows:

- We calculated the redshift-space correlation function for sources with $0.1 < z < 3.0$ in both the CLASXS and CDFN fields, assuming constant clustering in comoving coordinates. We found a 6.7σ clustering for pairs within $s < 20$ Mpc in the CLASXS field. The real-space correlation function over scales from 3 Mpc$< s < 200$ Mpc is found to be a power-law with $\gamma = 1.6^{+0.4}_{-0.3}$ and $s_0 = 8.05^{+1.4}_{-1.5}$ Mpc. The redshift-space correlation function for CDFN on scales of 1 Mpc$< s < 100$ Mpc is found to have similar correlation length $s_0 = 8.55^{+0.75}_{-0.74}$ Mpc, but the slope is shallower ($\gamma = 1.3 \pm 0.1$). The power-law slope in both fields tends to be shallower at small separations.

- We study the projected correlation function of both CLASXS and CDFN. The best-fit parameters for the real-space correlation functions are found to be $r_0 = 8.1^{+1.2}_{-2.2}$ Mpc, $\gamma = 2.1 \pm 0.5$ for CLASXS field, and $r_0 = 5.8^{+1.0}_{-1.5}$ Mpc, $\gamma = 1.38^{+0.12}_{-0.14}$ for CDFN field. Our result for the CDFN shows perfect agreement with the published results from Gilli et al. (2004). Fitting the combined data from both fields gives $r_0 = 6.1^{+0.4}_{-1.0}$ Mpc and $\gamma = 1.47^{+0.07}_{-0.10}$.

- Comparing the redshift- and real-space correlation function of the combined CLASXS and CDFN fields, we found the redshift distortion parameter $\beta = 0.4 \pm 0.2$ at an effective redshift $z = 0.94$. Under the assumption of ΛCDM cosmology, this implies a bias parameter $b \approx 2.04 \pm 1.02$ for the X-ray selected AGN.

- We tested whether the clustering of the X-ray sources is dependent on the X-ray spectra in the CLASXS field. Using a hardness ratio cut at $HR = 0.7$, we found no significant difference in clustering between hard and soft sources. This agrees with previous claims.

- With the large dynamic range in X-ray luminosity, we found very weak correlation between X-ray luminosity and clustering amplitude. We show that the data agrees with the expectations of the simplest model based on observations that connects the X-ray luminosity with the dark matter halo mass.

- We studied the evolution of the clustering using the redshift-space correlation function in 4 redshift intervals from ranging from 0.1 and 3.0. We found only a

mild evolution of AGN clustering in both CLASXS and CDFN samples. This qualitatively agrees with the results based on optically selected quasars from 2dF survey. The X-ray samples, however, show an equal or higher correlation amplitude than that of the 2dF sample. This again shows the correlation amplitude is insensitive to luminosity.

- We estimate the evolution of bias by comparing the observed clustering amplitude with expectations of the linear evolution of density fluctuations. The result shows that the bias increases rapidly with redshift ($b(z = 0.44) = 1.83$ and $b(z = 2.0) = 4.18$ in CLASXS field). This agrees with the findings from 2dF.

- Using the bias evolution model for dark halos from Sheth, Mo & Tormen (2001), we estimated the characteristic mass of AGNs in each redshift interval. We found the mass of the dark halo changes very little with redshift. The average halo mass is found to be log $(M_{halo}/M_{\odot}) \sim 12.4$.

Our results have demonstrated that deep X-ray surveys are a very powerful tool in probing large scale structure at $z \sim 0.5 - 2$. The higher spatial density and much better completeness compared to current optical surveys allows us to study clustering on scales only accessible to very large optical surveys such as the 2dF and the SDSS. Good quality optical identifications and redshift measurements are critical for the clustering analysis. This is best achieved by the high spatial resolution of *Chandra*, which provides accurate enough positions for unambiguous identifications. Since our results on the evolution of AGN clustering could still be affected by a small

number of large scale structures, as seen in Chandra Deep Field South, which also might be the cause of higher clustering amplitude at $z \sim 1$ in CDFN field, larger fields are still needed to improve the measurements.

Chapter 7

Conclusions

In this dissertation, I have presented the observation and analysis of the moderate deep 0.4 $\deg^2$ contiguous CLASXS survey. The X-ray sources are rigorously followed-up with large optical telescopes *Keck* and *Subaru*. The survey is so far the largest *Chandra* deep survey with high level of redshift completeness. The highlights from this work are:

- The number counts of hard X-ray selected AGNs at $\sim 10^{-14}$ erg cm^{-2} s^{-1} is better determined. The result agrees in general with other serendipitous surveys. Combined with the results from CDFN and ASCA observations, the 2-8 keV CXB is resolved within the error margin of the CXB itself.

- The flat spectra sources dominates the AGNs only at 2–8 keV fluxes below 10^{-14} erg cm^{-2} s^{-1}. This is why the hard X-ray sources were not detected in large numbers in pre-*Chandra* X-ray missions.

- Many of the bright sources show variability in X-ray.

- A 6.7σ clustering is detected using the point sources in CLASXS which have redshift measurements. The correlation function of the CLASXS sample agrees with that found in CDFN. The correlation amplitude from the X-ray survey agrees with that found using optical selected quasars.

- The correlation function does not depend strongly on the X-ray luminosity.
- The clustering evolution of the X-ray selected AGNs is measured for the first time using spatial correlation function. The clustering amplitude in comoving coordinate only show mild evolution.
- AGNs are biased tracers of the large scale structure. The bias increase very fast with redshift.

From the X-ray luminosity function derived from this and other large *Chandra* survey, Barger et al. (2005) conclude that, in the redshift range $0 \lesssim z \lesssim 1.2$, the luminosity of AGNs drop steadily with redshift. The AGN activity seems to quite down, just like star formation. On the other hand, the typical dark halo mass inferred from clustering seem to be rather stable over a wide range of redshifts and luminosity. This seem to be at odds with the the picture of pure gravitational collapse, where the density contrast determines the formation of galaxies or cluster of galaxies. The implication is that the growth of SMBH must has gone through some highly non-linear process, dominated by gas dynamics, and feedback processes from star formation and AGN activity.

We have shown that even with a field as small as ours, we are able to estimated the redshift distortion at $z \sim 1$. The importance of this parameter cannot be overstated, because it carries direct information of the mass density at high redshift. Only optical surveys like the 2dF and SDSS have achieved this. This result shows the potential of X-ray selected AGNs in the study of cosmology.

X-ray deep surveys are very powerful in finding AGNs in large numbers. This provides unique opertunity to study both AGNs and cosmology with large samples of X-ray selected AGNs. To achieve the same signal-to-noise ratio as the 2dF, a survey with similar depth as ours would only need to be a few square degrees. The advantage of *Chandra* is that it can provide enough accuracy for optical identification, but it not as powerful as *XMM-Newton*. The X-ray telescopes studied for the near future will mostly focus on spectroscopy rather than imaging, *Chandra* probably will be the only telescope to have the capability.

An alternative approach to the clustering of AGNs is to use powerful telescopes such as *XMM* and obtain redshift through photometric redshift. The identification is still the biggest problem for sources dimmer than $R = 24$. Dim sources have to be identified with the help of other AGN features. As most of the dim sources are optical normal, the task is hard. Photometric redshift can constrain redhsifts of known normal galaxies to a norminal $\delta z \sim 0.1$. It is unclear how this method perform on AGNs. If a wide field survey to reach a hundred sources per square degree, the optical magnitude of most of the sources at such flux level are well correlated with their X-ray flux. The identification at these magnitudes will be unique. Such surveys over a large field will improve significantly on the clustering of AGNs.

Appendix A

CLASXS X-ray Catalog

This appendix includes the CLASXS X-ray catalog. The line-to-line description of the catalog can be found in Chapter 3.

In Table A.1, we list the source positions, fluxes, and hardness ratios. In Table A.2, we list the source net counts, effective exposures, and detection information.

Table A.1: Basic properties

Column 1: Source number used in the catalog. The numbers correspond to ascending order of right ascension.

Column 2: Source name follows the IAU convention and should read CXC-CLASXS, plus the name given in the table.

Columns 3 − 4: The X-ray position, corrected for the aspect errors of the telescope, if applicable, and for the general astrometric solution by comparing with the optical images (see § 3.2.3). For sources with multiple detections in the three bands and the 9 observations, the best position is taken.

Columns 5 − 6: Statistical error of the X-ray position quoted from the *wavdetect* lists.

Columns 7 − 9 : X-ray fluxes in the soft, hard, and full bands in units of 10^{-15} erg cm^{-2} s^{-1} . If a source is detected in multiple observations, and if there are more than one observation in which the source effective area is more than 80% of the effective area at the aim point, then the mean flux is used; otherwise, the flux

from the observation that has the largest effective area is used. The errors quoted are the 1σ upper and lower limits, using the approximations from Gehrels (1986). For any source detected in one band but with a very weak signal in another, the background subtracted flux could be negative. In this case, only the upper limit is quoted.

Columns 10: Hardness ratio. The upper or lower limit is listed for a source with no net extracted photons in the soft or hard bands.

Table A.2: Additional Properties

Column 1: Source number.

Columns 2–4: Net counts in the soft, hard, and full bands. If a source is detected in multiple observations, then the observation in which the source has the largest effective area (see Column 8) is used. As in Table 2a, for the sources with negative counts, only the upper limits are listed.

Columns 5–7: Effective exposure time in each of the three energy bands from the exposure map.

Columns 8–9: Detection information. Column 8 is the LHNW field number where the source has the largest effective area. Column 9 lists the LHNW field numbers (each digit represents a field number) in which the source has been detected in at least one of the three bands. Sources with multiple detections are necessary for the detection of variability (see § 3.6).

Table A.1. Main *Chandra* Catalog: Basic Source Properties

#	name	α_{2000}	δ_{2000}	$\Delta\alpha('')$	$\Delta\delta('')$	$f_{0.4-2.0keV}$	$f_{2.0-8.0keV}$	$f_{0.4-8.0keV}$	HR
1	J103055.6+573319	10 30 55.62	+57 33 20.0	1.283	0.493	$3.8^{+0.79}_{-1.1}$	$3.7^{+1.4}_{-2.5}$	$7.5^{+1.4}_{-1.9}$	0.299
2	J103059.6+573844	10 30 59.68	+57 38 44.2	1.287	0.350	$1.8^{+0.52}_{-0.75}$	$5.3^{+2.1}_{-2.5}$	$5^{+1.3}_{-1.9}$	0.691
3	J103103.3+573650	10 31 03.32	+57 36 50.4	0.845	0.560	$3.2^{+0.68}_{-0.92}$	$13^{+3}_{-3.9}$	$16^{+2.5}_{-3.3}$	0.870
4	J103106.0+573748	10 31 06.06	+57 37 48.4	0.977	0.517	$3.7^{+0.82}_{-1.3}$	$0.74^{+0.67}_{-0.94}$	$4.3^{+0.91}_{-1.2}$	0.090
5	J103111.8+573521	10 31 11.83	+57 35 21.7	0.849	0.456	$3.2^{+0.87}_{-1.1}$	$0.91^{+0.54}_{-1.6}$	$4^{+1}_{-1.1}$	0.118
6	J103122.0+573134	10 31 22.06	+57 31 34.6	0.834	0.243	$3.7^{+0.81}_{-0.89}$	$19^{+3.9}_{-4.6}$	$21^{+3.1}_{-3.8}$	1.040
7	J103123.5+574309	10 31 23.55	+57 43 09.3	0.488	0.241	$15^{+1.2}_{-1.3}$	$25^{+2.9}_{-3.3}$	$40^{+2.6}_{-2.7}$	0.375
8	J103126.5+573743	10 31 26.59	+57 37 43.4	0.262	0.176	$1.2^{+0.39}_{-0.66}$	$4.9^{+1.8}_{-2.7}$	$6.5^{+1.8}_{-2}$	0.882
9	J103129.8+573712	10 31 29.84	+57 37 12.4	0.378	0.150	$2.5^{+0.55}_{-0.83}$	$11^{+2.7}_{-3.6}$	$14^{+2.4}_{-2.9}$	0.951
10	J103129.8+573243	10 31 29.86	+57 32 43.6	0.687	0.215	$0.34^{+0.23}_{-0.43}$	$0.78^{+0.69}_{-1.4}$	$1.8^{+0.81}_{-1.1}$	0.566
11	J103131.2+573934	10 31 31.26	+57 39 34.7	0.281	0.115	$16^{+1.9}_{-2.2}$	$8^{+2.3}_{-3}$	$24^{+2.6}_{-3.1}$	0.183
12	J103131.4+574334	10 31 31.49	+57 43 34.9	1.071	0.511	$2.3^{+0.62}_{-0.77}$	$5.2^{+1.7}_{-2.7}$	$6.5^{+1.4}_{-2}$	0.563
13	J103133.4+574211	10 31 33.41	+57 42 11.1	0.611	0.294	$2^{+0.53}_{-0.86}$	$5.6^{+1.8}_{-3.1}$	$9.3^{+2}_{-2.2}$	0.651
14	J103133.8+573909	10 31 33.83	+57 39 09.6	0.435	0.136	$3^{+0.72}_{-1.1}$	$1.2^{+0.83}_{-1.3}$	$4.1^{+0.93}_{-1.3}$	0.153
15	J103134.4+574223	10 31 34.41	+57 42 24.0	0.443	0.166	$14^{+1.1}_{-1.2}$	$23^{+2.8}_{-3.2}$	$35^{+2.4}_{-2.6}$	0.335
16	J103134.7+574446	10 31 34.71	+57 44 46.3	0.412	0.188	$27^{+2.1}_{-2.3}$	$48^{+5.6}_{-6.2}$	$76^{+4.8}_{-5.4}$	0.468
17	J103135.3+574304	10 31 35.35	+57 43 04.5	1.113	0.367	$3.5^{+0.98}_{-1.2}$	$0.34^{+0.27}_{-1.3}$	$2.6^{+0.7}_{-0.89}$	0.052
18	J103136.0+573312	10 31 36.01	+57 33 12.0	0.818	0.189	$1.3^{+0.6}_{-0.75}$	$0.56^{+0.47}_{-1.5}$	$2^{+0.73}_{-1.1}$	0.162
19	J103136.4+574312	10 31 36.48	+57 43 12.7	0.695	0.523	$0.47^{+0.23}_{-0.58}$	$4.5^{+1.7}_{-3.8}$	$6.7^{+2.2}_{-2.7}$	1.738
20	J103137.0+573200	10 31 37.08	+57 32 00.6	0.561	0.319	$8.1^{+1.4}_{-1.5}$	<2.1	$7.9^{+1.2}_{-1.6}$	<0.109
21	J103137.7+574004	10 31 37.75	+57 40 04.4	0.238	0.195	$1.1^{+0.34}_{-0.61}$	$7.8^{+2.7}_{-2.8}$	$8.2^{+2}_{-2.4}$	1.385
22	J103139.2+574027	10 31 39.22	+57 40 28.0	0.394	0.206	$2.9^{+0.67}_{-0.97}$	$2.2^{+1.1}_{-1.6}$	$5.3^{+1.2}_{-1.4}$	0.247
23	J103139.9+573838	10 31 39.92	+57 38 38.8	0.364	0.107	$2.4^{+0.6}_{-0.8}$	$4^{+1.3}_{-2.5}$	$6.8^{+1.4}_{-1.8}$	0.447
24	J103140.4+574235	10 31 40.47	+57 42 35.8	0.490	0.209	$4.3^{+0.75}_{-1}$	$16^{+3.1}_{-4.4}$	$20^{+2.7}_{-3.4}$	0.835
25	J103140.7+573103	10 31 40.79	+57 31 03.5	1.334	0.333	$5^{+1.5}_{-2.2}$	<0.0028	$0.76^{+0.25}_{-0.26}$	0.001
26	J103140.9+574116	10 31 40.94	+57 41 16.2	0.611	0.220	$3.2^{+1}_{-1.3}$	<0.082	$1.4^{+0.44}_{-0.63}$	0.019
27	J103141.1+573741	10 31 41.13	+57 37 41.7	0.286	0.112	$3.1^{+0.75}_{-0.92}$	$2.7^{+1.1}_{-2}$	$6.3^{+1.2}_{-1.7}$	0.279
28	J103142.0+573015	10 31 42.04	+57 30 15.8	0.460	0.229	$9.4^{+1.2}_{-1.5}$	$26^{+4}_{-5.4}$	$35^{+3.7}_{-4}$	0.656
29	J103143.3+573252	10 31 43.33	+57 32 52.6	0.146	0.057	$41^{+2.6}_{-2.7}$	$92^{+7.6}_{-8.4}$	$130^{+6.5}_{-7}$	0.555
30	J103143.3+573157	10 31 43.38	+57 31 57.6	0.425	0.155	$13^{+1.7}_{-1.8}$	$14^{+2.9}_{-4.2}$	$27^{+2.9}_{-3.4}$	0.317
31	J103143.7+574903	10 31 43.77	+57 49 03.9	0.974	0.560	$1.9^{+0.64}_{-1}$	$5.3^{+2.3}_{-3.6}$	$7.1^{+1.8}_{-2.8}$	0.653
32	J103145.8+573401	10 31 45.85	+57 34 01.8	0.227	0.099	$4.6^{+0.83}_{-1}$	$27^{+4.7}_{-5.2}$	$32^{+3.8}_{-4.6}$	1.163
33	J103145.8+573344	10 31 45.89	+57 33 44.7	0.436	0.204	$2.9^{+0.65}_{-0.87}$	$6.7^{+1.8}_{-3.1}$	$9.4^{+1.9}_{-2}$	0.566
34	J103145.9+573047	10 31 45.90	+57 30 48.0	0.621	0.614	$1.4^{+0.43}_{-0.77}$	$2.1^{+1.2}_{-1.9}$	$3.1^{+1.1}_{-1.2}$	0.417
35	J103146.0+574038	10 31 46.00	+57 40 38.8	0.240	0.125	$2.4^{+0.54}_{-0.84}$	$15^{+3.3}_{-4.3}$	$15^{+2.7}_{-3.2}$	1.222
36	J103147.6+573104	10 31 47.65	+57 31 04.1	0.517	0.259	$2.6^{+0.76}_{-1.1}$	$0.4^{+0.33}_{-1.3}$	$2.2^{+0.64}_{-0.9}$	0.074
37	J103148.1+574339	10 31 48.18	+57 43 39.8	0.915	0.420	$2.1^{+0.69}_{-0.71}$	<3.5	$4.5^{+1.2}_{-1.7}$	<0.444
38	J103148.2+574231	10 31 48.20	+57 42 31.2	0.364	0.334	$1.3^{+0.45}_{-0.61}$	$8.2^{+2.7}_{-3.1}$	$8.4^{+1.9}_{-2.8}$	1.265
39	J103148.3+574009	10 31 48.36	+57 40 09.6	0.264	0.122	$0.52^{+0.25}_{-0.43}$	$13^{+3.3}_{-4.6}$	$13^{+3.1}_{-3.4}$	3.772
40	J103150.5+574247	10 31 50.57	+57 42 47.4	0.256	0.161	$14^{+1.1}_{-1.2}$	$23^{+2.8}_{-3.1}$	$37^{+2.4}_{-2.6}$	0.468
41	J103150.9+574349	10 31 50.92	+57 43 49.1	0.286	0.148	$18^{+1.3}_{-1.4}$	$21^{+2.6}_{-2.9}$	$39^{+2.4}_{-2.6}$	0.349
42	J103154.8+574520	10 31 54.89	+57 45 20.9	0.725	0.390	$1.7^{+0.49}_{-0.73}$	$13^{+3.2}_{-4.1}$	$14^{+2.9}_{-3.2}$	1.396
43	J103155.3+574350	10 31 55.30	+57 43 50.7	0.497	0.247	$1.8^{+0.37}_{-0.45}$	$20^{+3}_{-3.4}$	$21^{+2.5}_{-2.8}$	1.847
44	J103156.3+574723	10 31 56.39	+57 47 23.2	0.476	0.209	$5.8^{+0.73}_{-0.83}$	$7.8^{+1.6}_{-2}$	$13^{+1.4}_{-1.6}$	0.224
45	J103156.6+573846	10 31 56.63	+57 38 46.0	0.078	0.033	$12^{+1.4}_{-1.4}$	$64^{+6.4}_{-7.3}$	$75^{+5.4}_{-6.2}$	1.079
46	J103157.3+574752	10 31 57.39	+57 47 52.1	0.372	0.127	$15^{+1.5}_{-1.9}$	$17^{+3.2}_{-3.9}$	$31^{+2.9}_{-3.4}$	0.342
47	J103158.7+573100	10 31 58.77	+57 31 00.1	0.500	0.265	$4.7^{+0.99}_{-1.1}$	$3.3^{+1.2}_{-2.2}$	$8^{+1.4}_{-1.8}$	0.229
48	J103159.9+574411	10 31 59.99	+57 44 11.3	0.363	0.193	$3.7^{+0.51}_{-0.59}$	$100^{+7}_{-7.5}$	$97^{+6}_{-6.4}$	3.374
49	J103201.3+573639	10 32 01.33	+57 36 39.3	0.281	0.203	$0.53^{+0.24}_{-0.46}$	$2.5^{+1.1}_{-2.3}$	$2.8^{+1.1}_{-1.5}$	0.986
50	J103201.5+574415	10 32 01.52	+57 44 15.8	0.469	0.192	$7.7^{+0.79}_{-0.87}$	$18^{+2.4}_{-2.8}$	$24^{+2.1}_{-2.2}$	0.579
51	J103202.0+573607	10 32 02.01	+57 36 07.5	0.169	0.118	$1.5^{+0.46}_{-0.66}$	$3.3^{+1.6}_{-1.7}$	$5^{+1.2}_{-1.7}$	0.548
52	J103202.9+573208	10 32 02.95	+57 32 08.7	0.161	0.074	$25^{+2}_{-2.2}$	$47^{+5.4}_{-6.1}$	$72^{+4.9}_{-4.9}$	0.480

Table A.1—Continued

#	name	α_{2000}	δ_{2000}	$\Delta\alpha('')$	$\Delta\delta('')$	$f_{0.4-2.0keV}$	$f_{2.0-8.0keV}$	$f_{0.4-8.0keV}$	HR
53	J103203.7+575211	10 32 03.79	+57 52 11.4	0.734	0.322	$5.1^{+0.92}_{-1}$	$21^{+3.7}_{-4.9}$	$28^{+3.4}_{-3.9}$	0.878
54	J103203.8+573459	10 32 03.82	+57 34 59.1	0.378	0.161	$1.1^{+0.39}_{-0.57}$	$2.2^{+0.97}_{-2.1}$	$3.3^{+0.89}_{-1.5}$	0.533
55	J103205.0+573554	10 32 05.10	+57 35 54.9	0.433	0.150	$0.24^{+0.15}_{-0.42}$	$2.8^{+1.7}_{-2}$	$2.8^{+1.2}_{-1.9}$	2.031
56	J103205.1+573600	10 32 05.11	+57 36 00.0	0.381	0.174	$0.68^{+0.32}_{-0.59}$	$0.58^{+0.5}_{-1.3}$	$0.9^{+0.55}_{-0.66}$	0.267
57	J103205.1+573854	10 32 05.12	+57 38 54.9	0.201	0.224	$0.43^{+0.24}_{-0.41}$	$2.2^{+1.3}_{-1.7}$	$2.4^{+0.94}_{-1.6}$	1.060
58	J103205.8+574427	10 32 05.83	+57 44 27.5	0.464	0.154	$5.7^{+0.76}_{-0.86}$	$4.9^{+1.2}_{-1.6}$	$10^{+1.2}_{-1.3}$	0.098
59	J103206.5+574817	10 32 06.51	+57 48 17.4	0.533	0.149	$3.2^{+0.65}_{-0.97}$	$5.6^{+1.8}_{-2.5}$	$7.9^{+1.4}_{-2.1}$	0.464
60	J103206.7+574546	10 32 06.74	+57 45 46.5	0.431	0.121	$4.9^{+0.64}_{-0.73}$	$7.7^{+1.5}_{-1.9}$	$12^{+1.4}_{-1.5}$	0.447
61	J103208.3+574122	10 32 08.38	+57 41 22.9	0.314	0.092	$0.39^{+0.28}_{-0.34}$	$0.74^{+0.66}_{-1.2}$	$1.8^{+0.65}_{-1.2}$	0.499
62	J103209.7+573850	10 32 09.77	+57 38 50.3	0.118	0.082	$5.5^{+0.66}_{-0.74}$	$11^{+1.9}_{-2.2}$	$17^{+1.6}_{-1.8}$	0.548
63	J103210.0+575012	10 32 10.08	+57 50 12.5	0.675	0.182	$1.4^{+0.5}_{-0.58}$	$4.2^{+1.8}_{-2.2}$	$6.2^{+1.5}_{-1.9}$	0.688
64	J103210.8+574300	10 32 10.82	+57 43 00.9	0.583	0.393	$0.8^{+0.35}_{-0.53}$	$2.2^{+1.3}_{-1.7}$	$3.4^{+1.2}_{-1.4}$	0.651
65	J103211.9+573228	10 32 11.96	+57 32 28.6	0.249	0.232	$0.42^{+0.21}_{-0.5}$	$1.1^{+0.69}_{-2}$	$1.7^{+0.7}_{-1.3}$	0.654
66	J103212.7+574534	10 32 12.70	+57 45 34.2	0.516	0.106	$1.5^{+0.37}_{-0.47}$	$1.3^{+0.85}_{-1.7}$	$2.1^{+0.52}_{-0.67}$	<0.359
67	J103213.2+573420	10 32 13.27	+57 34 20.6	0.162	0.101	$2.1^{+0.49}_{-0.75}$	$13^{+3.3}_{-3.5}$	$14^{+2.7}_{-2.8}$	1.208
68	J103213.5+574826	10 32 13.53	+57 48 26.2	0.316	0.271	$1.5^{+0.64}_{-1.1}$	$13^{+4.3}_{-7.2}$	$13^{+3.6}_{-5.9}$	1.586
69	J103213.7+575249	10 32 13.72	+57 52 49.1	0.689	0.366	$3.9^{+0.72}_{-1}$	$20^{+3.6}_{-5.1}$	$22^{+3.1}_{-3.8}$	1.052
70	J103214.3+573228	10 32 14.33	+57 32 28.6	0.359	0.220	$3.3^{+0.7}_{-1}$	$4.5^{+1.7}_{-2.4}$	$7.4^{+1.5}_{-1.9}$	0.382
71	J103214.7+575246	10 32 14.75	+57 52 47.0	0.571	0.275	$5.1^{+0.67}_{-0.76}$	$25^{+3.3}_{-3.8}$	$30^{+2.8}_{-3.1}$	1.235
72	J103214.9+575350	10 32 14.97	+57 53 50.2	1.374	0.450	$0.43^{+0.31}_{-0.43}$	$3.3^{+1.9}_{-2.7}$	$2.5^{+1.1}_{-2.2}$	1.442
73	J103215.1+574749	10 32 15.16	+57 47 49.8	0.487	0.138	$0.26^{+0.17}_{-0.38}$	$5.9^{+2.6}_{-2.9}$	$7.1^{+2.4}_{-2.7}$	3.403
74	J103215.4+573247	10 32 15.45	+57 32 47.4	0.494	0.290	$0.59^{+0.28}_{-0.46}$	$8^{+2.7}_{-3.6}$	$8.4^{+2}_{-3.3}$	2.307
75	J103215.8+574926	10 32 15.89	+57 49 26.1	0.098	0.039	$87^{+4}_{-4.3}$	$91^{+7.5}_{-8.4}$	$180^{+7.3}_{-7.6}$	0.315
76	J103216.7+574615	10 32 16.76	+57 46 15.6	0.253	0.084	$2.4^{+0.56}_{-0.77}$	14^{+3}_{-4}	$16^{+2.6}_{-3.4}$	1.167
77	J103217.1+575143	10 32 17.10	+57 51 43.7	0.779	0.372	$1.5^{+0.45}_{-0.64}$	$8.5^{+2.7}_{-3}$	$9.3^{+2.1}_{-2.6}$	1.165
78	J103218.1+573830	10 32 18.12	+57 38 30.1	0.180	0.089	$6.5^{+0.62}_{-0.68}$	$6.4^{+1.1}_{-1.3}$	$13^{+1.1}_{-1.2}$	0.289
79	J103219.1+573945	10 32 19.12	+57 39 45.8	0.382	0.389	$0.35^{+0.24}_{-0.42}$	<7.3	<5	<3.193
80	J103220.0+573420	10 32 20.03	+57 34 20.9	0.305	0.183	$0.29^{+0.2}_{-0.33}$	$9.7^{+3}_{-4.1}$	$8.8^{+2.3}_{-3.8}$	4.764
81	J103220.2+573211	10 32 20.23	+57 32 11.5	0.353	0.219	$6.2^{+1}_{-1.2}$	$8.8^{+2.5}_{-2.8}$	$14^{+2}_{-2.5}$	0.396
82	J103220.3+575658	10 32 20.37	+57 56 58.4	0.890	0.655	$1.9^{+0.68}_{-0.73}$	$9.1^{+3.1}_{-3.9}$	$9.7^{+2.6}_{-2.8}$	1.013
83	J103220.8+574921	10 32 20.89	+57 49 21.8	0.606	0.193	$1.5^{+0.47}_{-0.69}$	<2.8	$2.7^{+0.88}_{-1.3}$	<0.476
84	J103221.2+573754	10 32 21.21	+57 37 54.9	0.381	0.107	$0.97^{+0.45}_{-0.84}$	<0.076	$0.59^{+0.25}_{-0.61}$	0.045
85	J103221.7+573356	10 32 21.80	+57 33 56.4	0.235	0.136	$1.5^{+0.44}_{-0.74}$	$5.9^{+2}_{-2.9}$	$6.4^{+1.6}_{-2.1}$	0.846
86	J103222.1+573654	10 32 22.19	+57 36 54.7	0.121	0.101	$3.2^{+0.5}_{-0.58}$	$7.2^{+1.5}_{-1.8}$	$10^{+1.3}_{-1.5}$	0.515
87	J103222.2+573934	10 32 22.29	+57 39 34.8	0.144	0.090	$4.3^{+0.48}_{-0.54}$	$15^{+2.3}_{-2.7}$	$16^{+1.4}_{-1.5}$	0.498
88	J103222.8+573528	10 32 22.81	+57 35 28.5	0.249	0.232	$0.44^{+0.25}_{-0.42}$	<3.7	$1.5^{+0.77}_{-1.6}$	<1.568
89	J103222.9+575551	10 32 22.90	+57 55 51.0	0.654	0.240	$24^{+1.6}_{-1.7}$	$31^{+3.3}_{-3.7}$	$56^{+3.1}_{-3.3}$	0.409
90	J103222.9+573648	10 32 22.94	+57 36 48.5	0.226	0.169	$0.98^{+0.35}_{-0.69}$	$0.77^{+0.69}_{-1}$	$1.5^{+0.56}_{-0.93}$	0.252
91	J103223.3+573836	10 32 23.38	+57 38 36.8	0.325	0.000	$0.43^{+0.23}_{-0.47}$	$1^{+0.59}_{-1.9}$	$2.4^{+0.9}_{-1.2}$	0.581
92	J103224.1+573301	10 32 24.19	+57 33 01.4	0.460	0.191	$2.9^{+0.48}_{-0.57}$	$6.3^{+1.4}_{-1.8}$	$8.8^{+1.2}_{-1.4}$	0.454
93	J103224.6+575950	10 32 24.66	+57 59 50.2	1.120	0.454	$5.7^{+1.2}_{-1.3}$	$4.3^{+1.7}_{-2.7}$	$8.7^{+1.8}_{-1.9}$	0.245
94	J103224.9+573153	10 32 25.00	+57 31 53.8	1.075	0.384	$7.4^{+0.78}_{-0.86}$	$26^{+3.2}_{-3.6}$	$33^{+2.6}_{-2.8}$	1.375
95	J103225.0+572814	10 32 25.08	+57 28 14.2	0.716	0.321	$14^{+1.5}_{-1.8}$	$24^{+4.4}_{-4.4}$	$38^{+3.7}_{-3.9}$	0.451
96	J103226.0+574851	10 32 26.06	+57 48 51.7	0.491	0.134	$1.6^{+0.51}_{-0.76}$	$0.87^{+0.53}_{-1.5}$	$2.3^{+0.75}_{-0.94}$	0.193
97	J103227.0+573831	10 32 27.01	+57 38 31.4	0.210	0.114	$1.2^{+0.4}_{-0.61}$	$3.8^{+1.4}_{-2.6}$	$6^{+1.6}_{-1.8}$	0.735
98	J103227.1+574548	10 32 27.14	+57 45 48.1	0.419	0.121	$0.82^{+0.31}_{-0.52}$	$5.5^{+1.9}_{-2.9}$	$6.2^{+1.5}_{-2.4}$	1.318
99	J103227.9+573822	10 32 27.97	+57 38 22.5	0.059	0.041	$33^{+1.3}_{-1.4}$	$51^{+3.2}_{-3.4}$	$82^{+2.9}_{-3}$	0.490
100	J103228.3+575109	10 32 28.39	+57 51 09.3	0.461	0.239	$4.8^{+0.69}_{-0.79}$	$4^{+1.1}_{-1.5}$	$9.1^{+1.1}_{-1.3}$	0.331
101	J103228.6+575446	10 32 28.68	+57 54 46.1	0.860	0.460	$1.9^{+0.65}_{-0.71}$	$9.1^{+2.9}_{-3.7}$	$11^{+2.5}_{-3}$	0.994
102	J103229.0+573456	10 32 29.03	+57 34 56.2	0.584	0.216	$7.8^{+0.83}_{-0.92}$	$9.4^{+1.7}_{-2.1}$	$17^{+1.6}_{-1.7}$	0.266
103	J103229.0+574100	10 32 29.06	+57 41 00.2	0.343	0.252	$0.92^{+0.4}_{-0.46}$	$7.3^{+2.6}_{-2.9}$	$7.9^{+1.8}_{-2.8}$	1.505
104	J103229.4+574129	10 32 29.41	+57 41 29.1	0.394	0.347	$4.7^{+0.71}_{-0.83}$	$1.8^{+0.69}_{-1}$	$5.8^{+0.8}_{-0.91}$	0.308

Table A.1—Continued

#	name	α_{2000}	δ_{2000}	$\Delta\alpha('')$	$\Delta\delta('')$	$f_{0.4-2.0keV}$	$f_{2.0-8.0keV}$	$f_{0.4-8.0keV}$	HR
105	J103229.9+572939	10 32 29.94	+57 29 39.2	1.193	0.645	$1.4^{+0.51}_{-0.61}$	$8.9^{+2.8}_{-3.7}$	$10^{+2.1}_{-3.3}$	1.261
106	J103230.8+575539	10 32 30.89	+57 55 39.8	0.992	0.271	$6.2^{+1.1}_{-1.5}$	$4.1^{+1.7}_{-2.4}$	$9.9^{+1.8}_{-2.1}$	0.225
107	J103232.9+574915	10 32 32.91	+57 49 15.6	0.203	0.165	$0.8^{+0.38}_{-0.66}$	$0.25^{+0.18}_{-1.4}$	$1.2^{+0.56}_{-0.63}$	0.127
108	J103233.3+574811	10 32 33.35	+57 48 11.0	0.256	0.136	$0.51^{+0.23}_{-0.47}$	$4.5^{+1.9}_{-2.5}$	$4.4^{+1.4}_{-2}$	1.633
109	J103233.5+573720	10 32 33.59	+57 37 20.4	0.267	0.144	$1.5^{+0.32}_{-0.4}$	$6.5^{+1.5}_{-1.9}$	$6.9^{+1.2}_{-1.4}$	1.103
110	J103233.6+574353	10 32 33.69	+57 43 53.6	0.154	0.066	$5.4^{+0.65}_{-0.74}$	$11^{+1.9}_{-2.3}$	$17^{+1.7}_{-1.8}$	0.673
111	J103233.8+575624	10 32 33.81	+57 56 24.4	0.311	0.224	$2^{+0.65}_{-0.75}$	<5.1	$4.5^{+1.5}_{-1.7}$	<0.627
112	J103234.1+575622	10 32 34.18	+57 56 22.8	0.433	0.299	$3.5^{+0.96}_{-1.1}$	$1.1^{+0.71}_{-1.7}$	$4.6^{+1.2}_{-1.3}$	0.130
113	J103234.6+574210	10 32 34.68	+57 42 10.5	0.458	0.225	$0.4^{+0.22}_{-0.41}$	$6.3^{+2.6}_{-2.8}$	$5^{+1.8}_{-2.3}$	2.582
114	J103236.1+580033	10 32 36.17	+58 00 33.4	0.441	0.212	$31^{+2.7}_{-2.8}$	$21^{+3.7}_{-4.8}$	$53^{+4.1}_{-4.4}$	0.230
115	J103236.8+574743	10 32 36.81	+57 47 43.7	0.172	0.133	$0.96^{+0.37}_{-0.61}$	$1.1^{+0.74}_{-1.4}$	$2.7^{+0.88}_{-1}$	0.338
116	J103236.8+573521	10 32 36.87	+57 35 21.2	0.602	0.353	$2.8^{+0.85}_{-0.95}$	$0.22^{+0.17}_{-1.1}$	$2.2^{+0.58}_{-0.73}$	0.043
117	J103237.3+573339	10 32 37.31	+57 33 39.3	0.714	0.698	$2.1^{+0.65}_{-1.3}$	<0.06	$0.97^{+0.38}_{-0.46}$	0.020
118	J103237.5+574837	10 32 37.57	+57 48 37.5	0.196	0.193	$0.95^{+0.36}_{-0.64}$	$0.87^{+0.52}_{-1.6}$	$1.9^{+0.58}_{-1.1}$	0.284
119	J103237.5+575209	10 32 37.59	+57 52 09.3	0.575	0.471	$2.1^{+0.44}_{-0.54}$	$3.5^{+1.1}_{-1.5}$	$6^{+1}_{-1.2}$	0.509
120	J103239.3+575311	10 32 39.38	+57 53 11.6	0.210	0.070	$40^{+1.9}_{-2}$	$63^{+4.6}_{-5}$	$100^{+4.2}_{-4.4}$	0.435
121	J103239.4+574035	10 32 39.42	+57 40 35.5	0.157	0.170	$15^{+1.1}_{-1.2}$	$24^{+2.8}_{-3.1}$	$40^{+2.5}_{-2.6}$	0.574
122	J103239.4+573737	10 32 39.46	+57 37 37.3	0.683	0.362	$1.4^{+0.33}_{-0.42}$	$3.4^{+1.1}_{-1.4}$	$4.5^{+0.88}_{-1.1}$	0.432
123	J103240.0+573520	10 32 40.02	+57 35 20.5	0.771	0.339	$1.4^{+0.32}_{-0.41}$	$2.8^{+1.7}_{-3.3}$	$3.8^{+0.77}_{-0.94}$	<0.534
124	J103240.1+574512	10 32 40.11	+57 45 12.6	0.268	0.120	$1.6^{+0.51}_{-0.69}$	$1.6^{+0.85}_{-1.6}$	$3.1^{+0.95}_{-1}$	0.296
125	J103240.2+575205	10 32 40.20	+57 52 05.5	0.470	0.270	$1.8^{+0.58}_{-0.61}$	$4.9^{+1.5}_{-2.8}$	$7.3^{+1.5}_{-2.1}$	0.660
126	J103241.4+574807	10 32 41.47	+57 48 07.2	0.143	0.136	$1.4^{+0.47}_{-0.72}$	$1.3^{+0.9}_{-1.3}$	$2.8^{+0.97}_{-1}$	0.285
127	J103241.7+574332	10 32 41.78	+57 43 32.9	0.267	0.145	$0.11^{+0.094}_{-0.29}$	$14^{+4.2}_{-4.9}$	$12^{+3.2}_{-5.3}$	13.67
128	J103242.0+574005	10 32 42.02	+57 40 05.7	0.481	0.381	$0.76^{+0.23}_{-0.31}$	$21^{+3.3}_{-3.8}$	$20^{+2.8}_{-3.2}$	4.792
129	J103242.3+574426	10 32 42.32	+57 44 26.4	0.804	0.359	$6.5^{+0.73}_{-0.82}$	$13^{+2.1}_{-2.4}$	$20^{+1.8}_{-2}$	0.591
130	J103242.5+573006	10 32 42.58	+57 30 06.8	1.069	0.355	$3.3^{+1}_{-1.4}$	<5.6	$6.6^{+1.8}_{-3}$	<0.444
131	J103242.5+575620	10 32 42.58	+57 56 20.8	0.349	0.173	$7.9^{+1.3}_{-1.7}$	$5.3^{+1.7}_{-2.9}$	$14^{+2.2}_{-2.3}$	0.226
132	J103242.8+573159	10 32 42.83	+57 31 59.7	0.783	0.486	$3.1^{+0.77}_{-0.9}$	<9.6	$8.7^{+1.9}_{-2.6}$	<0.714
133	J103242.8+574503	10 32 42.84	+57 45 03.5	0.075	0.046	$12^{+1.3}_{-1.7}$	$26^{+4.5}_{-4.7}$	$37^{+3.8}_{-3.8}$	0.556
134	J103243.4+574503	10 32 43.45	+57 45 03.1	0.588	0.240	$15^{+1.1}_{-1.2}$	$25^{+2.8}_{-3.2}$	$40^{+2.5}_{-2.7}$	0.442
135	J103243.7+574834	10 32 43.79	+57 48 34.1	0.369	0.176	$0.6^{+0.29}_{-0.49}$	<1.7	$2.1^{+0.8}_{-1.3}$	<0.677
136	J103243.8+573558	10 32 43.80	+57 35 58.6	0.460	0.245	$1.2^{+0.31}_{-0.4}$	$3.7^{+1.1}_{-1.5}$	$4.6^{+0.91}_{-1.1}$	1.268
137	J103244.2+575415	10 32 44.22	+57 54 15.7	0.329	0.363	$0.84^{+0.35}_{-0.62}$	$5.9^{+2.6}_{-2.8}$	$4.5^{+1.4}_{-2.5}$	1.351
138	J103244.9+574949	10 32 44.94	+57 49 49.5	0.262	0.149	$2.4^{+0.46}_{-0.56}$	$5.2^{+1.4}_{-1.8}$	$6.7^{+1.1}_{-1.3}$	0.242
139	J103245.0+573841	10 32 45.04	+57 38 41.2	0.558	0.196	$1.1^{+0.3}_{-0.39}$	$4.1^{+1.2}_{-1.6}$	$4.9^{+0.99}_{-1.2}$	1.112
140	J103246.5+575851	10 32 46.54	+57 58 51.8	0.438	0.156	$9.6^{+1.4}_{-1.6}$	$14^{+3.4}_{-3.7}$	$24^{+2.9}_{-3.2}$	0.405
141	J103247.0+575510	10 32 47.03	+57 55 10.5	0.591	0.135	$2.8^{+0.72}_{-1.1}$	<1.9	$3.8^{+1}_{-1.4}$	<0.231
142	J103247.7+575829	10 32 47.76	+57 58 29.3	0.671	0.276	$1.6^{+0.54}_{-0.84}$	<3.5	$3.9^{+1.3}_{-1.7}$	<0.551
143	J103247.9+575624	10 32 47.98	+57 56 24.2	0.386	0.180	$3.9^{+0.91}_{-1.1}$	$7^{+2.2}_{-3.3}$	$10^{+2.1}_{-2.3}$	0.468
144	J103248.2+573627	10 32 48.23	+57 36 27.4	0.428	0.261	$1^{+0.37}_{-0.55}$	$2.3^{+1.1}_{-1.9}$	$3.2^{+1.1}_{-1.2}$	0.552
145	J103248.6+574156	10 32 48.66	+57 41 56.5	0.253	0.084	$0.84^{+0.24}_{-0.32}$	$8.2^{+1.9}_{-2.4}$	$7.5^{+1.4}_{-1.7}$	12.12
146	J103248.6+574128	10 32 48.70	+57 41 28.8	0.430	0.216	$2.6^{+0.35}_{-0.41}$	$19^{+2.2}_{-2.5}$	$21^{+1.9}_{-2}$	0.935
147	J103248.7+573820	10 32 48.73	+57 38 20.8	0.435	0.145	$2.2^{+0.71}_{-0.76}$	$0.82^{+0.48}_{-1.5}$	$3^{+0.81}_{-1}$	0.141
148	J103250.2+580217	10 32 50.23	+58 02 17.5	0.878	0.332	$6.8^{+1.3}_{-1.4}$	$6.4^{+2.5}_{-2.6}$	$13^{+2}_{-2.6}$	0.289
149	J103250.5+573819	10 32 50.59	+57 38 19.2	0.501	0.000	$0.32^{+0.23}_{-0.29}$	<2.2	$1.2^{+0.64}_{-1.4}$	<1.313
150	J103251.2+575832	10 32 51.26	+57 58 32.1	0.223	0.136	$11^{+1.6}_{-1.9}$	$10^{+2.9}_{-3.4}$	$21^{+2.8}_{-2.9}$	0.277
151	J103252.1+574547	10 32 52.16	+57 45 47.4	0.152	0.067	$2.8^{+0.46}_{-0.54}$	$5.5^{+1.3}_{-1.7}$	$8.2^{+1.1}_{-1.3}$	0.578
152	J103252.5+574427	10 32 52.58	+57 44 27.4	0.263	0.155	$1.2^{+0.45}_{-0.71}$	$0.57^{+0.5}_{-1.1}$	$2^{+0.64}_{-0.91}$	0.169
153	J103253.0+575357	10 32 53.09	+57 53 57.1	0.419	0.181	$0.65^{+0.3}_{-0.57}$	$5^{+1.7}_{-3.6}$	$5.5^{+1.9}_{-2.3}$	1.448
154	J103253.2+574116	10 32 53.28	+57 41 16.1	0.579	0.276	$2.8^{+0.41}_{-0.48}$	$2.5^{+0.7}_{-0.93}$	$5.6^{+0.71}_{-0.81}$	0.445
155	J103253.9+574149	10 32 53.91	+57 41 49.6	0.268	0.121	$7.5^{+0.51}_{-0.55}$	$12^{+1.3}_{-1.4}$	$20^{+1.1}_{-1.2}$	0.373
156	J103254.5+575426	10 32 54.59	+57 54 26.8	0.000	0.000	$0.4^{+0.26}_{-0.57}$	$0.33^{+0.24}_{-1.8}$	$0.82^{+0.41}_{-0.97}$	0.261

Table A.1—Continued

#	name	α_{2000}	δ_{2000}	$\Delta\alpha('')$	$\Delta\delta('')$	$f_{0.4-2.0keV}$	$f_{2.0-8.0keV}$	$f_{0.4-8.0keV}$	HR
157	J103256.1+574816	10 32 56.16	+57 48 16.9	0.114	0.073	$5.4^{+0.48}_{-0.52}$	$17^{+1.8}_{-2}$	$21^{+1.5}_{-1.6}$	0.667
158	J103257.5+574746	10 32 57.57	+57 47 47.0	0.187	0.099	$2^{+0.61}_{-0.84}$	$0.54^{+0.48}_{-1}$	$2.4^{+0.68}_{-0.91}$	0.115
159	J103257.7+574425	10 32 57.72	+57 44 25.1	0.177	0.192	$0.95^{+0.41}_{-0.66}$	$0.32^{+0.25}_{-1.3}$	$1.1^{+0.55}_{-0.62}$	0.135
160	J103258.0+572802	10 32 58.07	+57 28 02.0	1.130	0.374	$1.7^{+0.49}_{-0.79}$	$4.8^{+2.1}_{-2.5}$	$5.9^{+1.7}_{-1.8}$	0.670
161	J103259.1+575125	10 32 59.18	+57 51 25.2	0.775	0.619	$1.5^{+0.47}_{-0.88}$	$0.75^{+0.68}_{-1.1}$	$1.9^{+0.64}_{-1}$	0.179
162	J103259.7+575321	10 32 59.71	+57 53 21.2	0.229	0.137	$2^{+0.58}_{-0.89}$	$2.3^{+1.4}_{-1.7}$	$4.4^{+1.3}_{-1.4}$	0.346
163	J103301.7+574650	10 33 01.75	+57 46 51.0	0.000	0.000	$0.79^{+0.35}_{-0.52}$	$2^{+1.1}_{-1.9}$	$2.3^{+0.82}_{-1.4}$	0.606
164	J103301.9+574557	10 33 01.96	+57 45 57.7	0.230	0.107	$0.56^{+0.27}_{-0.46}$	<2.6	$1.9^{+0.71}_{-1.6}$	<0.976
165	J103302.4+572834	10 33 02.48	+57 28 34.6	0.538	0.296	$15^{+1.1}_{-1.2}$	$29^{+3.1}_{-3.4}$	$45^{+2.7}_{-2.9}$	0.605
166	J103302.7+580240	10 33 02.79	+58 02 40.7	0.592	0.311	$6.1^{+0.99}_{-1.4}$	$19^{+3.9}_{-5.1}$	$26^{+3.4}_{-3.9}$	0.720
167	J103303.6+575938	10 33 03.70	+57 59 38.2	0.326	0.337	$0.81^{+0.32}_{-0.64}$	$5.4^{+2.2}_{-3.2}$	$6.2^{+1.8}_{-2.5}$	1.290
168	J103303.9+573948	10 33 03.92	+57 39 48.8	0.140	0.201	$0.84^{+0.32}_{-0.54}$	$3.1^{+1.2}_{-2.4}$	$2.4^{+1}_{-1.3}$	0.795
169	J103304.1+573850	10 33 04.20	+57 38 50.5	0.253	0.168	$0.85^{+0.35}_{-0.62}$	$0.38^{+0.31}_{-1.2}$	$1.4^{+0.47}_{-0.85}$	0.161
170	J103305.4+574910	10 33 05.46	+57 49 10.0	0.229	0.143	$0.94^{+0.19}_{-0.23}$	$23^{+2.5}_{-2.7}$	$21^{+2}_{-2.2}$	2.723
171	J103307.0+574231	10 33 07.06	+57 42 31.2	0.487	0.201	$4^{+0.42}_{-0.47}$	$3.9^{+0.76}_{-0.93}$	$7.7^{+0.72}_{-0.8}$	0.137
172	J103308.0+573458	10 33 08.08	+57 34 58.1	0.348	0.104	$0.75^{+0.28}_{-0.5}$	$7.2^{+2.2}_{-3.2}$	$5.5^{+1.7}_{-2}$	1.708
173	J103308.3+574112	10 33 08.36	+57 41 12.1	0.382	0.213	$0.47^{+0.2}_{-0.47}$	$2.4^{+1}_{-2.3}$	$2.1^{+0.96}_{-1.2}$	1.025
174	J103308.3+573502	10 33 08.38	+57 35 02.0	0.255	0.136	$0.74^{+0.28}_{-0.49}$	$8.9^{+2.3}_{-3.8}$	$4.9^{+1.7}_{-2}$	2.048
175	J103308.8+575718	10 33 08.83	+57 57 18.9	0.171	0.069	$4.3^{+0.89}_{-1}$	$10^{+2.9}_{-3.3}$	$16^{+2.6}_{-2.8}$	0.590
176	J103308.8+573831	10 33 08.85	+57 38 31.7	0.098	0.046	$7.3^{+0.67}_{-0.74}$	$5^{+0.97}_{-1.2}$	$12^{+0.98}_{-1.1}$	0.106
177	J103308.8+575424	10 33 08.88	+57 54 24.6	0.201	0.106	$0.59^{+0.31}_{-0.64}$	$1.8^{+1.2}_{-2.4}$	2.9^{+1}_{-2}	0.712
178	J103309.3+575805	10 33 09.35	+57 58 05.7	0.272	0.121	$0.99^{+0.36}_{-0.69}$	$5.9^{+2.1}_{-3.5}$	$5.6^{+1.8}_{-2.4}$	1.199
179	J103310.3+574850	10 33 10.31	+57 48 50.5	0.851	0.513	$0.29^{+0.14}_{-0.22}$	$11^{+2.3}_{-3.1}$	$10^{+2.1}_{-2.6}$	5.120
180	J103310.3+575831	10 33 10.39	+57 58 31.4	0.371	0.108	$0.68^{+0.3}_{-0.63}$	<2.9	$2.2^{+1.2}_{-1.4}$	<0.915
181	J103310.5+572911	10 33 10.53	+57 29 11.3	0.711	0.300	$7.1^{+0.86}_{-0.97}$	$2^{+0.71}_{-1}$	$7.5^{+0.88}_{-0.99}$	0.180
182	J103310.5+574132	10 33 10.57	+57 41 32.5	0.283	0.146	$3^{+0.35}_{-0.4}$	$5.9^{+0.98}_{-1.2}$	$8.6^{+0.84}_{-0.93}$	0.316
183	J103310.9+574850	10 33 10.95	+57 48 50.4	0.803	0.428	$0.39^{+0.18}_{-0.22}$	9.4^{+2}_{-3}	$7^{+1.5}_{-2.2}$	3.591
184	J103312.2+574015	10 33 12.29	+57 40 15.6	0.243	0.135	$0.12^{+0.1}_{-0.27}$	$6.5^{+2.4}_{-3.6}$	$5.5^{+2}_{-3.1}$	6.845
185	J103312.3+574752	10 33 12.36	+57 47 52.2	0.165	0.108	<0.066	$8.3^{+3.1}_{-4.4}$	$5.7^{+2.6}_{-3.6}$	>13.56
186	J103312.5+573426	10 33 12.57	+57 34 26.8	0.133	0.066	$7.7^{+0.81}_{-0.9}$	$21^{+3.9}_{-4.5}$	$32^{+3.5}_{-3.5}$	0.551
187	J103312.6+574203	10 33 12.64	+57 42 03.8	0.202	0.108	<0.25	$16^{+2.3}_{-2.6}$	$15^{+3.3}_{-4.2}$	10.08
188	J103312.8+574202	10 33 12.89	+57 42 02.2	0.580	0.130	$0.29^{+0.21}_{-0.29}$	$6.3^{+2}_{-3.6}$	$7.2^{+1.9}_{-3.1}$	3.287
189	J103312.9+573406	10 33 12.97	+57 34 06.2	0.251	0.112	$2.6^{+0.45}_{-0.54}$	$5.3^{+1.3}_{-1.7}$	$7.7^{+1.1}_{-1.3}$	0.632
190	J103313.2+574026	10 33 13.21	+57 40 26.5	0.308	0.108	$0.51^{+0.23}_{-0.44}$	<2	$1.7^{+0.68}_{-1.3}$	<0.833
191	J103313.3+575141	10 33 13.38	+57 51 41.2	0.327	0.204	$1.3^{+0.47}_{-0.7}$	$2.8^{+1.2}_{-2.6}$	$3.3^{+0.97}_{-1.8}$	0.548
192	J103313.4+580452	10 33 13.45	+58 04 52.5	1.664	0.594	$1.5^{+0.48}_{-0.77}$	<9.4	$4.1^{+1.3}_{-2.7}$	<1.265
193	J103313.6+573554	10 33 13.62	+57 35 54.4	0.190	0.088	$2.5^{+0.6}_{-0.74}$	$2.9^{+1.1}_{-2}$	$5.4^{+1.1}_{-1.4}$	0.338
194	J103314.2+580037	10 33 14.26	+58 00 37.7	0.506	0.181	$2^{+0.57}_{-0.83}$	$5.9^{+2.4}_{-2.6}$	$8.4^{+2}_{-2.2}$	0.695
195	J103314.3+572544	10 33 14.34	+57 25 44.6	1.253	0.565	$0.98^{+0.42}_{-0.52}$	<3.7	$2.7^{+0.9}_{-1.7}$	<0.833
196	J103314.4+575701	10 33 14.46	+57 57 01.3	0.166	0.176	$1.1^{+0.44}_{-0.83}$	$0.49^{+0.4}_{-1.5}$	$1.7^{+0.74}_{-0.88}$	0.166
197	J103314.6+573449	10 33 14.65	+57 34 49.3	0.216	0.192	$0.99^{+0.36}_{-0.69}$	$1.6^{+1.1}_{-1.6}$	$2.5^{+1}_{-1.1}$	0.426
198	J103315.2+573959	10 33 15.21	+57 39 59.6	1.100	0.442	$0.37^{+0.19}_{-0.25}$	$0.86^{+0.61}_{-0.84}$	$0.88^{+0.35}_{-0.7}$	0.560
199	J103315.9+575028	10 33 16.00	+57 50 28.7	0.400	0.315	$2.4^{+0.32}_{-0.37}$	$5.1^{+0.95}_{-1.1}$	$7.5^{+0.82}_{-0.92}$	0.240
200	J103316.0+572253	10 33 16.01	+57 22 53.3	1.225	0.458	$2.9^{+0.69}_{-0.84}$	$12^{+3.1}_{-3.8}$	$15^{+2.6}_{-3}$	0.912
201	J103316.1+574244	10 33 16.17	+57 42 44.3	0.413	0.335	<0.16	$5.7^{+1.5}_{-1.9}$	$5.1^{+1.2}_{-1.5}$	10.23
202	J103316.5+572623	10 33 16.56	+57 26 23.9	0.375	0.159	$8.1^{+1.2}_{-1.5}$	$4.8^{+1.5}_{-2.4}$	$13^{+1.8}_{-2}$	0.206
203	J103317.1+575236	10 33 17.14	+57 52 36.5	1.007	0.512	$1.1^{+0.29}_{-0.48}$	$0.75^{+0.54}_{-0.66}$	$2.3^{+0.57}_{-0.66}$	0.218
204	J103317.6+573519	10 33 17.70	+57 35 19.1	0.980	0.448	$5.1^{+0.67}_{-0.77}$	$9^{+1.7}_{-2.1}$	$14^{+1.6}_{-1.7}$	0.705
205	J103318.1+572601	10 33 18.13	+57 26 01.4	0.311	0.105	$18^{+1.7}_{-2}$	$22^{+3.4}_{-4.6}$	$41^{+3.5}_{-3.7}$	0.359
206	J103319.0+575127	10 33 19.01	+57 51 27.2	0.291	0.216	$2.6^{+0.33}_{-0.37}$	$7.5^{+1.2}_{-1.4}$	$9.8^{+0.99}_{-1.1}$	0.659
207	J103319.3+572428	10 33 19.34	+57 24 28.4	0.616	0.617	$1.8^{+0.57}_{-0.69}$	$4.6^{+1.6}_{-2.7}$	$6.3^{+1.6}_{-1.8}$	0.612
208	J103319.3+575808	10 33 19.37	+57 58 09.0	0.099	0.059	$11^{+1.6}_{-1.7}$	$6.8^{+2}_{-2.7}$	$19^{+2.4}_{-2.4}$	0.210

Table A.1—Continued

#	name	α_{2000}	δ_{2000}	$\Delta\alpha('')$	$\Delta\delta('')$	$f_{0.4-2.0keV}$	$f_{2.0-8.0keV}$	$f_{0.4-8.0keV}$	HR
209	J103319.3+573525	10 33 19.39	+57 35 25.4	0.092	0.060	$4.4^{+0.57}_{-0.65}$	$19^{+2.6}_{-3}$	$23^{+2.2}_{-2.4}$	0.654
210	J103319.4+572711	10 33 19.41	+57 27 11.3	0.525	0.177	$2^{+0.56}_{-0.73}$	$5.7^{+1.7}_{-3}$	$7.6^{+1.6}_{-2.1}$	0.663
211	J103319.9+572841	10 33 19.94	+57 28 41.5	0.462	0.136	$3.9^{+0.98}_{-1}$	$1.3^{+0.93}_{-1.2}$	$5.1^{+1.1}_{-1.3}$	0.133
212	J103319.9+574820	10 33 19.99	+57 48 20.7	0.465	0.175	$4.4^{+0.44}_{-0.49}$	$7^{+1.1}_{-1.3}$	$11^{+0.96}_{-1}$	0.356
213	J103320.1+573720	10 33 20.14	+57 37 20.1	0.179	0.075	$2.5^{+0.65}_{-0.87}$	$0.65^{+0.59}_{-0.82}$	$2.8^{+0.64}_{-0.96}$	0.108
214	J103321.1+573857	10 33 21.11	+57 38 57.0	0.199	0.123	$0.77^{+0.34}_{-0.51}$	$0.65^{+0.58}_{-0.97}$	$1^{+0.4}_{-0.83}$	0.259
215	J103321.2+573214	10 33 21.25	+57 32 14.2	0.154	0.075	$22^{+1.1}_{-1.2}$	$25^{+2.2}_{-2.5}$	$47^{+2.1}_{-2.2}$	0.287
216	J103321.4+573335	10 33 21.46	+57 33 35.0	0.229	0.123	<0.042	$1.1^{+1}_{-1.7}$	$1.9^{+0.97}_{-2}$	3.864
217	J103322.2+573259	10 33 22.24	+57 32 59.2	0.514	0.251	$1^{+0.34}_{-0.65}$	$1.1^{+0.7}_{-1.4}$	$2.2^{+0.74}_{-0.99}$	0.304
218	J103322.7+575858	10 33 22.71	+57 58 58.4	0.256	0.084	$0.95^{+0.38}_{-0.74}$	$0.9^{+0.81}_{-1.3}$	$2.3^{+0.9}_{-1.1}$	0.292
219	J103324.3+572445	10 33 24.34	+57 24 45.8	0.322	0.133	$9.4^{+1.3}_{-1.3}$	$21^{+3.9}_{-4.1}$	$30^{+3.3}_{-3.5}$	0.550
220	J103324.5+573754	10 33 24.55	+57 37 54.6	0.260	0.224	$0.46^{+0.25}_{-0.47}$	$0.34^{+0.27}_{-1.3}$	$1.2^{+0.45}_{-0.86}$	0.235
221	J103325.5+575634	10 33 25.51	+57 56 34.4	0.139	0.161	$1.3^{+0.49}_{-0.67}$	$2.5^{+1.5}_{-1.8}$	$4^{+1.2}_{-1.7}$	0.502
222	J103325.5+580038	10 33 25.58	+58 00 38.8	0.338	0.200	$4.7^{+0.97}_{-1.1}$	$12^{+3.3}_{-3.6}$	$18^{+2.7}_{-3.2}$	0.615
223	J103326.1+580120	10 33 26.17	+58 01 20.6	0.251	0.154	$16^{+1.8}_{-2}$	$22^{+3.9}_{-4.9}$	$38^{+3.8}_{-3.8}$	0.383
224	J103326.9+573304	10 33 26.92	+57 33 04.6	0.750	0.319	$0.67^{+0.27}_{-0.52}$	$4.8^{+2.1}_{-2.5}$	$5^{+1.6}_{-2}$	1.358
225	J103327.2+572153	10 33 27.25	+57 21 53.8	1.013	0.372	$6.6^{+1.1}_{-1.5}$	$3.2^{+1.4}_{-2.1}$	$9.8^{+1.6}_{-2}$	0.177
226	J103327.4+573750	10 33 27.46	+57 37 50.3	0.395	0.109	$1.1^{+0.38}_{-0.51}$	$4^{+1.7}_{-2}$	$4.2^{+1.2}_{-1.6}$	0.812
227	J103327.5+573932	10 33 27.51	+57 39 32.5	0.978	0.353	$2.2^{+0.45}_{-0.54}$	$3.7^{+1}_{-1.6}$	$5.7^{+0.99}_{-1.1}$	0.434
228	J103327.6+574904	10 33 27.60	+57 49 04.0	0.287	0.299	$5.2^{+0.55}_{-0.61}$	$8.4^{+1.4}_{-1.6}$	$14^{+1.2}_{-1.3}$	0.341
229	J103328.6+573510	10 33 28.61	+57 35 10.9	0.324	0.174	<0.093	$1.2^{+0.65}_{-2.3}$	$1.8^{+0.75}_{-1.9}$	>2.114
230	J103328.7+573820	10 33 28.70	+57 38 20.9	0.347	0.155	$1.3^{+0.43}_{-0.6}$	<1.8	$2.2^{+0.66}_{-1.1}$	<0.378
231	J103329.2+574708	10 33 29.23	+57 47 08.1	0.488	0.426	$2.1^{+0.31}_{-0.36}$	$5.9^{+1.2}_{-1.5}$	$7.4^{+0.87}_{-0.97}$	1.844
232	J103329.6+575226	10 33 29.68	+57 52 26.6	0.383	0.123	$0.52^{+0.28}_{-0.53}$	$1.7^{+1.2}_{-2}$	$2.6^{+1}_{-1.6}$	0.748
233	J103330.4+574224	10 33 30.50	+57 42 24.1	0.455	0.348	$1.9^{+0.29}_{-0.33}$	$1.7^{+0.5}_{-0.67}$	$3.8^{+0.5}_{-0.57}$	0.228
234	J103331.7+575458	10 33 31.75	+57 54 58.3	0.231	0.107	<0.33	$0.9^{+0.79}_{-1.7}$	$1.5^{+0.69}_{-1.4}$	>0.650
235	J103332.5+573020	10 33 32.54	+57 30 20.1	0.702	0.428	$0.72^{+0.3}_{-0.54}$	$11^{+3.1}_{-4.3}$	$8.2^{+2.4}_{-3.1}$	2.401
236	J103332.6+574111	10 33 32.61	+57 41 12.0	0.579	0.336	$0.1^{+0.086}_{-0.34}$	$9.1^{+2.9}_{-5.1}$	$7.9^{+2.5}_{-4.5}$	10.02
237	J103332.6+575214	10 33 32.67	+57 52 14.7	0.990	0.434	$0.76^{+0.22}_{-0.36}$	$2.7^{+1.1}_{-1.2}$	$3.9^{+0.91}_{-1.1}$	0.787
238	J103332.6+574442	10 33 32.67	+57 44 42.9	0.299	0.130	$0.31^{+0.12}_{-0.17}$	$16^{+2.5}_{-2.9}$	$15^{+2.2}_{-2.6}$	4.085
239	J103332.6+575046	10 33 32.69	+57 50 46.5	0.928	0.234	$0.96^{+0.3}_{-0.36}$	$2.4^{+1}_{-1.2}$	$3.1^{+0.78}_{-0.94}$	0.589
240	J103333.8+574052	10 33 33.84	+57 40 52.9	0.705	0.416	$0.92^{+0.3}_{-0.32}$	$3.3^{+1.1}_{-1.5}$	$4.4^{+1}_{-1.1}$	0.789
241	J103333.8+574027	10 33 33.89	+57 40 27.7	0.874	0.533	$0.26^{+0.15}_{-0.2}$	$3.2^{+1.2}_{-1.8}$	$3.9^{+1.2}_{-1.3}$	2.096
242	J103334.0+573334	10 33 34.02	+57 33 34.7	0.378	0.275	$1^{+0.37}_{-0.59}$	$1.5^{+0.74}_{-1.9}$	$2.4^{+0.81}_{-1.1}$	0.397
243	J103334.0+575601	10 33 34.07	+57 56 01.9	0.000	0.139	$0.43^{+0.22}_{-0.51}$	$8.2^{+2.8}_{-4.3}$	$5.7^{+2.3}_{-2.5}$	2.993
244	J103334.4+575323	10 33 34.46	+57 53 23.8	0.193	0.132	$2.1^{+0.28}_{-0.32}$	$18^{+2}_{-2.2}$	$19^{+1.6}_{-1.8}$	1.555
245	J103335.5+574334	10 33 35.51	+57 43 34.4	0.273	0.112	$1.7^{+0.29}_{-0.34}$	$8.1^{+1.4}_{-1.6}$	$8.6^{+1.1}_{-1.3}$	1.106
246	J103336.2+573223	10 33 36.22	+57 32 23.6	0.656	0.361	$1.2^{+0.54}_{-0.59}$	$0.32^{+0.26}_{-1.2}$	$1.9^{+0.57}_{-0.83}$	0.109
247	J103336.3+573106	10 33 36.33	+57 31 06.9	0.305	0.116	$1^{+0.35}_{-0.54}$	$32^{+5.7}_{-6.3}$	$31^{+4.5}_{-5.8}$	4.443
248	J103337.5+575227	10 33 37.56	+57 52 27.8	1.125	0.296	$0.24^{+0.22}_{-0.29}$	$3.2^{+1.9}_{-2.5}$	$2.1^{+1.2}_{-1.9}$	2.216
249	J103337.9+574238	10 33 37.96	+57 42 38.8	0.138	0.055	$21^{+1.1}_{-1.2}$	$18^{+1.9}_{-2.1}$	$39^{+1.9}_{-1.9}$	0.273
250	J103338.0+575801	10 33 38.09	+57 58 01.4	0.184	0.166	$3.1^{+0.52}_{-0.61}$	$8.9^{+1.8}_{-2.2}$	$12^{+1.5}_{-1.7}$	0.794
251	J103338.1+574544	10 33 38.18	+57 45 44.3	0.059	0.021	$33^{+1.4}_{-1.4}$	$43^{+3}_{-3.2}$	$77^{+2.8}_{-2.9}$	0.348
252	J103338.4+575858	10 33 38.46	+57 58 58.8	0.203	0.225	$0.75^{+0.36}_{-0.62}$	$1.3^{+0.81}_{-2.1}$	$2.5^{+0.86}_{-1.5}$	0.463
253	J103338.8+573201	10 33 38.83	+57 32 01.2	0.567	0.231	$0.76^{+0.37}_{-0.4}$	$8.9^{+2.6}_{-3.6}$	$7^{+1.8}_{-2.8}$	2.041
254	J103339.2+574816	10 33 39.23	+57 48 16.3	0.227	0.162	$0.66^{+0.21}_{-0.32}$	$2.3^{+0.8}_{-1.4}$	$3^{+0.69}_{-1}$	0.766
255	J103339.6+573817	10 33 39.61	+57 38 17.1	0.000	0.123	$0.27^{+0.17}_{-0.38}$	$1.1^{+0.66}_{-2}$	$2^{+0.93}_{-1.2}$	0.882
256	J103340.2+574234	10 33 40.25	+57 42 34.6	0.380	0.204	$1.6^{+0.32}_{-0.48}$	$5^{+1.4}_{-1.5}$	$6.1^{+1.1}_{-1.3}$	0.696
257	J103341.4+574903	10 33 41.41	+57 49 03.1	0.290	0.108	$3^{+0.39}_{-0.44}$	$2.4^{+0.61}_{-0.79}$	$5^{+0.58}_{-0.66}$	0.432
258	J103341.5+572847	10 33 41.55	+57 28 47.8	0.254	0.092	$2.5^{+0.64}_{-0.77}$	$4.3^{+1.7}_{-2}$	$6.7^{+1.3}_{-1.8}$	0.456
259	J103341.5+573644	10 33 41.56	+57 36 44.5	0.110	0.079	$8.1^{+0.74}_{-0.81}$	$2.5^{+0.65}_{-0.84}$	$9.5^{+0.81}_{-0.88}$	0.145
260	J103341.6+574042	10 33 41.62	+57 40 42.4	0.280	0.216	$2.9^{+0.68}_{-0.88}$	$2.1^{+1}_{-1.6}$	$4.6^{+1.1}_{-1.1}$	0.227

Table A.1—Continued

#	name	α_{2000}	δ_{2000}	$\Delta\alpha('')$	$\Delta\delta('')$	$f_{0.4-2.0keV}$	$f_{2.0-8.0keV}$	$f_{0.4-8.0keV}$	HR
261	J103343.6+574044	10 33 43.67	+57 40 44.1	0.135	0.094	$11^{+0.67}_{-0.71}$	$12^{+1.3}_{-1.5}$	$23^{+1.2}_{-1.3}$	0.347
262	J103343.6+572446	10 33 43.67	+57 24 46.7	0.201	0.224	$0.67^{+0.28}_{-0.49}$	$6.1^{+2}_{-3.2}$	$5.9^{+1.9}_{-2.1}$	1.670
263	J103344.7+575118	10 33 44.79	+57 51 18.5	0.660	0.265	$0.98^{+0.28}_{-0.37}$	<2.5	$2^{+0.57}_{-0.84}$	<0.599
264	J103345.0+574910	10 33 45.06	+57 49 10.5	0.085	0.039	$19^{+0.96}_{-1}$	$15^{+1.6}_{-1.7}$	$34^{+1.6}_{-1.6}$	0.293
265	J103345.5+572731	10 33 45.59	+57 27 31.6	0.261	0.129	$1^{+0.38}_{-0.69}$	$0.58^{+0.51}_{-1.1}$	$2.2^{+0.62}_{-1.1}$	0.197
266	J103347.4+573744	10 33 47.46	+57 37 44.7	0.202	0.148	$2.3^{+0.45}_{-0.54}$	$2.1^{+0.77}_{-1.1}$	$4^{+0.69}_{-0.82}$	0.482
267	J103347.9+575036	10 33 47.99	+57 50 36.7	0.238	0.210	$0.94^{+0.32}_{-0.35}$	$1.1^{+0.66}_{-0.81}$	$2.1^{+0.58}_{-0.69}$	0.331
268	J103348.1+574719	10 33 48.14	+57 47 19.6	0.101	0.053	$5.3^{+0.49}_{-0.54}$	$6.7^{+1}_{-1.2}$	$13^{+0.98}_{-1.1}$	0.333
269	J103348.2+575807	10 33 48.28	+57 58 07.1	0.370	0.184	$1.1^{+0.3}_{-0.4}$	$4.9^{+1.4}_{-1.9}$	$6.7^{+1.3}_{-1.5}$	1.075
270	J103348.3+575321	10 33 48.34	+57 53 21.3	0.749	0.285	$1.7^{+0.27}_{-0.32}$	$5.8^{+1.1}_{-1.3}$	$7.5^{+0.91}_{-1}$	0.654
271	J103348.4+575650	10 33 48.42	+57 56 50.7	0.437	0.134	$0.15^{+0.13}_{-0.41}$	$1.4^{+0.79}_{-3}$	$2.9^{+1.5}_{-1.7}$	1.720
272	J103348.6+575049	10 33 48.60	+57 50 49.9	0.295	0.195	$0.62^{+0.22}_{-0.3}$	$9.1^{+2.2}_{-2.4}$	$8.9^{+1.6}_{-2.2}$	2.420
273	J103348.7+574223	10 33 48.80	+57 42 23.8	0.242	0.156	$0.24^{+0.14}_{-0.18}$	$3.5^{+1.2}_{-1.8}$	$3.9^{+1}_{-1.5}$	2.417
274	J103348.8+574148	10 33 48.81	+57 41 48.9	0.346	0.128	$2.1^{+0.34}_{-0.4}$	$2.9^{+0.77}_{-1}$	$5.3^{+0.72}_{-0.82}$	0.441
275	J103348.8+572956	10 33 48.84	+57 29 56.9	0.217	0.104	$1.8^{+0.39}_{-0.48}$	$3.9^{+1.4}_{-2.7}$	$4.4^{+1.4}_{-1.8}$	1.154
276	J103348.9+574432	10 33 48.90	+57 44 32.3	0.199	0.094	$1.7^{+0.39}_{-0.51}$	$5.4^{+1.6}_{-1.7}$	$6.6^{+1.2}_{-1.4}$	0.695
277	J103349.1+573213	10 33 49.14	+57 32 13.2	0.268	0.163	$2.5^{+0.44}_{-0.53}$	$3.4^{+1}_{-1.3}$	$6.1^{+0.93}_{-1.1}$	0.440
278	J103349.3+575444	10 33 49.31	+57 54 44.8	0.141	0.095	$2.1^{+0.64}_{-1}$	$0.82^{+0.74}_{-1.3}$	$2.7^{+0.85}_{-1.2}$	0.152
279	J103350.6+572953	10 33 50.63	+57 29 53.8	0.204	0.150	$0.99^{+0.37}_{-0.66}$	$0.62^{+0.55}_{-1}$	$1.8^{+0.55}_{-0.99}$	0.213
280	J103350.6+580114	10 33 50.68	+58 01 14.2	0.292	0.394	$2.3^{+0.43}_{-0.52}$	$30^{+3.8}_{-4.3}$	$31^{+3.2}_{-3.6}$	1.846
281	J103351.0+575126	10 33 51.03	+57 51 26.3	0.594	0.331	$1.1^{+0.29}_{-0.42}$	$2.2^{+0.95}_{-1.1}$	$2.9^{+0.68}_{-0.94}$	0.502
282	J103351.6+572502	10 33 51.61	+57 25 02.9	0.154	0.083	$10^{+1.4}_{-1.4}$	$14^{+2.7}_{-3.9}$	$24^{+2.8}_{-3}$	0.371
283	J103352.4+574635	10 33 52.43	+57 46 35.2	0.202	0.108	$0.38^{+0.16}_{-0.28}$	<2.1	$0.87^{+0.38}_{-0.82}$	<1.084
284	J103352.5+580024	10 33 52.59	+58 00 24.0	0.567	0.441	$0.73^{+0.35}_{-0.58}$	<3.1	$1.6^{+0.87}_{-1.5}$	<0.915
285	J103352.8+575005	10 33 52.81	+57 50 05.6	0.213	0.101	$0.75^{+0.21}_{-0.33}$	$10^{+2.1}_{-2.5}$	$9.4^{+1.6}_{-2.1}$	2.257
286	J103353.2+573241	10 33 53.24	+57 32 41.0	0.152	0.082	$17^{+1}_{-1.1}$	$14^{+1.6}_{-1.8}$	$31^{+1.6}_{-1.7}$	0.208
287	J103353.2+575025	10 33 53.28	+57 50 25.3	0.203	0.091	$2.9^{+0.34}_{-0.39}$	$11^{+1.5}_{-1.7}$	$14^{+1.3}_{-1.4}$	1.005
288	J103353.6+575157	10 33 53.67	+57 51 57.7	0.521	0.287	$0.43^{+0.15}_{-0.32}$	$4.9^{+1.4}_{-2.2}$	$5.5^{+1.3}_{-1.7}$	1.961
289	J103355.0+575934	10 33 55.07	+57 59 34.9	0.890	0.321	$0.81^{+0.42}_{-0.92}$	<0.097	$1.2^{+0.55}_{-0.72}$	0.062
290	J103355.2+573716	10 33 55.24	+57 37 16.7	0.945	0.609	$1.1^{+0.29}_{-0.38}$	$6.7^{+1.3}_{-1.6}$	$7.8^{+1.4}_{-1.7}$	2.217
291	J103356.2+575449	10 33 56.21	+57 54 49.1	0.251	0.206	$1.5^{+0.24}_{-0.28}$	$25^{+2.5}_{-2.7}$	$23^{+2}_{-2.2}$	2.763
292	J103356.4+573925	10 33 56.42	+57 39 25.7	0.213	0.514	$0.87^{+0.36}_{-0.47}$	<3.5	$2.3^{+0.94}_{-1.3}$	<0.853
293	J103357.7+573654	10 33 57.74	+57 36 54.5	0.095	0.090	$20^{+1.1}_{-1.1}$	$38^{+3.4}_{-3.7}$	$57^{+2.4}_{-2.5}$	0.549
294	J103357.8+574942	10 33 57.83	+57 49 42.8	0.148	0.090	$3.3^{+0.38}_{-0.43}$	$8.3^{+1.2}_{-1.4}$	$11^{+1}_{-1.1}$	0.313
295	J103358.2+574242	10 33 58.24	+57 42 42.8	0.292	0.155	$0.88^{+0.21}_{-0.27}$	$3.8^{+0.96}_{-1.2}$	$4.6^{+0.81}_{-0.96}$	1.107
296	J103358.2+573206	10 33 58.28	+57 32 06.1	0.288	0.196	$0.99^{+0.39}_{-0.6}$	$1^{+0.65}_{-1.5}$	$2.2^{+0.65}_{-1.2}$	0.313
297	J103358.6+574316	10 33 58.66	+57 43 17.0	0.290	0.193	$1.3^{+0.26}_{-0.32}$	$3.5^{+1.4}_{-2}$	$3.8^{+0.67}_{-0.8}$	0.542
298	J103358.9+573935	10 33 58.91	+57 39 35.5	0.344	0.249	$4^{+0.41}_{-0.45}$	$5.6^{+0.94}_{-1.1}$	$10^{+0.86}_{-0.93}$	0.323
299	J103359.0+574442	10 33 59.02	+57 44 42.6	0.217	0.100	$0.39^{+0.16}_{-0.3}$	$0.39^{+0.35}_{-0.54}$	$0.86^{+0.3}_{-0.52}$	0.292
300	J103359.7+574420	10 33 59.71	+57 44 20.6	0.404	0.088	$0.13^{+0.08}_{-0.23}$	$1.9^{+0.9}_{-1.6}$	$2.4^{+0.93}_{-1.2}$	2.376
301	J103359.9+575900	10 33 59.91	+57 59 00.3	0.353	0.350	$1^{+0.28}_{-0.37}$	$8.1^{+1.9}_{-2.3}$	$7.4^{+1.4}_{-1.7}$	1.509
302	J103400.7+574446	10 34 00.70	+57 44 46.5	0.297	0.071	$0.72^{+0.27}_{-0.39}$	$0.41^{+0.37}_{-0.61}$	$1.5^{+0.47}_{-0.55}$	0.194
303	J103400.8+574743	10 34 00.87	+57 47 43.9	0.000	0.000	$0.68^{+0.32}_{-0.56}$	$7.8^{+2.4}_{-4.5}$	$6.4^{+1.9}_{-3.3}$	1.983
304	J103400.8+572851	10 34 00.90	+57 28 51.5	0.215	0.110	$1.4^{+0.45}_{-0.63}$	$3.4^{+1.6}_{-2.1}$	$5.1^{+1.3}_{-1.6}$	0.608
305	J103401.0+573324	10 34 01.00	+57 33 24.6	0.302	0.199	$3.5^{+0.53}_{-0.62}$	$7.7^{+1.6}_{-1.9}$	$11^{+1.4}_{-1.6}$	0.828
306	J103401.2+574227	10 34 01.22	+57 42 27.4	0.404	0.205	$0.17^{+0.13}_{-0.15}$	$5^{+1.6}_{-2}$	$4.4^{+1.1}_{-1.9}$	4.149
307	J103401.8+573328	10 34 01.85	+57 33 28.5	0.380	0.107	$0.54^{+0.33}_{-0.39}$	$1.5^{+1}_{-1.6}$	$1.4^{+0.6}_{-1.3}$	0.649
308	J103401.9+574356	10 34 01.95	+57 43 56.3	0.240	0.095	$0.68^{+0.21}_{-0.35}$	<1.9	$2.2^{+0.67}_{-0.77}$	<0.639
309	J103402.6+575002	10 34 02.63	+57 50 02.8	0.519	0.095	<0.007	$1.7^{+1.2}_{-1.6}$	$2.8^{+1.4}_{-2}$	22.66
310	J103402.7+575116	10 34 02.77	+57 51 16.7	0.346	0.328	$0.34^{+0.18}_{-0.22}$	$1.3^{+0.54}_{-1.3}$	$1.9^{+0.7}_{-0.76}$	0.828
311	J103403.2+573911	10 34 03.22	+57 39 12.0	0.357	0.210	$0.81^{+0.18}_{-0.22}$	$5^{+1}_{-1.3}$	$5.6^{+0.84}_{-0.97}$	1.345
312	J103403.4+573407	10 34 03.45	+57 34 07.4	0.670	0.252	$1.3^{+0.26}_{-0.31}$	$3.3^{+0.85}_{-1.1}$	$4.6^{+0.74}_{-0.87}$	0.852

Table A.1—Continued

#	name	α_{2000}	δ_{2000}	$\Delta\alpha('')$	$\Delta\delta('')$	$f_{0.4-2.0keV}$	$f_{2.0-8.0keV}$	$f_{0.4-8.0keV}$	HR
313	J103404.4+575655	10 34 04.41	+57 56 55.3	0.551	0.138	$1.8^{+0.39}_{-0.48}$	$12^{+2.2}_{-2.7}$	$13^{+1.8}_{-2.1}$	1.500
314	J103404.5+575159	10 34 04.54	+57 51 59.7	0.666	0.271	$0.47^{+0.19}_{-0.28}$	$1.7^{+0.67}_{-1.3}$	$1.6^{+0.57}_{-0.78}$	0.786
315	J103404.5+575241	10 34 04.60	+57 52 41.3	0.437	0.133	$2^{+0.32}_{-0.37}$	$1.6^{+0.63}_{-0.92}$	$2.7^{+0.42}_{-0.49}$	<0.387
316	J103404.9+574156	10 34 04.94	+57 41 57.0	0.515	0.204	$0.38^{+0.18}_{-0.23}$	<2.6	$1.4^{+0.54}_{-0.94}$	<1.305
317	J103405.4+573615	10 34 05.44	+57 36 15.2	0.240	0.204	$2.3^{+0.35}_{-0.41}$	$3.1^{+0.94}_{-1.3}$	$5^{+0.83}_{-0.98}$	0.371
318	J103406.0+572003	10 34 06.09	+57 20 03.9	1.196	0.366	$4.6^{+1.1}_{-1.3}$	$0.96^{+0.58}_{-1.7}$	$5.4^{+1.1}_{-1.4}$	0.093
319	J103406.1+572032	10 34 06.13	+57 20 32.1	0.776	0.401	$6.3^{+1}_{-1.3}$	$10^{+2.6}_{-3.6}$	$17^{+2.4}_{-2.8}$	0.432
320	J103406.2+575327	10 34 06.22	+57 53 27.2	0.249	0.093	$7.8^{+0.58}_{-0.63}$	$15^{+1.6}_{-1.8}$	$24^{+1.4}_{-1.5}$	0.567
321	J103406.2+575005	10 34 06.29	+57 50 05.5	0.393	0.184	$0.41^{+0.2}_{-0.34}$	$4.6^{+1.5}_{-2.5}$	$3.9^{+1.1}_{-2}$	1.924
322	J103406.6+575607	10 34 06.65	+57 56 07.3	0.193	0.081	$10^{+0.94}_{-1}$	$19^{+2.5}_{-2.9}$	$29^{+2.2}_{-2.4}$	0.499
323	J103406.7+580236	10 34 06.78	+58 02 36.1	0.397	0.168	$22^{+1.8}_{-2.1}$	$59^{+6.4}_{-6.9}$	$82^{+5.4}_{-6}$	0.632
324	J103407.6+572104	10 34 07.67	+57 21 04.9	0.848	0.450	$0.47^{+0.28}_{-0.38}$	$14^{+4.2}_{-4.5}$	$11^{+3.2}_{-3.6}$	4.329
325	J103407.9+575420	10 34 07.98	+57 54 21.0	0.798	0.285	$1.5^{+0.6}_{-0.72}$	<3.4	$3.7^{+1.4}_{-1.5}$	<0.559
326	J103408.4+574510	10 34 08.44	+57 45 10.8	0.160	0.164	$0.34^{+0.17}_{-0.24}$	$2.8^{+1.2}_{-1.5}$	$3.6^{+1.1}_{-1.3}$	1.530
327	J103409.0+572528	10 34 09.04	+57 25 28.5	0.173	0.095	$2.8^{+0.66}_{-0.79}$	$7.8^{+2.3}_{-2.9}$	$10^{+1.7}_{-2.4}$	0.652
328	J103409.2+571823	10 34 09.23	+57 18 23.8	0.679	0.340	$18^{+1.9}_{-1.9}$	$25^{+4.3}_{-4.7}$	$43^{+3.6}_{-4.2}$	0.382
329	J103409.4+572953	10 34 09.47	+57 29 53.8	0.128	0.086	$3.2^{+0.7}_{-0.87}$	$5.4^{+1.8}_{-2.4}$	$8.7^{+1.5}_{-2}$	0.448
330	J103409.5+574728	10 34 09.58	+57 47 28.4	0.109	0.061	$3.2^{+0.35}_{-0.39}$	$12^{+1.4}_{-1.6}$	$15^{+1.2}_{-1.3}$	0.913
331	J103410.2+580346	10 34 10.21	+58 03 46.9	0.300	0.149	$55^{+3.1}_{-3.2}$	$100^{+8.4}_{-8.8}$	$160^{+7.5}_{-7.6}$	0.488
332	J103410.5+573415	10 34 10.53	+57 34 15.1	0.189	0.069	$25^{+1.1}_{-1.2}$	$39^{+2.8}_{-3}$	$65^{+2.5}_{-2.6}$	0.301
333	J103410.6+575601	10 34 10.63	+57 56 01.1	1.157	0.534	$0.23^{+0.2}_{-0.34}$	$4.8^{+2.5}_{-3.4}$	$6.7^{+2.2}_{-3.6}$	3.295
334	J103410.6+572153	10 34 10.64	+57 21 54.0	0.670	0.406	$0.89^{+0.33}_{-0.59}$	$3.5^{+1.5}_{-2.6}$	$4.6^{+1.3}_{-2}$	0.869
335	J103410.6+573327	10 34 10.64	+57 33 27.9	0.192	0.376	$0.5^{+0.21}_{-0.51}$	$4.4^{+1.6}_{-3.1}$	$5.1^{+1.5}_{-2.3}$	1.610
336	J103410.7+575918	10 34 10.76	+57 59 18.8	0.721	0.481	$2.5^{+0.5}_{-0.61}$	$2.8^{+0.97}_{-1.4}$	$5.7^{+0.97}_{-1.1}$	0.318
337	J103411.2+575528	10 34 11.26	+57 55 28.7	0.253	0.134	$0.97^{+0.38}_{-0.59}$	$1.5^{+0.69}_{-2}$	$2.7^{+0.94}_{-1.1}$	0.414
338	J103411.5+574327	10 34 11.58	+57 43 27.7	0.165	0.216	$0.32^{+0.12}_{-0.27}$	<2.8	$2.1^{+0.71}_{-1}$	<1.600
339	J103412.3+573022	10 34 12.35	+57 30 22.6	0.221	0.130	$1.3^{+0.43}_{-0.66}$	$1.5^{+0.77}_{-1.9}$	$3.4^{+1}_{-1.1}$	0.351
340	J103412.4+574359	10 34 12.46	+57 43 59.9	0.326	0.204	$0.19^{+0.094}_{-0.22}$	$3.9^{+1.5}_{-1.6}$	$3.7^{+1.1}_{-1.5}$	3.206
341	J103412.8+574831	10 34 12.89	+57 48 31.4	0.203	0.084	$0.93^{+0.23}_{-0.39}$	$3.5^{+1.1}_{-1.6}$	$4.7^{+0.94}_{-1.2}$	0.813
342	J103412.9+572818	10 34 12.99	+57 28 18.8	0.149	0.088	$3.6^{+0.76}_{-0.94}$	$3.9^{+1.4}_{-2.2}$	$8.4^{+1.4}_{-1.8}$	0.326
343	J103413.6+573402	10 34 13.63	+57 34 02.6	0.455	0.198	$1.9^{+0.34}_{-0.4}$	$1.5^{+0.81}_{-1.4}$	$3^{+0.5}_{-0.59}$	<0.386
344	J103413.9+574641	10 34 13.97	+57 46 41.5	0.153	0.092	$0.38^{+0.13}_{-0.19}$	$23^{+3}_{-3.4}$	$20^{+2.6}_{-3}$	12.60
345	J103413.9+574547	10 34 13.99	+57 45 47.3	0.254	0.099	$0.49^{+0.17}_{-0.31}$	$1.9^{+0.89}_{-1.1}$	$2.2^{+0.69}_{-0.85}$	0.831
346	J103414.3+572227	10 34 14.33	+57 22 27.7	0.456	0.301	$0.95^{+0.38}_{-0.56}$	$2.5^{+1.1}_{-2.4}$	$3.5^{+0.96}_{-1.7}$	0.626
347	J103414.5+573453	10 34 14.58	+57 34 53.5	0.367	0.141	$1.9^{+0.4}_{-0.49}$	$2.3^{+0.81}_{-1.2}$	$3.6^{+0.71}_{-0.86}$	0.524
348	J103414.5+574641	10 34 14.59	+57 46 41.8	0.322	0.124	$0.39^{+0.14}_{-0.29}$	$16^{+2.9}_{-3.5}$	$4.4^{+1.5}_{-1.7}$	5.402
349	J103414.8+575400	10 34 14.81	+57 54 00.4	0.232	0.104	$0.1^{+0.085}_{-0.32}$	$9.4^{+2.8}_{-4.8}$	$7.3^{+2.9}_{-3.6}$	10.55
350	J103414.9+573036	10 34 14.97	+57 30 36.6	0.249	0.134	$0.55^{+0.25}_{-0.47}$	<2.6	$1.8^{+0.95}_{-1.2}$	<0.989
351	J103415.3+572125	10 34 15.34	+57 21 25.5	0.660	0.294	$4^{+0.86}_{-0.95}$	$6.5^{+1.9}_{-3}$	$11^{+1.9}_{-2.1}$	0.441
352	J103415.5+575935	10 34 15.52	+57 59 35.4	0.392	0.165	$3.1^{+0.65}_{-0.9}$	$9.4^{+2.2}_{-3.5}$	$12^{+1.9}_{-2.7}$	0.698
353	J103416.3+580331	10 34 16.37	+58 03 31.8	0.904	0.357	$7.4^{+1.2}_{-1.3}$	$4.5^{+1.5}_{-2.3}$	$12^{+1.7}_{-2.1}$	0.208
354	J103417.0+574321	10 34 17.07	+57 43 22.0	0.250	0.268	$0.42^{+0.18}_{-0.41}$	<0.066	$0.66^{+0.23}_{-0.39}$	0.073
355	J103417.4+575022	10 34 17.44	+57 50 22.9	0.122	0.086	$12^{+1}_{-1.1}$	$13^{+1.9}_{-2.4}$	$26^{+1.8}_{-2.1}$	0.307
356	J103418.6+573829	10 34 18.65	+57 38 29.4	0.327	0.109	$1.4^{+0.45}_{-0.67}$	<1.9	$2.6^{+0.76}_{-1.2}$	<0.370
357	J103419.6+574449	10 34 19.64	+57 44 49.2	0.584	0.245	$14^{+1.1}_{-1.2}$	$24^{+2.8}_{-3.2}$	$37^{+2.5}_{-2.6}$	0.524
358	J103419.9+574152	10 34 19.91	+57 41 52.1	0.342	0.275	$0.51^{+0.19}_{-0.36}$	<2.4	$1.4^{+0.63}_{-0.83}$	<0.953
359	J103420.1+571832	10 34 20.17	+57 18 32.8	1.132	0.638	$1.5^{+0.53}_{-0.6}$	$12^{+3.4}_{-4.2}$	$14^{+2.9}_{-3.3}$	1.503
360	J103420.3+575305	10 34 20.37	+57 53 05.7	0.654	0.307	$2.8^{+0.45}_{-0.61}$	$6.8^{+1.5}_{-2}$	$9.4^{+1.3}_{-1.5}$	0.580
361	J103420.5+574903	10 34 20.55	+57 49 03.4	0.263	0.099	$0.21^{+0.11}_{-0.21}$	$4.7^{+1.4}_{-2.2}$	$4.9^{+1.3}_{-1.7}$	3.417
362	J103421.3+575016	10 34 21.32	+57 50 16.6	0.171	0.123	$4.2^{+0.48}_{-0.54}$	$11^{+1.6}_{-1.9}$	$16^{+1.4}_{-1.6}$	0.756
363	J103421.3+574630	10 34 21.34	+57 46 30.0	0.208	0.114	$1.1^{+0.27}_{-0.38}$	$4.9^{+1.4}_{-1.6}$	$5.7^{+1}_{-1.4}$	0.923
364	J103421.6+575030	10 34 21.64	+57 50 30.8	0.246	0.177	$4.2^{+0.43}_{-0.48}$	$4.5^{+0.83}_{-1}$	$8.4^{+0.77}_{-0.84}$	0.307

Table A.1—Continued

#	name	α_{2000}	δ_{2000}	$\Delta\alpha('')$	$\Delta\delta('')$	$f_{0.4-2.0keV}$	$f_{2.0-8.0keV}$	$f_{0.4-8.0keV}$	HR
365	J103422.0+575231	10 34 22.02	+57 52 31.1	0.508	0.094	$0.85^{+0.21}_{-0.27}$	$3.8^{+0.97}_{-1.3}$	$3.9^{+0.75}_{-0.91}$	1.257
366	J103424.4+575812	10 34 24.40	+57 58 12.7	0.213	0.121	$2.2^{+0.48}_{-0.6}$	$0.81^{+0.46}_{-1.5}$	$3.7^{+0.7}_{-0.84}$	0.161
367	J103425.3+574922	10 34 25.32	+57 49 22.9	0.272	0.136	$2.3^{+0.43}_{-0.56}$	$2.2^{+0.89}_{-1}$	$5^{+0.79}_{-1}$	0.290
368	J103425.6+575516	10 34 25.69	+57 55 16.2	0.173	0.141	$0.88^{+0.32}_{-0.61}$	$1.5^{+0.69}_{-1.9}$	$2.4^{+0.91}_{-1}$	0.443
369	J103428.2+572907	10 34 28.25	+57 29 07.4	0.804	0.327	$1.2^{+0.42}_{-0.58}$	$6.8^{+2.1}_{-3.4}$	$8^{+1.8}_{-2.6}$	1.124
370	J103428.7+574058	10 34 28.70	+57 40 58.0	0.290	0.252	$0.63^{+0.25}_{-0.49}$	$6.2^{+2.3}_{-2.6}$	$4^{+1.4}_{-1.9}$	1.745
371	J103429.6+574327	10 34 29.66	+57 43 27.7	0.432	0.214	$0.31^{+0.12}_{-0.18}$	$4.2^{+1.1}_{-1.5}$	$4.9^{+1}_{-1.2}$	3.274
372	J103429.6+575217	10 34 29.67	+57 52 17.5	0.385	0.085	$4.2^{+0.5}_{-0.57}$	$5.3^{+1.1}_{-1.3}$	$9.5^{+0.98}_{-1.1}$	0.106
373	J103429.7+575058	10 34 29.73	+57 50 58.2	0.253	0.177	$8^{+0.59}_{-0.64}$	$9.8^{+1.2}_{-1.4}$	$19^{+1.2}_{-1.2}$	0.329
374	J103429.9+573749	10 34 29.95	+57 37 49.2	0.149	0.064	$2.9^{+0.35}_{-0.39}$	$9.5^{+1.3}_{-1.5}$	$12^{+1.1}_{-1.2}$	1.142
375	J103430.1+574426	10 34 30.14	+57 44 26.9	0.492	0.331	$1.2^{+0.32}_{-0.41}$	$2.5^{+0.89}_{-1.3}$	$4.3^{+0.85}_{-1}$	0.232
376	J103430.5+572847	10 34 30.58	+57 28 47.0	0.317	0.169	$3.6^{+0.55}_{-0.64}$	$6.5^{+1.5}_{-1.8}$	$11^{+1.3}_{-1.5}$	0.993
377	J103432.2+575410	10 34 32.23	+57 54 10.6	0.232	0.106	$1.2^{+0.54}_{-0.59}$	$0.37^{+0.3}_{-1.1}$	$1.6^{+0.54}_{-0.79}$	0.123
378	J103432.6+575417	10 34 32.67	+57 54 17.3	0.158	0.216	$0.65^{+0.34}_{-0.43}$	$1.2^{+0.8}_{-1.5}$	$1.7^{+0.62}_{-1.1}$	0.480
379	J103432.8+574301	10 34 32.86	+57 43 01.6	0.357	0.292	$0.28^{+0.18}_{-0.37}$	$6.1^{+2.1}_{-3.7}$	$6.5^{+2.3}_{-2.6}$	3.327
380	J103433.5+575746	10 34 33.58	+57 57 46.6	0.186	0.083	<0.033	$60^{+9.5}_{-12}$	58^{+10}_{-11}	>108.8
381	J103433.6+573231	10 34 33.68	+57 32 31.2	0.137	0.071	$31^{+1.8}_{-1.9}$	$4.7^{+1}_{-1.3}$	$27^{+1.6}_{-1.7}$	0.079
382	J103434.9+574214	10 34 34.92	+57 42 14.2	0.359	0.336	$0.8^{+0.21}_{-0.28}$	$3.2^{+0.92}_{-1.2}$	$3.3^{+0.69}_{-0.85}$	0.154
383	J103435.1+572759	10 34 35.19	+57 27 59.3	1.299	0.616	$2.9^{+0.5}_{-0.6}$	$11^{+2.5}_{-4.1}$	$9.7^{+1.4}_{-1.6}$	0.830
384	J103435.7+574625	10 34 35.73	+57 46 25.9	0.526	0.162	$3.1^{+0.4}_{-0.45}$	$8.9^{+1.4}_{-1.7}$	$12^{+1.2}_{-1.3}$	0.926
385	J103435.8+580118	10 34 35.81	+58 01 18.6	0.485	0.297	$0.91^{+0.4}_{-0.45}$	$16^{+3.7}_{-4.9}$	$15^{+3.1}_{-3.9}$	2.851
386	J103436.7+574124	10 34 36.77	+57 41 24.6	0.314	0.164	$2.2^{+0.41}_{-0.5}$	$4^{+1.3}_{-1.8}$	$5.7^{+0.95}_{-1.1}$	<0.368
387	J103437.1+572807	10 34 37.13	+57 28 07.2	0.347	0.147	$2^{+0.44}_{-0.54}$	$4.1^{+1.2}_{-1.6}$	$5.2^{+0.94}_{-1.1}$	0.109
388	J103437.7+575443	10 34 37.78	+57 54 43.5	0.961	0.487	$7.5^{+1.2}_{-1.2}$	$9.5^{+2.5}_{-3}$	$17^{+2.2}_{-2.6}$	0.363
389	J103437.9+573516	10 34 37.93	+57 35 16.3	0.313	0.195	<0.06	$9^{+2.8}_{-5.3}$	$8.2^{+3.2}_{-4}$	15.44
390	J103438.8+575012	10 34 38.81	+57 50 13.0	0.399	0.168	$7.7^{+0.58}_{-0.62}$	$12^{+1.4}_{-1.5}$	$19^{+1.2}_{-1.3}$	0.547
391	J103439.7+573529	10 34 39.75	+57 35 29.4	0.215	0.075	$1.5^{+0.46}_{-0.71}$	$1.4^{+0.69}_{-1.7}$	$3.2^{+0.79}_{-1.2}$	0.273
392	J103439.8+573804	10 34 39.88	+57 38 04.4	0.183	0.079	$3.5^{+0.81}_{-1}$	$0.88^{+0.57}_{-1.2}$	$3.9^{+0.79}_{-1.1}$	0.103
393	J103439.9+574354	10 34 39.92	+57 43 55.0	0.205	0.129	$32^{+1.6}_{-1.7}$	$47^{+3.8}_{-4.1}$	$80^{+3.4}_{-3.6}$	0.438
394	J103440.1+574556	10 34 40.20	+57 45 56.1	0.461	0.231	$0.66^{+0.25}_{-0.55}$	$2.5^{+1.2}_{-2.2}$	$3.8^{+1.2}_{-1.7}$	0.846
395	J103440.5+573845	10 34 40.57	+57 38 45.7	0.220	0.115	$1.7^{+0.49}_{-0.65}$	$4.1^{+1.4}_{-2.4}$	$5.8^{+1.3}_{-1.7}$	0.571
396	J103440.8+575017	10 34 40.90	+57 50 17.9	0.440	0.372	$0.16^{+0.11}_{-0.18}$	$5.1^{+1.5}_{-2.5}$	$4.8^{+1.5}_{-1.7}$	4.532
397	J103440.9+574714	10 34 40.97	+57 47 15.0	0.297	0.229	$8^{+0.6}_{-0.64}$	$12^{+1.4}_{-1.6}$	$21^{+1.3}_{-1.4}$	0.976
398	J103441.3+575335	10 34 41.33	+57 53 35.6	0.138	0.063	$9.7^{+0.9}_{-0.99}$	$10^{+1.7}_{-2}$	$20^{+1.6}_{-1.8}$	0.299
399	J103441.5+573240	10 34 41.56	+57 32 40.4	0.377	0.148	$2.3^{+0.45}_{-0.54}$	$2.4^{+0.83}_{-1.2}$	$4.7^{+0.79}_{-0.93}$	0.413
400	J103441.9+575858	10 34 41.92	+57 58 58.7	0.232	0.204	$0.2^{+0.18}_{-0.28}$	<3.5	$2^{+1.1}_{-2}$	<2.825
401	J103442.3+572608	10 34 42.33	+57 26 09.0	0.253	0.200	$2.6^{+0.66}_{-0.98}$	$2.2^{+0.92}_{-2.3}$	$5.3^{+1.1}_{-1.7}$	0.267
402	J103442.3+575343	10 34 42.40	+57 53 43.8	0.203	0.257	<0.047	$2.9^{+1.5}_{-3.4}$	$4.7^{+2.1}_{-3}$	>7.736
403	J103442.5+573911	10 34 42.59	+57 39 11.8	0.230	0.174	$0.24^{+0.16}_{-0.34}$	$6.7^{+2.1}_{-3.8}$	$4.6^{+1.7}_{-2.6}$	3.991
404	J103444.5+572824	10 34 44.56	+57 28 24.4	0.202	0.175	$7.8^{+0.85}_{-0.95}$	$6.8^{+1.4}_{-1.8}$	$15^{+1.4}_{-1.6}$	0.320
405	J103445.1+575543	10 34 45.14	+57 55 43.9	0.209	0.194	$1.7^{+0.57}_{-0.87}$	$0.23^{+0.17}_{-1.2}$	$1.8^{+0.59}_{-0.69}$	0.068
406	J103445.1+572416	10 34 45.18	+57 24 16.4	0.734	0.432	$3.1^{+0.7}_{-0.93}$	$5.6^{+2}_{-2.7}$	$8.5^{+1.6}_{-2.2}$	0.480
407	J103445.2+574034	10 34 45.26	+57 40 34.7	0.398	0.149	$0.68^{+0.31}_{-0.58}$	$0.32^{+0.25}_{-1.3}$	$1.6^{+0.62}_{-0.73}$	0.167
408	J103445.5+574534	10 34 45.54	+57 45 34.4	0.001	0.224	$0.87^{+0.34}_{-0.71}$	$0.3^{+0.24}_{-1.3}$	$1^{+0.46}_{-0.69}$	0.137
409	J103446.5+574039	10 34 46.56	+57 40 39.1	0.233	0.208	$2.6^{+0.72}_{-0.89}$	$0.56^{+0.5}_{-0.93}$	$2.9^{+0.73}_{-0.92}$	0.095
410	J103446.6+573738	10 34 46.69	+57 37 38.3	0.172	0.164	$1.2^{+0.43}_{-0.58}$	<1.7	$2.1^{+0.73}_{-1.1}$	<0.382
411	J103446.9+575127	10 34 46.98	+57 51 28.0	0.210	0.088	$34^{+1.7}_{-1.8}$	$38^{+3.4}_{-3.7}$	$74^{+3.2}_{-3.4}$	0.359
412	J103447.0+580221	10 34 47.00	+58 02 21.1	0.516	0.557	$2.1^{+0.65}_{-0.8}$	$1.8^{+0.98}_{-1.7}$	$4.1^{+1}_{-1.4}$	0.268
413	J103447.6+574957	10 34 47.63	+57 49 57.5	0.444	0.325	$2^{+0.32}_{-0.38}$	$17^{+2.2}_{-2.5}$	$18^{+1.9}_{-2.1}$	1.345
414	J103447.7+572808	10 34 47.78	+57 28 08.7	0.241	0.252	$9^{+1.3}_{-1.4}$	$17^{+3.1}_{-4.3}$	$25^{+3}_{-3.1}$	0.485
415	J103448.5+574135	10 34 48.51	+57 41 35.5	0.186	0.342	$0.46^{+0.28}_{-0.33}$	$5.9^{+2.4}_{-2.7}$	$4.9^{+1.5}_{-2.4}$	2.139
416	J103448.5+574413	10 34 48.56	+57 44 13.4	0.309	0.215	$0.19^{+0.18}_{-0.25}$	$3.2^{+1.5}_{-2.7}$	$3.5^{+1.3}_{-2.3}$	2.662

Table A.1—Continued

#	name	α_{2000}	δ_{2000}	$\Delta\alpha('')$	$\Delta\delta('')$	$f_{0.4-2.0keV}$	$f_{2.0-8.0keV}$	$f_{0.4-8.0keV}$	HR
417	J103448.8+575001	10 34 48.84	+57 50 01.1	0.471	0.193	$2.9^{+0.62}_{-0.97}$	$6.6^{+1.9}_{-3.2}$	$8.5^{+1.9}_{-1.9}$	0.563
418	J103449.2+574749	10 34 49.27	+57 47 49.3	0.400	0.364	$1.9^{+0.33}_{-0.38}$	$6.5^{+1.3}_{-1.6}$	$8.6^{+1.1}_{-1.2}$	0.529
419	J103449.4+575518	10 34 49.45	+57 55 18.6	0.244	0.086	$3.2^{+0.52}_{-0.61}$	$4.4^{+1.2}_{-1.5}$	$7.8^{+1.1}_{-1.2}$	0.219
420	J103449.6+574652	10 34 49.64	+57 46 52.1	0.308	0.059	$0.94^{+0.2}_{-0.25}$	$6.7^{+1.2}_{-1.5}$	$7^{+0.97}_{-1.1}$	0.273
421	J103449.6+575808	10 34 49.64	+57 58 08.6	0.352	0.125	$0.7^{+0.3}_{-0.48}$	$5^{+1.7}_{-3}$	$5.5^{+1.8}_{-1.9}$	1.374
422	J103449.6+572544	10 34 49.68	+57 25 44.3	0.557	0.575	$1.7^{+0.55}_{-0.66}$	<4.4	$3.7^{+1.1}_{-1.7}$	<0.625
423	J103450.0+573212	10 34 50.07	+57 32 12.4	0.854	0.390	$0.68^{+0.22}_{-0.31}$	$8.2^{+3.1}_{-4.6}$	$5.1^{+1.2}_{-1.6}$	<1.979
424	J103450.5+574257	10 34 50.51	+57 42 57.7	0.412	0.132	$1.4^{+0.39}_{-0.64}$	$28^{+5}_{-5.8}$	$24^{+4.2}_{-4.3}$	3.108
425	J103450.5+574116	10 34 50.53	+57 41 16.4	0.301	0.245	$1.6^{+0.4}_{-0.51}$	$0.5^{+0.33}_{-0.66}$	$2.1^{+0.47}_{-0.58}$	0.177
426	J103451.0+573751	10 34 51.03	+57 37 51.3	0.215	0.090	$1.4^{+0.44}_{-0.65}$	$2.6^{+1.3}_{-1.8}$	$4.2^{+1}_{-1.6}$	0.486
427	J103451.0+573343	10 34 51.03	+57 33 43.3	0.318	0.105	$1.7^{+0.54}_{-0.75}$	$1.6^{+0.83}_{-1.8}$	$3.2^{+0.94}_{-1.2}$	0.278
428	J103451.3+573317	10 34 51.34	+57 33 17.7	0.432	0.268	$0.12^{+0.1}_{-0.32}$	$1.7^{+1.2}_{-2.1}$	$2.9^{+1.3}_{-1.9}$	2.368
429	J103451.3+572822	10 34 51.35	+57 28 22.8	0.739	0.431	$1.5^{+0.49}_{-0.81}$	$0.87^{+0.48}_{-1.8}$	$2.6^{+0.89}_{-0.99}$	0.201
430	J103451.9+573933	10 34 51.93	+57 39 33.4	0.000	0.000	$0.58^{+0.28}_{-0.44}$	$1.7^{+0.83}_{-2}$	$1.7^{+0.78}_{-1.1}$	0.667
431	J103452.0+575402	10 34 52.06	+57 54 02.8	0.108	0.087	$1.4^{+0.42}_{-0.67}$	$3.1^{+1.3}_{-2.3}$	$4.4^{+1.3}_{-1.4}$	0.565
432	J103452.1+573420	10 34 52.10	+57 34 20.1	0.418	0.108	$1.1^{+0.46}_{-0.69}$	$0.25^{+0.18}_{-1.4}$	$1.4^{+0.56}_{-0.72}$	0.100
433	J103452.8+574642	10 34 52.87	+57 46 42.6	0.236	0.099	$2.1^{+0.38}_{-0.46}$	$1.7^{+0.6}_{-0.85}$	$3.6^{+0.56}_{-0.66}$	0.027
434	J103453.0+574032	10 34 53.02	+57 40 32.5	0.250	0.134	$0.78^{+0.38}_{-0.41}$	$2.7^{+1.4}_{-1.9}$	$3.3^{+1.1}_{-1.4}$	0.769
435	J103453.3+573446	10 34 53.34	+57 34 47.0	0.190	0.108	$5.2^{+0.96}_{-1.2}$	$3.9^{+1.4}_{-2.1}$	$9.4^{+1.5}_{-1.8}$	0.237
436	J103453.4+573353	10 34 53.42	+57 33 53.6	0.324	0.261	$1.3^{+0.4}_{-0.71}$	$1.1^{+0.73}_{-1.4}$	$1.9^{+0.67}_{-0.98}$	0.268
437	J103453.8+574320	10 34 53.88	+57 43 20.9	0.464	0.136	$5.8^{+1.4}_{-1.9}$	<0.058	$2.2^{+0.47}_{-0.71}$	0.009
438	J103454.7+574205	10 34 54.79	+57 42 05.5	0.240	0.107	$10^{+0.9}_{-0.99}$	$15^{+2.1}_{-2.4}$	$25^{+1.9}_{-2}$	0.395
439	J103454.9+574654	10 34 54.95	+57 46 54.7	0.213	0.135	$1.3^{+0.27}_{-0.33}$	$2.5^{+0.73}_{-0.98}$	$4.2^{+0.68}_{-0.8}$	0.315
440	J103456.0+574600	10 34 56.01	+57 46 00.6	0.173	0.135	$0.22^{+0.13}_{-0.37}$	$6^{+2.2}_{-3.3}$	$5.1^{+1.6}_{-3}$	4.052
441	J103456.2+574724	10 34 56.23	+57 47 24.5	0.379	0.407	$1.6^{+0.35}_{-0.42}$	$20^{+3.1}_{-3.6}$	$21^{+2.7}_{-2.9}$	2.190
442	J103456.5+573759	10 34 56.57	+57 37 59.1	0.177	0.101	$6.2^{+0.72}_{-0.81}$	$7.6^{+1.5}_{-1.8}$	$14^{+1.4}_{-1.6}$	0.202
443	J103456.6+574740	10 34 56.61	+57 47 40.0	0.240	0.116	$1.1^{+0.35}_{-0.58}$	$6.8^{+2.4}_{-2.6}$	$4.8^{+1.6}_{-1.7}$	1.235
444	J103456.8+573311	10 34 56.89	+57 33 11.9	0.277	0.146	$8.4^{+1.3}_{-1.8}$	$3^{+1.2}_{-2.3}$	$10^{+1.6}_{-2.1}$	0.137
445	J103456.9+574822	10 34 56.96	+57 48 22.8	0.227	0.112	$2.2^{+0.64}_{-0.8}$	<1.5	$2.9^{+0.77}_{-1.2}$	<0.230
446	J103457.5+575705	10 34 57.57	+57 57 05.2	0.257	0.080	$0.9^{+0.29}_{-0.58}$	$14^{+3.4}_{-4.3}$	$11^{+2.6}_{-3.3}$	2.501
447	J103457.6+573756	10 34 57.66	+57 37 56.4	0.307	0.108	$0.38^{+0.2}_{-0.39}$	$8.4^{+2.5}_{-3.9}$	$8.3^{+2.2}_{-3.2}$	3.366
448	J103457.9+573756	10 34 57.92	+57 37 56.1	0.229	0.161	$2.3^{+0.4}_{-0.48}$	$13^{+2.2}_{-2.6}$	$16^{+1.9}_{-2.1}$	0.943
449	J103457.9+575047	10 34 57.93	+57 50 47.7	0.458	0.270	$0.63^{+0.38}_{-0.45}$	$0.27^{+0.2}_{-1.3}$	$1.5^{+0.51}_{-0.86}$	0.159
450	J103458.3+574612	10 34 58.33	+57 46 12.8	0.381	0.149	$0.23^{+0.15}_{-0.36}$	$4.7^{+1.7}_{-3.2}$	$4.6^{+1.9}_{-2}$	3.142
451	J103458.4+574139	10 34 58.49	+57 41 39.8	0.477	0.240	$4.2^{+0.58}_{-0.67}$	$8.4^{+1.7}_{-2}$	$12^{+1.4}_{-1.6}$	0.581
452	J103459.0+573032	10 34 59.01	+57 30 32.6	0.340	0.276	$20^{+1.4}_{-1.5}$	$15^{+2.2}_{-2.5}$	$35^{+2.2}_{-2.4}$	0.226
453	J103500.3+574327	10 35 00.35	+57 43 27.1	0.377	0.136	$0.96^{+0.35}_{-0.67}$	$0.93^{+0.55}_{-1.7}$	$2.3^{+0.86}_{-0.93}$	0.298
454	J103500.3+573032	10 35 00.36	+57 30 32.9	0.316	0.190	$32^{+1.8}_{-1.9}$	$15^{+2}_{-2.3}$	$42^{+2.3}_{-2.4}$	0.150
455	J103501.1+575700	10 35 01.20	+57 57 00.8	0.222	0.146	$0.86^{+0.35}_{-0.5}$	$6.9^{+2.3}_{-3.1}$	$7.1^{+1.9}_{-2.3}$	1.499
456	J103502.0+575006	10 35 02.01	+57 50 06.4	0.277	0.146	$0.72^{+0.16}_{-0.2}$	$25^{+2.5}_{-2.8}$	$23^{+2.2}_{-2.4}$	3.699
457	J103503.3+574107	10 35 03.35	+57 41 07.3	0.360	0.202	$2.3^{+0.41}_{-0.49}$	$5.5^{+1.3}_{-1.7}$	$7.7^{+1.1}_{-1.3}$	0.517
458	J103504.0+574352	10 35 04.10	+57 43 52.6	0.270	0.115	$1.3^{+0.32}_{-0.4}$	$3^{+2.5}_{-6.7}$	$3.3^{+0.71}_{-0.88}$	0.232
459	J103505.3+574201	10 35 05.32	+57 42 01.0	0.556	0.495	$1.2^{+0.48}_{-0.53}$	<3.4	$2.5^{+0.87}_{-1.5}$	<0.675
460	J103505.4+575219	10 35 05.41	+57 52 19.2	0.505	0.203	$1.8^{+0.63}_{-0.73}$	$0.86^{+0.51}_{-1.6}$	$2.7^{+0.87}_{-0.95}$	0.175
461	J103506.8+573638	10 35 06.90	+57 36 38.5	0.433	0.134	$0.6^{+0.27}_{-0.57}$	$4.1^{+1.7}_{-3.1}$	$4^{+1.5}_{-2}$	1.287
462	J103507.3+574310	10 35 07.37	+57 43 11.0	0.754	0.324	$0.43^{+0.24}_{-0.42}$	$11^{+3.3}_{-4.3}$	$8.8^{+2.3}_{-3.8}$	3.713
463	J103508.1+573849	10 35 08.18	+57 38 49.6	0.142	0.144	$8.3^{+0.83}_{-0.92}$	$14^{+2.1}_{-2.4}$	$22^{+1.9}_{-2}$	0.350
464	J103508.2+575857	10 35 08.22	+57 58 57.6	0.562	0.169	<0.38	$5.4^{+2.1}_{-3.2}$	$3.2^{+1.4}_{-2.2}$	>2.391
465	J103508.2+574818	10 35 08.23	+57 48 18.1	0.205	0.163	$0.81^{+0.3}_{-0.54}$	$2.1^{+0.87}_{-2.1}$	$2.6^{+0.93}_{-1.2}$	0.618
466	J103508.4+575743	10 35 08.46	+57 57 43.8	0.192	0.286	$0.5^{+0.21}_{-0.5}$	$9.4^{+2.5}_{-4.3}$	$8.8^{+2.1}_{-3.5}$	2.971
467	J103508.5+575839	10 35 08.54	+57 58 39.7	0.511	0.275	$2.1^{+0.51}_{-0.79}$	$10^{+2.7}_{-3.5}$	$13^{+2.3}_{-3}$	1.022
468	J103509.5+580155	10 35 09.53	+58 01 55.8	0.933	0.864	$3^{+0.75}_{-0.93}$	$2.7^{+1.5}_{-1.6}$	$5.4^{+1.3}_{-1.4}$	0.282

Table A.1—Continued

#	name	α_{2000}	δ_{2000}	$\Delta\alpha('')$	$\Delta\delta('')$	$f_{0.4-2.0keV}$	$f_{2.0-8.0keV}$	$f_{0.4-8.0keV}$	HR
469	J103510.1+574414	10 35 10.18	+57 44 14.1	0.147	0.118	$0.41^{+0.22}_{-0.42}$	$16^{+4}_{-5.4}$	$15^{+3.3}_{-4.7}$	5.245
470	J103510.5+573049	10 35 10.59	+57 30 49.6	0.859	0.570	$2^{+0.55}_{-0.7}$	<9.2	$5.9^{+1.7}_{-2}$	<0.960
471	J103512.1+575547	10 35 12.17	+57 55 47.9	0.076	0.063	$40^{+2.5}_{-2.9}$	$110^{+8.7}_{-9.7}$	$150^{+7.8}_{-7.8}$	0.646
472	J103513.3+573940	10 35 13.39	+57 39 40.6	0.551	0.219	$4.6^{+0.59}_{-0.68}$	$16^{+2.3}_{-2.7}$	$21^{+2}_{-2.2}$	0.835
473	J103514.2+575704	10 35 14.27	+57 57 04.1	0.526	0.362	$1.5^{+0.46}_{-0.85}$	$0.65^{+0.58}_{-1.1}$	$2.2^{+0.8}_{-0.84}$	0.163
474	J103515.2+573056	10 35 15.24	+57 30 56.9	0.826	0.481	$0.32^{+0.22}_{-0.34}$	$46^{+7.5}_{-10}$	$43^{+7.9}_{-8.3}$	14.94
475	J103516.1+574554	10 35 16.10	+57 45 54.7	0.181	0.099	$4.2^{+0.96}_{-1.3}$	$5.9^{+2}_{-3.7}$	$11^{+2}_{-2.7}$	0.391
476	J103518.7+573351	10 35 18.80	+57 33 51.3	0.634	0.632	$0.43^{+0.24}_{-0.39}$	$7.6^{+2.9}_{-3.3}$	$7.9^{+2.3}_{-3}$	2.814
477	J103519.5+575438	10 35 19.57	+57 54 38.6	0.590	0.400	$1.8^{+0.51}_{-0.89}$	$1.1^{+0.73}_{-1.5}$	$2.8^{+0.81}_{-1.1}$	0.209
478	J103519.6+574721	10 35 19.65	+57 47 21.2	0.158	0.083	$2.3^{+0.57}_{-0.7}$	$9.8^{+2.5}_{-3.3}$	$12^{+2.1}_{-2.4}$	0.908
479	J103519.9+575057	10 35 19.95	+57 50 57.3	0.233	0.142	$3.4^{+0.67}_{-0.89}$	$11^{+2.8}_{-3.1}$	$16^{+1.8}_{-2}$	0.735
480	J103520.9+573349	10 35 20.98	+57 33 49.2	0.630	0.397	$2.1^{+0.57}_{-0.74}$	$4.3^{+1.9}_{-2.1}$	$6.5^{+1.4}_{-1.9}$	0.516
481	J103522.1+573720	10 35 22.13	+57 37 21.0	0.331	0.169	$7^{+0.76}_{-0.85}$	$10^{+2.3}_{-2.9}$	$15^{+1.5}_{-1.7}$	0.448
482	J103522.9+574116	10 35 22.91	+57 41 16.8	0.176	0.088	$15^{+1.6}_{-1.6}$	$22^{+2.7}_{-3.1}$	$40^{+2.5}_{-2.7}$	0.515
483	J103522.9+574606	10 35 22.97	+57 46 06.1	0.417	0.136	$0.11^{+0.094}_{-0.29}$	$6.3^{+2.7}_{-3.3}$	$7.3^{+2.2}_{-3.7}$	7.251
484	J103523.6+574530	10 35 23.65	+57 45 30.1	0.180	0.105	$1.4^{+0.44}_{-0.6}$	$4.9^{+1.5}_{-2.9}$	$6.4^{+1.4}_{-2.1}$	0.786
485	J103524.2+574435	10 35 24.20	+57 44 35.1	0.258	0.150	$0.53^{+0.26}_{-0.41}$	$3.9^{+1.9}_{-2.1}$	$4.1^{+1.3}_{-1.9}$	1.411
486	J103526.0+575536	10 35 26.01	+57 55 36.8	0.455	0.297	$2.3^{+0.6}_{-0.7}$	$27^{+5.1}_{-5.4}$	$26^{+4.1}_{-4.4}$	2.074
487	J103526.0+575218	10 35 26.05	+57 52 19.0	0.577	0.262	$2.1^{+0.45}_{-0.55}$	$1.4^{+0.6}_{-0.94}$	$3.5^{+0.66}_{-0.79}$	0.257
488	J103526.6+580029	10 35 26.61	+58 00 29.3	1.204	0.428	$1.2^{+0.45}_{-0.56}$	$13^{+3.4}_{-4.5}$	$11^{+2.7}_{-3.2}$	2.025
489	J103527.1+574708	10 35 27.18	+57 47 08.3	0.251	0.232	$0.66^{+0.31}_{-0.54}$	$0.45^{+0.38}_{-1.2}$	$1.6^{+0.55}_{-0.93}$	0.230
490	J103527.4+574159	10 35 27.49	+57 41 59.0	0.354	0.338	$1.3^{+0.32}_{-0.41}$	$3.9^{+1.2}_{-1.6}$	$4.8^{+0.96}_{-1.2}$	1.714
491	J103528.1+574613	10 35 28.17	+57 46 13.5	0.219	0.095	$3^{+0.65}_{-0.9}$	$4.3^{+1.7}_{-2.1}$	$6.6^{+1.4}_{-1.6}$	0.400
492	J103528.9+574231	10 35 28.91	+57 42 31.6	0.215	0.183	$3.3^{+0.54}_{-0.63}$	$4.9^{+1.3}_{-1.6}$	$8.6^{+1.1}_{-1.3}$	0.176
493	J103529.0+573602	10 35 29.09	+57 36 02.0	0.188	0.315	$0.94^{+0.42}_{-0.45}$	$9.4^{+2.9}_{-3.6}$	$9^{+2.2}_{-2.8}$	1.762
494	J103530.2+574909	10 35 30.29	+57 49 09.7	0.165	0.165	$0.64^{+0.25}_{-0.52}$	<2.9	$2^{+0.86}_{-1.4}$	<0.950
495	J103530.9+573835	10 35 30.97	+57 38 36.0	0.757	0.654	$2.6^{+0.68}_{-0.87}$	$2.9^{+1.6}_{-1.8}$	$6.6^{+1.3}_{-1.8}$	0.334
496	J103531.0+574545	10 35 31.04	+57 45 45.0	0.112	0.061	$5.8^{+0.91}_{-1}$	25^{+4}_{-5}	$30^{+3.6}_{-3.7}$	0.929
497	J103531.7+575217	10 35 31.76	+57 52 17.4	0.454	0.363	$3.7^{+0.83}_{-0.86}$	$12^{+3}_{-3.6}$	$17^{+2.7}_{-2.8}$	0.750
498	J103531.8+575255	10 35 31.82	+57 52 55.0	0.831	0.689	$1.5^{+0.35}_{-0.44}$	$3.7^{+1.1}_{-1.5}$	$4.9^{+0.95}_{-1.2}$	0.788
499	J103531.8+573544	10 35 31.90	+57 35 44.3	0.477	0.341	$8^{+0.81}_{-0.89}$	$20^{+3.4}_{-4.8}$	$31^{+2.4}_{-2.6}$	0.689
500	J103532.2+575632	10 35 32.20	+57 56 32.8	0.632	0.497	$0.71^{+0.29}_{-0.51}$	$19^{+4.6}_{-5.2}$	$18^{+3.5}_{-4.9}$	4.010
501	J103532.2+574644	10 35 32.29	+57 46 44.7	0.160	0.130	$1.5^{+0.48}_{-0.66}$	$2.2^{+1}_{-1.9}$	$4^{+0.95}_{-1.5}$	0.393
502	J103533.1+574814	10 35 33.17	+57 48 14.0	0.225	0.112	$0.35^{+0.19}_{-0.39}$	$16^{+4.4}_{-4.5}$	$17^{+3.4}_{-5}$	6.075
503	J103533.8+573845	10 35 33.90	+57 38 45.8	0.483	0.744	$0.37^{+0.18}_{-0.48}$	$7^{+2.1}_{-4.1}$	$8.7^{+2.3}_{-3.3}$	2.931
504	J103534.0+574231	10 35 34.03	+57 42 31.4	0.359	0.379	$1.5^{+0.59}_{-0.84}$	$0.41^{+0.33}_{-1.6}$	$1.4^{+0.53}_{-0.97}$	0.116
505	J103534.3+574354	10 35 34.38	+57 43 54.6	0.485	0.169	$1.1^{+0.36}_{-0.56}$	$6^{+2.3}_{-2.5}$	$7.3^{+1.6}_{-2.4}$	1.129
506	J103535.0+575036	10 35 35.01	+57 50 36.7	0.291	0.173	$5^{+0.94}_{-1.2}$	$1.5^{+0.88}_{-1.3}$	$6.2^{+1.1}_{-1.3}$	0.125
507	J103536.1+575343	10 35 36.11	+57 53 43.3	0.851	0.644	<0.075	<0.34	$0.59^{+0.53}_{-0.94}$	0.958
508	J103536.4+574910	10 35 36.41	+57 49 10.1	0.140	0.222	$0.068^{+0.052}_{-0.34}$	$6.5^{+2.5}_{-4.2}$	$5.9^{+2.2}_{-3.8}$	10.87
509	J103539.7+574254	10 35 39.75	+57 42 54.4	0.353	0.166	$2.1^{+0.65}_{-0.74}$	$1.5^{+0.75}_{-1.7}$	$4.2^{+1.1}_{-1.2}$	0.231
510	J103540.0+574947	10 35 40.00	+57 49 47.0	0.202	0.088	$0.81^{+0.31}_{-0.52}$	$6.1^{+2.2}_{-2.8}$	$5.9^{+1.7}_{-2.2}$	1.442
511	J103540.8+575037	10 35 40.87	+57 50 37.6	0.371	0.270	$1.3^{+0.46}_{-0.57}$	$4.9^{+1.9}_{-2.4}$	$6.8^{+1.4}_{-2.2}$	0.811
512	J103543.8+574441	10 35 43.80	+57 44 41.4	0.204	0.149	$4.7^{+0.94}_{-1}$	$5.9^{+1.6}_{-2.9}$	$10^{+1.8}_{-2}$	0.359
513	J103547.2+574902	10 35 47.25	+57 49 02.1	0.250	0.268	$0.73^{+0.28}_{-0.61}$	$1.1^{+0.66}_{-1.7}$	$1.5^{+0.73}_{-0.86}$	0.402
514	J103547.8+574303	10 35 47.88	+57 43 03.6	0.329	0.249	$11^{+1.9}_{-2.1}$	$18^{+4.3}_{-6.3}$	$30^{+4.1}_{-5.3}$	0.451
515	J103548.6+574333	10 35 48.70	+57 43 33.3	0.491	0.362	$1.8^{+0.51}_{-0.67}$	$6.9^{+2}_{-3.3}$	$8.5^{+1.8}_{-2.3}$	0.851
516	J103550.8+575201	10 35 50.85	+57 52 01.1	0.924	0.475	$1^{+0.4}_{-0.52}$	$8.9^{+2.7}_{-3.6}$	$9.8^{+2.4}_{-2.6}$	1.602
517	J103551.0+574332	10 35 51.02	+57 43 33.0	0.107	0.091	$43^{+2.6}_{-2.9}$	$73^{+6.7}_{-7.6}$	$120^{+6}_{-6.4}$	0.450
518	J103600.7+574803	10 36 00.75	+57 48 03.6	0.464	0.303	$2^{+0.53}_{-0.66}$	$29^{+4.9}_{-6.1}$	$25^{+4.1}_{-4.3}$	2.460
519	J103601.8+574336	10 36 01.83	+57 43 36.1	0.637	0.463	$2.3^{+0.61}_{-0.75}$	$7.5^{+2}_{-3.4}$	$9.1^{+2}_{-2.1}$	0.734
520	J103602.1+575132	10 36 02.12	+57 51 32.8	1.363	0.623	$0.38^{+0.2}_{-0.43}$	$18^{+3.9}_{-6.1}$	$18^{+4.3}_{-4.5}$	6.164

Table A.1—Continued

#	name	α_{2000}	δ_{2000}	$\Delta\alpha('')$	$\Delta\delta('')$	$f_{0.4-2.0keV}$	$f_{2.0-8.0keV}$	$f_{0.4-8.0keV}$	HR
521	J103603.6+574813	10 36 03.63	+57 48 13.9	0.846	0.507	$2.6^{+0.67}_{-0.97}$	$0.89^{+0.54}_{-1.5}$	$3.4^{+0.78}_{-1.2}$	0.138
522	J103604.2+574748	10 36 04.22	+57 47 48.3	0.358	0.544	$2.4^{+0.58}_{-0.94}$	$1.9^{+1.2}_{-1.4}$	$4.4^{+1}_{-1.4}$	0.257
523	J103607.6+575009	10 36 07.61	+57 50 09.2	0.542	0.530	$1.1^{+0.35}_{-0.67}$	$46^{+7.4}_{-8.5}$	$45^{+7}_{-7.1}$	5.454
524	J103611.8+575055	10 36 11.84	+57 50 56.0	0.919	0.661	$4.1^{+0.81}_{-1.2}$	$3.7^{+1.3}_{-2.7}$	$8.9^{+1.6}_{-2.2}$	0.282
525	J103612.3+574624	10 36 12.39	+57 46 24.4	0.907	0.449	$1.7^{+0.52}_{-0.76}$	$2.2^{+1.3}_{-1.5}$	$4.6^{+1.1}_{-1.6}$	0.365

Table A.2. Main *Chandra* Catalog: Additional Source Properties

#	n_{soft}	n_{hard}	n_{full}	t_{soft}	t_{hard}	t_{full}	Field #s	Detections
1	$19.6^{+5.92}_{-4.07}$	$5.77^{+3.8}_{-2.17}$	$24.8^{+6.25}_{-4.78}$	3.22E+04	3.15E+04	3.21E+04	4	4
2	$10.8^{+4.56}_{-3.13}$	$7.27^{+3.49}_{-2.87}$	$12.8^{+4.89}_{-3.37}$	3.35E+04	3.25E+04	3.33E+04	4	4
3	$19.8^{+5.73}_{-4.25}$	$17^{+5.2}_{-4.09}$	$37.7^{+7.54}_{-5.82}$	3.37E+04	3.32E+04	3.37E+04	4	4
4	$16.5^{+5.68}_{-3.61}$	$1.45^{+1.83}_{-1.32}$	$20.9^{+5.8}_{-4.41}$	3.40E+04	3.30E+04	3.40E+04	4	4
5	$14.1^{+4.71}_{-3.82}$	$1.67^{+2.95}_{-0.996}$	$17.3^{+4.9}_{-4.4}$	3.22E+04	3.22E+04	3.24E+04	4	4
6	$23.3^{+5.57}_{-5.06}$	$24.1^{+5.88}_{-4.96}$	$44.7^{+8.01}_{-6.43}$	3.31E+04	3.29E+04	3.32E+04	4	4
7	$99.6^{+11.4}_{-9.62}$	$36.6^{+7.51}_{-5.69}$	$135^{+12.5}_{-11.7}$	3.46E+04	3.39E+04	3.45E+04	4	47
8	$7.72^{+4.22}_{-2.51}$	$6.93^{+3.83}_{-2.53}$	$15.3^{+4.63}_{-4.17}$	3.44E+04	3.50E+04	3.45E+04	4	4
9	$16.6^{+5.61}_{-3.68}$	$15.9^{+5.16}_{-3.89}$	$32.9^{+6.86}_{-5.67}$	3.60E+04	3.62E+04	3.63E+04	4	4
10	$2.06^{+2.57}_{-1.38}$	$1.17^{+2.12}_{-1.04}$	$5.13^{+3.24}_{-2.31}$	3.42E+04	3.43E+04	3.44E+04	4	4
11	$66^{+9.2}_{-8.07}$	$12^{+4.56}_{-3.42}$	$78.6^{+10.3}_{-8.49}$	2.85E+04	2.83E+04	2.81E+04	4	4
12	$14.1^{+4.74}_{-3.8}$	$7.83^{+4.11}_{-2.61}$	$18.8^{+5.68}_{-4.09}$	3.48E+04	3.43E+04	3.48E+04	4	4
13	$11.6^{+4.93}_{-3.05}$	$7.66^{+4.28}_{-2.44}$	$23.4^{+5.5}_{-5.13}$	3.17E+04	3.21E+04	3.21E+04	4	4
14	$14.7^{+5.27}_{-3.53}$	$2.24^{+2.39}_{-1.56}$	$17.8^{+5.52}_{-4.01}$	3.45E+04	3.44E+04	3.47E+04	4	4
15	$64.3^{+8.74}_{-8.28}$	$20.5^{+5.06}_{-4.93}$	$88.1^{+10.3}_{-9.51}$	3.27E+04	3.11E+04	3.25E+04	4	47
16	$159^{+13.9}_{-12.4}$	$73.1^{+9.48}_{-8.63}$	$232^{+16.7}_{-14.8}$	3.43E+04	3.37E+04	3.43E+04	4	47
17	$13.1^{+4.62}_{-3.65}$	$0.678^{+2.61}_{-0.544}$	$14.1^{+4.77}_{-3.76}$	3.16E+04	3.11E+04	3.25E+04	4	4
18	$5.3^{+3.08}_{-2.48}$	$0.892^{+2.4}_{-0.758}$	$6.93^{+3.83}_{-2.53}$	2.84E+04	2.95E+04	2.81E+04	4	4
19	$2.65^{+3.26}_{-1.31}$	$4.56^{+3.81}_{-1.74}$	$10.2^{+4.1}_{-3.28}$	2.90E+04	2.88E+04	2.90E+04	4	4
20	$38.3^{+6.88}_{-6.48}$	<5.4	$37.8^{+7.45}_{-5.91}$	3.51E+04	3.43E+04	3.50E+04	4	4
21	$7.62^{+4.32}_{-2.4}$	$10.5^{+3.81}_{-3.58}$	$17.1^{+5.06}_{-4.23}$	3.67E+04	3.64E+04	3.69E+04	4	4
22	$16.7^{+5.49}_{-3.8}$	$4.13^{+3.03}_{-2.06}$	$21.2^{+5.48}_{-4.73}$	3.67E+04	3.65E+04	3.69E+04	4	4
23	$14.9^{+5.02}_{-3.77}$	$6.64^{+4.12}_{-2.24}$	$22.9^{+5.96}_{-4.67}$	3.67E+04	3.65E+04	3.70E+04	4	4
24	$28.6^{+6.85}_{-4.96}$	$23.6^{+6.38}_{-4.46}$	$50.7^{+8.45}_{-6.86}$	3.58E+04	3.53E+04	3.58E+04	4	47
25	$9.91^{+4.35}_{-3.04}$	$0.0105^{+1.82}_{-0.0105}$	$11.4^{+3.99}_{-3.7}$	3.26E+04	3.16E+04	3.23E+04	4	4
26	$10.1^{+4.16}_{-3.22}$	$0.199^{+1.63}_{-0.199}$	$9.92^{+4.34}_{-3.04}$	3.21E+04	3.21E+04	3.22E+04	4	4
27	$17.1^{+5.13}_{-4.16}$	$4.81^{+3.56}_{-1.99}$	$23.6^{+6.35}_{-4.49}$	3.52E+04	3.55E+04	3.54E+04	4	4
28	$57.6^{+9.01}_{-7.24}$	$36.5^{+7.6}_{-5.6}$	$93.1^{+10.5}_{-9.76}$	3.39E+04	3.28E+04	3.38E+04	4	4
29	$262^{+17.1}_{-16.3}$	$143^{+13}_{-11.9}$	$390^{+21}_{-19.5}$	3.60E+04	3.53E+04	3.59E+04	4	4
30	$64.1^{+8.91}_{-8.11}$	$19.6^{+5.94}_{-4.05}$	$80.7^{+10.3}_{-8.73}$	3.01E+04	2.90E+04	2.96E+04	4	4
31	$7.84^{+4.1}_{-2.62}$	$4.99^{+3.38}_{-2.17}$	$12.7^{+5.02}_{-3.25}$	2.27E+04	2.21E+04	2.27E+04	7	7
32	$30^{+6.57}_{-5.41}$	$34.2^{+6.64}_{-6.05}$	$65.8^{+9.41}_{-7.86}$	3.41E+04	3.35E+04	3.43E+04	4	4
33	$18.8^{+5.59}_{-4.18}$	$10.6^{+4.83}_{-2.86}$	$28.4^{+5.98}_{-5.64}$	3.64E+04	3.61E+04	3.66E+04	4	4
34	$7.63^{+4.31}_{-2.41}$	$3.08^{+2.83}_{-1.74}$	$9.41^{+3.69}_{-3.37}$	3.32E+04	3.21E+04	3.29E+04	4	4
35	$15.6^{+5.49}_{-3.56}$	$18.9^{+5.49}_{-4.27}$	$30^{+6.49}_{-5.5}$	3.42E+04	3.40E+04	3.42E+04	4	4
36	$10.9^{+4.48}_{-3.21}$	$0.795^{+2.49}_{-0.661}$	$10.9^{+4.49}_{-3.2}$	3.34E+04	3.25E+04	3.32E+04	4	4
37	$11.5^{+3.92}_{-3.77}$	<5.13	$12.9^{+4.76}_{-3.5}$	3.22E+04	3.18E+04	3.13E+04	4	47
38	$8.07^{+3.87}_{-2.85}$	$10.3^{+3.96}_{-3.42}$	$16.6^{+5.57}_{-3.72}$	3.33E+04	3.35E+04	3.38E+04	4	4

Table A.2—Continued

#	n_{soft}	n_{hard}	n_{full}	t_{soft}	t_{hard}	t_{full}	Field #s	Detections
39	$3.93^{+3.22}_{-1.87}$	$14.8^{+5.12}_{-3.67}$	$18.3^{+5.01}_{-4.52}$	3.72E+04	3.72E+04	3.75E+04	4	4
40	$89.5^{+9.98}_{-9.91}$	$41.7^{+7.88}_{-6.11}$	$125^{+12.2}_{-11.2}$	3.60E+04	3.58E+04	3.62E+04	4	47
41	$97.1^{+10.7}_{-9.97}$	$33.9^{+6.94}_{-5.75}$	$129^{+12}_{-11.7}$	3.28E+04	3.28E+04	3.28E+04	4	47
42	$10.8^{+4.61}_{-3.08}$	$15^{+4.92}_{-3.87}$	$26.3^{+5.91}_{-5.32}$	3.27E+04	3.26E+04	3.27E+04	7	7
43	$15.8^{+5.23}_{-3.81}$	$29.6^{+6.95}_{-5.04}$	$45.7^{+8.18}_{-6.41}$	3.44E+04	3.47E+04	3.49E+04	4	47
44	$39.2^{+7.08}_{-6.44}$	$8.74^{+4.37}_{-2.7}$	$46.5^{+8.36}_{-6.38}$	3.51E+04	3.49E+04	3.51E+04	7	47
45	$86.4^{+9.86}_{-9.71}$	$94.9^{+10.9}_{-9.6}$	$180^{+14.9}_{-13}$	3.79E+04	3.85E+04	3.84E+04	4	4
46	$85.6^{+10.8}_{-8.81}$	$28.9^{+6.5}_{-5.31}$	$110^{+11.9}_{-10.1}$	3.52E+04	3.48E+04	3.51E+04	7	7
47	$25.3^{+5.72}_{-5.32}$	$5.67^{+3.9}_{-2.07}$	$30.8^{+6.83}_{-5.34}$	3.49E+04	3.40E+04	3.47E+04	4	4
48	$31^{+6.67}_{-5.5}$	$104^{+11.7}_{-9.76}$	$129^{+12.3}_{-11.4}$	3.52E+04	3.49E+04	3.52E+04	4	47
49	$3.83^{+3.32}_{-1.77}$	$3.7^{+3.46}_{-1.64}$	$7.03^{+3.73}_{-2.63}$	3.85E+04	3.76E+04	3.85E+04	4	4
50	$51.6^{+8.64}_{-6.8}$	$29.6^{+6.91}_{-5.08}$	$76.8^{+9.96}_{-8.61}$	3.51E+04	3.48E+04	3.52E+04	4	47
51	$9.89^{+4.37}_{-3.01}$	$5.45^{+2.92}_{-2.63}$	$15.7^{+5.34}_{-3.71}$	3.76E+04	3.78E+04	3.78E+04	4	4
52	$157^{+13.7}_{-12.4}$	$73.9^{+9.71}_{-8.52}$	$227^{+15.6}_{-15.5}$	3.57E+04	3.51E+04	3.57E+04	4	4
53	$33.3^{+6.55}_{-5.97}$	$28.7^{+6.74}_{-5.07}$	$65^{+9.14}_{-8.01}$	3.48E+04	3.42E+04	3.46E+04	7	67
54	$6.97^{+3.8}_{-2.56}$	$3.68^{+3.47}_{-1.62}$	$10.6^{+4.82}_{-2.87}$	3.77E+04	3.74E+04	3.79E+04	4	4
55	$1.71^{+2.92}_{-1.03}$	$3.43^{+2.48}_{-2.09}$	$5.01^{+3.36}_{-2.19}$	3.59E+04	3.55E+04	3.59E+04	4	4
56	$3.83^{+3.32}_{-1.77}$	$1.02^{+2.27}_{-0.882}$	$3.41^{+2.5}_{-2.07}$	3.56E+04	3.53E+04	3.53E+04	4	4
57	$3.03^{+2.88}_{-1.69}$	$3.34^{+2.57}_{-2}$	$5.85^{+3.73}_{-2.25}$	3.68E+04	3.82E+04	3.83E+04	4	4
58	$29.2^{+6.27}_{-5.54}$	$2.9^{+3.01}_{-1.55}$	$33.2^{+6.57}_{-5.95}$	3.54E+04	3.58E+04	3.56E+04	7	47
59	$19.6^{+5.97}_{-4.02}$	$9.04^{+4.07}_{-3}$	$25.5^{+6.65}_{-4.59}$	3.59E+04	3.57E+04	3.59E+04	7	7
60	$21.5^{+6.24}_{-4.18}$	$9.7^{+4.56}_{-2.83}$	$30.1^{+6.46}_{-5.53}$	3.59E+04	3.62E+04	3.61E+04	7	47
61	$2.46^{+2.17}_{-1.78}$	$1.24^{+2.05}_{-1.1}$	$5.7^{+3.88}_{-2.09}$	3.68E+04	3.70E+04	3.71E+04	4	4
62	$32.2^{+6.49}_{-5.85}$	$17.6^{+5.71}_{-3.82}$	$47.9^{+8.12}_{-6.77}$	3.71E+04	3.70E+04	3.73E+04	4	247
63	$9.32^{+3.79}_{-3.28}$	$6.33^{+3.25}_{-2.73}$	$17^{+5.16}_{-4.13}$	3.60E+04	3.55E+04	3.59E+04	7	7
64	$5.05^{+3.33}_{-2.23}$	$3.33^{+2.58}_{-1.99}$	$9.34^{+3.76}_{-3.3}$	3.51E+04	3.55E+04	3.53E+04	7	7
65	$2.68^{+3.23}_{-1.34}$	$1.7^{+2.93}_{-1.02}$	$4.77^{+3.61}_{-1.95}$	3.58E+04	3.47E+04	3.57E+04	4	4
66	$5.6^{+3.98}_{-2}$	<2.5	$5.11^{+3.27}_{-2.29}$	3.63E+04	3.67E+04	3.65E+04	7	47
67	$14.6^{+5.33}_{-3.47}$	$17.4^{+4.79}_{-4.51}$	$31.4^{+6.24}_{-5.92}$	3.70E+04	3.65E+04	3.71E+04	4	4
68	$4.82^{+3.56}_{-2}$	$7.75^{+4.19}_{-2.54}$	$10.6^{+4.77}_{-2.92}$	1.61E+04	1.63E+04	1.50E+04	7	7
69	$24.6^{+6.46}_{-4.58}$	$25.6^{+6.58}_{-4.65}$	$45.8^{+7.98}_{-6.61}$	3.36E+04	3.32E+04	3.35E+04	7	7
70	$18.6^{+5.83}_{-3.93}$	$7.02^{+3.75}_{-2.62}$	$24^{+6.01}_{-4.83}$	3.35E+04	3.30E+04	3.34E+04	4	4
71	$32^{+6.74}_{-5.6}$	$38.9^{+7.43}_{-6.09}$	$71.6^{+9.97}_{-8.02}$	3.30E+04	3.25E+04	3.34E+04	7	67
72	$2.33^{+2.3}_{-1.65}$	$3.26^{+2.65}_{-1.92}$	$3.82^{+3.34}_{-1.76}$	2.79E+04	2.70E+04	2.75E+04	6	6
73	$1.91^{+2.72}_{-1.23}$	$6.42^{+3.16}_{-2.82}$	$10.3^{+3.96}_{-3.43}$	3.58E+04	3.54E+04	3.58E+04	7	7
74	$4^{+3.16}_{-1.93}$	$9.04^{+4.06}_{-3}$	$13.5^{+5.31}_{-3.22}$	3.44E+04	3.37E+04	3.45E+04	4	4
75	$463^{+22.6}_{-21.4}$	$144^{+13.2}_{-11.8}$	$601^{+25.4}_{-24.7}$	3.28E+04	3.23E+04	3.28E+04	7	7
76	$16.8^{+5.36}_{-3.93}$	$19.8^{+5.72}_{-4.27}$	$36.6^{+7.52}_{-5.67}$	3.67E+04	3.70E+04	3.69E+04	7	7

Table A.2—Continued

#	n_{soft}	n_{hard}	n_{full}	t_{soft}	t_{hard}	t_{full}	Field #s	Detections
77	$9.92^{+4.34}_{-3.05}$	$11.4^{+4}_{-3.69}$	$20^{+5.52}_{-4.46}$	3.57E+04	3.53E+04	3.56E+04	7	7
78	$21.9^{+5.85}_{-4.57}$	$6.23^{+3.34}_{-2.63}$	$28.8^{+6.67}_{-5.13}$	3.73E+04	3.67E+04	3.75E+04	4	247
79	$2.12^{+2.5}_{-1.45}$	<9.07	<6.28	2.99E+04	2.90E+04	2.95E+04	7	7
80	$2.15^{+2.48}_{-1.47}$	$9.99^{+4.27}_{-3.11}$	$11.6^{+4.97}_{-3.01}$	3.67E+04	3.59E+04	3.67E+04	4	4
81	$36.9^{+7.27}_{-5.93}$	$14.3^{+4.52}_{-4.01}$	$48.7^{+8.31}_{-6.71}$	3.54E+04	3.47E+04	3.53E+04	4	4
82	$9.44^{+3.66}_{-3.4}$	$9.21^{+3.9}_{-3.16}$	$16.3^{+4.73}_{-4.32}$	2.67E+04	2.57E+04	2.63E+04	6	6
83	$9.87^{+4.39}_{-2.99}$	<6.56	$8.94^{+4.16}_{-2.9}$	3.70E+04	3.69E+04	3.70E+04	7	7
84	$3.83^{+3.32}_{-1.77}$	$0.172^{+1.65}_{-0.172}$	$3.52^{+3.64}_{-1.45}$	3.43E+04	3.39E+04	3.44E+04	4	4
85	$9.64^{+4.62}_{-2.77}$	$7.96^{+3.98}_{-2.75}$	$15^{+4.93}_{-3.86}$	3.39E+04	3.31E+04	3.39E+04	4	4
86	$23.3^{+5.56}_{-5.07}$	$11.8^{+4.79}_{-3.19}$	$34.1^{+6.79}_{-5.9}$	3.69E+04	3.61E+04	3.70E+04	4	24
87	$43.4^{+7.17}_{-6.97}$	$21.2^{+5.46}_{-4.74}$	$62.9^{+9.08}_{-7.82}$	3.68E+04	3.60E+04	3.68E+04	4	247
88	$3.03^{+2.88}_{-1.69}$	<5.94	$2.82^{+3.09}_{-1.48}$	3.53E+04	3.25E+04	3.55E+04	4	4
89	$126^{+12.6}_{-10.9}$	$50.1^{+8.06}_{-7.1}$	$176^{+14.7}_{-12.9}$	3.34E+04	3.25E+04	3.30E+04	7	67
90	$5.63^{+3.94}_{-2.03}$	$1.39^{+1.89}_{-1.26}$	$5.84^{+3.74}_{-2.24}$	3.68E+04	3.60E+04	3.69E+04	4	4
91	$2.82^{+3.09}_{-1.48}$	$1.6^{+3.02}_{-0.927}$	$7.14^{+3.63}_{-2.74}$	3.69E+04	3.61E+04	3.69E+04	4	4
92	$17.6^{+5.73}_{-3.8}$	$7.82^{+4.12}_{-2.6}$	$22.5^{+5.29}_{-5.13}$	3.58E+04	3.50E+04	3.57E+04	4	24
93	$25.3^{+5.79}_{-5.25}$	$5.87^{+3.71}_{-2.27}$	$26.3^{+5.83}_{-5.4}$	2.86E+04	2.71E+04	2.75E+04	6	6
94	$25.7^{+6.47}_{-4.77}$	$34.7^{+7.26}_{-5.6}$	$57^{+8.56}_{-7.57}$	3.46E+04	3.40E+04	3.45E+04	2	24
95	$77.8^{+10.1}_{-8.61}$	$33.5^{+6.31}_{-6.22}$	$110^{+11.4}_{-10.6}$	3.25E+04	3.10E+04	3.19E+04	4	4
96	$8.87^{+4.23}_{-2.83}$	$1.72^{+2.9}_{-1.05}$	$10.1^{+4.11}_{-3.27}$	3.74E+04	3.75E+04	3.75E+04	7	7
97	$7.89^{+4.05}_{-2.68}$	$5.7^{+3.88}_{-2.1}$	$16.3^{+4.75}_{-4.3}$	3.66E+04	3.60E+04	3.64E+04	4	4
98	$5.85^{+3.73}_{-2.25}$	$7.86^{+4.08}_{-2.64}$	$13.5^{+5.31}_{-3.22}$	3.73E+04	3.80E+04	3.77E+04	7	7
99	$192^{+15.3}_{-13.4}$	$92.7^{+11}_{-9.35}$	$266^{+17.4}_{-16.2}$	3.66E+04	3.61E+04	3.67E+04	4	247
100	$21.4^{+5.3}_{-4.91}$	$7.08^{+3.68}_{-2.68}$	$28.3^{+6.02}_{-5.6}$	3.65E+04	3.65E+04	3.66E+04	7	67
101	$10.4^{+3.87}_{-3.52}$	$10.1^{+4.15}_{-3.23}$	$21.1^{+5.52}_{-4.69}$	2.89E+04	2.83E+04	2.87E+04	6	6
102	$46.4^{+7.44}_{-7.15}$	$12.4^{+4.19}_{-3.79}$	$56.7^{+8.92}_{-7.2}$	3.62E+04	3.61E+04	3.62E+04	2	24
103	$6.36^{+3.21}_{-2.76}$	$9.44^{+3.66}_{-3.4}$	$15.6^{+5.44}_{-3.61}$	3.59E+04	3.54E+04	3.60E+04	4	4
104	$14.8^{+5.18}_{-3.62}$	$4.48^{+2.68}_{-2.41}$	$20.6^{+6.06}_{-4.15}$	3.57E+04	3.51E+04	3.57E+04	4	47
105	$8.29^{+3.65}_{-3.08}$	$10.1^{+4.21}_{-3.18}$	$18.5^{+5.93}_{-3.83}$	3.13E+04	3.01E+04	3.09E+04	4	4
106	$27.6^{+6.73}_{-4.89}$	$6.08^{+3.49}_{-2.48}$	$32.1^{+6.66}_{-5.69}$	2.92E+04	2.86E+04	2.89E+04	6	6
107	$3.93^{+3.22}_{-1.87}$	$0.502^{+2.79}_{-0.368}$	$5.42^{+2.95}_{-2.6}$	3.54E+04	3.54E+04	3.59E+04	7	7
108	$3.73^{+3.43}_{-1.66}$	$6.18^{+3.4}_{-2.58}$	$8.95^{+4.16}_{-2.91}$	3.80E+04	3.85E+04	3.83E+04	7	7
109	$9.76^{+4.5}_{-2.88}$	$10.6^{+4.81}_{-2.88}$	$20.1^{+5.46}_{-4.52}$	3.60E+04	3.54E+04	3.61E+04	4	24
110	$39.3^{+7.01}_{-6.51}$	$26.2^{+5.92}_{-5.32}$	$66.2^{+8.92}_{-8.36}$	3.78E+04	3.75E+04	3.77E+04	7	247
111	$10.3^{+3.94}_{-3.45}$	<6.67	$10.3^{+3.93}_{-3.46}$	2.94E+04	2.87E+04	2.91E+04	6	6
112	$14.2^{+4.59}_{-3.94}$	$1.82^{+2.81}_{-1.14}$	$17.4^{+4.79}_{-4.5}$	2.94E+04	2.88E+04	2.92E+04	6	6
113	$2.91^{+2.99}_{-1.57}$	$7.43^{+3.33}_{-3.03}$	$8.17^{+3.77}_{-2.95}$	3.67E+04	3.62E+04	3.65E+04	7	7
114	$138^{+12.6}_{-11.9}$	$30.7^{+6.89}_{-5.28}$	168^{+14}_{-13}	2.90E+04	2.80E+04	2.86E+04	6	6

Table A.2—Continued

#	n_{soft}	n_{hard}	n_{full}	t_{soft}	t_{hard}	t_{full}	Field #s	Detections
115	$5.85^{+3.73}_{-2.25}$	$2.02^{+2.61}_{-1.34}$	$10.3^{+3.99}_{-3.39}$	3.70E+04	3.77E+04	3.84E+04	7	7
116	$12.3^{+4.21}_{-3.78}$	$0.543^{+2.74}_{-0.409}$	$15^{+4.91}_{-3.89}$	3.71E+04	3.71E+04	3.72E+04	2	2
117	$7.5^{+4.44}_{-2.28}$	$0.155^{+1.67}_{-0.155}$	$7.27^{+3.5}_{-2.86}$	3.36E+04	3.45E+04	3.35E+04	2	2
118	$5.75^{+3.83}_{-2.14}$	$1.66^{+2.97}_{-0.982}$	$7.56^{+4.38}_{-2.34}$	3.79E+04	3.85E+04	3.82E+04	7	7
119	$10.7^{+4.74}_{-2.95}$	$5.39^{+2.98}_{-2.57}$	$18^{+5.31}_{-4.22}$	2.88E+04	2.86E+04	2.87E+04	6	67
120	$192^{+15.1}_{-13.6}$	$83^{+10.1}_{-9.11}$	$270^{+17.9}_{-16}$	2.93E+04	2.91E+04	2.92E+04	6	67
121	$71.8^{+9.7}_{-8.3}$	$40.9^{+7.58}_{-6.26}$	$110^{+11.4}_{-10.6}$	3.53E+04	3.50E+04	3.54E+04	4	247
122	$9.85^{+4.41}_{-2.97}$	$4.25^{+2.9}_{-2.19}$	$12.3^{+4.3}_{-3.68}$	3.62E+04	3.61E+04	3.63E+04	2	24
123	$11.7^{+4.82}_{-3.16}$	<6.6	$14.5^{+4.33}_{-4.2}$	3.73E+04	3.75E+04	3.75E+04	2	24
124	$10^{+4.26}_{-3.12}$	$2.95^{+2.96}_{-1.6}$	$12.4^{+4.16}_{-3.83}$	3.85E+04	3.83E+04	3.85E+04	7	7
125	$11.5^{+3.94}_{-3.75}$	$7.58^{+4.36}_{-2.37}$	$20.6^{+6.04}_{-4.17}$	3.61E+04	3.61E+04	3.61E+04	7	7
126	$7.87^{+4.07}_{-2.65}$	$2.28^{+2.34}_{-1.61}$	$10.5^{+3.78}_{-3.6}$	3.54E+04	3.60E+04	3.53E+04	7	7
127	$0.905^{+2.38}_{-0.771}$	$12.3^{+4.27}_{-3.71}$	$11.6^{+4.96}_{-3.02}$	3.77E+04	3.74E+04	3.76E+04	7	7
128	$4.66^{+3.71}_{-1.84}$	$22.1^{+5.62}_{-4.8}$	$24.5^{+5.51}_{-5.33}$	3.52E+04	3.48E+04	3.53E+04	4	247
129	$41.9^{+7.63}_{-6.36}$	$24.2^{+5.77}_{-5.07}$	$65.9^{+9.3}_{-7.97}$	3.63E+04	3.55E+04	3.61E+04	2	127
130	$9.97^{+4.29}_{-3.09}$	<4.77	$10.6^{+4.84}_{-2.85}$	1.71E+04	1.67E+04	1.72E+04	2	2
131	$34.6^{+7.34}_{-5.53}$	$7.67^{+4.27}_{-2.45}$	$44.4^{+7.31}_{-6.99}$	2.88E+04	2.82E+04	2.86E+04	6	6
132	$17.2^{+5.03}_{-4.26}$	<13.3	$19.7^{+5.8}_{-4.19}$	3.06E+04	2.94E+04	3.01E+04	4	4
133	$69.6^{+9.83}_{-7.93}$	$38.4^{+6.83}_{-6.53}$	$101^{+10.6}_{-10.5}$	3.34E+04	3.31E+04	3.32E+04	7	7
134	$130^{+12.7}_{-11.1}$	$55.9^{+8.67}_{-7.32}$	$185^{+15}_{-13.2}$	3.60E+04	3.51E+04	3.57E+04	2	127
135	$3.94^{+3.22}_{-1.87}$	<2.85	$5.85^{+3.73}_{-2.25}$	3.61E+04	3.73E+04	3.64E+04	7	7
136	$6.72^{+4.05}_{-2.31}$	$8.56^{+4.55}_{-2.52}$	$13.6^{+5.21}_{-3.32}$	3.78E+04	3.80E+04	3.81E+04	2	24
137	$4.82^{+3.56}_{-2}$	$6.47^{+3.1}_{-2.87}$	$7.61^{+4.33}_{-2.4}$	2.99E+04	2.97E+04	2.98E+04	6	6
138	$14.7^{+5.24}_{-3.55}$	$3.61^{+3.54}_{-1.55}$	$20.1^{+5.43}_{-4.56}$	3.73E+04	3.77E+04	3.75E+04	7	67
139	$6.91^{+3.86}_{-2.51}$	$7.62^{+4.31}_{-2.41}$	$12.1^{+4.41}_{-3.57}$	3.61E+04	3.58E+04	3.61E+04	2	24
140	$49.1^{+7.94}_{-7.09}$	$19.4^{+5.04}_{-4.72}$	$67.1^{+9.08}_{-8.31}$	3.02E+04	2.94E+04	2.98E+04	6	6
141	$12.8^{+4.91}_{-3.35}$	<4.21	$12.9^{+4.82}_{-3.44}$	3.02E+04	3.01E+04	3.02E+04	6	6
142	$7.83^{+4.11}_{-2.61}$	<4.58	$9.1^{+4}_{-3.06}$	2.78E+04	2.69E+04	2.77E+04	6	6
143	$19.1^{+5.36}_{-4.41}$	$8.91^{+4.2}_{-2.87}$	$25.3^{+5.73}_{-5.31}$	2.83E+04	2.82E+04	2.81E+04	6	6
144	$6.96^{+3.81}_{-2.55}$	$3.86^{+3.29}_{-1.8}$	$10.4^{+3.84}_{-3.54}$	3.83E+04	3.85E+04	3.86E+04	2	2
145	$0.778^{+2.51}_{-0.644}$	$9.32^{+3.79}_{-3.27}$	$6.92^{+3.84}_{-2.52}$	3.64E+04	3.60E+04	3.62E+04	7	27
146	$21.1^{+5.6}_{-4.61}$	$19.3^{+5.1}_{-4.66}$	$39.4^{+6.86}_{-6.66}$	3.82E+04	3.75E+04	3.81E+04	2	1247
147	$11.4^{+3.98}_{-3.71}$	$1.64^{+2.99}_{-0.959}$	$14.1^{+4.71}_{-3.82}$	3.59E+04	3.63E+04	3.60E+04	2	2
148	$30.4^{+6.18}_{-5.81}$	$8.5^{+3.44}_{-3.28}$	$37.7^{+7.54}_{-5.82}$	2.78E+04	2.69E+04	2.75E+04	6	6
149	$2.46^{+2.17}_{-1.78}$	<4.76	$2.78^{+3.12}_{-1.44}$	3.87E+04	3.87E+04	3.89E+04	2	2
150	$49^{+8.03}_{-7}$	$13.3^{+4.42}_{-3.84}$	$59.4^{+8.31}_{-8.08}$	2.72E+04	2.65E+04	2.73E+04	6	6
151	$19^{+5.45}_{-4.31}$	$10.6^{+4.78}_{-2.91}$	$28.6^{+6.88}_{-4.92}$	3.76E+04	3.64E+04	3.73E+04	7	27
152	$6.86^{+3.9}_{-2.46}$	$1.14^{+2.15}_{-1}$	$8.95^{+4.16}_{-2.91}$	3.79E+04	3.70E+04	3.77E+04	7	7

Table A.2—Continued

#	n_{soft}	n_{hard}	n_{full}	t_{soft}	t_{hard}	t_{full}	Field #s	Detections
153	$3.82^{+3.34}_{-1.75}$	$5.55^{+4.03}_{-1.95}$	$9.2^{+3.9}_{-3.16}$	3.03E+04	3.04E+04	3.04E+04	6	6
154	$12.4^{+4.15}_{-3.84}$	$5.44^{+2.94}_{-2.62}$	$17.6^{+5.69}_{-3.84}$	3.45E+04	3.39E+04	3.42E+04	7	247
155	$48.9^{+8.13}_{-6.89}$	$18^{+5.32}_{-4.21}$	$68.2^{+9.1}_{-8.41}$	3.62E+04	3.57E+04	3.60E+04	7	1247
156	$1.91^{+2.72}_{-1.23}$	$0.502^{+2.79}_{-0.368}$	$2.7^{+3.2}_{-1.36}$	3.05E+04	3.07E+04	3.06E+04	6	6
157	$41.1^{+7.35}_{-6.48}$	$26.9^{+6.35}_{-5.08}$	$64.6^{+9.49}_{-7.65}$	3.75E+04	3.68E+04	3.74E+04	7	167
158	$10^{+4.26}_{-3.12}$	$1.14^{+2.15}_{-1}$	$12^{+4.58}_{-3.41}$	3.75E+04	3.69E+04	3.74E+04	7	7
159	$4.95^{+3.43}_{-2.13}$	$0.649^{+2.64}_{-0.515}$	$5.43^{+2.94}_{-2.61}$	3.74E+04	3.63E+04	3.72E+04	7	7
160	$9.7^{+4.56}_{-2.82}$	$6.31^{+3.26}_{-2.71}$	$14.4^{+4.42}_{-4.11}$	3.19E+04	3.10E+04	3.15E+04	5	5
161	$7.57^{+4.37}_{-2.36}$	$1.35^{+1.93}_{-1.22}$	$7.82^{+4.12}_{-2.6}$	3.39E+04	3.39E+04	3.39E+04	7	7
162	$9.79^{+4.48}_{-2.91}$	$3.4^{+2.5}_{-2.06}$	$13.4^{+4.29}_{-3.98}$	3.04E+04	3.06E+04	3.05E+04	6	6
163	$5.05^{+3.32}_{-2.23}$	$3.02^{+2.89}_{-1.68}$	$6.76^{+4.01}_{-2.35}$	3.58E+04	3.52E+04	3.57E+04	7	7
164	$3.94^{+3.22}_{-1.87}$	<3.78	$4.53^{+3.85}_{-1.71}$	3.71E+04	3.64E+04	3.70E+04	7	7
165	$70.9^{+9.56}_{-8.31}$	$41.7^{+7.81}_{-6.18}$	$112^{+11.1}_{-11}$	3.43E+04	3.33E+04	3.39E+04	5	25
166	$32.5^{+7.28}_{-5.24}$	$22.8^{+6.05}_{-4.58}$	$55^{+8.47}_{-7.39}$	2.91E+04	2.83E+04	2.87E+04	6	6
167	$4.7^{+3.68}_{-1.88}$	$6.01^{+3.57}_{-2.4}$	$10.9^{+4.46}_{-3.23}$	3.01E+04	2.99E+04	3.03E+04	6	6
168	$5.85^{+3.73}_{-2.25}$	$4.68^{+3.69}_{-1.86}$	$6.22^{+3.35}_{-2.62}$	3.68E+04	3.69E+04	3.57E+04	2	2
169	$4.84^{+3.53}_{-2.02}$	$0.781^{+2.51}_{-0.647}$	$6.65^{+4.11}_{-2.25}$	3.82E+04	3.81E+04	3.82E+04	2	2
170	$8.98^{+4.13}_{-2.93}$	$24.1^{+5.9}_{-4.94}$	$30.5^{+7.11}_{-5.06}$	3.66E+04	3.60E+04	3.65E+04	7	167
171	$28.8^{+6.67}_{-5.14}$	$3.92^{+3.23}_{-1.86}$	$32.4^{+6.28}_{-6.06}$	3.85E+04	3.83E+04	3.85E+04	2	127
172	$5.75^{+3.83}_{-2.14}$	$9.87^{+4.39}_{-2.99}$	$11.3^{+4.13}_{-3.56}$	3.86E+04	3.88E+04	3.87E+04	2	2
173	$3.58^{+3.58}_{-1.52}$	$3.66^{+3.5}_{-1.59}$	$5.25^{+3.12}_{-2.43}$	3.93E+04	3.91E+04	3.94E+04	2	2
174	$5.75^{+3.83}_{-2.14}$	$11.6^{+4.93}_{-3.06}$	$9.26^{+3.84}_{-3.22}$	3.87E+04	3.82E+04	3.86E+04	2	2
175	$24.1^{+5.83}_{-5.01}$	$14.3^{+4.56}_{-3.97}$	$41.3^{+7.14}_{-6.69}$	3.16E+04	3.16E+04	3.16E+04	6	6
176	$60.3^{+8.5}_{-8.02}$	$6.5^{+3.08}_{-2.9}$	$67.2^{+9.07}_{-8.32}$	4.04E+04	4.07E+04	4.07E+04	2	247
177	$2.82^{+3.09}_{-1.48}$	$1.98^{+2.65}_{-1.3}$	$5.64^{+3.94}_{-2.04}$	2.65E+04	2.60E+04	2.60E+04	6	6
178	$5.64^{+3.94}_{-2.04}$	$6.75^{+4.01}_{-2.35}$	$10.1^{+4.2}_{-3.19}$	3.00E+04	2.99E+04	2.99E+04	6	6
179	$4.03^{+3.13}_{-1.96}$	$19.8^{+5.72}_{-4.27}$	$23.9^{+6.03}_{-4.81}$	6.71E+04	6.45E+04	6.63E+04	1	1
180	$3.71^{+3.44}_{-1.65}$	<5.02	$4.4^{+2.76}_{-2.33}$	2.94E+04	2.91E+04	2.92E+04	6	6
181	$29.2^{+6.2}_{-5.6}$	$5.14^{+3.23}_{-2.32}$	$32.8^{+7.01}_{-5.51}$	3.50E+04	3.42E+04	3.47E+04	5	25
182	$22.9^{+5.98}_{-4.65}$	$7.23^{+3.53}_{-2.83}$	$28.9^{+6.54}_{-5.27}$	3.91E+04	3.90E+04	3.92E+04	2	127
183	$5.32^{+3.05}_{-2.5}$	$18.6^{+5.87}_{-3.89}$	$18.7^{+5.76}_{-4}$	6.66E+04	6.46E+04	6.64E+04	1	1
184	$1.01^{+2.28}_{-0.876}$	$6.97^{+3.8}_{-2.56}$	$6.86^{+3.9}_{-2.46}$	3.97E+04	4.00E+04	3.99E+04	2	2
185	<0.752	$7.03^{+3.73}_{-2.63}$	$5.15^{+3.23}_{-2.33}$	3.64E+04	3.60E+04	3.63E+04	7	7
186	$57.4^{+8.23}_{-7.9}$	$31.1^{+6.54}_{-5.63}$	$90.5^{+10}_{-9.96}$	3.34E+04	3.29E+04	3.32E+04	2	25
187	$0.423^{+1.4}_{-0.423}$	$4.25^{+2.9}_{-2.19}$	$6.79^{+3.97}_{-2.39}$	3.89E+04	3.88E+04	3.90E+04	2	127
188	$2.33^{+2.3}_{-1.65}$	$7.62^{+4.31}_{-2.41}$	$11.6^{+4.95}_{-3.03}$	3.89E+04	3.88E+04	3.90E+04	2	2
189	$14^{+4.79}_{-3.74}$	$8.72^{+4.38}_{-2.68}$	$22^{+5.74}_{-4.68}$	3.69E+04	3.63E+04	3.68E+04	2	25
190	$3.83^{+3.32}_{-1.77}$	<3.72	$4.73^{+3.64}_{-1.91}$	3.97E+04	4.00E+04	4.00E+04	2	2

Table A.2—Continued

#	n_{soft}	n_{hard}	n_{full}	t_{soft}	t_{hard}	t_{full}	Field #s	Detections
191	$6.96^{+3.8}_{-2.56}$	$3.72^{+3.43}_{-1.66}$	$8.53^{+4.57}_{-2.49}$	3.09E+04	3.01E+04	3.05E+04	6	6
192	$7.8^{+4.14}_{-2.58}$	<9.72	$6.51^{+4.25}_{-2.11}$	2.80E+04	2.69E+04	2.75E+04	6	6
193	$17.1^{+5.13}_{-4.16}$	$5.71^{+3.86}_{-2.11}$	$22.8^{+6.05}_{-4.58}$	4.07E+04	4.03E+04	4.07E+04	2	2
194	$10.9^{+4.55}_{-3.14}$	$7.45^{+3.31}_{-3.05}$	$19.3^{+5.11}_{-4.65}$	3.03E+04	2.99E+04	3.01E+04	6	6
195	$6.28^{+3.3}_{-2.67}$	<5.43	$6.57^{+4.19}_{-2.17}$	3.46E+04	3.42E+04	3.44E+04	5	5
196	$4.74^{+3.64}_{-1.92}$	$0.79^{+2.5}_{-0.656}$	$6.34^{+3.24}_{-2.73}$	3.01E+04	3.02E+04	3.02E+04	6	6
197	$5.64^{+3.94}_{-2.04}$	$2.32^{+2.31}_{-1.64}$	$7.45^{+3.31}_{-3.05}$	3.25E+04	3.13E+04	3.20E+04	2	2
198	$4.27^{+2.89}_{-2.2}$	$2.34^{+2.28}_{-1.67}$	$4.67^{+3.7}_{-1.85}$	6.29E+04	6.17E+04	6.25E+04	1	1
199	$11.9^{+4.67}_{-3.31}$	$2.77^{+3.14}_{-1.43}$	$15.6^{+5.5}_{-3.54}$	3.02E+04	2.93E+04	2.98E+04	6	167
200	$18.1^{+5.26}_{-4.27}$	$16.1^{+4.94}_{-4.11}$	$33.1^{+6.74}_{-5.79}$	3.34E+04	3.27E+04	3.31E+04	5	5
201	$1.13^{+2.15}_{-0.999}$	$11.5^{+5.01}_{-2.97}$	$10.3^{+3.92}_{-3.47}$	3.85E+04	3.83E+04	3.85E+04	2	12
202	$42.6^{+7.99}_{-6.15}$	$8.71^{+4.39}_{-2.67}$	$51.3^{+7.91}_{-7.4}$	3.50E+04	3.47E+04	3.49E+04	5	5
203	$11.6^{+4.95}_{-3.03}$	$2.47^{+2.16}_{-1.79}$	$17.2^{+4.97}_{-4.32}$	6.56E+04	6.38E+04	6.49E+04	1	1
204	$31.9^{+6.8}_{-5.54}$	$21.7^{+6.05}_{-4.38}$	$52.5^{+7.8}_{-7.65}$	3.41E+04	3.29E+04	3.32E+04	5	25
205	$103^{+11.6}_{-9.74}$	$36.5^{+7.59}_{-5.6}$	$139^{+12.7}_{-11.9}$	3.50E+04	3.47E+04	3.49E+04	5	5
206	$6.85^{+3.92}_{-2.44}$	$4.4^{+2.75}_{-2.34}$	$11.4^{+3.97}_{-3.72}$	3.07E+04	2.99E+04	3.01E+04	6	167
207	$11.2^{+4.22}_{-3.47}$	$6.77^{+3.99}_{-2.37}$	$17.3^{+4.91}_{-4.38}$	3.44E+04	3.40E+04	3.42E+04	5	5
208	$52.4^{+7.83}_{-7.61}$	$11^{+4.4}_{-3.29}$	$65.4^{+8.65}_{-8.49}$	3.10E+04	3.10E+04	3.10E+04	6	6
209	$35.9^{+7.11}_{-5.92}$	$23.4^{+5.5}_{-5.13}$	$60.9^{+8.97}_{-7.68}$	3.77E+04	3.74E+04	3.79E+04	2	25
210	$13^{+4.7}_{-3.56}$	$8.56^{+4.55}_{-2.51}$	$20.9^{+5.73}_{-4.48}$	3.55E+04	3.52E+04	3.54E+04	5	5
211	$18.4^{+4.88}_{-4.65}$	$2.42^{+2.2}_{-1.75}$	$22.1^{+5.67}_{-4.75}$	3.40E+04	3.35E+04	3.38E+04	5	5
212	$44.3^{+7.39}_{-6.91}$	$15.2^{+4.75}_{-4.05}$	$58.2^{+8.42}_{-7.83}$	6.88E+04	6.63E+04	6.80E+04	1	167
213	$13.9^{+4.89}_{-3.64}$	$1.46^{+1.83}_{-1.32}$	$15.6^{+5.44}_{-3.61}$	4.02E+04	3.88E+04	4.00E+04	2	2
214	$5.05^{+3.32}_{-2.23}$	$1.32^{+1.97}_{-1.18}$	$4.63^{+3.74}_{-1.81}$	4.03E+04	4.05E+04	4.07E+04	2	2
215	$154^{+13.5}_{-12.4}$	$43.2^{+7.43}_{-6.71}$	$192^{+14.6}_{-14.1}$	3.81E+04	3.72E+04	3.78E+04	2	235
216	$0.342^{+1.48}_{-0.342}$	$1.3^{+1.99}_{-1.17}$	$2.82^{+3.09}_{-1.47}$	3.91E+04	3.85E+04	3.90E+04	2	2
217	$6.61^{+4.15}_{-2.21}$	$1.98^{+2.65}_{-1.3}$	$9.06^{+4.04}_{-3.02}$	3.87E+04	3.80E+04	3.85E+04	2	2
218	$4.72^{+3.66}_{-1.89}$	$1.37^{+1.91}_{-1.24}$	$7.3^{+3.46}_{-2.9}$	3.10E+04	3.09E+04	3.09E+04	6	6
219	$57.4^{+8.18}_{-7.95}$	$31.4^{+6.27}_{-5.9}$	$88.1^{+10.3}_{-9.51}$	3.49E+04	3.46E+04	3.47E+04	5	5
220	$2.93^{+2.98}_{-1.58}$	$0.668^{+2.62}_{-0.534}$	$5.64^{+3.94}_{-2.04}$	4.01E+04	3.89E+04	4.00E+04	2	2
221	$7.07^{+3.69}_{-2.67}$	$3.43^{+2.48}_{-2.09}$	$10.9^{+4.51}_{-3.18}$	3.16E+04	3.05E+04	3.13E+04	6	6
222	$25.3^{+5.81}_{-5.23}$	$15.4^{+4.59}_{-4.21}$	$42.9^{+7.67}_{-6.47}$	3.02E+04	2.99E+04	3.00E+04	6	6
223	$81.9^{+10.2}_{-8.95}$	$30.9^{+6.77}_{-5.4}$	$107^{+10.9}_{-10.8}$	2.98E+04	2.93E+04	2.96E+04	6	6
224	$4.7^{+3.67}_{-1.88}$	$6.29^{+3.29}_{-2.68}$	$10.2^{+4.07}_{-3.31}$	3.58E+04	3.52E+04	3.57E+04	2	2
225	$29.6^{+6.91}_{-5.08}$	$5.06^{+3.31}_{-2.24}$	$34.9^{+7.04}_{-5.82}$	3.07E+04	2.95E+04	2.98E+04	5	5
226	$8.08^{+3.86}_{-2.86}$	$6.37^{+3.21}_{-2.77}$	$12^{+4.54}_{-3.44}$	4.00E+04	3.88E+04	3.99E+04	2	2
227	$25.1^{+6.01}_{-5.03}$	$10.7^{+4.68}_{-3}$	$34.1^{+6.8}_{-5.9}$	6.35E+04	6.25E+04	6.32E+04	1	12
228	$40.2^{+7.15}_{-6.53}$	$13.6^{+5.25}_{-3.28}$	$53.7^{+8.72}_{-7}$	3.49E+04	3.45E+04	3.48E+04	7	167

Table A.2—Continued

#	n_{soft}	n_{hard}	n_{full}	t_{soft}	t_{hard}	t_{full}	Field #s	Detections
229	<1.16	$1.53^{+3.1}_{-0.855}$	$3.52^{+3.64}_{-1.45}$	4.00E+04	3.90E+04	3.98E+04	2	2
230	$8.99^{+4.12}_{-2.94}$	<3.93	$8.67^{+4.43}_{-2.63}$	4.00E+04	3.91E+04	4.00E+04	2	2
231	$7.3^{+3.46}_{-2.9}$	$13.4^{+4.34}_{-3.92}$	$18.4^{+4.88}_{-4.65}$	3.49E+04	3.46E+04	3.48E+04	7	167
232	$2.93^{+2.98}_{-1.58}$	$2.13^{+2.5}_{-1.45}$	$5.96^{+3.62}_{-2.35}$	3.11E+04	3.02E+04	3.07E+04	6	6
233	$11.7^{+4.81}_{-3.18}$	$2.68^{+3.23}_{-1.34}$	$14.2^{+4.67}_{-3.87}$	3.84E+04	3.83E+04	3.85E+04	2	127
234	<1.83	$1.15^{+2.14}_{-1.01}$	$3.73^{+3.43}_{-1.66}$	3.09E+04	2.99E+04	3.08E+04	6	6
235	$4.78^{+3.59}_{-1.96}$	$11^{+4.45}_{-3.24}$	$12.1^{+4.5}_{-3.49}$	3.28E+04	3.13E+04	3.15E+04	2	25
236	$0.779^{+2.51}_{-0.645}$	$7.62^{+4.32}_{-2.41}$	$7.62^{+4.32}_{-2.4}$	3.48E+04	3.39E+04	3.51E+04	2	2
237	$9.64^{+4.62}_{-2.76}$	$7.45^{+3.32}_{-3.04}$	$19.1^{+5.35}_{-4.41}$	6.74E+04	6.61E+04	6.69E+04	1	1
238	$5.38^{+3}_{-2.56}$	$21.7^{+6.1}_{-4.32}$	$21.3^{+5.35}_{-4.85}$	6.87E+04	6.77E+04	6.79E+04	1	17
239	$11.2^{+4.22}_{-3.47}$	$6.44^{+3.14}_{-2.84}$	$16.1^{+4.94}_{-4.1}$	6.39E+04	6.24E+04	6.37E+04	1	1
240	$11.4^{+3.99}_{-3.7}$	$8.97^{+4.14}_{-2.92}$	$21.2^{+5.44}_{-4.77}$	6.56E+04	6.52E+04	6.55E+04	1	12
241	$3.33^{+2.58}_{-1.99}$	$6.93^{+3.84}_{-2.52}$	$12.3^{+4.29}_{-3.69}$	6.50E+04	6.46E+04	6.50E+04	1	1
242	$6.84^{+3.92}_{-2.44}$	$2.65^{+3.26}_{-1.3}$	$9.07^{+4.03}_{-3.03}$	3.85E+04	3.74E+04	3.84E+04	2	2
243	$2.72^{+3.19}_{-1.37}$	$7.86^{+4.08}_{-2.64}$	$7.45^{+3.31}_{-3.05}$	3.13E+04	3.03E+04	3.10E+04	6	6
244	$8.99^{+4.12}_{-2.94}$	$13.5^{+4.21}_{-4.05}$	$20.9^{+5.75}_{-4.45}$	3.09E+04	2.98E+04	3.07E+04	6	168
245	$13.5^{+4.24}_{-4.02}$	$15^{+4.98}_{-3.82}$	$22.4^{+5.38}_{-5.04}$	6.87E+04	6.91E+04	6.90E+04	1	12
246	$6.45^{+3.13}_{-2.85}$	$0.692^{+2.6}_{-0.558}$	$9.87^{+4.39}_{-2.99}$	3.79E+04	3.70E+04	3.75E+04	2	2
247	$7.85^{+4.09}_{-2.63}$	$34.2^{+6.66}_{-6.04}$	$41.6^{+7.91}_{-6.08}$	3.71E+04	3.64E+04	3.68E+04	5	235
248	$1.5^{+1.79}_{-1.36}$	$3.29^{+2.62}_{-1.95}$	$3.16^{+2.75}_{-1.82}$	3.12E+04	3.10E+04	3.11E+04	8	8
249	$238^{+16.1}_{-15.8}$	$65.6^{+9.6}_{-7.68}$	$300^{+18.2}_{-17.4}$	6.79E+04	6.83E+04	6.82E+04	1	127
250	$17.6^{+5.69}_{-3.84}$	$13.6^{+5.27}_{-3.26}$	$27.1^{+6.19}_{-5.23}$	3.07E+04	2.98E+04	3.04E+04	6	68
251	$419^{+21.1}_{-20.8}$	$150^{+12.9}_{-12.6}$	$567^{+25}_{-23.6}$	6.61E+04	6.80E+04	6.53E+04	1	167
252	$3.92^{+3.23}_{-1.86}$	$1.77^{+2.86}_{-1.09}$	$6.72^{+4.04}_{-2.32}$	3.04E+04	2.96E+04	3.01E+04	6	6
253	$5.48^{+2.9}_{-2.66}$	$11^{+4.42}_{-3.27}$	$12.6^{+5.07}_{-3.19}$	3.70E+04	3.64E+04	3.67E+04	5	5
254	$8.87^{+4.23}_{-2.83}$	$6.74^{+4.02}_{-2.34}$	$15.6^{+5.44}_{-3.61}$	7.13E+04	7.06E+04	7.13E+04	1	1
255	$1.92^{+2.71}_{-1.24}$	$1.65^{+2.97}_{-0.977}$	$5.22^{+3.15}_{-2.4}$	3.77E+04	3.69E+04	3.75E+04	2	2
256	$20.5^{+6.14}_{-4.07}$	$14.4^{+4.47}_{-4.07}$	$32^{+6.69}_{-5.65}$	6.80E+04	6.84E+04	6.83E+04	1	12
257	$27.4^{+5.87}_{-5.55}$	$11.8^{+4.79}_{-3.19}$	$38.5^{+6.73}_{-6.63}$	7.10E+04	7.05E+04	7.10E+04	1	167
258	$16.2^{+4.92}_{-4.13}$	$7.37^{+3.39}_{-2.97}$	$22.7^{+6.15}_{-4.48}$	3.75E+04	3.74E+04	3.75E+04	5	5
259	$53^{+8.31}_{-7.27}$	$7.5^{+4.44}_{-2.28}$	$54.6^{+8.85}_{-7.01}$	3.90E+04	3.80E+04	3.88E+04	2	235
260	$17.9^{+5.37}_{-4.16}$	$4.01^{+3.14}_{-1.95}$	$20.5^{+5.06}_{-4.92}$	3.86E+04	3.78E+04	3.85E+04	2	12
261	$72.5^{+9.03}_{-8.96}$	$24.7^{+6.32}_{-4.72}$	$98.2^{+10.8}_{-10.1}$	3.84E+04	3.77E+04	3.83E+04	2	123
262	$4.82^{+3.55}_{-2}$	$7.83^{+4.11}_{-2.61}$	$11.3^{+4.09}_{-3.6}$	3.70E+04	3.60E+04	3.65E+04	5	5
263	$12^{+4.56}_{-3.42}$	<8.26	$10.8^{+4.57}_{-3.12}$	6.71E+04	6.68E+04	6.60E+04	1	1
264	$193^{+14.6}_{-14.2}$	$55.4^{+8.04}_{-7.82}$	$245^{+17.1}_{-15.2}$	6.46E+04	6.31E+04	6.36E+04	1	1678
265	$5.75^{+3.83}_{-2.14}$	$1.14^{+2.15}_{-1}$	$9.58^{+4.68}_{-2.7}$	3.75E+04	3.76E+04	3.76E+04	5	5
266	$12^{+4.54}_{-3.44}$	$5.68^{+3.9}_{-2.08}$	$15.3^{+4.69}_{-4.11}$	3.86E+04	3.79E+04	3.85E+04	2	23

Table A.2—Continued

#	n_{soft}	n_{hard}	n_{full}	t_{soft}	t_{hard}	t_{full}	Field #s	Detections
267	$10.4^{+3.85}_{-3.53}$	$3.4^{+2.51}_{-2.06}$	$14.2^{+4.65}_{-3.88}$	6.54E+04	6.45E+04	6.50E+04	1	1
268	$71.3^{+9.17}_{-8.71}$	$23.9^{+6.03}_{-4.81}$	$96.7^{+11.2}_{-9.56}$	7.26E+04	7.30E+04	7.30E+04	1	167
269	$6.06^{+3.52}_{-2.46}$	$6.34^{+3.24}_{-2.74}$	$13.6^{+5.27}_{-3.26}$	2.89E+04	2.81E+04	2.86E+04	6	68
270	$26.6^{+6.62}_{-4.81}$	$16.8^{+5.43}_{-3.86}$	$44.2^{+7.52}_{-6.78}$	6.60E+04	6.34E+04	6.55E+04	1	168
271	$0.896^{+2.39}_{-0.762}$	$1.5^{+3.13}_{-0.825}$	$4.48^{+2.67}_{-2.42}$	3.03E+04	2.96E+04	3.00E+04	6	6
272	$8.03^{+3.9}_{-2.82}$	$19.4^{+5.02}_{-4.75}$	$26.7^{+6.55}_{-4.88}$	6.47E+04	6.46E+04	6.47E+04	1	1
273	$3.35^{+2.56}_{-2.01}$	$7.92^{+4.02}_{-2.71}$	$12.7^{+4.95}_{-3.32}$	7.04E+04	6.88E+04	6.98E+04	1	1
274	$24.4^{+5.53}_{-5.31}$	$10.5^{+4.88}_{-2.81}$	$35^{+6.93}_{-5.94}$	6.97E+04	6.80E+04	6.91E+04	1	13
275	$4.95^{+3.43}_{-2.13}$	$5.7^{+3.87}_{-2.1}$	$10.2^{+4.09}_{-3.29}$	3.81E+04	3.81E+04	3.81E+04	5	25
276	$18.9^{+5.55}_{-4.21}$	$13.3^{+4.35}_{-3.91}$	$30.2^{+6.37}_{-5.61}$	5.80E+04	5.89E+04	5.88E+04	1	1
277	$18.2^{+5.13}_{-4.39}$	$7.91^{+4.03}_{-2.69}$	$24.7^{+6.39}_{-4.65}$	3.72E+04	3.67E+04	3.70E+04	5	25
278	$8.75^{+4.35}_{-2.71}$	$1.3^{+1.99}_{-1.16}$	$9.98^{+4.28}_{-3.1}$	2.97E+04	2.88E+04	2.95E+04	6	6
279	$5.75^{+3.83}_{-2.14}$	$1.23^{+2.06}_{-1.1}$	$7.62^{+4.32}_{-2.41}$	3.82E+04	3.82E+04	3.82E+04	5	5
280	$15.5^{+4.47}_{-4.32}$	$27.5^{+5.76}_{-5.66}$	$43.6^{+8.13}_{-6.17}$	2.89E+04	2.78E+04	2.85E+04	6	68
281	$12.8^{+4.93}_{-3.33}$	$6.34^{+3.24}_{-2.73}$	$16.8^{+5.38}_{-3.91}$	6.52E+04	6.44E+04	6.49E+04	1	1
282	$58.5^{+8.18}_{-8.08}$	$21.6^{+6.18}_{-4.24}$	$79.3^{+9.66}_{-9.13}$	3.39E+04	3.37E+04	3.35E+04	5	5
283	$4.84^{+3.53}_{-2.02}$	<7.77	$3.69^{+3.47}_{-1.62}$	6.59E+04	6.68E+04	6.73E+04	1	1
284	$3.99^{+3.16}_{-1.93}$	<5.27	$3.01^{+2.9}_{-1.67}$	2.92E+04	2.80E+04	2.87E+04	6	6
285	$10.7^{+4.76}_{-2.93}$	$24^{+5.96}_{-4.88}$	$31.6^{+7.09}_{-5.25}$	7.07E+04	7.05E+04	7.08E+04	1	1
286	$129^{+12.4}_{-11.3}$	$26.7^{+6.51}_{-4.92}$	$153^{+13}_{-12.7}$	3.45E+04	3.43E+04	3.45E+04	5	235
287	$39.7^{+7.66}_{-6.02}$	$39.8^{+7.57}_{-6.11}$	$82.7^{+10.5}_{-8.75}$	7.04E+04	7.02E+04	7.04E+04	1	168
288	$5.52^{+4.06}_{-1.92}$	$10.7^{+4.7}_{-2.99}$	$17.8^{+5.49}_{-4.04}$	6.42E+04	6.35E+04	6.43E+04	1	1
289	$2.77^{+3.14}_{-1.43}$	$0.166^{+1.66}_{-0.166}$	$5.23^{+3.14}_{-2.41}$	2.81E+04	2.72E+04	2.77E+04	6	6
290	$4.86^{+3.52}_{-2.03}$	$10.4^{+3.88}_{-3.51}$	$17.2^{+5.04}_{-4.25}$	3.40E+04	3.28E+04	3.31E+04	5	235
291	$11.7^{+4.9}_{-3.08}$	$31.3^{+6.3}_{-5.87}$	$41.6^{+7.97}_{-6.02}$	2.97E+04	2.89E+04	2.93E+04	6	168
292	$6.2^{+3.38}_{-2.6}$	<8.57	$6.09^{+3.48}_{-2.49}$	3.77E+04	3.72E+04	3.77E+04	2	2
293	120^{+12}_{-11}	$64.8^{+9.32}_{-7.82}$	$221^{+16.2}_{-14.6}$	3.76E+04	3.69E+04	3.75E+04	2	1235
294	$52^{+8.28}_{-7.17}$	$15.9^{+5.19}_{-3.86}$	$68.2^{+9.12}_{-8.39}$	7.10E+04	6.92E+04	7.11E+04	1	168
295	$7.65^{+4.29}_{-2.43}$	$8.26^{+3.68}_{-3.05}$	$16.9^{+5.32}_{-3.97}$	6.64E+04	6.48E+04	6.65E+04	1	12
296	$5.95^{+3.63}_{-2.35}$	$1.85^{+2.78}_{-1.17}$	$8.53^{+4.58}_{-2.48}$	3.73E+04	3.71E+04	3.72E+04	5	5
297	$14.5^{+5.43}_{-3.36}$	$7.75^{+4.19}_{-2.53}$	$20.8^{+5.9}_{-4.31}$	6.67E+04	6.56E+04	6.70E+04	1	12
298	$26.4^{+5.79}_{-5.45}$	$8.41^{+3.52}_{-3.2}$	$36.6^{+7.56}_{-5.63}$	3.75E+04	3.69E+04	3.74E+04	2	123
299	$4.74^{+3.64}_{-1.92}$	$1.37^{+1.92}_{-1.23}$	$6.72^{+4.05}_{-2.32}$	7.30E+04	7.20E+04	7.30E+04	1	1
300	$1.71^{+2.92}_{-1.03}$	$3.91^{+3.25}_{-1.84}$	$7.14^{+3.63}_{-2.74}$	6.40E+04	6.17E+04	6.33E+04	1	1
301	$6.16^{+3.42}_{-2.55}$	$9.18^{+3.93}_{-3.13}$	$14.3^{+4.53}_{-4.01}$	3.59E+04	3.54E+04	3.57E+04	8	68
302	$6.97^{+3.8}_{-2.56}$	$1.33^{+1.96}_{-1.19}$	$11.3^{+4.13}_{-3.56}$	6.27E+04	6.15E+04	6.27E+04	1	1
303	$3.94^{+3.22}_{-1.87}$	$7.56^{+4.38}_{-2.34}$	$8.67^{+4.43}_{-2.63}$	2.90E+04	2.81E+04	2.73E+04	1	1
304	$8.99^{+4.12}_{-2.94}$	$5.23^{+3.14}_{-2.41}$	$15.1^{+4.84}_{-3.95}$	3.69E+04	3.53E+04	3.69E+04	5	5

Table A.2—Continued

#	n_{soft}	n_{hard}	n_{full}	t_{soft}	t_{hard}	t_{full}	Field #s	Detections
305	$15.8^{+5.28}_{-3.77}$	$13^{+4.71}_{-3.56}$	$28.9^{+6.59}_{-5.22}$	3.49E+04	3.46E+04	3.47E+04	5	235
306	$2.47^{+2.16}_{-1.79}$	$10.2^{+4.04}_{-3.34}$	$11.6^{+4.98}_{-3}$	6.89E+04	6.86E+04	6.94E+04	1	1
307	$3.43^{+2.48}_{-2.09}$	$2.2^{+2.43}_{-1.52}$	$3.71^{+3.45}_{-1.64}$	3.52E+04	3.47E+04	3.49E+04	5	5
308	$8.67^{+4.43}_{-2.63}$	<6.07	$12.3^{+4.26}_{-3.72}$	6.91E+04	6.83E+04	6.89E+04	1	1
309	$0.106^{+1.72}_{-0.106}$	$2.38^{+2.24}_{-1.71}$	$4.14^{+3.01}_{-2.08}$	6.56E+04	6.49E+04	6.57E+04	1	1
310	$4.33^{+2.82}_{-2.27}$	$3.56^{+3.59}_{-1.5}$	$9.44^{+3.67}_{-3.39}$	6.82E+04	6.77E+04	6.81E+04	1	1
311	$4.27^{+2.89}_{-2.2}$	$5.69^{+3.89}_{-2.08}$	$9.51^{+4.75}_{-2.63}$	3.42E+04	3.39E+04	3.52E+04	2	123
312	$8.44^{+3.5}_{-3.23}$	$7.21^{+3.55}_{-2.81}$	$16.2^{+4.84}_{-4.21}$	3.55E+04	3.55E+04	3.52E+04	5	235
313	$9.17^{+3.94}_{-3.13}$	$13.6^{+5.27}_{-3.27}$	$20.9^{+5.75}_{-4.46}$	3.63E+04	3.58E+04	3.64E+04	8	68
314	$6.01^{+3.56}_{-2.41}$	$4.69^{+3.68}_{-1.87}$	$8.07^{+3.87}_{-2.85}$	6.81E+04	6.76E+04	6.81E+04	1	1
315	$7.85^{+4.09}_{-2.63}$	<3.49	$8.15^{+3.79}_{-2.93}$	3.55E+04	3.62E+04	3.57E+04	8	168
316	$5.25^{+3.12}_{-2.43}$	<7.39	$5.77^{+3.8}_{-2.17}$	6.96E+04	6.80E+04	6.91E+04	1	1
317	$15.4^{+4.6}_{-4.2}$	$5.81^{+3.77}_{-2.21}$	$21.9^{+5.91}_{-4.52}$	3.70E+04	3.77E+04	3.73E+04	3	235
318	$19^{+5.42}_{-4.34}$	$1.69^{+2.94}_{-1.01}$	$23.8^{+6.18}_{-4.65}$	3.12E+04	2.97E+04	3.09E+04	5	5
319	$33.8^{+7.05}_{-5.64}$	$13.9^{+4.95}_{-3.58}$	$48^{+8}_{-6.88}$	3.16E+04	3.00E+04	3.09E+04	5	5
320	$48.1^{+7.84}_{-7.05}$	$27.9^{+6.46}_{-5.16}$	$74.8^{+9.87}_{-8.48}$	3.59E+04	3.67E+04	3.62E+04	8	168
321	$3.93^{+3.23}_{-1.86}$	$7.7^{+4.24}_{-2.48}$	$9.53^{+4.73}_{-2.65}$	4.77E+04	4.86E+04	4.79E+04	1	1
322	$50.6^{+8.58}_{-6.73}$	$25.5^{+6.62}_{-4.61}$	$72.9^{+9.66}_{-8.45}$	3.65E+04	3.69E+04	3.67E+04	8	68
323	$138^{+13.2}_{-11.3}$	$86.1^{+10.2}_{-9.36}$	$223^{+16.3}_{-14.6}$	3.45E+04	3.42E+04	3.43E+04	8	8
324	$3.28^{+2.63}_{-1.94}$	$13.4^{+4.3}_{-3.96}$	$14.3^{+4.48}_{-4.05}$	3.44E+04	3.24E+04	3.37E+04	5	5
325	$7.29^{+3.47}_{-2.89}$	<4.11	$8.48^{+3.46}_{-3.26}$	2.74E+04	2.66E+04	2.72E+04	6	6
326	$4.21^{+2.94}_{-2.15}$	$6.29^{+3.29}_{-2.69}$	$12.1^{+4.41}_{-3.58}$	6.27E+04	6.11E+04	6.10E+04	1	1
327	$19.1^{+5.34}_{-4.42}$	$12.1^{+4.45}_{-3.53}$	$29.6^{+6.97}_{-5.02}$	3.74E+04	3.64E+04	3.70E+04	5	5
328	$98.4^{+10.5}_{-10.3}$	$35.2^{+6.76}_{-6.1}$	$131^{+12.9}_{-11}$	3.24E+04	3.03E+04	3.15E+04	5	5
329	$21^{+5.65}_{-4.56}$	$9.13^{+3.97}_{-3.09}$	$29.6^{+6.97}_{-5.02}$	3.79E+04	3.67E+04	3.75E+04	5	5
330	$24.9^{+6.12}_{-4.91}$	$22.1^{+5.62}_{-4.8}$	$42^{+7.56}_{-6.43}$	7.19E+04	6.99E+04	7.15E+04	1	189
331	$323^{+18.6}_{-18.4}$	$155^{+13.2}_{-12.7}$	$472^{+22.4}_{-22.1}$	3.39E+04	3.34E+04	3.36E+04	8	8
332	$147^{+13.3}_{-12}$	$45.4^{+7.35}_{-7.1}$	$193^{+15.1}_{-13.7}$	3.65E+04	3.74E+04	3.68E+04	3	235
333	$1.31^{+1.98}_{-1.17}$	$4.2^{+2.96}_{-2.13}$	$7.8^{+4.14}_{-2.58}$	2.87E+04	2.80E+04	2.84E+04	6	6
334	$5.75^{+3.83}_{-2.15}$	$4.8^{+3.58}_{-1.97}$	$10.7^{+4.7}_{-2.99}$	3.50E+04	3.35E+04	3.43E+04	5	5
335	$3.54^{+3.61}_{-1.48}$	$5.62^{+3.95}_{-2.02}$	$9.74^{+4.52}_{-2.86}$	3.63E+04	3.59E+04	3.61E+04	5	5
336	$14.9^{+5.01}_{-3.78}$	$4.62^{+3.75}_{-1.8}$	$20.6^{+6.02}_{-4.18}$	2.75E+04	2.67E+04	2.71E+04	6	68
337	$5.95^{+3.62}_{-2.35}$	$2.53^{+3.38}_{-1.19}$	$9.26^{+3.85}_{-3.21}$	3.64E+04	3.72E+04	3.66E+04	8	8
338	$4.53^{+3.85}_{-1.71}$	<7.13	$7.94^{+4}_{-2.72}$	7.11E+04	6.94E+04	7.06E+04	1	1
339	$7.87^{+4.07}_{-2.65}$	$2.67^{+3.24}_{-1.33}$	$12.4^{+4.16}_{-3.83}$	3.76E+04	3.62E+04	3.71E+04	5	5
340	$2.72^{+3.19}_{-1.37}$	$8.49^{+3.45}_{-3.28}$	$11.1^{+4.34}_{-3.35}$	7.15E+04	6.98E+04	7.10E+04	1	1
341	$12.5^{+5.19}_{-3.07}$	$9.85^{+4.41}_{-2.97}$	$23.9^{+6.07}_{-4.76}$	7.09E+04	6.87E+04	7.04E+04	1	1
342	$22^{+5.74}_{-4.68}$	$6.89^{+3.87}_{-2.49}$	$31.8^{+6.91}_{-5.43}$	3.76E+04	3.61E+04	3.71E+04	5	5

Table A.2—Continued

#	n_{soft}	n_{hard}	n_{full}	t_{soft}	t_{hard}	t_{full}	Field #s	Detections
343	$10.8^{+4.65}_{-3.04}$	<4.71	$12.3^{+4.23}_{-3.75}$	3.65E+04	3.74E+04	3.68E+04	3	235
344	$3.41^{+2.5}_{-2.07}$	$41.5^{+7.98}_{-6.01}$	$39.1^{+7.19}_{-6.33}$	6.91E+04	6.68E+04	6.88E+04	1	19
345	$6.65^{+4.11}_{-2.25}$	$5.27^{+3.1}_{-2.45}$	$11.2^{+4.23}_{-3.46}$	7.11E+04	6.78E+04	7.02E+04	1	1
346	$6.03^{+3.55}_{-2.42}$	$3.62^{+3.53}_{-1.56}$	$9.51^{+4.75}_{-2.63}$	3.53E+04	3.39E+04	3.45E+04	5	5
347	$11.7^{+4.88}_{-3.1}$	$6.29^{+3.29}_{-2.69}$	$16.1^{+5.02}_{-4.02}$	3.70E+04	3.81E+04	3.74E+04	3	35
348	$5.54^{+4.04}_{-1.93}$	$29^{+6.41}_{-5.39}$	$10.2^{+4.03}_{-3.36}$	6.77E+04	6.57E+04	6.72E+04	1	1
349	$0.8^{+2.49}_{-0.666}$	$8.67^{+4.44}_{-2.63}$	$7.24^{+3.52}_{-2.84}$	3.67E+04	3.76E+04	3.71E+04	8	8
350	$3.83^{+3.32}_{-1.77}$	<4.55	$4.32^{+2.84}_{-2.25}$	3.73E+04	3.59E+04	3.68E+04	5	5
351	$23.3^{+5.56}_{-5.07}$	$9.78^{+4.49}_{-2.9}$	$33.3^{+6.54}_{-5.99}$	3.45E+04	3.28E+04	3.38E+04	5	5
352	$20.7^{+5.92}_{-4.28}$	$14.6^{+5.35}_{-3.44}$	$33.5^{+7.34}_{-5.35}$	3.63E+04	3.66E+04	3.62E+04	8	8
353	$38.3^{+6.95}_{-6.41}$	$7.85^{+4.09}_{-2.64}$	$45.7^{+8.13}_{-6.46}$	3.42E+04	3.37E+04	3.40E+04	8	8
354	$3.6^{+3.56}_{-1.53}$	$0.26^{+1.57}_{-0.26}$	$6.76^{+4.01}_{-2.35}$	6.62E+04	6.45E+04	6.55E+04	1	1
355	$142^{+13.1}_{-11.7}$	$42.6^{+8.02}_{-6.12}$	$186^{+15}_{-13.3}$	6.91E+04	6.75E+04	6.87E+04	1	189
356	$8.88^{+4.22}_{-2.84}$	<3.97	$9.68^{+4.58}_{-2.8}$	3.68E+04	3.74E+04	3.70E+04	3	3
357	$52.7^{+8.67}_{-6.92}$	$26.9^{+6.32}_{-5.11}$	$79.2^{+9.7}_{-9.1}$	3.56E+04	3.48E+04	3.52E+04	9	139
358	$5.64^{+3.93}_{-2.04}$	<6.71	$5.23^{+3.15}_{-2.41}$	5.73E+04	5.64E+04	5.73E+04	1	1
359	$9.37^{+3.74}_{-3.33}$	$13.1^{+4.55}_{-3.72}$	$23.2^{+5.65}_{-4.98}$	3.23E+04	3.01E+04	3.13E+04	5	5
360	$33.6^{+7.28}_{-5.42}$	$18.9^{+5.56}_{-4.2}$	$51.1^{+8.13}_{-7.18}$	6.59E+04	6.38E+04	6.52E+04	1	1
361	$2.92^{+2.99}_{-1.58}$	$9.68^{+4.58}_{-2.81}$	$13.9^{+4.92}_{-3.61}$	6.92E+04	6.72E+04	6.91E+04	1	1
362	$58.4^{+8.27}_{-7.98}$	$43.1^{+7.51}_{-6.63}$	$101^{+11}_{-10.1}$	6.88E+04	6.71E+04	6.83E+04	1	189
363	$14.8^{+5.12}_{-3.68}$	$13.3^{+4.38}_{-3.88}$	$26.7^{+6.51}_{-4.92}$	7.02E+04	6.82E+04	6.98E+04	1	1
364	$46.5^{+8.4}_{-6.34}$	$13.9^{+4.89}_{-3.64}$	$59.9^{+8.93}_{-7.59}$	6.85E+04	6.69E+04	6.81E+04	1	189
365	$2.82^{+3.09}_{-1.48}$	$3.54^{+3.62}_{-1.47}$	$5.32^{+3.05}_{-2.5}$	3.42E+04	3.42E+04	3.49E+04	8	18
366	$9.99^{+4.27}_{-3.12}$	$1.6^{+3.03}_{-0.92}$	$14.6^{+5.33}_{-3.46}$	3.71E+04	3.66E+04	3.72E+04	8	68
367	$25.8^{+6.36}_{-4.87}$	$7.38^{+3.39}_{-2.97}$	$36.8^{+7.38}_{-5.81}$	6.89E+04	6.77E+04	6.86E+04	1	1
368	$5.64^{+3.94}_{-2.04}$	$2.55^{+3.36}_{-1.21}$	$8.36^{+3.58}_{-3.14}$	3.75E+04	3.82E+04	3.79E+04	8	8
369	$8.02^{+3.92}_{-2.8}$	$8.77^{+4.33}_{-2.73}$	$16.7^{+5.46}_{-3.83}$	3.45E+04	3.36E+04	3.40E+04	3	3
370	$4.71^{+3.66}_{-1.89}$	$8.37^{+3.57}_{-3.15}$	$8.07^{+3.87}_{-2.85}$	3.79E+04	3.86E+04	3.81E+04	3	3
371	$3.1^{+2.8}_{-1.76}$	$9.73^{+4.54}_{-2.85}$	$15.4^{+4.58}_{-4.21}$	6.89E+04	6.59E+04	6.79E+04	1	13
372	$18.1^{+5.24}_{-4.29}$	$1.92^{+2.71}_{-1.24}$	$20.9^{+5.75}_{-4.45}$	3.51E+04	3.49E+04	3.50E+04	8	18
373	$73.5^{+10.1}_{-8.12}$	$23.8^{+6.21}_{-4.63}$	$101^{+10.9}_{-10.2}$	6.69E+04	6.57E+04	6.66E+04	1	189
374	$15.7^{+5.34}_{-3.71}$	$18.5^{+4.86}_{-4.67}$	$35.7^{+7.32}_{-5.71}$	3.64E+04	3.73E+04	3.68E+04	3	123
375	$9.32^{+3.79}_{-3.27}$	$2.14^{+2.49}_{-1.46}$	$11.9^{+4.68}_{-3.31}$	3.61E+04	3.57E+04	3.62E+04	9	139
376	$9.53^{+4.73}_{-2.65}$	$9.18^{+3.92}_{-3.14}$	$20.5^{+6.15}_{-4.06}$	3.63E+04	3.52E+04	3.59E+04	5	35
377	$6.44^{+3.13}_{-2.84}$	$0.795^{+2.49}_{-0.661}$	$7.94^{+4}_{-2.72}$	3.84E+04	3.84E+04	3.84E+04	8	8
378	$4.32^{+2.84}_{-2.25}$	$2.07^{+2.56}_{-1.39}$	$5.71^{+3.87}_{-2.11}$	3.85E+04	3.84E+04	3.85E+04	8	8
379	$1.99^{+2.63}_{-1.32}$	$6.71^{+4.05}_{-2.31}$	$9.4^{+3.7}_{-3.36}$	3.50E+04	3.54E+04	3.51E+04	3	3
380	<0.446	$37.8^{+7.37}_{-5.99}$	$36.4^{+6.62}_{-6.41}$	3.77E+04	3.85E+04	3.81E+04	8	8

Table A.2—Continued

#	n_{soft}	n_{hard}	n_{full}	t_{soft}	t_{hard}	t_{full}	Field #s	Detections
381	$182^{+14.8}_{-13.2}$	$14.4^{+4.4}_{-4.13}$	$191^{+14.7}_{-13.9}$	3.67E+04	3.67E+04	3.65E+04	3	35
382	$6.48^{+3.1}_{-2.87}$	$1.01^{+2.28}_{-0.878}$	$7.55^{+4.39}_{-2.33}$	3.72E+04	3.77E+04	3.73E+04	3	13
383	$17.9^{+5.41}_{-4.12}$	$14.5^{+5.43}_{-3.37}$	$32.2^{+6.51}_{-5.84}$	3.32E+04	3.24E+04	3.30E+04	3	35
384	$7.48^{+3.29}_{-3.08}$	$6.85^{+3.91}_{-2.45}$	$13.9^{+4.96}_{-3.58}$	3.73E+04	3.69E+04	3.72E+04	9	19
385	$6.42^{+3.16}_{-2.82}$	$17.9^{+5.42}_{-4.11}$	$22.9^{+5.96}_{-4.68}$	3.55E+04	3.47E+04	3.49E+04	8	8
386	$6.61^{+4.15}_{-2.21}$	<3.35	$6.04^{+3.54}_{-2.43}$	3.61E+04	3.69E+04	3.62E+04	3	39
387	$10.9^{+4.54}_{-3.15}$	$1.16^{+2.13}_{-1.03}$	$14.1^{+4.73}_{-3.8}$	3.36E+04	3.27E+04	3.31E+04	5	35
388	$43.4^{+7.17}_{-6.98}$	$15.1^{+4.82}_{-3.97}$	$57.7^{+8.92}_{-7.33}$	3.50E+04	3.36E+04	3.44E+04	9	89
389	$0.486^{+1.34}_{-0.486}$	$7.51^{+4.43}_{-2.29}$	$7.24^{+3.52}_{-2.84}$	3.62E+04	3.63E+04	3.64E+04	3	3
390	$45.4^{+7.34}_{-7.11}$	$24.1^{+5.88}_{-4.96}$	$69.5^{+9.86}_{-7.9}$	3.74E+04	3.62E+04	3.69E+04	9	189
391	$9.79^{+4.47}_{-2.91}$	$2.68^{+3.23}_{-1.34}$	$13.6^{+5.21}_{-3.33}$	3.87E+04	3.87E+04	3.87E+04	3	3
392	$19^{+5.45}_{-4.31}$	$1.94^{+2.69}_{-1.26}$	$21.7^{+6.06}_{-4.36}$	3.86E+04	3.80E+04	3.85E+04	3	3
393	$173^{+14.5}_{-12.8}$	$76^{+9.8}_{-8.65}$	$247^{+16.3}_{-16.1}$	3.60E+04	3.61E+04	3.59E+04	3	139
394	$4.58^{+3.79}_{-1.76}$	$3.86^{+3.3}_{-1.8}$	$9.95^{+4.32}_{-3.07}$	3.76E+04	3.74E+04	3.75E+04	9	9
395	$12^{+4.54}_{-3.44}$	$6.81^{+3.96}_{-2.4}$	$18.8^{+5.66}_{-4.1}$	3.86E+04	3.83E+04	3.86E+04	3	3
396	$2.17^{+2.46}_{-1.49}$	$9.6^{+4.66}_{-2.72}$	$11.4^{+4}_{-3.69}$	6.60E+04	6.43E+04	6.54E+04	1	1
397	$21.8^{+5.92}_{-4.5}$	$20.9^{+5.79}_{-4.41}$	$45.9^{+7.89}_{-6.7}$	6.70E+04	6.56E+04	6.66E+04	1	189
398	$55.5^{+8.01}_{-7.85}$	$16.2^{+4.83}_{-4.22}$	$74^{+9.63}_{-8.6}$	3.80E+04	3.72E+04	3.80E+04	8	89
399	$15.9^{+5.15}_{-3.9}$	$6.55^{+4.22}_{-2.15}$	$21.2^{+5.48}_{-4.73}$	3.70E+04	3.68E+04	3.68E+04	3	35
400	$1.34^{+1.94}_{-1.21}$	<3.85	$2.91^{+2.99}_{-1.57}$	3.42E+04	3.43E+04	3.44E+04	8	8
401	$13.7^{+5.11}_{-3.43}$	$3.53^{+3.63}_{-1.46}$	$18.6^{+5.86}_{-3.9}$	3.31E+04	3.19E+04	3.27E+04	5	5
402	<0.446	$2.72^{+3.19}_{-1.38}$	$5.12^{+3.26}_{-2.3}$	3.49E+04	3.59E+04	3.60E+04	8	8
403	$1.92^{+2.71}_{-1.24}$	$7.59^{+4.35}_{-2.38}$	$6.86^{+3.9}_{-2.46}$	3.85E+04	3.82E+04	3.84E+04	3	3
404	$61^{+8.88}_{-7.76}$	$19.1^{+5.38}_{-4.38}$	$80.6^{+10.4}_{-8.61}$	3.50E+04	3.41E+04	3.46E+04	5	35
405	$7.87^{+4.07}_{-2.65}$	$0.532^{+2.76}_{-0.398}$	$10.3^{+3.99}_{-3.39}$	3.76E+04	3.68E+04	3.75E+04	8	8
406	$17.9^{+5.43}_{-4.1}$	$8.03^{+3.91}_{-2.81}$	$24.8^{+6.26}_{-4.78}$	3.37E+04	3.15E+04	3.29E+04	5	5
407	$3.84^{+3.31}_{-1.78}$	$0.635^{+2.65}_{-0.501}$	$7.33^{+3.44}_{-2.92}$	3.77E+04	3.72E+04	3.76E+04	3	3
408	$4.6^{+3.78}_{-1.78}$	$0.63^{+2.66}_{-0.496}$	$5.04^{+3.33}_{-2.22}$	3.78E+04	3.77E+04	3.78E+04	9	9
409	$13.1^{+4.56}_{-3.71}$	$1.24^{+2.05}_{-1.11}$	$16^{+5.06}_{-3.99}$	3.77E+04	3.74E+04	3.76E+04	3	3
410	$8.08^{+3.86}_{-2.86}$	<5.4	$7.98^{+3.96}_{-2.76}$	3.84E+04	3.77E+04	3.82E+04	3	3
411	$202^{+14.8}_{-14.7}$	$70.7^{+9.73}_{-8.15}$	$274^{+17.6}_{-16.5}$	3.73E+04	3.62E+04	3.68E+04	9	189
412	$11.2^{+4.24}_{-3.45}$	$3^{+2.91}_{-1.66}$	$14.8^{+5.17}_{-3.62}$	3.39E+04	3.38E+04	3.36E+04	8	8
413	$29.5^{+5.95}_{-5.85}$	$38.9^{+7.44}_{-6.08}$	$66.9^{+9.33}_{-8.06}$	6.51E+04	6.38E+04	6.47E+04	1	189
414	$54.2^{+8.15}_{-7.57}$	$25.6^{+6.56}_{-4.67}$	$76.5^{+9.29}_{-9.16}$	3.47E+04	3.37E+04	3.43E+04	5	35
415	$3.46^{+2.45}_{-2.11}$	$7.35^{+3.41}_{-2.95}$	$8.81^{+4.29}_{-2.77}$	3.71E+04	3.69E+04	3.70E+04	3	3
416	$1.45^{+1.84}_{-1.32}$	$3.87^{+3.28}_{-1.81}$	$5.82^{+3.76}_{-2.22}$	3.76E+04	3.77E+04	3.76E+04	9	9
417	$17.5^{+5.82}_{-3.71}$	$9.63^{+4.64}_{-2.75}$	$23.5^{+5.38}_{-5.25}$	3.39E+04	3.31E+04	3.34E+04	9	89
418	$24.9^{+6.18}_{-4.86}$	$12.9^{+4.81}_{-3.46}$	$38^{+7.18}_{-6.18}$	6.55E+04	6.41E+04	6.51E+04	1	189

Table A.2—Continued

#	n_{soft}	n_{hard}	n_{full}	t_{soft}	t_{hard}	t_{full}	Field #s	Detections
419	$19.7^{+5.86}_{-4.12}$	$4.17^{+2.98}_{-2.11}$	$24.3^{+5.65}_{-5.18}$	3.74E+04	3.61E+04	3.72E+04	8	89
420	$13.1^{+4.56}_{-3.7}$	$3.56^{+3.59}_{-1.5}$	$20.9^{+5.76}_{-4.45}$	3.84E+04	3.81E+04	3.83E+04	9	189
421	$4.94^{+3.43}_{-2.12}$	$6.7^{+4.07}_{-2.29}$	$11.5^{+3.93}_{-3.76}$	3.70E+04	3.65E+04	3.69E+04	8	8
422	$10.2^{+4.02}_{-3.36}$	<6.27	$9.71^{+4.55}_{-2.83}$	3.40E+04	3.25E+04	3.34E+04	5	5
423	$5.83^{+3.74}_{-2.23}$	<12	$5.6^{+3.98}_{-2}$	3.41E+04	3.30E+04	3.36E+04	5	35
424	$10.6^{+4.77}_{-2.92}$	$33.1^{+6.72}_{-5.8}$	$37.5^{+6.68}_{-6.51}$	3.70E+04	3.70E+04	3.70E+04	9	139
425	$4.7^{+3.67}_{-1.88}$	$0.828^{+2.46}_{-0.694}$	$6.45^{+3.12}_{-2.85}$	3.72E+04	3.70E+04	3.71E+04	3	39
426	$8.88^{+4.22}_{-2.84}$	$4.22^{+2.94}_{-2.15}$	$13.6^{+5.21}_{-3.33}$	3.66E+04	3.57E+04	3.65E+04	3	3
427	$9.99^{+4.27}_{-3.11}$	$2.78^{+3.13}_{-1.44}$	$12.1^{+4.45}_{-3.53}$	3.49E+04	3.50E+04	3.47E+04	3	3
428	$0.894^{+2.39}_{-0.76}$	$2.11^{+2.52}_{-1.43}$	$5.02^{+3.36}_{-2.2}$	3.71E+04	3.69E+04	3.69E+04	3	3
429	$7.76^{+4.18}_{-2.55}$	$1.51^{+3.12}_{-0.835}$	$10.4^{+3.89}_{-3.49}$	3.44E+04	3.32E+04	3.39E+04	5	5
430	$4.04^{+3.11}_{-1.98}$	$2.66^{+3.25}_{-1.32}$	$5.12^{+3.26}_{-2.3}$	3.78E+04	3.72E+04	3.76E+04	3	3
431	$8.78^{+4.33}_{-2.73}$	$4.82^{+3.55}_{-2}$	$13.4^{+4.28}_{-3.98}$	3.68E+04	3.58E+04	3.66E+04	8	8
432	$5.05^{+3.32}_{-2.23}$	$0.502^{+2.79}_{-0.368}$	$7.2^{+3.56}_{-2.8}$	3.49E+04	3.45E+04	3.46E+04	3	3
433	$12^{+4.54}_{-3.44}$	$0.329^{+1.5}_{-0.329}$	$13.8^{+5}_{-3.53}$	3.67E+04	3.67E+04	3.67E+04	9	19
434	$5.49^{+2.89}_{-2.67}$	$4.19^{+2.96}_{-2.13}$	$9.19^{+3.92}_{-3.15}$	3.74E+04	3.71E+04	3.73E+04	3	39
435	$29^{+6.47}_{-5.34}$	$6.97^{+3.8}_{-2.56}$	$37^{+7.18}_{-6.01}$	3.48E+04	3.52E+04	3.47E+04	3	3
436	$7.62^{+4.31}_{-2.41}$	$2.04^{+2.59}_{-1.36}$	$7.95^{+3.99}_{-2.73}$	3.74E+04	3.71E+04	3.72E+04	3	3
437	$15.9^{+5.14}_{-3.9}$	$0.154^{+1.67}_{-0.154}$	$17.6^{+5.7}_{-3.83}$	3.11E+04	3.10E+04	3.11E+04	9	9
438	$73.7^{+9.9}_{-8.33}$	$28^{+6.33}_{-5.29}$	$98.5^{+11.5}_{-9.46}$	3.78E+04	3.64E+04	3.68E+04	9	39
439	$8.78^{+4.33}_{-2.73}$	$2.75^{+3.16}_{-1.41}$	$12.3^{+4.26}_{-3.72}$	3.87E+04	3.85E+04	3.87E+04	9	19
440	$1.71^{+2.92}_{-1.03}$	$6.93^{+3.84}_{-2.52}$	$7.56^{+4.38}_{-2.34}$	3.88E+04	3.89E+04	3.88E+04	9	9
441	$20.1^{+5.47}_{-4.51}$	$43^{+7.65}_{-6.49}$	$65.3^{+8.78}_{-8.37}$	6.44E+04	6.29E+04	6.39E+04	1	19
442	$28.1^{+6.28}_{-5.34}$	$5.64^{+3.93}_{-2.04}$	$37.3^{+6.88}_{-6.32}$	3.77E+04	3.75E+04	3.76E+04	3	39
443	$7.77^{+4.17}_{-2.55}$	$9.47^{+3.63}_{-3.43}$	$10.5^{+3.78}_{-3.6}$	3.76E+04	3.71E+04	3.74E+04	9	9
444	$34.5^{+7.44}_{-5.43}$	$4.79^{+3.58}_{-1.97}$	$38.6^{+7.65}_{-5.87}$	2.81E+04	2.84E+04	2.80E+04	3	3
445	$12.1^{+4.43}_{-3.55}$	<3.89	$11.7^{+4.85}_{-3.13}$	3.63E+04	3.60E+04	3.63E+04	9	9
446	$6.54^{+4.23}_{-2.14}$	$16^{+5.08}_{-3.97}$	$19^{+5.4}_{-4.36}$	3.68E+04	3.60E+04	3.66E+04	8	8
447	$2.91^{+3}_{-1.57}$	$9.74^{+4.53}_{-2.86}$	$12.8^{+4.92}_{-3.34}$	3.76E+04	3.74E+04	3.75E+04	3	3
448	$6.44^{+3.13}_{-2.84}$	$6.04^{+3.53}_{-2.44}$	$16.6^{+5.63}_{-3.67}$	3.76E+04	3.73E+04	3.75E+04	3	39
449	$3.45^{+2.46}_{-2.11}$	$0.541^{+2.75}_{-0.407}$	$6.78^{+3.99}_{-2.38}$	3.82E+04	3.76E+04	3.79E+04	9	9
450	$1.81^{+2.82}_{-1.13}$	$5.7^{+3.87}_{-2.1}$	$7.45^{+3.31}_{-3.05}$	3.90E+04	3.91E+04	3.91E+04	9	9
451	$15.7^{+5.42}_{-3.63}$	$9.04^{+4.07}_{-3}$	$23.1^{+5.73}_{-4.9}$	3.66E+04	3.63E+04	3.64E+04	3	39
452	$122^{+11.9}_{-11.2}$	$26.8^{+6.44}_{-4.98}$	$148^{+13.4}_{-11.9}$	3.37E+04	3.26E+04	3.32E+04	5	35
453	$5.64^{+3.94}_{-2.03}$	$1.65^{+2.98}_{-0.973}$	$8.45^{+3.48}_{-3.24}$	3.67E+04	3.61E+04	3.61E+04	9	9
454	$153^{+13.8}_{-11.9}$	$22.5^{+5.3}_{-5.12}$	$164^{+14.2}_{-12.4}$	3.49E+04	3.41E+04	3.44E+04	3	35
455	$6.06^{+3.52}_{-2.46}$	$9.05^{+4.05}_{-3.01}$	$14.1^{+4.68}_{-3.85}$	3.64E+04	3.63E+04	3.64E+04	8	8
456	$6.96^{+3.81}_{-2.55}$	$25.3^{+5.72}_{-5.32}$	$31.6^{+7.08}_{-5.27}$	3.86E+04	3.80E+04	3.83E+04	9	189

Table A.2—Continued

#	n_{soft}	n_{hard}	n_{full}	t_{soft}	t_{hard}	t_{full}	Field #s	Detections
457	$16.2^{+4.9}_{-4.15}$	$8.09^{+3.85}_{-2.88}$	$23.5^{+6.43}_{-4.4}$	3.73E+04	3.61E+04	3.68E+04	9	39
458	$4.95^{+3.43}_{-2.13}$	$1.12^{+2.16}_{-0.99}$	$8.36^{+3.58}_{-3.14}$	3.93E+04	3.84E+04	3.89E+04	9	39
459	$7.43^{+3.34}_{-3.02}$	<6.11	$6.73^{+4.03}_{-2.33}$	3.42E+04	3.41E+04	3.42E+04	3	3
460	$9.32^{+3.79}_{-3.27}$	$1.64^{+2.99}_{-0.963}$	$11.4^{+4.02}_{-3.67}$	3.56E+04	3.56E+04	3.52E+04	9	9
461	$3.7^{+3.46}_{-1.63}$	$4.74^{+3.63}_{-1.92}$	$7.16^{+3.6}_{-2.76}$	3.12E+04	3.11E+04	3.08E+04	3	3
462	$3^{+2.91}_{-1.66}$	$11.1^{+4.35}_{-3.34}$	$11.6^{+4.99}_{-2.99}$	3.35E+04	3.33E+04	3.32E+04	3	3
463	$54.2^{+8.2}_{-7.53}$	$18.9^{+5.55}_{-4.21}$	$75.1^{+9.56}_{-8.78}$	3.66E+04	3.64E+04	3.65E+04	3	39
464	<3.43	$5.99^{+3.59}_{-2.39}$	$5^{+3.37}_{-2.18}$	3.40E+04	3.38E+04	3.39E+04	8	8
465	$5.75^{+3.83}_{-2.14}$	$3.55^{+3.6}_{-1.49}$	$8.15^{+3.79}_{-2.93}$	3.95E+04	3.95E+04	3.95E+04	9	9
466	$3.57^{+3.58}_{-1.51}$	$10.6^{+4.83}_{-2.86}$	$13.5^{+5.32}_{-3.21}$	3.58E+04	3.58E+04	3.58E+04	8	8
467	$13.6^{+5.19}_{-3.34}$	$14^{+4.78}_{-3.76}$	$27.8^{+6.57}_{-5.05}$	3.47E+04	3.50E+04	3.46E+04	8	8
468	$16.1^{+5.02}_{-4.03}$	$4.47^{+2.68}_{-2.41}$	$19.3^{+5.16}_{-4.6}$	3.40E+04	3.35E+04	3.38E+04	8	8
469	$2.93^{+2.98}_{-1.58}$	$14.9^{+5.07}_{-3.73}$	$17.8^{+5.55}_{-3.98}$	3.43E+04	3.33E+04	3.44E+04	9	9
470	$13.1^{+4.61}_{-3.65}$	<14.1	$13.2^{+4.47}_{-3.79}$	3.45E+04	3.36E+04	3.40E+04	3	3
471	$232^{+16.6}_{-14.8}$	$149^{+13.4}_{-12}$	$374^{+19.9}_{-19.8}$	3.24E+04	3.22E+04	3.23E+04	8	89
472	$28^{+6.38}_{-5.24}$	$22.7^{+6.2}_{-4.43}$	$51.4^{+7.82}_{-7.49}$	3.58E+04	3.47E+04	3.51E+04	9	39
473	$7.58^{+4.36}_{-2.37}$	$1.24^{+2.05}_{-1.1}$	$9.49^{+3.61}_{-3.45}$	3.54E+04	3.52E+04	3.54E+04	8	8
474	$2.25^{+2.38}_{-1.57}$	$32.6^{+7.21}_{-5.31}$	$33.4^{+6.42}_{-6.1}$	3.19E+04	3.09E+04	3.13E+04	3	3
475	$17.9^{+5.45}_{-4.08}$	$6.6^{+4.16}_{-2.2}$	$25.7^{+6.42}_{-4.81}$	2.53E+04	2.39E+04	2.53E+04	9	9
476	$3.08^{+2.82}_{-1.74}$	$8.32^{+3.62}_{-3.11}$	$12^{+4.52}_{-3.46}$	3.55E+04	3.41E+04	3.49E+04	3	3
477	$9.56^{+4.7}_{-2.69}$	$1.98^{+2.65}_{-1.31}$	$10.9^{+4.49}_{-3.2}$	3.48E+04	3.45E+04	3.47E+04	8	8
478	$17.1^{+5.13}_{-4.16}$	$14.9^{+5.02}_{-3.78}$	$30.2^{+6.37}_{-5.61}$	3.94E+04	3.79E+04	3.89E+04	9	9
479	$23.8^{+6.19}_{-4.65}$	$17.3^{+4.88}_{-4.41}$	$40.9^{+7.55}_{-6.29}$	3.80E+04	3.77E+04	3.78E+04	9	89
480	$13^{+4.67}_{-3.6}$	$6.42^{+3.15}_{-2.82}$	$19.8^{+5.7}_{-4.28}$	3.53E+04	3.37E+04	3.46E+04	3	3
481	$46.3^{+7.53}_{-7.06}$	$20.6^{+6.1}_{-4.11}$	$62.3^{+8.66}_{-8.11}$	3.53E+04	3.50E+04	3.52E+04	3	39
482	$95.5^{+10.3}_{-10.2}$	$47.8^{+8.17}_{-6.71}$	$158^{+14}_{-12.2}$	3.62E+04	3.51E+04	3.57E+04	9	39
483	$0.905^{+2.38}_{-0.771}$	$6.29^{+3.29}_{-2.69}$	$8.67^{+4.43}_{-2.63}$	3.91E+04	3.74E+04	3.86E+04	9	9
484	$10^{+4.26}_{-3.12}$	$7.51^{+4.43}_{-2.3}$	$17.6^{+5.76}_{-3.77}$	3.87E+04	3.70E+04	3.80E+04	9	9
485	$4.04^{+3.11}_{-1.98}$	$5.44^{+2.93}_{-2.62}$	$8.88^{+4.22}_{-2.84}$	3.94E+04	3.76E+04	3.87E+04	9	9
486	$15.2^{+4.72}_{-4.08}$	$31.4^{+6.25}_{-5.92}$	$43.3^{+7.32}_{-6.83}$	3.44E+04	3.41E+04	3.43E+04	8	8
487	$16.1^{+4.96}_{-4.09}$	$4.07^{+3.08}_{-2.01}$	$20.5^{+5.07}_{-4.92}$	3.70E+04	3.63E+04	3.66E+04	9	89
488	$7.24^{+3.53}_{-2.83}$	$15^{+4.99}_{-3.81}$	$18.1^{+5.2}_{-4.33}$	3.20E+04	3.27E+04	3.33E+04	8	8
489	$3.94^{+3.22}_{-1.87}$	$0.878^{+2.41}_{-0.744}$	$6.76^{+4.01}_{-2.35}$	3.91E+04	3.78E+04	3.87E+04	9	9
490	$4.47^{+2.69}_{-2.4}$	$7.42^{+3.34}_{-3.02}$	$10.7^{+4.69}_{-3}$	3.62E+04	3.51E+04	3.57E+04	9	39
491	$18.8^{+5.66}_{-4.1}$	$7.2^{+3.56}_{-2.8}$	$23.2^{+5.67}_{-4.96}$	3.73E+04	3.58E+04	3.69E+04	9	9
492	$15.7^{+5.38}_{-3.67}$	$2.72^{+3.19}_{-1.38}$	$20.3^{+5.25}_{-4.74}$	3.52E+04	3.45E+04	3.51E+04	9	39
493	$6.46^{+3.12}_{-2.86}$	$11.2^{+4.25}_{-3.44}$	$16^{+5.07}_{-3.98}$	3.45E+04	3.39E+04	3.42E+04	3	3
494	$4.61^{+3.77}_{-1.79}$	<4.67	$4.96^{+3.42}_{-2.14}$	3.84E+04	3.71E+04	3.79E+04	9	9

Table A.2—Continued

#	n_{soft}	n_{hard}	n_{full}	t_{soft}	t_{hard}	t_{full}	Field #s	Detections
495	$14^{+4.78}_{-3.75}$	$4.46^{+2.69}_{-2.4}$	$21.7^{+6.06}_{-4.36}$	3.35E+04	3.18E+04	3.27E+04	9	9
496	$42.1^{+7.42}_{-6.57}$	$37.8^{+7.45}_{-5.91}$	$76.4^{+9.34}_{-9.12}$	3.86E+04	3.72E+04	3.81E+04	9	9
497	$23.5^{+5.41}_{-5.22}$	$17.2^{+5.05}_{-4.25}$	$41.5^{+7}_{-6.84}$	3.43E+04	3.35E+04	3.40E+04	9	89
498	$9.03^{+4.07}_{-2.99}$	$6.95^{+3.82}_{-2.55}$	$14.8^{+5.18}_{-3.62}$	3.34E+04	3.25E+04	3.30E+04	8	89
499	$41^{+7.5}_{-6.34}$	$27.6^{+6.74}_{-4.88}$	$72.2^{+9.37}_{-8.63}$	3.42E+04	3.34E+04	3.39E+04	3	39
500	$4.84^{+3.53}_{-2.02}$	$19.2^{+5.19}_{-4.57}$	$23.6^{+6.34}_{-4.5}$	3.38E+04	3.35E+04	3.37E+04	8	8
501	$10^{+4.26}_{-3.12}$	$3.81^{+3.34}_{-1.75}$	$14.6^{+5.33}_{-3.47}$	3.84E+04	3.72E+04	3.80E+04	9	9
502	$2.82^{+3.09}_{-1.48}$	$16.5^{+4.6}_{-4.45}$	$21.6^{+6.16}_{-4.26}$	3.84E+04	3.70E+04	3.79E+04	9	9
503	$2.58^{+3.33}_{-1.24}$	$7.5^{+4.44}_{-2.29}$	$12.8^{+4.86}_{-3.4}$	3.43E+04	3.40E+04	3.41E+04	3	3
504	$6.06^{+3.52}_{-2.46}$	$0.682^{+2.61}_{-0.548}$	$5.71^{+3.87}_{-2.11}$	3.06E+04	2.94E+04	2.98E+04	9	9
505	$7.86^{+4.08}_{-2.65}$	$8.45^{+3.49}_{-3.23}$	$16.6^{+5.58}_{-3.72}$	3.83E+04	3.64E+04	3.75E+04	9	9
506	$25.8^{+6.38}_{-4.85}$	$3.15^{+2.76}_{-1.81}$	$30^{+6.51}_{-5.48}$	3.75E+04	3.64E+04	3.71E+04	9	9
507	$0.463^{+1.36}_{-0.463}$	$0.428^{+1.4}_{-0.428}$	$1.27^{+2.02}_{-1.13}$	3.32E+04	3.20E+04	3.27E+04	9	9
508	$0.552^{+2.74}_{-0.418}$	$5.81^{+3.77}_{-2.21}$	$5.81^{+3.77}_{-2.21}$	3.80E+04	3.68E+04	3.75E+04	9	9
509	$12.3^{+4.24}_{-3.74}$	$2.71^{+3.2}_{-1.37}$	$17.3^{+4.88}_{-4.41}$	3.76E+04	3.58E+04	3.68E+04	9	9
510	$5.83^{+3.75}_{-2.22}$	$8.16^{+3.78}_{-2.95}$	$12.1^{+4.48}_{-3.5}$	3.75E+04	3.64E+04	3.71E+04	9	9
511	$9.21^{+3.9}_{-3.16}$	$7.22^{+3.54}_{-2.82}$	$17.5^{+5.8}_{-3.73}$	3.71E+04	3.58E+04	3.66E+04	9	9
512	$27.3^{+5.98}_{-5.44}$	$9.52^{+4.74}_{-2.65}$	$35.3^{+6.64}_{-6.22}$	3.50E+04	3.40E+04	3.45E+04	9	9
513	$4.56^{+3.81}_{-1.74}$	$1.8^{+2.83}_{-1.12}$	$5.37^{+3.01}_{-2.54}$	3.72E+04	3.64E+04	3.68E+04	9	9
514	$32.3^{+6.39}_{-5.96}$	$14.7^{+5.24}_{-3.55}$	$47.6^{+8.38}_{-6.51}$	1.80E+04	1.81E+04	1.75E+04	9	9
515	$12^{+4.54}_{-3.44}$	$9.66^{+4.6}_{-2.78}$	$20.9^{+5.71}_{-4.5}$	3.64E+04	3.44E+04	3.56E+04	9	9
516	$7.14^{+3.62}_{-2.74}$	$11^{+4.39}_{-3.3}$	$18.4^{+4.95}_{-4.57}$	3.57E+04	3.44E+04	3.52E+04	9	9
517	$269^{+17.7}_{-16.1}$	$115^{+12}_{-10.5}$	$380^{+20.7}_{-19.3}$	3.62E+04	3.44E+04	3.55E+04	9	9
518	$14.1^{+4.73}_{-3.81}$	$33.9^{+7.03}_{-5.66}$	$41.4^{+7.08}_{-6.75}$	3.61E+04	3.52E+04	3.57E+04	9	9
519	$15.1^{+4.85}_{-3.94}$	$10.6^{+4.81}_{-2.88}$	$23.4^{+5.49}_{-5.14}$	3.53E+04	3.38E+04	3.47E+04	9	9
520	$2.78^{+3.13}_{-1.43}$	$16.6^{+5.63}_{-3.66}$	$20.4^{+5.09}_{-4.89}$	3.51E+04	3.40E+04	3.46E+04	9	9
521	$12.8^{+4.88}_{-3.38}$	$1.73^{+2.9}_{-1.05}$	$15.6^{+5.53}_{-3.52}$	3.58E+04	3.49E+04	3.54E+04	9	9
522	$13.6^{+5.27}_{-3.27}$	$3.39^{+2.52}_{-2.05}$	$16.8^{+5.37}_{-3.92}$	3.58E+04	3.48E+04	3.53E+04	9	9
523	$7.55^{+4.39}_{-2.33}$	$39.1^{+7.21}_{-6.31}$	$47.5^{+7.42}_{-7.32}$	3.20E+04	3.03E+04	3.08E+04	9	9
524	$20.5^{+6.14}_{-4.06}$	$5.57^{+4.01}_{-1.97}$	$27.6^{+6.75}_{-4.87}$	3.14E+04	3.01E+04	2.94E+04	9	9
525	$9.87^{+4.39}_{-3}$	$3.5^{+2.41}_{-2.16}$	$15.7^{+5.4}_{-3.64}$	3.50E+04	3.39E+04	3.45E+04	9	9

Appendix B

Blackhole mass and X-ray luminosity

In this appendix I discuss the relationship between X-ray luminosity and blackhole mass. A strong correlation between the bolometric luminosity and the mass of supermassive blackhole in an AGN is expected if the supermassive blackhole radiates at a universal Eddington ratio. Surprisingly, using a compiled sample of AGNs with various mass estimates and optical luminosities, (Woo & Urry 2002) claimed that there is little correlation between blackhole mass and bolometric luminosity. However, the bolometric corrections these author used are too simple to deal with the complex extinction in the AGN. This probably explains in part the lack of correlation found in their study.

Being mostly unaffected by absorption (Mushotzky 2004), and most likely coming from regions very close to the blackhole, the hard X-ray radiation should be a better indicator of the energy output of AGNs than the radiation in optical band. We will therefore test the correlation using X-ray luminosity.

While spatially resolved kinematic methods provides very accurate mass estimates, the method is only limited to nearby galaxies. Very few blackhole mass can be measured directly. The best method to measure a sizable sample of blackhole mass in AGNs is reverberation mapping (Peterson 1993). The method assumes that the broad emission lines in AGNs are produced by gas clouds moving at virial velocity v around the blackholes. The radius of the broad line region R_{BLR} is obtained

by measuring the the time lag between the variation of the continuum (presumably from the accretion disk) and the response to the variation in the broad emission lines. The blackhole mass is then

$$M_{BH} = \frac{v^2 R_{BLR}}{G}. \tag{B.1}$$

Even though there has been evidence (Krolik 2001) that the broad line clouds are indeed virialized, the existence of outflow could lead to an overestimation of blackhole mass from Equation B.1.

We search the archive (using BROWSE on HEASARC database) for the hard X-ray fluxes for the 36 broadline AGNs with reverberation mapping mass estimates compiled by Woo & Urry (2002). The *ASCA, HEAO-1* catalogs are searched. In cases where there is no listing of hard X-ray fluxes in these database, we use the *ROSAT* fluxes and convert the 0.5–2 keV flux to 2–10 keV by assuming the source spectra can be described with a single power-law with a photo index of $\Gamma = 1.8$. The redshift, blackhole mass, and the X-ray flux are listed in Table B.1. The rest frame 2–10 keV luminosity are calculated with the standard ΛCDM cosmology. The K-correction is performed assuming a single power-law spectrum with $\Gamma = 1.8$. We plot the blackhole mass versus X-ray luminosity in Figure 63. The data clearly shows a correlation between $\log M_{BH}$ and $\log L_x$. Using linear regression we found

$$\log L_x = (1.03 \pm 0.20) \log M_{BH} + 35.88. \tag{B.2}$$

This agrees perfectly with the same relation found in Barger et al. (2005).

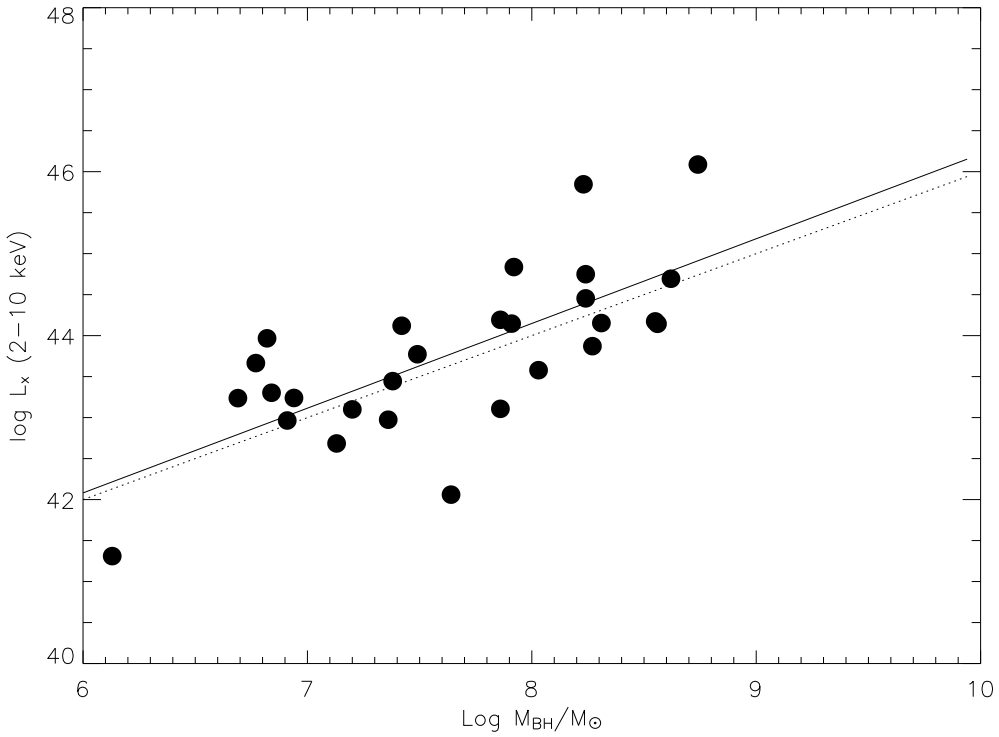

Figure 63: The blackhole mass from reverberation mapping and their 2–10 keV luminosities. The solid line shows the best-fit. The dotted line shows the relation in Equation 6.21 (Barger et al. 2005).

Table B.1. X-ray fluxes for AGNs Compiled in Woo & Urry (2002)

name	redshift	$f_{2-10\ \mathrm{keV}}$[a]	$\log(M_{BH}/\mathrm{M}_{\odot})$
3C120	0.033	4.5	7.42
3C390.3	0.056	1.7	8.55
AKN120	0.032	2.7	8.27
F9	0.047	2.3	7.91
IC4329a	0.016	6.9	6.77
Mrk79	0.022	1.0	7.86
Mrk110	0.035	2.8	6.82
Mrk335	0.026	.96	6.69
Mrk509	0.034	5.0	7.86
Mrk590	0.026	.70	7.2
Mrk817	0.032	.....	7.6
NGC3227	0.004	2.8	7.64
NGC3516	0.009	4.5	7.36
NGC3783	0.01	6.7	6.94
NGC4051	0.002	2.0	6.13
NGC4151	0.003	21.	7.13
NGC4593	0.009	4.4	6.91
NGC5548	0.017	5.0	8.03
NGC7469	0.016	3.0	6.84
PG0026+129	.14	.....	7.58
PG0052+251	0.16	.....	8.41
PG0804+761	0.1	.95	8.24
PG0844+349	0.064	.24	7.38
PG0953+414	0.239	.27	8.24
PG1211+143	0.085	.28	7.49
PG1229+204	0.064	1.2	8.56
PG1307+085	0.155	.....	7.9
PG1351+640	0.087	.....	8.48
PG1411+442	0.089	.....	7.57

Table B.1—Continued

name	redshift	$f_{2-10\ \mathrm{keV}}$[a]	$\log(M_{BH}/\mathrm{M}_\odot)$
PG1426+015	0.086	3.2	7.92
PG1613+658	0.129	.95	8.62
PG1617+175	0.114	.....	7.88
PG1700+518	0.292	.043	8.31
PG2130+099	0.061	.....	7.74
PG1226+023	0.158	15.	8.74
PG1704+608	0.371	1.2	8.23

[a]Unit: $10^{-11}\,\mathrm{erg\,cm^{-2}\,s^{-1}}$

Appendix C

Notes On Cosmology

In this Appendix I will review the basic concepts and some commonly used equations in cosmology. The purpose is to provide needed context and tools to understand the results of our deep survey.

C.1 Standard picture

Modern cosmology is based on a minimal set of assumptions called the *Cosmological principle*, which states that the universe is *uniform* and *isotropic*. This means for any observer "free falling" in the universe, at least on large enough scales, the universe looks the same no matter where you are or which direction you look at. In other words, the spacetime can be sliced into hypersurfaces of constant time.

This lead to the *Robertson-Walker* metric in Riemann geometry,

$$ds^2 = dt^2 - R^2(t)\left[\frac{dr^2}{1-kr^2} + r^2(d\theta^2 + \sin^2\theta d\phi^2)\right], \tag{C.1}$$

where $k = -1, 0, 1$ correspond to open, closed and spatially flat geometries. R(t) is the scaling factor and the coordinates (r, θ, ϕ) can be treated as angles. Let $dx = dr/\sqrt{1-kr^2}$, the expansion velocity

$$\frac{d(R(t)x)}{dt} = \frac{\dot{R}}{R}Rx \equiv H(t)d \tag{C.2}$$

where $H(t)$ is the Hubble function. At present epoch, this gives the *Hubble Law*:

$$v = H_0 d \tag{C.3}$$

where H_0 is the Hubble constant. In the expanding universe, the observed wavelength of light from distant galaxies will be redshifted, and the redshift ($z \equiv \Delta\lambda/\lambda$) can be found to be

$$z = \frac{R_0}{R(t)} - 1. \tag{C.4}$$

By pluging Equation C.1 into Einstein equation and assume the universe is made of perfect fluid, one gets the *Friedman-Lemaître* Equation,

$$H(t)^2 = (\frac{\dot{R}}{R})^2 = \frac{8\pi G\rho}{3} - \frac{kc^2}{R^2} + \frac{\Lambda c^2}{3}, \tag{C.5}$$

and

$$\frac{\ddot{R}}{R} = \frac{\Lambda c^2}{3} - \frac{4\pi G}{3}(\rho + 3p/c^2), \tag{C.6}$$

where Λ is the cosmological constant. Conservation of energy yields

$$\dot{\rho} = -3H(t)(\rho + p/c^2). \tag{C.7}$$

To complete the equations, the equation of state is needed, which commonly assume the form

$$p = wc^2\rho. \tag{C.8}$$

In case of relativistic particle/radiation dominated equation of state, $w = 1/3$; in the matter dominated case, $w = 0$; and in the cosmological constant/dark energy dominated case, $w = -1$. From Equation C.7, we have

$$\rho \propto R^{-3(1+w)} \tag{C.9}$$

We next introduce some commonly used cosmological parameters in the standard model. By defining the density parameter

$$\Omega_M = \frac{8\pi G\rho_0}{3H_0^2}, \tag{C.10}$$

the normalized cosmological constant

$$\Omega_\Lambda = \frac{\Lambda c^2}{3H^2}, \tag{C.11}$$

and normalized Hubble function

$$H(z) = H_0 E(z), \tag{C.12}$$

the Friedman Equation can be written as

$$E(z)^2 = \Omega_M(1+z)^3 + \Omega_\Lambda + (1 - \Omega_M - \Omega_\Lambda)(1+z)^2, \tag{C.13}$$

where we have used Equation C.8 and Equation C.7 to eliminate ρ and p. The evolution of Ω_M and Ω_Λ are simply

$$\Omega_M(z) = \frac{\Omega_M}{E(z)^2}(1+z)^3 \tag{C.14}$$

$$\Omega_\Lambda(z) = \frac{\Omega_\Lambda}{E(z)^2} \tag{C.15}$$

Sometimes, we use the curvature density parameter Ω_k, which can be defined using Friedman Equation,

$$\Omega_k = 1 - \Omega_M - \Omega_\Lambda. \tag{C.16}$$

In Figure 64 we show the evolution of Ω_M and Ω_Λ in the ΛCDM model. At $z >> 1$, $\Omega_M \rightarrow 1$, approaching an Einstein–de Sitter model.

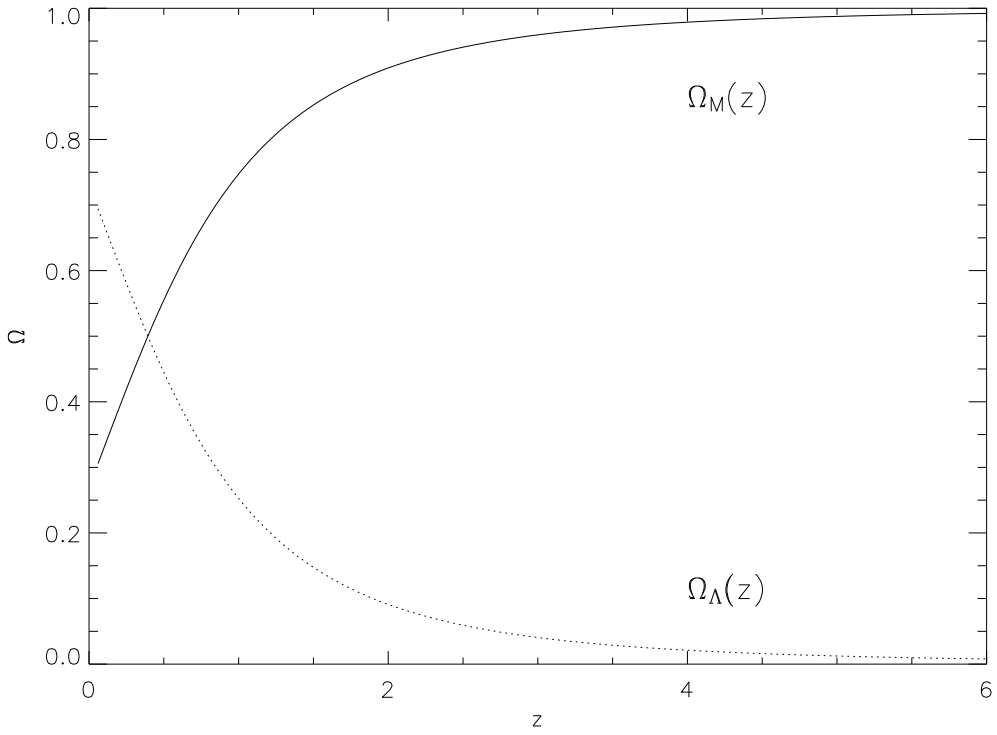

Figure 64: The evolution of Ω_M (solid line) and Ω_Λ (dotted line).

C.2 Cosmological distances

The *comoving distance* is the distance between two objects if both are locked in the Hubble flow and measured at present epoch. The comoving distance can be obtained directly from the Robertson-Walker metric (Equation C.1). We first

look at the comoving distance of a galaxy at redshift of z. Along the line-of-sight $(d\theta = 0, d\phi = 0)$ we have

$$\tilde{r} = \int_0^r \frac{dr}{1 - kr^2} = \int_0^t \frac{c}{R(t)} dt. \tag{C.17}$$

Using Equation C.12 and the definition of redshift, and scale $\tilde{r}$ with R_0, we have

$$D_c = R_0 \tilde{r} = \frac{c}{H_0} \int_0^z \frac{dz'}{E(z')} \tag{C.18}$$

On the other hand, if the two objects are at the same redshift but are separated by some angle $\delta\psi$, then the the comoving distance $D\delta\psi$ gives the separation of the two objects at the presnet epoch. When studying the large scale structure, we need to calculate the comoving distance between two objects in different directions and with different redshifts. It can be shown that (Matarrese et al. 1997),

$$d = \sqrt{\eta D_1^2 + D_2^2 - 2\eta D_1 D_2 \cos\theta}, \tag{C.19}$$

where

$$\eta = \sqrt{1 + \Omega_k (\frac{H_0 D_1}{c})^2} + \frac{D_1 \cos\theta}{D_2} \left(1 - \sqrt{1 + \Omega_k (\frac{H_0 D_2}{c})^2} \right). \tag{C.20}$$

In observational cosmology there are a few "distances" defined so that the relations in the Euclidean space can be applied. If a galaxy has a physical size dl, and the anglular diameter is $d\psi$, we can define *angular diameter distance* so that

$$dl = D_A d\psi. \tag{C.21}$$

The *luminosity distance* is defined so that a galaxy at redshift of z have luminosity of L, then the observed flux is

$$f = \frac{L}{4\pi D_L^2} \tag{C.22}$$

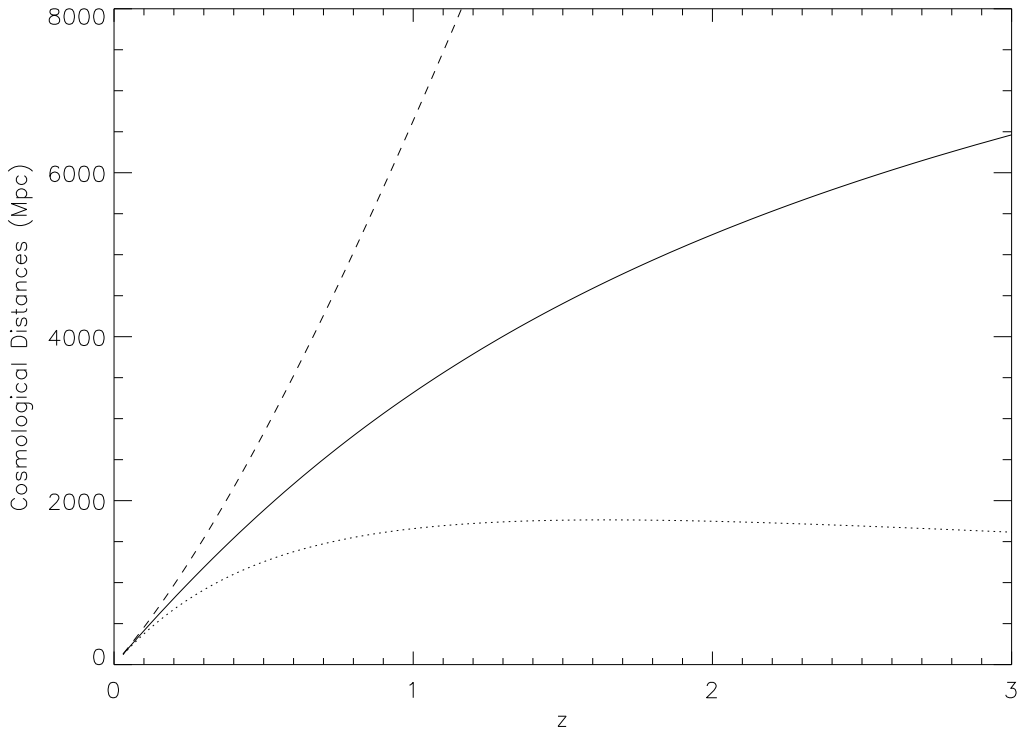

Figure 65: Comoving distance (solid line), angular size distance (dotted-line) and luminosity distance (dashed-line) as a function of redshift. We have chosen $k = 0$ and $\Omega_\Lambda = 0.73$. (dotted line).

These distances are related to the comoving distance in a simple way,

$$D_A = \frac{D}{1+z} \tag{C.23}$$

$$D_L = D(1+z) = (1+z)^2 D_A \tag{C.24}$$

The cosmological distances as a function of redshift in a ΛCDM cosmology is shown in Figure 65.

In some circumstances such as in the gravitational lensing equation, the angular distance between two objects at different redshifts need to be calculated. For $\Omega_k \geq 0$, the angular distance of object 2 seen from object 1 is

$$D_A(z_1, z_2) = \frac{1}{1+z_2}\left(D_2\sqrt{1+\Omega_k D_1^2 H_0^2/c^2} - D_1\sqrt{1+\Omega_k D_2^2 H_0^2/c^2}\right). \tag{C.25}$$

This implies the *reciprocity theorem*:

$$\frac{D_A(z_1, z_2)}{D_A(z_2, z_1)} = \frac{1 + z_1}{1 + z_2}. \tag{C.26}$$

When $k = 0$, Equation C.25 simplifies to

$$D_A(z_1, z_2) = \frac{1}{1 + z_2}(D_2 - D_1). \tag{C.27}$$

BIBLIOGRAPHY

Adelberger, K. L., Steidel, C. C., Giavalisco, M., Dickinson, M., Pettini, M., & Kellogg, M. 1998, ApJ, 505, 18

Akiyama, M. 2005, ArXiv Astrophysics e-prints

Akiyama, M., Ueda, Y., Ohta, K., Takahashi, T., & Yamada, T. 2003, ApJS, 148, 275

Akylas, A., Georgantopoulos, I., & Plionis, M. 2000, MNRAS, 318, 1036

Alexander, D. M., Bauer, F. E., Brandt, W. N., Schneider, D. P., Hornschemeier, A. E., Vignali, C., Barger, A. J., Broos, P. S., Cowie, L. L., Garmire, G. P., Townsley, L. K., Bautz, M. W., Chartas, G., & Sargent, W. L. W. 2003, AJ, 126, 539

Alexander, D. M., Brandt, W. N., Hornschemeier, A. E., Garmire, G. P., Schneider, D. P., Bauer, F. E., & Griffiths, R. E. 2001, AJ, 122, 2156

Andreani, P. & Cristiani, S. 1992, ApJ, 398, L13

Baldi, A., Molendi, S., Comastri, A., Fiore, F., Matt, G., & Vignali, C. 2002, ApJ, 564, 190

Barger, A. J., Cowie, L. L., Capak, P., Alexander, D. M., Bauer, F. E., Fernandez, E., Brandt, W. N., Garmire, G. P., & Hornschemeier, A. E. 2003, AJ, 126, 632

Barger, A. J., Cowie, L. L., Mushotzky, R. F., Yang, Y., Wang, W.-H., Steffen, A. T., & Capak, P. 2005, AJ, 129, 578

Basilakos, S., Georgakakis, A., Plionis, M., & Georgantopoulos, I. 2004, ApJ, 607, L79

Bauer, F. E., Alexander, D. M., Brandt, W. N., Schneider, D. P., Treister, E., Hornschemeier, A. E., & Garmire, G. P. 2004, AJ, 128, 2048

Bertin, E. & Arnouts, S. 1996, A&AS, 117, 393

Brandt, W. N. & Hasinger, G. 2005, ArXiv Astrophysics e-prints

Carrera, F. J., Fabian, A. C., & Barcons, X. 1997, MNRAS, 285, 820

Carroll, S. M., Press, W. H., & Turner, E. L. 1992, ARA&A, 30, 499

Cash, W. 1979, ApJ, 228, 939

Coil, A. L., Davis, M., Madgwick, D. S., Newman, J. A., Conselice, C. J., Cooper, M., Ellis, R. S., Faber, S. M., Finkbeiner, D. P., Guhathakurta, P., Kaiser, N., Koo, D. C., Phillips, A. C., Steidel, C. C., Weiner, B. J., Willmer, C. N. A., & Yan, R. 2004, ApJ, 609, 525

Cowie, L. L., Garmire, G. P., Bautz, M. W., Barger, A. J., Brandt, W. N., & Hornschemeier, A. E. 2002, ApJ, 566, L5

Cowie, L. L., Songaila, A., Hu, E. M., & Cohen, J. G. 1996, AJ, 112, 839

Croom, S. M., Boyle, B. J., Shanks, T., Smith, R. J., Miller, L., Outram, P. J., Loaring, N. S., Hoyle, F., & da Ângela, J. 2005, MNRAS, 356, 415

Croom, S. M. & Shanks, T. 1996, MNRAS, 281, 893

Croom, S. M., Shanks, T., Boyle, B. J., Smith, R. J., Miller, L., Loaring, N. S., & Hoyle, F. 2001, MNRAS, 325, 483

da Ângela, J., Outram, P. J., Shanks, T., Boyle, B. J., Croom, S. M., Loaring, N. S., Miller, L., & Smith, R. J. 2005, MNRAS, 360, 1040

Davis, M. & Peebles, P. J. E. 1983, ApJ, 267, 465

Dickey, J. M. & Lockman, F. J. 1990, ARA&A, 28, 215

Efron, B. 1982, The Jackknife, the Bootstrap, and Other Resampling Plans (Philadelphia: SIAM)

Elvis, M., Wilkes, B. J., McDowell, J. C., Green, R. F., Bechtold, J., Willner, S. P., Oey, M. S., Polomski, E., & Cutri, R. 1994, ApJS, 95, 1

Fan, X., Strauss, M. A., Schneider, D. P., Gunn, J. E., Lupton, R. H., Yanny, B., Anderson, S. F., Anderson, J. E., Annis, J., Bahcall, N. A., Bakken, J. A., Bastian, S., Berman, E., Boroski, W. N., Briegel, C., Briggs, J. W., Brinkmann, J., Carr, M. A., Colestock, P. L., Connolly, A. J., Crocker, J. H., Csabai, I., Czarapata, P. C., Davis, J. E., Doi, M., Elms, B. R., Evans, M. L., Federwitz, G. R., Frieman, J. A., Fukugita, M., Gurbani, V. K., Harris, F. H., Heckman, T. M., Hennessy, G. S., Hindsley, R. B., Holmgren, D. J., Hull, C., Ichikawa, S., Ichikawa, T., Ivezić , Ž., Kent, S., Knapp, G. R., Kron, R. G., Lamb, D. Q., Leger, R. F., Limmongkol, S., Lindenmeyer, C., Long, D. C., Loveday, J., MacKinnon, B., Mannery, E. J., Mantsch, P. M., Margon, B., McKay, T. A., Munn, J. A., Nash, T., Newberg, H. J., Nichol, R. C., Nicinski, T., Okamura, S., Ostriker,

J. P., Owen, R., Pauls, A. G., Peoples, J., Petravick, D., Pier, J. R., Pordes, R., Prosapio, A., Rechenmacher, R., Richards, G. T., Richmond, M. W., Rivetta, C. H., Rockosi, C. M., Sandford, D., Sergey, G., Sekiguchi, M., Shimasaku, K., Siegmund, W. A., Smith, J. A., Stoughton, C., Szalay, A. S., Szokoly, G. P., Tucker, D. L., Vogeley, M. S., Waddell, P., Wang, S., Weinberg, D. H., Yasuda, N., & York, D. G. 1999, AJ, 118, 1

Ferrarese, L. 2002, ApJ, 578, 90

Ferrarese, L. & Merritt, D. 2000, ApJ, 539, L9

Fiore, F., La Franca, F., Vignali, C., Comastri, A., Matt, G., Perola, G. C., Cappi, M., Elvis, M., & Nicastro, F. 2000, New Astronomy, 5, 143

Fischer, J.-U., Hasinger, G., Schwope, A. D., Brunner, H., Boller, T., Trumper, J., Voges, W., & Neizvestny, S. 1998, Astronomische Nachrichten, 319, 347

Freeman, P. E., Kashyap, V., Rosner, R., & Lamb, D. Q. 2002, ApJS, 138, 185

Fry, J. N. 1996, ApJ, 461, L65+

Gebhardt, K., Bender, R., Bower, G., Dressler, A., Faber, S. M., Filippenko, A. V., Green, R., Grillmair, C., Ho, L. C., Kormendy, J., Lauer, T. R., Magorrian, J., Pinkney, J., Richstone, D., & Tremaine, S. 2000, ApJ, 539, L13

Gehrels, N. 1986, ApJ, 303, 336

Giacconi, R., Gursky, H., Paolini, F. R., & Rossi, B. B. 1962, Physical Review Letters, 9, 439

Giacconi, R., Zirm, A., Wang, J., Rosati, P., Nonino, M., Tozzi, P., Gilli, R., Mainieri, V., Hasinger, G., Kewley, L., Bergeron, J., Borgani, S., Gilmozzi, R., Grogin, N., Koekemoer, A., Schreier, E., Zheng, W., & Norman, C. 2002, ApJS, 139, 369

Giavalisco, M. & Dickinson, M. 2001, ApJ, 550, 177

Gilli, R., Cimatti, A., Daddi, E., Hasinger, G., Rosati, P., Szokoly, G., Tozzi, P., Bergeron, J., Borgani, S., Giacconi, R., Kewley, L., Mainieri, V., Mignoli, M., Nonino, M., Norman, C., Wang, J., Zamorani, G., Zheng, W., & Zirm, A. 2003, ApJ, 592, 721

Gilli, R., Daddi, E., Zamorani, G., Tozzi, P., Borgani, S., Bergeron, J., Giacconi, R., Hasinger, G., Mainieri, V., Norman, C., Rosati, P., Szokoly, G., & Zheng, W. 2005, A&A, 430, 811

Giveon, U., Maoz, D., Kaspi, S., Netzer, H., & Smith, P. S. 1999, MNRAS, 306, 637

Grazian, A., Negrello, M., Moscardini, L., Cristiani, S., Haehnelt, M. G., Matarrese, S., Omizzolo, A., & Vanzella, E. 2004, AJ, 127, 592

Gursky, H. & Schwartz, D. A. 1977, ARA&A, 15, 541

Hamilton, A. J. S. 1992, ApJ, 385, L5

Harrison, F. A., Eckart, M. E., Mao, P. H., Helfand, D. J., & Stern, D. 2003, ApJ, 596, 944

Hasinger, G., Burg, R., Giacconi, R., Schmidt, M., Trumper, J., & Zamorani, G. 1998, A&A, 329, 482

Ho, L. C. 2005, ArXiv Astrophysics e-prints

Hornschemeier, A. E., Bauer, F. E., Alexander, D. M., Brandt, W. N., Sargent, W. L. W., Vignali, C., Garmire, G. P., & Schneider, D. P. 2003, Astronomische Nachrichten, 324, 12

Ivezić, Ž., Menou, K., Knapp, G. R., Strauss, M. A., Lupton, R. H., Vanden Berk, D. E., Richards, G. T., Tremonti, C., Weinstein, M. A., Anderson, S., Bahcall, N. A., Becker, R. H., Bernardi, M., Blanton, M., Eisenstein, D., Fan, X., Finkbeiner, D., Finlator, K., Frieman, J., Gunn, J. E., Hall, P. B., Kim, R. S. J., Kinkhabwala, A., Narayanan, V. K., Rockosi, C. M., Schlegel, D., Schneider, D. P., Strateva, I., SubbaRao, M., Thakar, A. R., Voges, W., White, R. L., Yanny, B., Brinkmann, J., Doi, M., Fukugita, M., Hennessy, G. S., Munn, J. A., Nichol, R. C., & York, D. G. 2002, AJ, 124, 2364

Kaiser, N. 1987, MNRAS, 227, 1

Kauffmann, G. & Haehnelt, M. 2000, MNRAS, 311, 576

Kauffmann, G. & Haehnelt, M. G. 2002, MNRAS, 332, 529

Kawara, K., Matsuhara, H., Okuda, H., Taniguchi, Y., Sato, Y., Sofue, Y., Wakamatsu, K., Oyabu, S., Sanders, D. B., & Cowie, L. L. 2004, A&A, 413, 843

Kim, D.-W., Cameron, R. A., Drake, J. J., Evans, N. R., Freeman, P., Gaetz, T. J., Ghosh, H., Green, P. J., Harnden, F. R., Karovska, M., Kashyap, V., Maksym, P. W., Ratzlaff, P. W., Schlegel, E. M., Silverman, J. D., Tananbaum, H. D., Vikhlinin, A. A., Wilkes, B. J., & Grimes, J. P. 2004, ApJS, 150, 19

Koekemoer, A. M., Moustakas, L., Alexander, D., Bauer, F., Bergeron, J., Brandt, W. N., Conselice, C., Chary, R., Yan, H., Cristiani, S., Dickinson, M., Grogin, N., Treister, E., Urry, C. M., Mainieri, V., Stern, D., & GOODS. 2004, American Astronomical Society Meeting Abstracts, 205,

Krolik, J. H. 1999, Active galactic nuclei : from the central black hole to the galactic environment (Active galactic nuclei : from the central black hole to the galactic environment /Julian H. Krolik. Princeton, N. J. : Princeton University Press, c1999.)

—. 2001, ApJ, 551, 72

Kuraszkiewicz, J. K., Wilkes, B. J., Hooper, E. J., McLeod, K. K., Wood, K., Bjorkman, J., Delain, K. M., Hughes, D. H., Elvis, M. S., Impey, C. D., Lonsdale, C. J., Malkan, M. A., McDowell, J. C., & Whitney, B. 2003, ApJ, 590, 128

Kushino, A., Ishisaki, Y., Morita, U., Yamasaki, N. Y., Ishida, M., Ohashi, T., & Ueda, Y. 2002, PASJ, 54, 327

Landy, S. D. & Szalay, A. S. 1993, ApJ, 412, 64

Lonsdale, C., Polletta, M. d. C., Surace, J., Shupe, D., Fang, F., Xu, C. K., Smith, H. E., Siana, B., Rowan-Robinson, M., Babbedge, T., Oliver, S., Pozzi, F.,

Davoodi, P., Owen, F., Padgett, D., Frayer, D., Jarrett, T., Masci, F., O'Linger, J., Conrow, T., Farrah, D., Morrison, G., Gautier, N., Franceschini, A., Berta, S., Perez-Fournon, I., Hatziminaoglou, E., Afonso-Luis, A., Dole, H., Stacey, G., Serjeant, S., Pierre, M., Griffin, M., & Puetter, R. 2004, ApJS, 154, 54

Magliocchetti, M., Maddox, S. J., Jackson, C. A., Bland-Hawthorn, J., Bridges, T., Cannon, R., Cole, S., Colless, M., Collins, C., Couch, W., Dalton, G., de Propris, R., Driver, S. P., Efstathiou, G., Ellis, R. S., Frenk, C. S., Glazebrook, K., Lahav, O., Lewis, I., Lumsden, S., Peacock, J. A., Peterson, B. A., Sutherland, W., & Taylor, K. 2002, MNRAS, 333, 100

Manners, J. C., Johnson, O., Almaini, O., Willott, C. J., Gonzalez-Solares, E., Lawrence, A., Mann, R. G., Perez-Fournon, I., Dunlop, J. S., McMahon, R. G., Oliver, S. J., Rowan-Robinson, M., & Serjeant, S. 2003, MNRAS, 343, 293

Marshall, F. E., Boldt, E. A., Holt, S. S., Miller, R. B., Mushotzky, R. F., Rose, L. A., Rothschild, R. E., & Serlemitsos, P. J. 1980, ApJ, 235, 4

Matarrese, S., Coles, P., Lucchin, F., & Moscardini, L. 1997, MNRAS, 286, 115

Matt, G. 2002, Royal Society of London Philosophical Transactions Series A, 360, 2045

Mo, H. J., Jing, Y. P., & Boerner, G. 1992, ApJ, 392, 452

Mo, H. J. & White, S. D. M. 1996, MNRAS, 282, 347

Moretti, A., Campana, S., Lazzati, D., & Tagliaferri, G. 2003, ApJ, 588, 696

Mullis, C. R., Henry, J. P., Gioia, I. M., Böhringer, H., Briel, U. G., Voges, W., & Huchra, J. P. 2004, ApJ, 617, 192

Mushotzky, R. 2004, How are AGN Found? (ASSL Vol. 308: Supermassive Black Holes in the Distant Universe), 53

Mushotzky, R. F., Cowie, L. L., Barger, A. J., & Arnaud, K. A. 2000, Nature, 404, 459

Navarro, J. F., Frenk, C. S., & White, S. D. M. 1997, ApJ, 490, 493

Nusser, A. & Davis, M. 1994, ApJ, 421, L1

Osmer, P. S. 1981, ApJ, 247, 762

Peebles, P. J. E. 1980, The large-scale structure of the universe (Research supported by the National Science Foundation. Princeton, N.J., Princeton University Press, 1980. 435 p.)

Peterson, B. M. 1993, PASP, 105, 247

Popowski, P. A., Weinberg, D. H., Ryden, B. S., & Osmer, P. S. 1998, ApJ, 498, 11

Pounds, K. A. 1979, Royal Society of London Proceedings Series A, 366, 375

Puchnarewicz, E. M., Mason, K. O., Romero-Colmenero, E., Carrera, F. J., Hasinger, G., McMahon, R., Mittaz, J. P. D., Page, M. J., & Carballo, R. 1996, MNRAS, 281, 1243

Revnivtsev, M., Sazonov, S., Jahoda, K., & Gilfanov, M. 2004, A&A, 418, 927

Reynolds, C. S. & Nowak, M. A. 2003, Phys. Rep., 377, 389

Richards, G. T., Fan, X., Schneider, D. P., Vanden Berk, D. E., Strauss, M. A., York, D. G., Anderson, J. E., Anderson, S. F., Annis, J., Bahcall, N. A., Bernardi, M., Briggs, J. W., Brinkmann, J., Brunner, R., Burles, S., Carey, L., Castander, F. J., Connolly, A. J., Crocker, J. H., Csabai, I., Doi, M., Finkbeiner, D., Friedman, S. D., Frieman, J. A., Fukugita, M., Gunn, J. E., Hindsley, R. B., Ivezić, Ž., Kent, S., Knapp, G. R., Lamb, D. Q., Leger, R. F., Long, D. C., Loveday, J., Lupton, R. H., McKay, T. A., Meiksin, A., Merrelli, A., Munn, J. A., Newberg, H. J., Newcomb, M., Nichol, R. C., Owen, R., Pier, J. R., Pope, A., Richmond, M. W., Rockosi, C. M., Schlegel, D. J., Siegmund, W. A., Smee, S., Snir, Y., Stoughton, C., Stubbs, C., SubbaRao, M., Szalay, A. S., Szokoly, G. P., Tremonti, C., Uomoto, A., Waddell, P., Yanny, B., & Zheng, W. 2001, AJ, 121, 2308

Sadler, E. M., Jackson, C. A., Cannon, R. D., McIntyre, V. J., Murphy, T., Bland-Hawthorn, J., Bridges, T., Cole, S., Colless, M., Collins, C., Couch, W., Dalton, G., De Propris, R., Driver, S. P., Efstathiou, G., Ellis, R. S., Frenk, C. S., Glazebrook, K., Lahav, O., Lewis, I., Lumsden, S., Maddox, S., Madgwick, D., Norberg, P., Peacock, J. A., Peterson, B. A., Sutherland, W., & Taylor, K. 2002, MNRAS, 329, 227

Sandage, A. R. 1971, in Pontificiae Academiae Scientiarum Scripta Varia, Proceedings of a Study Week on Nuclei of Galaxies, held in Rome, April 13-18, 1970, Amsterdam: North Holland, and New York: American Elsevier, 1971, edited by D.J.K. O'Connell., p.271, 271–+

Schmidt, M. 1968, ApJ, 151, 393

Schmidt, M. 1969, in Quasars and high-energy astronomy, 55–+

—. 1970, ApJ, 162, 371

Schneider, D., Fan, X., Hall, P., Jester, S., Richards, G., Stoughton, C., Strauss, M., Subbarao, M., vanden Berk, D., Anderson, S., Brandt, W., Gunn, J., Trump, J., York, D., & York, D. 2004, in ASP Conf. Ser. 311: AGN Physics with the Sloan Digital Sky Survey, 425

Seljak, U. 2002, MNRAS, 337, 774

Shafer, R. A. & Fabian, A. C. 1983, in IAU Symp. 104: Early Evolution of the Universe and its Present Structure, 333–342

Shanks, T. & Boyle, B. J. 1994, MNRAS, 271, 753

Shanks, T., Fong, R., Boyle, B. J., & Peterson, B. A. 1987, MNRAS, 227, 739

Shaver, P. A. 1984, A&A, 136, L9+

Sheth, R. K., Mo, H. J., & Tormen, G. 2001, MNRAS, 323, 1

Shields, G. A., Gebhardt, K., Salviander, S., Wills, B. J., Xie, B., Brotherton, M. S., Yuan, J., & Dietrich, M. 2003, ApJ, 583, 124

Spergel, D. N., Verde, L., Peiris, H. V., Komatsu, E., Nolta, M. R., Bennett, C. L., Halpern, M., Hinshaw, G., Jarosik, N., Kogut, A., Limon, M., Meyer, S. S., Page,

L., Tucker, G. S., Weiland, J. L., Wollack, E., & Wright, E. L. 2003, ApJS, 148, 175

Steffen, A. T., Barger, A. J., Capak, P., Cowie, L. L., Mushotzky, R. F., & Yang, Y. 2004, AJ, 128, 1483

Treyer, M., Scharf, C., Lahav, O., Jahoda, K., Boldt, E., & Piran, T. 1998, ApJ, 509, 531

Veilleux, S. 2002, in ASP Conf. Ser. 284: AGN Surveys, 111–+

Veron, P. & Hawkins, M. R. S. 1995, A&A, 296, 665

Veron-Cetty, M.-P. & Veron, P. 1984, A Catalogue of quasars and active nuclei (ESO Scientific Report, Garching: European Southern Observatory (ESO), 1984)

Vikhlinin, A. & Forman, W. 1995, ApJ, 455, L109+

Vikhlinin, A., Forman, W., Jones, C., & Murray, S. 1995, ApJ, 451, 553

Wake, D. A., Miller, C. J., Di Matteo, T., Nichol, R. C., Pope, A., Szalay, A. S., Gray, A., Schneider, D. P., & York, D. G. 2004, ApJ, 610, L85

Ward, M., Penston, M. V., Blades, J. C., & Turtle, A. J. 1980, MNRAS, 193, 563

Weisskopf, M. C., Aldcroft, T. L., Bautz, M., Cameron, R. A., Dewey, D., Drake, J. J., Grant, C. E., Marshall, H. L., & Murray, S. S. 2003, Experimental Astronomy, 16, 1

White, R. L., Becker, R. H., Gregg, M. D., Laurent-Muehleisen, S. A., Brotherton, M. S., Impey, C. D., Petry, C. E., Foltz, C. B., Chaffee, F. H., Richards, G. T., Oegerle, W. R., Helfand, D. J., McMahon, R. G., & Cabanela, J. E. 2000, ApJS, 126, 133

Woo, J. & Urry, C. M. 2002, ApJ, 579, 530

Worsley, M. A., Fabian, A. C., Bauer, F. E., Alexander, D. M., Hasinger, G., Mateos, S., Brunner, H., Brandt, W. N., & Schneider, D. P. 2005, MNRAS, 357, 1281

Wyithe, J. S. B. & Loeb, A. 2003, ApJ, 595, 614

Yang, Y., Mushotzky, R. F., Barger, A. J., Cowie, L. L., Sanders, D. B., & Steffen, A. T. 2003, ApJ, 585, L85

Yang, Y., Mushotzky, R. F., Steffen, A. T., Barger, A. J., & Cowie, L. L. 2004, AJ, 128, 1501

Zickgraf, F.-J., Engels, D., Hagen, H.-J., Reimers, D., & Voges, W. 2003, A&A, 406, 535